Nonlinear Block Copolymer Nanoreactor-Enabled Precision Synthesis of Metal Oxide Nanoparticles with Controlled Dimensions and Compositions and Investigation into Their Electrocatalytic and Magnetic Properties

A Dissertation

Presented to

The Academic Faculty

by

Yeu-Wei Harn

In Partial Fulfillment

of the Requirements for the Degree

Doctor of Philosophy in the

School of Materials Science and Engineering

Georgia Institute of Technology

August 2020

Nonlinear Block Copolymer Nanoreactor-Enabled Precision Synthesis of Metal Oxide Nanoparticles with Controlled Dimensions and Compositions and Investigation into Their Electrocatalytic and Magnetic Properties

To be approved by:

Dr. Zhiqun Lin, Advisor
School of Materials Science and Engineering
Georgia Institute of Technology

Dr. Zhong Lin Wang, Co-Advisor
School of Materials Science and Engineering
Georgia Institute of Technology

Dr. Seung Soon Jang
School of Materials Science and Engineering
Georgia Institute of Technology

Dr. Vladimir Tsukruk
School of Materials Science and Engineering
Georgia Institute of Technology

Dr. Younan Xia
The Wallace H. Coulter Department of Biomedical Engineering
Georgia Institute of Technology

Dr. Lei Zhu
School of Macromolecular Science and Engineering
Case Western Reserve University

Date Approved: July 21, 2020

Dedicated to My Beloved Family

ACKNOWLEDGEMENT

I would first like to express my sincere gratitude to my advisor Dr. Zhiqun Lin. He is always supportive of student's ideas and providing insightful thoughts on both research direction and result analysis. He often reminds us of the importance of finding the mechanism of the results fundamentally and conducting research systematically. His diligence and passion for science will continuously be the characters that I would like to follow. The time he spent with me for discussing the results, revising the research articles and proposal reports, and holding meetings and conferences is really grateful and will not be forgotten. I would also like to thank all my committee members: Dr. Zhong Lin Wang, Dr. Seung Soon Jang, Dr. Vladimir Tsukruk, Dr. Younan Xia, and Dr. Lei Zhu for their time and help for serving as my Ph.D. proposal and defense committee and sharing their valuable insights and suggestions.

I would also like to thank all the NanoFM group members, who have provided lots of help and encouragements both on research and daily-life perspectives. I really enjoyed the friendly and collaborative working environment in our group. I have witnessed so many people came and left during my Ph.D. study in the group. However, I do appreciate and cherish every chance to encounter new members no matter how long they stay in the group. In particular, I would like to thank Dr. Xinchang Peng, Dr. Yanjie He, Dr. Beibei Jiang, Dr. Zili Li, Dr. Ming He, Dr. Yihuang Chen, Dr. Shuang Pan, Dr. James Iocozzia, Dr. Young Jun Yoon, Dr. Zewei Wang, Dr. Xun Cui, Dr. Yan Yan, Dr. Shiqiang Zhao, Dr. Xiao Li, Dr. Hefeng Zhang, Chao Yang for their helpful guidance and discussion on my research. I am also grateful for the help and support from the members in the nanoreactor subgroup: Jiwoo Yu, Shuang Liang, Mingyue Zhang, Woosung Choi, Dingfeng Shen, and Dr. Baoying Dai. I would like to thank Aurelia Wang, Matt Rager, Dr. Meng Zhang, Dr. Chuntao Lan, Dr. Yajing Chang, Dr. Kunjie Yuan, Dr. Bing Wang, Dr. Hongwei Mi,

Dr. Jiabin Qi, Dr. Johnson Lu for enriching my Ph.D. life in GaTech. I would also like to thank current NanoFM group members, Dr. Shumeng Hao, Dr. Jiawei Zhang, Gill Biesold-Mcgee, Chris Sewell, Songru Jia, Likun Gao, and Wendan Xue.

Lastly, I would like to thank my family for supporting me to pursuit Ph.D. degree in the U.S and endure all my highs and lows during the process. They always provide effective suggestions in terms of research and how to work with others as a group to me. I would not have accomplished this degree without them. I believe Ph.D. study is a valuable experience in my life and all I have learned during this period can be used in the future; therefore, I really appreciate the chance to begin this adventure.

TABLE OF CONTENTS

LIST OF FIGURES

LIST OF TABLES

SUMMARY

Colloidal nanocrystals carry a wide array of intriguing features, thereby rendering a rich diversity of applications in optics, electronics, optoelectronics, catalysis, sensors, energy conversion and storage, nanotechnology, biotechnology, among other areas. Despite copious past works on development of synthetic approaches, the ability to craft functional nanocrystals with precisely controlled compositions and dimensions under mild reaction condition and facile purification process is comparatively few and limited in scope. In this thesis, we developed a general and robust star-like block copolymer nanoreactor strategy for precision synthesis of an assortment of metal oxide nanoparticles controlled dimensions, compositions and surface chemistry, followed by investigation into their size- and composition-dependent electrocatalytic and magnetic properties.

We first successfully synthesize both amphiphilic and hydrophilic star-like diblock and triblock copolymers, which can subsequently function as nanoreactors for templating the precision synthesis of inorganic nanoparticles. In particular, the molecular weights and molecular weight distribution of star-like block copolymers can be readily controlled with the addition of linear initiator as living radical polymerization is achieved. Furthermore, the dual pH-responsive behavior of double hydrophilic star-like diblock copolymer is found, suggesting the potential application as polymer nanocarriers for control-release of drugs.

By capitalizing on amphiphilic star-like diblock copolymer as nanoreactors, perovskite oxide (i.e., $BaTiO_3$, $PbTiO_3$ and doped $BaTiO_3$), La-based perovskite and layered perovskite (i.e., $LaFeO_3$, $LaMnO_3$ and La_2CoO_4) and magnetic spinel ferrite (i.e., $CoFe_2O_4$, $MnFe_2O_4$ and $NiFe_2O_4$) nanoparticles with controllable size can be obtained. Due to the unique compositional versatility and structural stability of perovskites, investigation into electrocatalytic performance of all the as-

synthesized nanoparticles with perovskite and layered perovskite structure is conducted. First, we report the scrutiny of size- and dopant-dependent oxygen reduction reaction (ORR) activities of an array of pristine $BaTiO_3$ and La- or Co-doped $BaTiO_3$ nanoparticles. The ORR activities are found to progressively decrease with the increasing size of $BaTiO_3$ NPs because of increased active sites and electroconductivity. On the other hand, La- and Co-doped $BaTiO_3$ NPs display markedly improved ORR performance over the pristine counterpart, which can be attributed to the reduced limiting barrier and the possibly-increased conductivity that are verified by density functional theory-based first principle calculations. Second, the bifunctional electrocatalytic activity of $LaFeO_3$, $LaMnO_3$ and La_2CoO_4 nanoparticles for both ORR and oxygen evolution reaction (OER) have been revealed. Among all, layered La_2CoO_4 perovskite nanoparticles exhibit remarkable activity and excellent stability (i.e., with the oxygen activity (ΔE) of 0.88 V when D = 8.5 nm), which is greater than that of the previously reported perovskite and perovskite derivative electrocatalysts. The superior catalytic performances of layered La_2CoO_4 perovskite NPs may be resulted from highly active lattice oxygen and an increased concentration of hydroxyl groups, corroborated by the pH-dependent OER behavior and XPS of O 1s results, respectively. Finally, three representative spinel ferrites (i.e., $MnFe_2O_4$, $NiFe_2O_4$, $CoFe_2O_4$) nanoparticles with tunable size are prepared. The size- and composition-dependent magnetic properties are explored and discussed. Moreover, by changing the outer block of the star-like diblock copolymer, hydrophilic poly(ethylene glycol)-ligated spinel ferrite nanoparticles can be acquired, leading to possible biomedical applications. By extension, amphiphilic star-like block copolymer nanoreactor strategy is anticipated to enable the crafting of an exciting variety of other functional nanomaterials with tailored sizes, compositions and surface chemistry. As such, the fundamental correlations between

morphologies, compositions and properties of judiciously designed nanomaterials can be elucidated, rendering the optimized materials performance.

CHAPTER 1. INTRODUCTION

1.1 Background of non-linear block copolymer synthesis

1.1.1 General strategies for synthesis of non-linear polymers

Designing new advanced materials with a controllable molecular structure is essential because it can have a significant influence on the macroscopic properties. For polymers, knowing the chain topology, composition, functionality, and polydispersity of the chain length can lead to optimizing properties for desired applications.[1-5] **Figure 1.1** shows some examples of polymer with various molecular structures, i.e., including change in topology, composition, and functionality.[6] Since the properties are affected by how these macromolecules self-assemble or how they are pre-assembled into larger domains, enhanced control over macromolecular structure is required, which can be achieved by living or controlled polymerization that proceeds with a high degree of selectivity.[7-9] Non-linear polymers, such as cyclic, dendritic,[10-11] brush,[12-14] star-shaped,[15-20] and hyperbranched[21] polymers generally offer lower melt and solution viscosities compared to their linear analogues with similar molecular weight.[22-23] The introduction of even a small fraction of branched polymers can considerably affect the properties like crystallinity, melting point, glass transition temperature, intrinsic viscosity, and viscoelastic behavior.

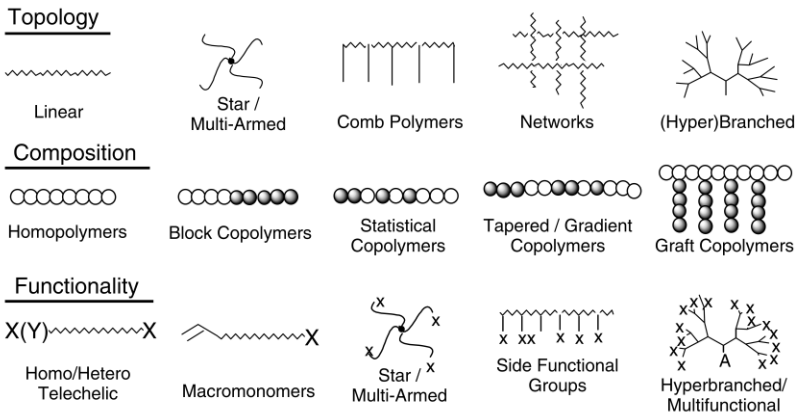

Figure 1.1 Examples of polymer structure with varied topology, composition, and functionality.[6]

Among the common non-linear molecular structures, the star-shaped polymer is the one with the simplest structure. Star-shaped polymers can be described as a single branch point that gives birth to multiple linear polymeric chains, i.e., each polymeric arm has only one branching point.[24-25] Because of the distinct molecular structure, star-shaped polymers demonstrate intriguing features like better solubility, higher functional degree on the surface, lower viscosity compared to their linear polymer counterparts, etc.[26-32] Furthermore, diverse structures with different physical and chemical properties can be self-assembled by star-shaped polymers, opening an avenue for applications in coating, gene therapy, drug delivery,[33-35] separation engineering, etc. Synthesis of star-shaped polymers via living polymerization can be divided into three categories, namely the "coupling-onto" approach,[36-39] the "arm first" approach,[40-41] and the "core-first" approach.[42-43] In the "coupling-onto" method, linear polymeric chains with reactive chain end group and a multifunctional coupling agent (core) are first prepared. The star-shaped polymers are then formed by a coupling reaction between the two.

Because of the slow reaction between the polymeric arm and the core, the "coupling-onto" method can provide the advantages of high coupling efficiency and benign reaction conditions (for instance, click reaction).[44-46] In the "arm first" synthesis, the polymeric chains are prepared first, followed by cross-linking of those arms with the presence of a small amount of suitable multifunctional monomers (usually divinyl cross-linker), eventually resulting in star-shaped polymers.[47-49] Miktoarm star-shaped block copolymers can be produced by initiating those preserved initiating sites with another monomer.[50-52] Notably, the polymerization sequence of cross-linker and monomer, addition of the cross-linker as well as the molar ratios of monomer, cross-linker, and initiator are all critical parameters for obtaining star-shaped polymers.[53-54] Despite the advantage of precisely-controlled arm length, this approach suffers from undefined

star-shaped polymers (i.e., uncertain chain number per star-shaped polymer, thus a broad distribution of the number of arms per polymer); lack of appropriate multifunctional deactivating agents; requisition of long fractionation time to separate the pure star-shaped polymers from unreacted linear polymers and typically non-reactive function of the polymeric ends, preventing this star-shaped polymer from continue participating in further reactions. On the other hand, for "core-first" synthesis, a multifunctional initiator is prepared and serve as the initiator for the subsequent polymerization of monomers to form the arms. The number of arms can be precisely controlled by a pre-designed number of functionalities on the core. Therefore, a well-defined star-shaped polymeric structure with narrow molecular weight distribution among polymer chains can be acquired.[42, 55-57] Nonetheless, this approach also involves a major difficulty of designing and pre-synthesizing multifunctional initiators from which polymer arms can be grown. Moreover, the number of arms per star-shaped polymer might be more restricted, especially with ionic living polymerization.[42, 58-59] Enough number of ion pairs on the star-shaped molecule in close proximity are required when the number of initiating sites increases, possibly leading to lower solubility and stability. Therefore, star-shaped polymers with a large number of arms are not as commonly seen in the literature with this synthetic approach.[24]

Star-shaped polymers can be assigned into two categories, regular star-shaped polymer, and miktoarm star-shaped polymer. Regular ones indicate each polymeric arm within the polymer has the same arm segments, either with homopolymer arms or block copolymer arms. In contrast, miktoarm ones generally imply there is a difference between polymeric chains. Depending on what the difference is, the miktoarm star-shaped polymers can be further categorized into several types, including different chemical structures, topologies, molecular weights, and functional groups (**Figure 1.2**). While anticipated to possess intriguing morphological nanostructures and

supramolecular assemblies, synthesis of miktoarm star-shaped polymers with well-defined structures and multiple precisely designed arms is challenging due to complicated synthesizing and purification procedures.[56, 60-61]

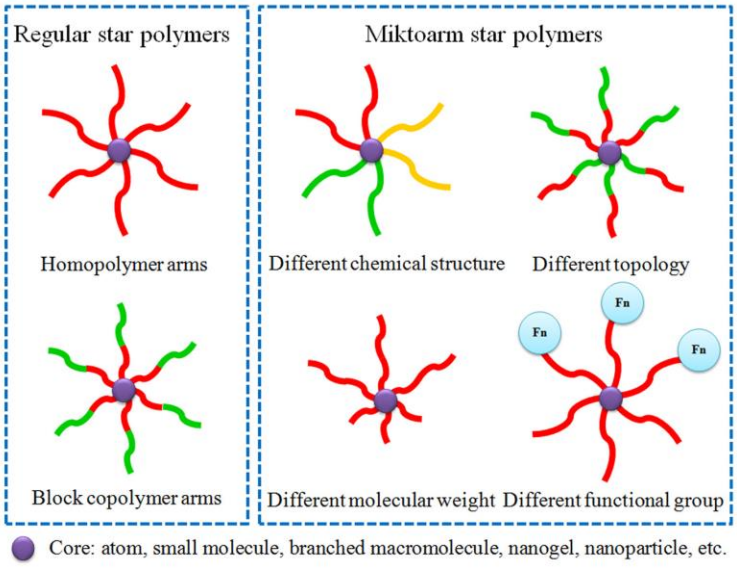

Figure 1.2. Classification of star-shaped polymers.[62]

The capability to form a star-shaped polymer with well-defined structure is desired because it can not only give the possibility to optimize their characteristics, but also elucidate the correlations between their structure and physical/chemical properties. Notably, the well-defined structure here means uniformity in terms of composition and molecular architecture (e.g., molecular weight, molecular weight distribution, and arm number). Despite the successful preparation of star-shaped polymers via living ionic processes, they are limited by harsh reaction conditions and monomer selections. Living/controlled radical polymerization (CRP), such as atom transfer radical polymerization (ATRP), nitroxide-mediated polymerization (NMP), reversible addition-fragmentation chain transfer (RAFT), living anionic/cationic polymerization and ring-opening metathesis polymerization (ROP), has become a robust method for preparing well-defined star-shaped polymers since it doesn't possess those disadvantages.[7, 63] Linear correlation between the

molecular weight of the as-synthesized polymer and monomer conversion is the typical feature that can be found with CRP. The most prominent reactions of CRPs include ATRP, NMP, and RAFT process, which are often employed for the synthesis of polymer with complex architectures. Precisely controlled degree of polymerization and the molecular weight distribution of the as-synthesized polymers can be acquired via all these synthetic methodologies.[2, 4, 64-66] The basic mechanism for CRP involves the controllability between the ratio of active and dormant species (which can be subsequently reactivated). In CRP, radicals add only a few monomer molecules before being converted into dormant species. Thus, the radical lifetime has been prolonged by alternating short activity periods and longer dormant periods. Particularly, polymers synthesized by CRP can show narrow molecular weight distribution due to the fast initiation of dormant species, making all polymer chains grow concurrently.[67-69] Furthermore, in terms of synthesizing star-shaped polymers by CRP, the mechanism can be described as a 2 steps process: preparation of core or scaffold of the star-shaped polymer with various functional groups (typically in a "core-first" approach), and the subsequent polymerization, which the polymer chains are inserted between the core structure and the chain end-functional group (e.g., the dithioester moiety for RAFP process, the halide group for ATRP and the nitroxide for NMP). The simple scheme of this process can be found in **Figure 1.3**. A variety of initiators with a pre-designed number of functionalities were prepared and various monomers had been chosen for subsequent polymerization from those initiators.[70-73]

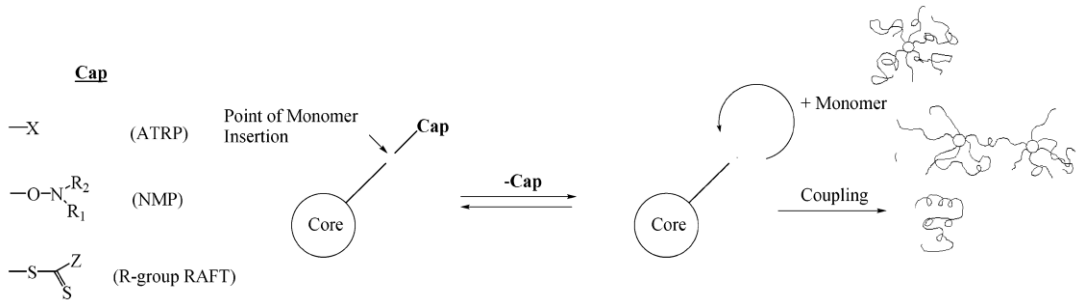

Figure 1.3 Basic principle for synthesizing star-shaped polymer via ATRP, NMR, and R-group RAFT system.[74]

RAFT is a type of CRP using chain transfer agents (CTA, RAFT agent) in the form of a thiocarbonylthio compound to mediate the molecular weight and polydispersity of the as-synthesized polymers. RAFT shows high compatibility with diverse monomers, including methacrylates, methacrylamides, acrylonitrile, styrene, butadiene, vinyl acetate, and N-vinylpyrrolidone, and the process can tolerate a wide range of reaction condition as compared to other CRP. We note that the functional groups of RAFT agent (Z and R group) must be chosen judiciously based on the reaction conditions and type of monomers because they can have significant influences on the polymerization (i.e., Z group affects the rates of the reaction and R group need to stabilize the radical while unstabilize the dormant species).[75-79] The necessity for expensive, colored, or toxic RAFT agents in many cases is the main disadvantage of RAFT.

ATRP, including conventional ATRP, electron transfer ATRP, and electrochemically mediated ATRP, is one of the most commonly-used methods for preparing non-linear polymers and has been studied systematically over the past decades. Star-shaped polymers with controllable molecular weight, low polydispersity (typically < 1.1), and pre-designed composition and functionalities can be produced under suitable reaction conditions. ATRP, as one kind of CRP, involves the reversible deactivation of radicals. The initiators and dormant species for ATRP are alkyl halides (RX) and halogen-capped chains, separately. Transition metal complex is employed during ATRP to reduce

the activation energy for radical generation and to activate initiator and dormant chain ends as well as to deactivate radicals afterward. Therefore, the metal catalyst renders two functions during ATRP, first is the activation step involves radical generation from R-X or dormant polymer chain ends, second is the deactivation step involves the re-formation of dormant species after radical propagation. Copper, among all the transition metal catalysts used in ATRP (e.g., Ru, Fe, Ni, Os, Re, Co, Ti, etc.) is the most intensively-employed element because of its high availability, low cost, and robustness. A variety of Cu complexes have been utilized as catalysts for ATRP. By rationally designing or choosing the ligands used, copper catalyst amount can be reduced to < 100 ppm.[80-84] During the past several years, metal-free ATRP has been developed, which might be able to solve the potential problem of residual metal catalysts after polymerization and purification for some applications. The regeneration of activators of metal-free ATRP or low ppm (of catalyst) ATRP is often obtained by various external stimuli, such as electrical current, photoirradiation, sono-mechanical energy, etc.[85-86] The polymerization stops when those external stimuli are removed because small amounts of radicals terminate and irreversibly convert into deactivator species. Therefore, precise and temporal control of the polymerization can be achieved. Despite the advantages of the absence of residual catalysts and milder reaction parameters, some of the metal-free ATRP reactions suffer from low initiation and irradiation efficiency, complicated synthetic and purification steps for the catalysts as well as the necessitate of the expansion of monomer scope.[87-89] In the future, a better understanding of the kinetics of ATRP quantitatively is important to scale up polymerization processes and further mechanistic analysis, which will be beneficial to the design of the benign polymerization system, faster polymerizations with higher monomer conversions.

1.1.2 Properties and applications of star-shaped polymers

Star-shaped polymers, with at least three polymeric chains grown from one functional core, have gained extensive attention due to their unique topological architecture and attractive physical/chemical properties, such as the exclusive hydrodynamic volumes and encapsulation capabilities because of their globular structures, lower solution viscosity in dilute solutions compared to corresponding linear polymers with same molecular weight due to fewer polymer chain entanglements, various internal and peripheral active groups that can be designed with desired functionalities, enhanced optoelectronic properties and remarkable stimuli-responsiveness due to dense functionalities. Compared to dendritic polymers, star-shaped polymers possess reduced shell density with increased arm length, thus rendering different properties of viscosity and flexibility as well as a lower steric hindrance.[90-94] All the above-mentioned distinct features make star-shaped polymers promising candidates for applications in energy-related fields (i.e., light-emitting diodes, solar cells, and thin-film transistors) and biomedical fields, such as drug/gene delivery, diagnosis, antibacterial/antifouling coatings, and implanted medical devices.[62, 95-99]

The prerequisite of star-shaped polymers for biomedical applications includes well-defined structure, functionality, stimuli-responsiveness, biocompatibility, and biostability. Particularly, designing star-shaped polymer with special functionalities is advantageous because star-shaped architecture has a large number of internal and peripheral active groups, resulting in functionality with high density after modification. Diverse synthetic approaches have been proposed to prepare star-shaped polymers with different functionalities, depending on their specific biomedical applications. For instance, folic acid and alendronic acid are active targeting units assigned for solid tumor targeting and bone targeting, respectively, thus drug delivery efficiency is proved to

be enhanced after modifying drug carriers with these targeting units.[100-102] Li *et al.* have synthesized star-shaped polymer with γ-cyclodextrin as core and oligoethylenimine conjugated with folic acid as arms. This specific star-shaped polymer serving as a drug carrier demonstrates several functions. First, the genes can be efficiently condensed by the cationic arms, and the genes can be delivered into tumor cells with targeting folate receptor of high density. Second, the folate receptor can maintain its function and continuously facilitating cell endocytosis due to the reduction cleavable disulfide bond between oligoethylenimine and folic acid.[103] On the other hand, hydrophilic polymers have been intensively studied as the functional group of the star-shaped polymers due to their remarkable properties, such as better biocompatibility, improved antifouling capability, and hydrophilicity. For example, the drug carries that are made of poly(ethylene glycol)-capped star-shaped polymers demonstrate prolong circulation time due to reduced protein adsorption and improved biocompatibility.[104-108] Antifouling coating of these functionalized star-shaped polymers to resist protein adsorption can also be beneficial to the fabrication of medical devices. Therefore, by judiciously choosing and adding functional groups within star-shaped polymers, a variety of effects can be introduced. It is of particular importance to design the ideal star-shaped polymer system for biomedical applications because multi-functionality is often needed to fulfill the requests of complex physiological conditions.

Stimuli-responsive polymers show observable property changes, including conformational change, reversible solubility variations, and reversible self-assembly, when different environmental condition is applied (e.g., enzymatic reactions, pH value, change in redox potential, temperature, and light).[109-112] Compared to linear polymers, star-shaped polymers can demonstrate stronger stimuli responsiveness due to a more compact structure. Furthermore, various factors of the structure, like arm number, arm length, and core shape can influence the transformation

behavior under external stimuli. Consequently, star-shaped polymers can be employed as smart systems for a variety of biomedical applications, such as target drug delivery, shape-memory biomaterials, and self-healing biomaterials. pH value is a common stimulus because of the intrinsic difference in physiologic pH at the different parts of the body, leading to the possible application as carriers for targeted drug/gene delivery. For example, doxorubicin can be released effectively in the intracellular acidic components, resulting in more efficient tumor therapy by the amphiphilic star-shaped polymers with pH-sensitive hydrazine bond serving as drug carrier that were synthesized by Gong *et al*.[113] In another example, star-shaped polymers with thermo-responsive poly(N-isopropyl acrylamide) (PNIPAAm) as outer block show three-stage transition behavior when temperature changes, which can potentially be employed as temperature-sensitive drug delivery carrier an embolic agent in biomedical fields.[62]

Due to the high demands and widespread use of electronic devices, the rechargeable lithium-ion batteries have not only been widely used as energy supply and storage, but also have attracted much attention as popular research topics. Typically, the lithium-ion battery electrolytes can be categorized into two types, namely solid electrolytes, and liquid electrolytes. Solid electrolytes are regarded as safer electrolytes among the two because of their excellent chemical stability and the adaption of geometry. Various polymers, including poly(vinyl chloride), poly(methyl methacrylate), poly(ethylene oxide) (PEO) and poly(vinylidene fluoride) (PVDF), have been proposed as candidates for solid electrolytes.[114-117] How to enhance ionic conductivity while maintaining mechanical properties is the biggest difficulty of polymer solid electrolyte. Xue *et al.* have synthesized PEO-based star-shaped polymers with varied chain length arms and used them for solid electrolyte (blend with PVDF). The advantages of star-shaped polymers lie in fast molecular motion, thus enhanced conductivity compared to linear polymer because they are harder

to crystallize, improved pore porosity and connectivity as well as better electromechanical stability, indicating star-shaped polymers might be promising electrolytes in lithium-ion battery applications.[118] Moreover, star-shaped polymers can also be employed in application towards solar cells.[119-120] Organic and polymeric photovoltaics, particularly bulk heterojunction solar cells have been of great interest because of their large-scale production feasibility, low fabrication cost, tunable electronic properties, and lightweight over their inorganic counterpart. Key factors for achieving excellent solar cell performance include broad adsorption bands, efficient energy transfer, and efficient hole transport. By synthesizing star-shaped polymers with four blue emissive polymeric chains and three different electron-deficient cores, partial energy transfer from arms to cores can be produced; reduced bandgap can be observed, and enhanced thermal stability can be achieved. Undesired defects in polyfluorene chains can be avoided due to better controllability of chain aggregation and exciton diffusion with the star-shaped architecture. Overall electronic properties prove that star-shaped conjugated polymers can be used for photovoltaic applications.[121] With distinct features star-shaped polymers can provide, they have no doubt can be capitalized in various fields. Nevertheless, difficulties such as residual copper ions (particularly harmful in biomedical applications), a clear understanding of structure-property-function relationships due to the large diversity of star-shaped polymers as well as the development of synergistic and multifunctional star-shaped polymers that can be applied in the complex environment of the human body still need to be addressed. Therefore, persistent efforts for star-shaped polymer related topics are still required.

1.2 Synthesis of perovskite oxide materials and their electrocatalytic properties

1.2.1 Introduction of perovskite oxide materials

Perovskite oxides, having the general formula of ABO_3, are functional ceramic materials that can be used in various applications, such as fuel cells, batteries, transducer, actuators, electromechanical devices, and thermistors, among others.[122-136] Several combinations are possible for A and B cations, resulting in various possible respective valence states. Barium titanate ($BaTiO_3$), lead titanate ($PbTiO_3$), lead zirconate titanate (PZT), lead lanthanum zirconate titanate (PLZT), I-V of $KNbO_3$ and III-III of $LaCoO_3$, etc. are some of the popular materials in the perovskite oxide family. One of the biggest advantages of perovskite phases is that they possess high reactivity and flexibility regarding both oxygen stoichiometry and A-site/B-site cation substitution.[137-142] Different structures render different properties, such as ferroelasticity for $SrTiO_3$, ferroelectricity for $BaTiO_3$, ferromagnetism for $YTiO_3$, piezoelectricity for PZT and pyroelectricity for $LiTaO_3$. Most of these distinct properties occur when the structure deviates from the cubic state, i.e., the phase transition from symmetric structure to distorted structure.[143-144] Generally, the appearance of the distorted structure comes from (1) a shift in the position of the cation on either A-site or B-site from their original positions, (2) a rotation of the BO_6 octahedra around one axis, (3) a deformation of the octahedra, and (4) a distortion of the whole unit-cell by elongating the structure in a specific direction. The Goldschmidt tolerance factor (*t*) is typically used to estimate the internal strains in the perovskite structures regarding the different ionic radius of the cations and interatomic bond lengths:[145-146]

$$t = \frac{r_A + r_O}{\sqrt{2} \times (r_B + r_O)} \quad \text{or} \quad t = \frac{d_{AO}}{\sqrt{2} \times d_{BO}}$$

, where r_A, r_B, and r_O are the radius of ions on A-site, B-site, and oxygen, respectively while d_{AO} and d_{BO} are the distance between cation on A-site/B-site and oxygen, respectively. Strains are minimized with cubic structure when $t = 1$, whereas nonnegligible strains exist, compensated by atomic shifts when $t \neq 0$. For example, when $t > 1$, A-O bonds are stretched and the symmetry becomes rhombohedral, while when $t < 1$, the structure is compressed, and the symmetry becomes tetragonal or orthorhombic. When the value of $t < 0.86$, the perovskite structure is generally regarded as unstable and the atomic arrangement possibly transforms into a layered configuration.[147-151]

Here, among all the perovskite oxides, a brief introduction to lead-free ferroelectric, $BaTiO_3$, will be first provided below owing to its excellent dielectric and ferroelectric properties. Since the discovery of $BaTiO_3$ in 1945, it has been the most extensively-studied ferroelectric material.[152-160] $BaTiO_3$ demonstrates four-phase transitions from cubic, tetragonal, orthorhombic to rhombohedral crystal structures as the temperature decreases.[161-165] At a temperature higher than 120 ^oC, it exists in a face-centered cubic (FCC) structure with larger cation Ba^{2+} and O^{2-} ions forming FCC lattice whereas smaller cation Ti^{4+} occupying octahedral interstitial sites (**Figure 1.4 (a)**). The cubic phase is paraelectric because at a higher temperature, thermal vibration is high enough to result in the random orientation of the Ti^{4+} ions, thus polarization along different directions cancel out each other and no net dipole moment exists after the electric field is removed. As the temperature drops below 120 ^oC, $BaTiO_3$ undergoes a paraelectric to ferroelectric phase transition, from cubic to tetragonal crystal structure ($T < 120\ ^oC$), further transits to orthorhombic phase ($T < 5\ ^oC$) and finally to rhombohedral phase ($T < -90\ ^oC$). All three crystal structures mentioned above can be regarded as elongation of the cubic structure in different directions. Tetragonal structure elongates along c-axis ([001] direction, **Figure 1.4 (b)**); orthorhombic structure elongates along the face

diagonal ([011] direction), and rhombohedral structure elongates along the body diagonal ([111] direction). Due to the distortion of the crystal, a net displacement between cation and anion occurs, leading to the presence of spontaneous polarization and so-called ferroelectric behavior. The characteristics of ferroelectric materials include when applying an electric field of sufficient magnitude, spontaneous polarization aligned with specific direction will be generated, and upon removal of the electric field, the polarization will not return to its original direction and magnitude. Lastly, the polarization direction can be switched when applying the electric field in a different direction. Clearly, $BaTiO_3$ shows ferroelectric behavior when it is with the specific crystal structure, i.e., tetragonal, orthorhombic, and rhombohedral.

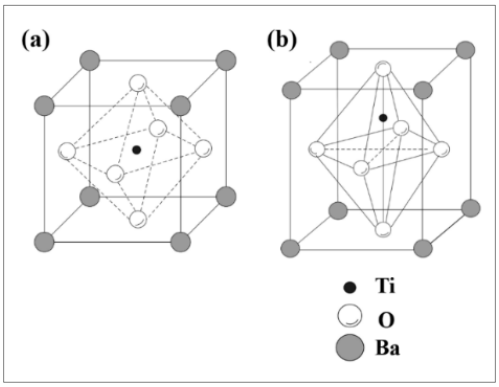

Figure 1.4 Schematic of the perovskite structure of $BaTiO_3$ of **(a)** Cubic structure and **(b)** Tetragonal structure.[166]

When reducing the size of $BaTiO_3$ material into the nanoscale regime, it can demonstrate unique dielectric and ferroelectric properties that are very different from that of the bulk counterpart.[167-172] The dielectric properties of $BaTiO_3$ were found to be highly dependent on grain size mainly result from the changes of characteristics of domains, significant surface energy, and modified long-range dipole interaction when grain size reduces. There are usually two kinds of domains, 90^o and 180^o domains exist in $BaTiO_3$ ferroelectric ceramics. The presence of 90^o domain

can reduce strain energy whereas the presence of 180^{o} domain can reduce the depolarization energy. With a larger grain size, both two types of domains present in the material (**Figure 1.5 (a)**). As the grain size decreases, the width of 90^{o} domain walls decreases and the total number of domain walls increases (**Figure 1.5 (b)**), leading to higher dielectric constant. After reaching a maximum dielectric constant when the grain size is around 0.8-1 μm, dielectric constant starts to decrease due to reduced 90^{o} domain wall as grain size continues to decrease. On the other hand, there are always compensation charges (Q), including those coming from the external circuit, defects, impurities, etc. that exist in the material, trying to compensate the electric field produced by the spontaneous polarization within ferroelectrics and thus reducing depolarization energy. The total compensation charge can be expressed as:[173]

$$Q = P \times S$$

, where P is the polarization, and S is the total surface area of the grain. According to the equation, when the grain size decreases, S increases, thus more mobile charges are required to reduce depolarization energy. 180^{o} domain increases when charges are not enough to completely compensate the electric field, as shown in **Figure 1.5 (c)**. Continue reducing grain size results in the replacement of part of 180^{o} domain wall into grain boundary accompany by a decline in dielectric constant. When grain size further reduces to a couple of tens of nanometers, the grain first becomes single-domain (**Figure 1.5 (d)**) then eventually the disappearance of ferroelectric characterization can be observed (so-called the “critical size”, **Figure 1.5 (e)**).

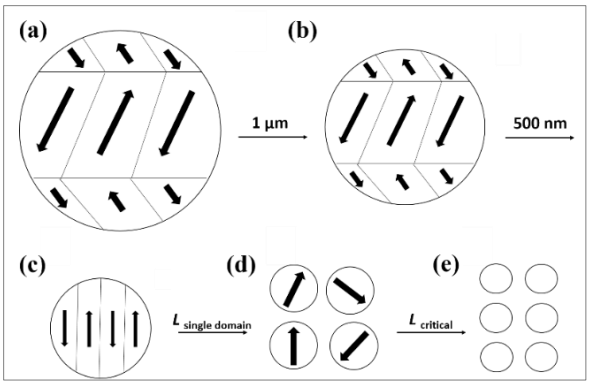

Figure 1.5 Domain structure evolution as crystal size decreases: **(a)** Mixture of two types of domains, **(b)** 90° and **(c)** 180° domain dominate **(d)** single domain and **(e)** non-ferroelectric phase.[173]

1.2.2 Possible derivatives of the perovskite structure

Besides the flexibility of tuning the stoichiometry, i.e., the substitution of the cations on A or B-sites as well as the tolerance of oxygen concentration, perovskites are also well-known for acceptance of various structures.[174-175] For instance, perovskites of the layered structures with the general formula of $A_{n-1}A'_2B_nO_{3n+1}$ can be formed when alternating layers of perovskite-type (ABO_3) and rock-salt type (AO) are intergrown. This structure is called Ruddlesden-Popper phase, and the first-discovered material with this structure was K_2NiF_4.[176-178] In addition to Ruddlesden-Popper phase, derivative structures from original perovskite can typically be acquired by 2 approaches, i.e., changing the intergrowth layer and tuning the oxygen content via oxidation and reduction process (**Figure 1.6**). Remarkably, by conducting those modifications, the capability of tailoring valence states of the ions with different coordination numbers can be achieved, opening avenues to understand the correlation between these intrinsic morphology/physiochemical properties and the desired performance.

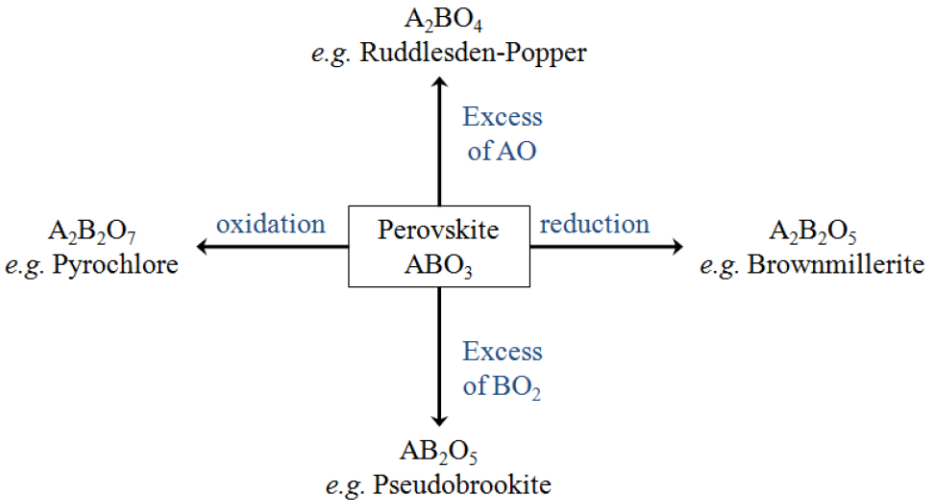

Figure 1.6 Perovskite derivatives obtained by tuning the stoichiometry of cation on A or B-sites (i.e., changing the intergrowth layer, vertical direction) and O anion (horizontal direction).

Various techniques, including thermal treatment, partial pressure of different oxidizing or reducing gases or electrochemistry, can be applied to form perovskites with diverse oxygen amount, and this process is generally reversible. By reducing the stoichiometric ABO_3 perovskite phases, $ABO_{2.5}$ Brownmillerite-type structure can be obtained. Intermediate phases (ABO_{3-x}) can also be stable with different values of x due to the ordering of oxygen vacancies. During the reduction process, O^{2-} anions are removed from the lattice; oxygen vacancies are generated and the coordination numbers/valence states of the cations on B-sites are changed. Therefore, original octahedra BO_6 is substituted by a polyhedral BO_x. Intriguingly, because of specific ion conduction, oxygen ions are removed with an anisotropic diffusion pathway along with the [110] type on the perovskite structure.

Below, we specifically pick Ruddlesden-Popper phase as an example as a derivative structure of perovskites and discuss their various structures in more detail. As mentioned earlier,

Ruddlesden-Popper structure possesses a general formula of $A_{n-1}A'_2B_nO_{3n+1}$. A different number of *n* can exist by introducing additional ABO_3 blocks in the unit cells, whereas the structure with all kinds of *n* value corresponds to the same space group *I*4/mmm. The unit-cell structure with *n* = 1, 2, and 3 can be found in **Figure 1.7**. In particular, the A' cations are characterized by cuboctahedra anionic coordination with a coordination number of 12, while the A cations are located at the interface between layers with a coordination number of 9. The B cations are located at the center of the octahedral formed by 6 oxygen anions located at the apex. The general formula can be simplified into $A_{n+1}B_nO_{3n+1}$ if A and A' cations are identical.[179-181]

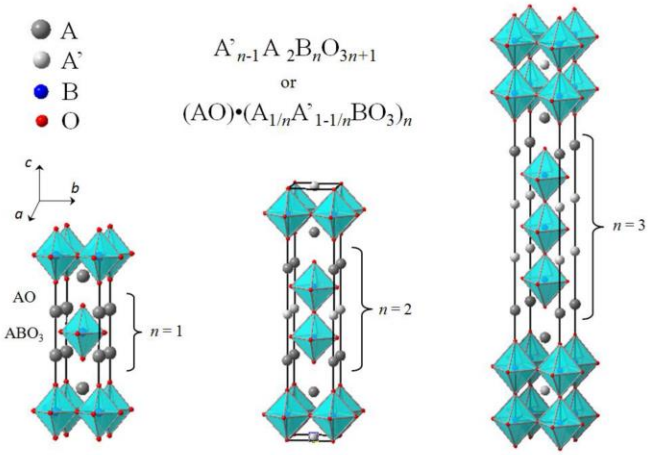

Figure 1.7 Unit-cell structure of Ruddlesden-Popper phases with various thickness number of perovskite layers (n=1, 2, 3).

The La_2MO_4 system, corresponding to the general formula of $A_{n+1}B_nO_{3n+1}$ when n=1, consists of the composition with A = La and B = a transition metal (M), such as Co, Ni, and Cu. At a higher temperature regime, the tetragonal K_2NiF_4-type structure presents, which is called "High Temperature Tetragonal" phase (HTT, T phase) with *I*4/mmm space group.[179] Ideally, MO_6 octahedra are perfectly aligned along the *c*-axis and it is generally difficult to accommodate extra oxygen on interstitial sites. The internal strain of the structure can also be calculated based on

Goldschmidt factor *t*. $t = 1$ when La_2MO_4 is in HTT (T) phase, and transfer into either tetragonal or orthorhombic when $0.86 < t < 1$, accompanied by the compression of the MO_2 planes due to the occurrence of stronger strains. Finally, the structure changes to T'-type phase when $t < 0.86$.[182] The difference between T-type and T'-type phase will be discussed clearly in the next paragraph. There are some approaches to reduce the internal strain within the structure, such as partial substitution (or doping) of La by alkaline metals with smaller ionic radius and tilting the octahedra from the *c*-axis, verified by the observation of phase transition at different temperature regime.

As mentioned before, T'-type phase is also common in Ruddlesden-Popper structure. When A-sites are occupied by the cation from the lanthanide family, all compounds stabilize in T'-type phase except only La adopts T-type phase. The reason lies in different radius between the ions.[183] La ions, with large ionic radius, destabilize T'-type phase due to the size mismatch while other lanthanides with smaller ionic radii prefer to crystallize in T'-configuration. The different between T-type and T'-type phase lies in the position of oxygen in the unit cell. In T-type phase, apical sites are occupied while interstitial sites are empty, and vice-versa for T'-type phase. Nevertheless, they still both correspond to the *I*4/mmm space group. Because of the empty apical position with T'-type phase, the structure frustration induced by the Jahn-Teller effect resulted from BO_6 octahedra can be released, leading to smaller lattice length along the *c*-axis. Oppositely, the lattice length along with *a*-axis increases in T'-type phase compared to T-type phase. Consider both changes in different axes, T'-type phase eventually demonstrates a larger volume of the unit cell compared to that of T-type phase. Even though the Goldschmidt factor *t* can provide information on the stable structure to some extent, several exceptions in predicting the materials with A_2BO_4 stoichiometry still exist. Therefore, a modified tolerance factor *tf* has been proposed:[184]

$$tf = \frac{3\sqrt{2}r_O + 2\sqrt{6}(r_O + r_A)}{9(r_B + r_O)}$$

By considering the bond distance between A-O, B-O, and O-O, the equation can provide perfect differentiation of T-type and T'-type phases. When *tf* falls within 0.96-1.00 range, the material prefers to have T'-type phase, while when *tf* falls within 1.00-1.14 regime, the material becomes T-type phase.

In addition to the complicated yet intriguing structure of Ruddlesden-Popper perovskites, they have attracted great attention because of their distinct properties, such as mixed ionic-electronic conductivity (MIEC) and excellent anisotropic oxygen ion diffusion as well as proton conductivity.[185-191] For instance, A_2BO_4 is reported to demonstrate fast anisotropic oxygen exchange and diffusion kinetics: $La_2NiO_{4+\delta}$ shows 10^2 to 10^3 times larger oxygen interstitial diffusion and surface exchange coefficients along *ab* plane compared to that along *c* plane. These features make this type of material useful in various applications, including electrode materials in solid oxide fuel cells,[192-197] rechargeable metal-air batteries,[177, 198] solar cell materials,[199] oxygen separation membranes,[200] and efficient electro- and photocatalysts. Particularly, they are suitable cathode materials for higher temperatures (i.e., $600 < T < 800$ ^oC) fuel cell applications due to their high oxygen conductivity. Moreover, by simply partial doping with different types of cations and tuning the oxygen content, not only the structure of this layered perovskite can be changed, but also their physical and chemical properties may be optimized for different applications. Ruddlesden-Popper perovskites can also be utilized as catalysts in numerous catalyzed reactions, such as oxidation for CO, decomposition of NO, breaking down phenolic pollutants, CH_4/CO_2 reforming, oxygen evolution reaction (OER) and oxygen reduction reaction (ORR).[201-205]

1.2.3 Routes to perovskite oxide materials and the derivatives

For synthesizing perovskite oxides, there are a variety of approaches. Here, we first discuss the synthetic methods for $BaTiO_3$ as an example. Notably, the quality of the product is not only affected by the synthetic procedures, but also by the starting materials used. Traditionally, based on solid-state reactions, $BaTiO_3$ is synthesized by mixing $BaCO_3$ and TiO_2 powders at high temperatures (1100-1400 ^oC). Despite some of the advantages of this method, it mainly suffers from a high degree of particle agglomeration (rendering large particle size, typically 2-5 μm), extreme reaction condition, high impurity contents, and wide size distribution.

Many wet-chemical approaches, such as organo-metallic, solvothermal/hydrothermal,[206-209] molten salt, co-precipitation, and sol-gel methods are then being developed.[210-215] The hydrothermal method is attractive because $BaTiO_3$ powder can be synthesized easily (i.e., under moderate temperature condition, typically around 100-300 ^oC) without using any elaborate apparatus or expensive reagents, making them ideal for the post-synthetic sintering process. Note that a strong alkaline condition is often required, and the particle sizes are normally in the range of a few hundred nanometers. Coprecipitation is also a simple and convenient method for synthesizing ferroelectric ceramics, except optimal experimental conditions need to be modulated (i.e. to tune the degree of precipitation for both precursors) to obtain the product with the correct stoichiometric ratio between barium and titanium. By the sol-gel method, sol and gel are first formed by hydrolyzing chemical precursor, crystallized products can then be induced after heat treatment. It's an effective way to produce powders with high purity, small size, and relatively good uniformity.[216-220] Among all the precursors used, single bimetallic alkoxide molecular precursors can ensure simultaneous hydrolysis and correct stoichiometry of the product. For example, by employing a specific bimetallic source ($BaTi(O_2CC_7H_{15}[OCH(CH_3)_2]_5)$) as the

precursor, O'Brien *et al.* demonstrated that $BaTiO_3$ nanoparticles (NPs) of 6-12 nm can be synthesized at the temperature as low as 140 ^oC.[155] Brutchey *et al.* reported a novel approach, which prepared crystalline $BaTiO_3$ by the kinetically controlled vapor diffusion of $H_2O_{(g)}/HCl_{(g)}$ into a non-aqueous solution containing another bimetallic alkoxide ($BaTi[OCH_2CH(CH_3)OCH_3]_6$) at room temperature. The keys for successfully synthesizing $BaTiO_3$ NPs at such a low temperature are utilizing single-source bimetallic alkoxide as well as temporally controlled catalytic hydrolysis/polycondensation.[221] In addition to 0D NPs, 1D $BaTiO_3$ nanowires were synthesized by Urban *et al.* using barium titanium isopropoxide with coordinating ligands at 280 °C for 6 h.[222] Despite the advantages of lower reaction temperature, and relatively simple reactants and synthetic procedure, the size and shape of the synthesized $BaTiO_3$ NPs can still not be facilely and precisely tailored. To date, a variety of $BaTiO_3$ nanostructures, including nanodots,[223-226] nanoparticles,[227-231] nanorods, nanocubes, and nanowires with different crystalline phases have been successfully synthesized by the advanced approaches mentioned above. Moreover, many advanced techniques like piezoresponse force microscopy (PFM), neutron scattering, and electron microscopy had been applied to understand the effects of size, shape, microstructure and surface conditions (i.e., defects on the surface or various kinds of capping agents) of $BaTiO_3$ nanomaterials on their electric, dielectric and ferroelectric properties.

Similarly, there are also a variety of methods for preparing Ruddlesden-Popper perovskites, but they generally required high-temperature reaction conditions or implemented in combination with post-high temperature treatments (> 1000 ^oC).[232-235] Typical approaches that are commonly-used are sol-gel synthesis,[236] co-precipitation,[237] spray pyrolysis,[192] and combustion methods,[238] etc. The synthesis of this specific layered perovskite structure is actually quite challenging, not only the ratio between precursors as well as the reaction temperature need to be precisely tuned,

but the oxygen content of the product possibly needs to be controlled by reacting under different atmosphere (e.g., relatively low oxygen partial pressure, reductive atmosphere, etc.). For instance, Zhang *et al.* proposed to synthesize Ruddlesden-Popper La_2MO_4 (M = Ni and Co) layered perovskite and found that pure phase can only be acquired if the reaction temperature was higher than 1100 ^oC. A mixture of layered-perovskite and perovskite was observed when reacting at 850 ^oC.[236] Therefore, it might be beneficial to understand phase transformation behavior by employing in-situ structure diffraction techniques, thus providing guidelines for synthesizing layered perovskites with pure phase. In another example, Weidenthaler *et al.* have reported fabricating layered $La_2CoO_{4\pm\delta}$ perovskite by reducing $LaCoO_3$ perovskite material under a controlled reducing atmosphere (i.e., a mixture of H_2/N_2) and reaction temperature. If the amount of H_2 is too high, the original perovskite may be completely reduced, whereas if the temperature is not within a suitable range, intermediate phases, or complete decomposition of perovskite into simple oxide may occur. They have identified the layered perovskite can be formed at the temperature as low as 650 ^oC, which is generally hard to achieve, with this reducing approach. Notably, even under the optimal condition conducted in this paper, the final product was still a mixture of $La_2CoO_{4\pm\delta}$ and CoO/Co^o, further indicating the difficulty for obtaining layered perovskites with high purity at lower reaction temperature (i.e., phase segregation can be observed in **Figure 1.8**) and distinguishing between stoichiometric, non-stoichiometric and single oxides product due to the similarity in the diffraction peaks.[179]

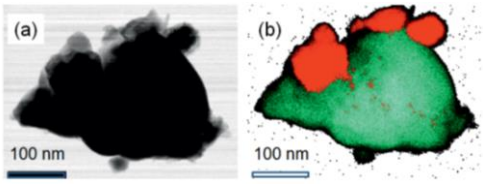

Figure 1.8 (a) STEM image of $La_2CoO_4\pm_\delta$ and **(b)** EDX mapping of La and Co: La-Co phase (green), Co-containing phase (red).[179]

1.2.4 Perovskite oxide materials as electrocatalysts for ORR and OER

In a variety of energy conversion devices such as fuel cells and metal-air batteries, improving the kinetics of oxygen reduction reaction (ORR) and oxygen evolution reaction (OER) are the key approach to optimize the device efficiency.[239-241] Since both reactions have high activation barriers, the overall performance of the energy conversion devices can be seriously limited. Therefore, the introduction of the catalysts is required to reduce the energy barrier and facilitate the reaction. Currently, the noble metal-based electrocatalysts are still being regarded as the best candidates for catalyzing ORR (e.g., Pt) and OER (e.g., IrO_2 and RuO_2). Nevertheless, noble metal electrocatalysts still possess their disadvantages, such as high cost thus limited supply; relatively lower stability, which is possibly due to the tendency to aggregate under working conditions, as well as lacking bifunctionality for serving as good catalysts for both ORR and OER reactions. Discovery of electrocatalysts with low cost and high performance thus gain significant interest among the research society. Perovskite oxides have been regarded as potential candidates among nonprecious catalysts due to their distinct features. First, they can accommodate multiple various cations on A-sites and B-sties, rendering the opportunity to tailor and/or optimize their electronic and catalytic properties.[242-243] Second, partial doping with cations of different ionic radius or valence at the A and B sites can be facilely achieved because of high structure flexibility, leading to changes in the valence states of the cations on A-site and B-site and the formation of charged defects (i.e., oxygen vacancies, electron or cation vacancies) that might be beneficial for ORR and OER reaction.[137, 244-246] Lastly, perovskite oxides are chemically stable under oxidative electrochemical reactions. However, the electrocatalytic performance of most of these studied perovskite catalysts is still insufficient when compared to the precious metals, possibly originated from a lack of understanding of the mechanism of the oxygen electrocatalysis. Furthermore, the

long-standing size effect problem on ORR has yet to be solved due to the incapability of precisely tuning the size of the perovskite catalysts.

The catalytic mechanism of perovskite oxide is different from that of precious metal catalysts since the activity mainly results from the transition metals (typically occupying B-sites). **Figure 1.9** depicts the commonly-accepted pathway for the ORR reaction.[247-248] In brief, the surface M-OH^- species are first formed by coordination between oxygen atom of the H_2O molecule and the transition metal. These species then continue reacting with oxygen, resulting in the oxidation of transition metal (M) and replacement of surface hydroxide (OH^-) to O_2^{2-}, as indicated in step 1. In step 2, surface O_2^{2-} gets protonated while M is being reduced, followed by the oxidation of M and formation of surface O^{2-} (step 3). Finally, surface OH^- is regenerated through the substitution of O^{2-} by OH^- (step 4). From the 4 steps pathway, we can find the binding (i.e., adsorption and desorption) of oxygen on the perovskite surface plays a crucial role in materials' ORR activity. In addition, there are several important factors identified for evaluating the ORR performance of the perovskite electrocatalysts. First is the overlap between the e_g orbital of transition metal and the sp_σ orbital of oxygen.[242, 249] Those possess higher overlap integral are typically regarded as more active electrocatalysts. Second is e_g filling of the transition metal itself. It is generally believed that higher e_g filling interferes with the activation of oxygen and the binding of the reaction intermediate, while lower e_g filling inhibits the desorption of the intermediate. Therefore, e_g filling value around 1 is regarded as the optimal electronic structure for providing higher ORR activity.[250-252] Third, the strength of metal-oxygen bonds, which can be influenced by energetic similarity (covalency) and spatial overlap (hybridization) of metal *3d* orbitals and O *2p* states, is verified to eventually affect catalytic performance.[242] For instance, choosing transition metals that are more electronegative or with higher oxidation state lowers the metal *3d* orbitals into O *2p* states,

resulting in increased bond covalency and hybridization.[253] However, from the results in the literature, we can find that it is not enough to anticipate the ORR performance only based on those mentioned factors. Other descriptors also contribute to the intrinsic ORR activity of the perovskites and need to be discovered under continued researching.

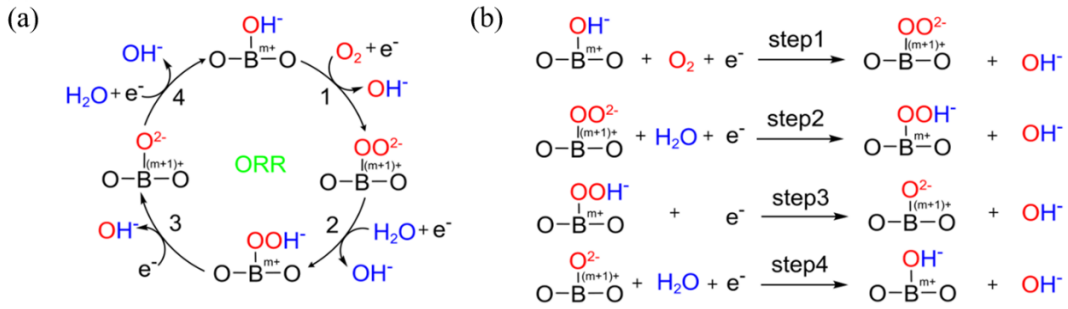

Figure 1.9 (a) ORR mechanism with perovskites serve as electrocatalysts, and **(b)** the detailed steps of ORR by equations.[247]

Figure 1.10 depicts the pathway of the OER process, which is regarded as a reverse process of ORR. The transition metal is also considered as the main active site for OER when using perovskite as the electrocatalyst, and the e_g filling is also thought to be a critical parameter for deciphering the intrinsic OER activity of perovskite oxide materials. When the occupancy of e_g is close to 1.2, the OER performance is believed to be optimized.[137, 247, 254] Compared to ORR, the stability of the electrocatalysts under OER condition is even more important because the structure (i.e., generation of defects such as cation vacancy or oxygen vacancy and varied valence of cation and crystallinity) and intrinsic OER activity of perovskites may change under the high potential applied during OER process.

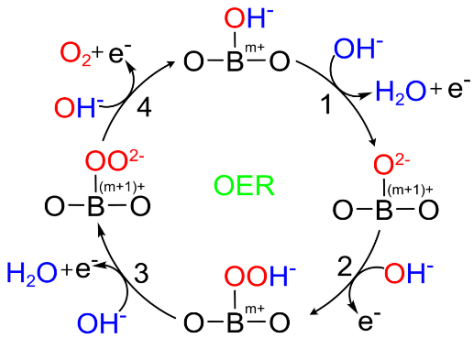

Figure 1.10 OER pathway proposed for perovskite electrocatalysts.[247]

To enhance electrocatalytic performance, several approaches have been applied, including adjusting composition (e.g., completely changing the cation types or partial doping on both A-site and B-site), changing the crystal structure and tuning the oxygen content of the material, possibly resulting in modification of electronic state and eventually different binding energy and/or Gibb's free energy of the reaction. Next, we will explain these strategies in more detail.

In particular, even though cation on A-site is generally not considered as the active site for ORR and OER reaction, doping and/or substituting cations on A-site can still affect the electrocatalytic performance because it might still change the crystal structure as well as the electronic state. Strontium (Sr) is the cation that has often been used as an A-site dopant. For example, doping $LaCoO_3$ with Sr has been reported with enhanced activity of the perovskite electrocatalysts. Two reasons attribute to the result. First, due to the change in the crystal structure, atoms have a higher tendency to align along with the Co-O-Co bond, leading to a higher overlap between the band structure of O *2p* and Co *3d*. Second, since the dopant (Sr^{2+}) has different valence with A-site cation (La^{3+}), the formation of Co with different oxidation states is required to compensate for the charge imbalance. Both reasons can cause better electrocatalytic performance.[255-256] Other reasons that have mentioned in literature for improved activity after A-

site doping include the introduction of local stress, the occurrence of the secondary phase, or the modification of the bond strength via changing/shifting the electronic state.[252, 257] Notably, despite the effectiveness of enhancing the activity after partial A-site doping, the stability of the structure is something that needs to be cautious about because a higher degree of substitution may cause the breakdown of the structure. In addition to doping concentration, pre-designed reaction conditions and/or annealing treatment might be required to obtain perovskite catalysts with optimal electronic configuration and high stability under ORR and OER measurements.

B-site replacement is another effective approach for tuning ORR and OER activity of the perovskite catalyst since transition metal located on B-site is generally regarded as the active site for the catalytic reactions.[258-260] For instance, Cobalt (Co) has been chosen as the dopant of $SrTiO_3$ perovskite material. Both OER activity and stability have been improved compared to the pristine perovskite, and the reasons for the enhancement have been assigned to optimized e_g filling (~1.16) and lower Co-O bond strengths, facilitating the formation of oxygen vacancy thus higher activity.[261] The synergistic effect between two kinds of transition metal ions (e.g., Ni and Co) have also been proved to improve both ORR and OER activity and stability since the introduction of transition metal with different valence (Co^{3+}/ Co^{2+}, Ni^{3+}/ Ni^{2+}) can change the binding energy of the OH^- adsorption and O_2 desorption.[262] Shao *et al.* picked palladium (Pd) as the dopant of $LaFeO_3$ perovskites. The enhancement of the ORR performance (i.e., higher mass activity, better durability and higher tolerance to methanol, **Figure 1.11**) can be observed even with small doping concentration, which was attributed to stabilization of the unusual oxidation states of $3^+/4^+$ for Pd, thus optimal e_g orbital filling and the downshift of the *d*-band center (easier desorption of the generated OH^- and more active sites for further O_2 adsorption).[263] In addition to doping with metal ions, doping the perovskite oxide with non-metal elements on B-site are also proved to be feasible.

Employing phosphor (P) as the dopant in perovskite structure materials (such as $SrCoO_3$, $LaFeO_3$, etc.) with improved OER and ORR activity was found, resulting from increased electric conductivity, changed valence state of original cation on B-site, and thus tailored adsorption and desorption behavior of the intermediates during the reaction.[264-265]

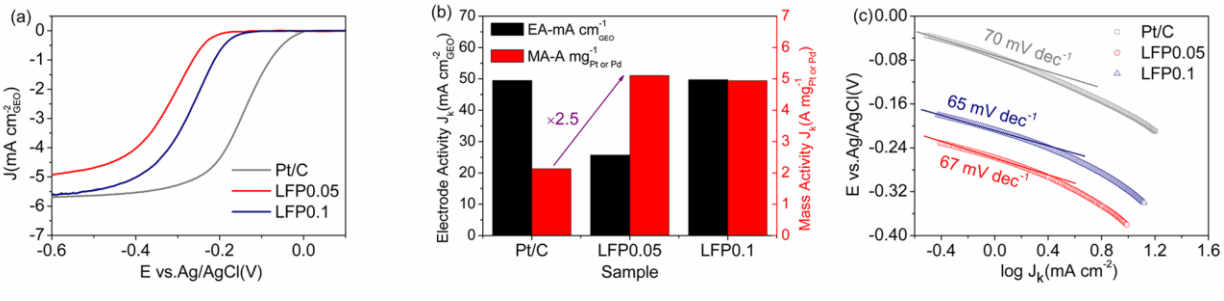

Figure 1.11 (a) LSV curve of Pd-doped $LaFeO_3$ and commercial 20 wt% Pt/C on RDE at 1600 rpm rotation speed in an O_2-saturated 0.1 M KOH electrolyte. **(b)** ORR electrode activity (EA) and mass activity (MA) and **(c)** Tafel plots of the corresponding three samples.[263]

The reactivity of the perovskites can also be affected by oxygen non-stoichiometry, specifically oxygen vacancies.[266-268] Generally, it is believed that the conductivity of the materials can be improved, and the adsorption of intermediates can be promoted with higher oxygen vacancy concentration. Non-stoichiometric perovskites can be rendered by several methods. First is by A-site doping or B-site doping with cations of different valences. For example, when doping $LaCoO_3$ with Sr, both the occurrence of the oxidation of Co (i.e., increased overlap of the Co *3d* orbitals and O *2p* states) and the generation of oxygen vacancies can be observed to reach charge neutrality. The relationship of Sr doping concentration and the electroactivity can be found in **Figure 1.12**, suggesting the best OER performance can be found when La cations are completely substituted by Sr cations.[247] Second, oxygen vacancies can also be generated into the pristine perovskite structure by pre-designed heat treatment/annealing process.[269-270] For example, after successfully obtaining

$BaTiO_3$ nanomaterials, Wu *et al.* had proposed to introduce oxygen vacancies into the structure by annealing the sample in the reductive atmosphere at high temperature (1300 ^oC) under vacuum. The $BaTiO_3$ nanomaterials transformed into hexagonal $BaTiO_{3-x}$, proved by X-ray diffraction and neutron diffraction characterizations. Both enhanced activities in ORR and OER compared to stoichiometric $BaTiO_3$ were observed and attributed to the promotion of reactants adsorption and charge transfer because of the generation of oxygen vacancies.[270] In another research, Yang *et al.* prepared $Ca_2Mn_2O_5$ from perovskite $CaMnO_3$ through a reductive annealing approach under mild reaction temperature. This oxygen-deficient perovskite was then used as electrocatalyst for OER in alkaline media and remarkable performance was observed (i.e., reaching an OER mass activity of 30.1 A/g at 1.70 V). They concluded the high OER performance may be the result of (1) facile transport of OH^- ion due to the changed unit cell structure, (2) electronic structure of cation on B-site with high spin electron occupying e_g orbitals, and (3) promoted bond formation between manganese cation and OH^- via oxygen vacancy.[269]

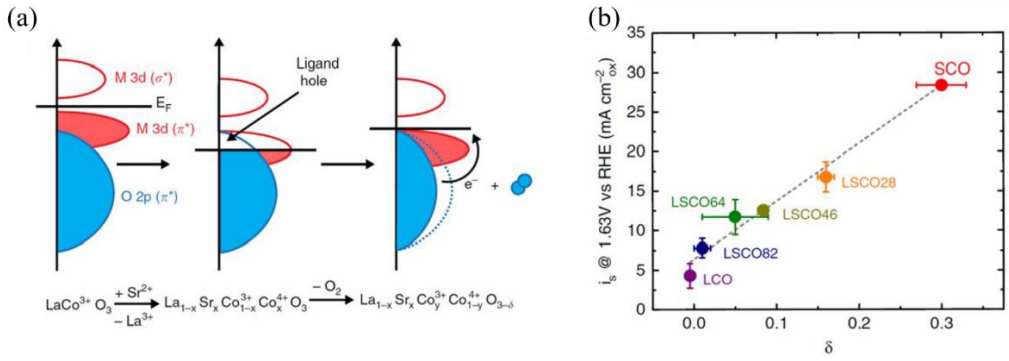

Figure 1.12 (a) Scheme showing the generation of oxygen vacancies with the introduction of Sr in $LaCoO_3$ perovskites. **(b)** OER activity of $La_{1-x}Sr_xCoO_{3-\delta}$ with varied Sr doping concentration.[247]

Intriguingly, different crystal structures of the perovskites might render different electroactivity as well. Sunarso *et al.* synthesized $LaNiO_{3-\delta}$ perovskites with different crystal

structures by heating the product at various temperatures, i.e., 400, 600 and 800°C, and observed the transition in crystal structure from rhombohedral to cubic. $LaNiO_3$ electrocatalysts of cubic structure demonstrated enhanced ORR and OER activities compared to that of rhombohedral ones (**Figure 1.13**). The improved performance was originated from the elongated Ni-O bond length, thus change in Ni-O bond covalency and adjustment of the binding ability with the oxygen (i.e., the removal and adsorption of the oxygen).[271]

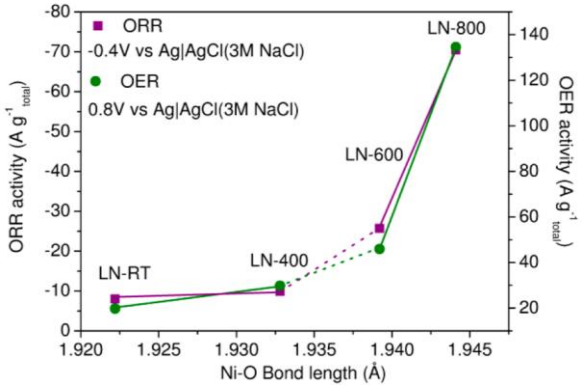

Figure 1.13 Relationship of the ORR/OER activity of $LaNiO_3$ and their Ni-O bond length.[271]

Other research directions include synthesizing perovskite electrocatalysts with higher surface area, which is difficult because high-temperature calcination is generally required for synthesizing perovskites as well as synthesizing composite electrocatalysts (i.e., combining perovskite oxides with other carbon-based materials).[272-273] In addition to the effect of increasing conductivity when combining to carbon-based materials, some synergistic effects are also observed. For instance, when mixing perovskites and the XC-72, a change from the $2e^-$ pathway to the preferred $4e^-$ pathway was found. The change in reaction mechanism and enhanced ORR and OER activity result from the presence of Co with lower valence (reduced by carbon), thus increased intrinsic conductivity.[274] Furthermore, carbon-based materials can also catalyze the disproportionation of

HO_2^- to generate O_2 (in ORR) and facilitate the disproportionation of the intermediate peroxide (in OER).

Compared to the perovskite structure, Ruddlesden-Popper perovskites that serve as electrocatalysts for ORR and OER are relatively less-studied. Huang et al. have synthesized perovskite $LaNiO_3$ (LNO) nanorod and layered $LaNi_2O_4$ perovskite particle and compared their ORR and OER activity after dispersing them on reduced graphene oxide (rGO). LNO-NR/rGO demonstrated better performance in both ORR and OER measurement, following direct $4e^-$ pathway in ORR with lower onset potential and bigger anodic current for OER. They only attributed the difference in performance to morphologic difference (i.e., LNO was in nanorod form whereas $LaNi_2O_4$ was in particle form), thus leading to different conductivity and electroactivity. Further studies can be conducted to investigate the dependence of different crystal structures on electroactivity if the morphology effect can be excluded.[275] Due to the high ionic-electronic conductivity of layered perovskites, most of the research focuses on their properties as high temperatures. Huan *et al.* unveiled the intrinsic effects of a series of Ruddlesden-Popper perovskite catalysts toward ORR and OER activity at high temperature and investigated the influence of low-valence ion doping and high-valence ion doping. First, the excellent intrinsic OER and ORR performance (i.e., before doping) was originated from the increased amount of interstitial O^{2-} of fast migration and highly active lattice oxygen. Second, intriguing observations of low-valence ion doping decreased electroactivity because of suppressed activity of lattice oxygen and decreased interstitial O^{2-} concentration, and high-valence ion doping enhanced electroactivity because of the opposite effect were discovered. The results suggested that by judiciously choosing dopant type, Ruddlesden-Popper perovskites can be promising candidates as oxygen electrodes for solid oxide fuel cells and solid oxide electrolysis cells.[197] In another example, Jung *et al.* reported doped

layered La_2NiO_4 perovskite can serve as efficient bifunctional electrocatalysts for both ORR and OER in an aqueous alkaline electrolyte. Remarkably reduced discharge-charge voltage gaps and high stability during cycling were found with these catalysts in lithium-air and zinc-air batteries applications, which can be explained by higher Ni oxidation state (with suitable doping concentration) as well as the structure-enriched surface hydroxide coverage.[198] Takeguchi *et al.* capitalized another type of Ruddlesden-Popper perovskites, $LaSr_3Fe_3O_{10}$ (n = 3) as a reversible air electrode catalyst for rechargeable metal-air batteries. Outstanding catalytic activities of this layered perovskite can be corroborated with almost negligible overpotentials of both ORR and OER, resulting from easily removable oxygen due to the layered structure.[177]

In summary, perovskites have been verified as promising ORR and OER bifunctional catalysts. Furthermore, the flexibility of these perovskite electrocatalysts in changing the composition and crystal structure may elucidate the relationship of composition, stoichiometry, oxygen deficiency, crystal structure, and ORR/OER performance, and finally lead to the optimal design of the catalysts. However, related studies are still in their early stage and some knowledge and guideline need to be continuously developed. First, due to the complexity of the catalytic process (interplaying factors), the dependency of performance on other intrinsic properties is still unclear to some extent. Pre-design models and systematic studies need to be proposed to understand their correlations. Second, the stability of the perovskite structure needs to be considered when partial doping of cations on A- and/or B-site is conducted and the balance between stability (especially under measuring condition) and activity needs to be determined. Third, both the ORR and OER activities of perovskites are generally inferior to other noble-metal systems, how to further improve the ORR/OER performance is thus another critical research direction. Finally, the synergistic effects between the perovskite oxides and the secondary component in the composite

electrocatalysts are not fully clarified. Further understanding and exploitation should be conducted. Overall, perovskite oxides can be potential candidates as electrocatalysts for advanced energy conversion devices including fuel cells and metal-air batteries, thus widespread applications of these materials might be expected in the future.

1.3 Synthesis of spinel magnetic materials and study of size and composition effects on magnetic properties

1.3.1 Introduction of magnetic properties

The magnetic properties of the material, fundamentally speaking, are the result of the electrons of the atom. At the atomic level, two types of electron motion, spin, and orbital contribute to the magnetic moment of the material. Among all the magnetic-related parameters, susceptibility (χ), i.e., the ratio of magnetization to the magnetic field, and its temperature and field dependencies renders an evaluation of the magnetic behavior of various types of magnetic materials. Based on the response of the magnetic dipole and the net magnetization with and/or without the applied magnetic field, magnetic materials can typically be classified into 5 categories, namely *diamagnetic*, *paramagnetic*, *ferromagnetic*, *ferrimagnetic* and *antiferromagnetic*.[276-280] **Figure 1.14** depicts the magnetic dipole alignment in the presence and absence of applied magnetic fields for each type of magnetic material. Briefly, *diamagnetic* materials do not have net magnetization without applied magnetic field while having magnetic dipole oriented in the opposite direction of the applied magnetic field. Therefore, the *diamagnetic* materials are repelled by a magnetic field. Oppositely, *paramagnetic* materials already possess nonzero magnetic moment because of unpaired electrons, and they show magnetic dipole moments of the same direction of the applied magnetic field. But the values of susceptibility are relatively small, within the order of 10^{-3} to 10^{-5}. For these two types of magnetic materials, the magnetic dipoles orient back to zero magnetization (*diamagnet*) or the intrinsically preferred direction (*paramagnet*) when the applied magnetic field is removed. On the other hand, *ferromagnetic*, *ferrimagnetic*, and *antiferromagnetic* can all be counted as a different category since partial magnetic dipoles remain even after the

magnetic field had been removed. The differences among these three kinds of magnetic materials lie in the alignment of the neighboring magnetic dipoles. *Ferromagnetic* materials have all the magnetic dipoles align in the same direction via the exchange coupling between neighboring moments whereas both *antiferromagnetic* and *ferrimagnetic* materials have the neighboring magnetic dipoles align in the opposite direction. *Ferromagnetic* materials therefore generally render larger magnetization in a relatively weak magnetic field compared to the other two. Due to the difference in the magnitude of the neighboring magnetic dipoles, *antiferromagnetic* materials demonstrate zero net magnetization (equal magnitude of the oppositely aligned magnetic moment that completely cancels out each other), while *ferrimagnetic* materials demonstrate some net magnetization (the magnitude of the magnetic moment in one direction is larger than that in the opposite direction).[281]

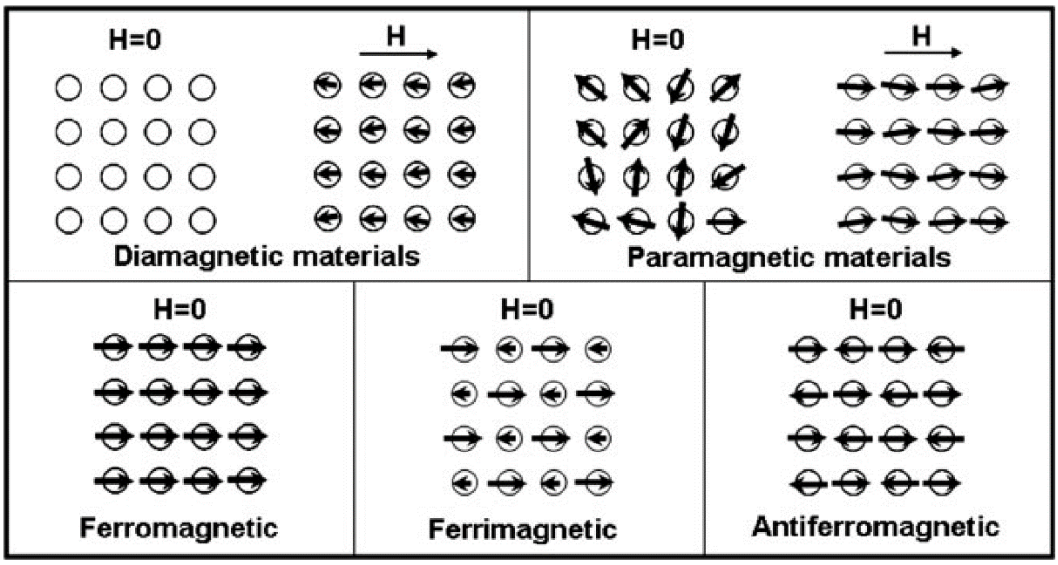

Figure 1.14 Magnetic dipole moments and the behavior with and without the applied magnetic field. Based on the alignment of the magnetic dipole moment under different conditions, materials can be categorized into 5 types, i.e., *diamagnetic*, *paramagnetic*, *ferromagnetic*, *ferrimagnetic*, and *antiferromagnetic*.[281]

Typical hysteresis loop for both ferro- or ferrimagnetic materials can be used to describe the magnetic behaviors, with some basic parameters like magnetization *M* or flux density *B* against the magnetic field strength *H*. Due to the response time for the reorientation of the magnetic dipole moment or the motion of magnetic domain walls, there's always a delay between magnetization and external magnetic field, leading to the formation of the hysteresis loop.[282-283] **Figure 1.15** shows the hysteresis loop, i.e., magnetization versus the applied magnetic field, from which we can obtain the saturation magnetization (M_s, or the maximum value of *M*), remanence magnetization (M_r, or the residual magnetization when the magnetic field is completely removed), and the coercivity (H_c, external filed needed to reduce the magnetization back to zero). If the materials can be magnetized in a weak field (around 10 Oe), they are regarded as soft magnets. For instance, some permalloy (NiFe alloys) or amorphous metal alloys can be magnetized at only 12 mOe applied magnetic field. Oppositely, if the materials need relatively large external fields to demagnetize and re-orientate the original magnetic dipole moment, they are regarded as hard magnets.

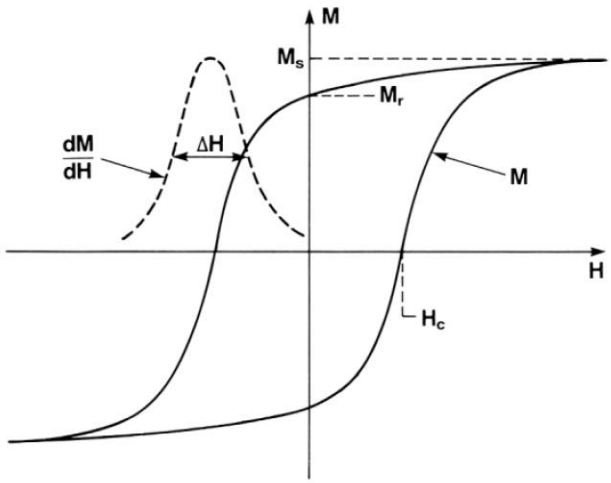

Figure 1.15 Typical hysteresis loop of a ferro- or ferrimagnetic material, from which we can obtain M_s, M_r, and H_c.[281]

Block temperature (T_B) is another critical parameter for evaluating the magnetic properties, representing at a specific temperature, the thermal energy (k_BT) is comparable to the magnetic anisotropy energy, i.e., the energy barrier for spins to flip. The blocking temperature can be acquired from the zero-field cooling (ZFC)-field cooling (FC) measurement (**Figure 1.16**).[284-285] In ZFC measurement, a sample is first cooled down to low temperature (e.g., 2-10 K) in the absence of an external magnetic field, followed by heating up under a weak external field while recording the sample magnetization as a function of temperature. In FC measurement, the sample is first cooled with the applied external field and the same magnetic field is continuously applied as the temperature increases. T_B is then identified as the maximum point in the ZFC curve. Notably, the value of T_B depends on the measuring time since it is the comparison between the difference of measuring time and the relaxation time of the magnetic dipoles. Thus, if the measuring time is less than the relaxation time, the magnetic materials are in a "block" regime while if the measuring time is greater than the relaxation time, we can then observe the flipping behavior of the dipoles.

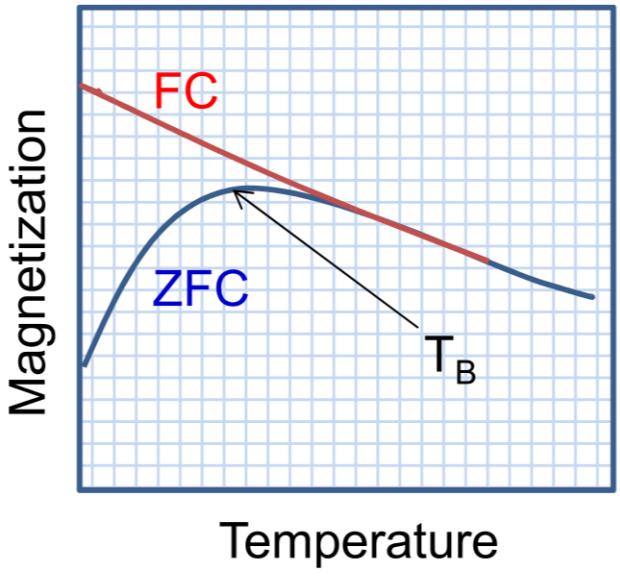

Figure 1.16 Typical ZFC-FC curves for evaluating the blocking temperature of the magnetic materials.[166]

In contrast to bulk magnetic materials, unique properties have been observed when reducing the materials to nanometer-scale majorly due to the high surface-to-volume ratio. Magnetic nanoparticles (NPs) have thus been intensively investigated and continue to sustain interest due to their potential applications in various fields, including high-density data storage, sensing, drug delivery, hyperthermia, etc. Specific magnetic properties of magnetic NPs are required for different applications.[286-295] For instance, higher saturation magnetization as well as superparamagnetic behavior are preferred for biosensing applications because they can provide higher sensitivity and efficiency.

The magnetic behavior relies on two mechanisms, i.e., exchange interaction and anisotropy. The exchange interaction results from the combination of electrostatic coupling between electron orbitals and the requirement to fulfill the Pauli Exclusion Principle, leading to long-range spin-spin interaction with the macroscopic range. Ideally, the exchange interactions should be isotropic while in reality, since the electron orbitals interact with the potential created by the crystal lattice, the spherical symmetry is broken, resulting in the spin orientation having preferred spatial direction. This phenomenon is called magnetic anisotropy. *Magnetocrystalline anisotropy*, *shape anisotropy*, *magnetostriction,* and *stress anisotropy* can all contribute to magnetic anisotropy. In particular, *surface anisotropy* plays a more significant role when the size of magnetic materials decreases within the nanometer-range.[296-305]

Magnetocrystalline anisotropy, which is an intrinsic property, derives from the coupling between spin and orbital, affecting the magnetization under applied magnetic field. Hard magnetic materials generally demonstrate larger *magnetocrystalline anisotropy*, i.e., the energy needed for changing the orientation of the magnetic dipole moments, thus rendering larger coercivity in hysteresis measurement. Soft magnetic materials, on the other hand, demonstrate smaller

magnetocrystalline anisotropy as well as smaller coercivity. *Shape anisotropy*, which is an extrinsic property, is caused by magnetostatic energy. Specifically, this energy can be of importance when the magnetic materials are with non-spherical morphology. *Surface anisotropy* is originated from the discontinuity for magnetic interactions of the surface layer, and it is more predominant when the sizes of the magnetic materials decrease. The canted and/or disordered surface spins might be induced by the local crystal field, the lower coordination number of the surface atoms, as well as broken magnetic exchange bond. In brief, the effective anisotropy constant (K_{eff}) of a spherical particle can be described as the equation below:[306-309]

$$K_{eff} = K + \frac{6}{d} \times K_s$$

where K is magnetocrystalline anisotropy constant, K_s is surface anisotropy constant, and d is the diameter of the particle. The equation thus indicates how significant the size of the nanoparticles can have on the magnetic properties.

1.3.2 Superparamagnetism and structure of spinel magnetic nanoparticles

Bulk magnetic materials consist of multiple magnetic domains, referring to the area with uniform magnetization, and the interface between the domains, which are called domain walls. With reducing the size of the magnetic materials, domains will start to re-orientate themselves to reach the status with minimum energy. For example, when the dimension of the material is reduced below a critical length (R_c), the magnetic material will become single-domain because it requires higher energy for maintaining domain walls. This critical size can be influenced by spontaneous magnetization, the anisotropy constant (K), and the exchange energy density, thus typically fall within a wide size range from 10-800 nm.[310-317] If we continuously reduce the dimension of the magnetic materials, the superparamagnetic behavior can be observed. This phenomenon occurs when the magnitude of the magnetic anisotropy energy is comparable to or even lower than the thermal energy, leading to thermally fluctuated magnetic moment and a single-spin-within-paramagnetic material-like behavior.[281, 318-322]

Stoner-Wohlfarth is a simple model for describing the magnetic behavior within single-domain, isotropic spherical particles without the applied magnetic field. The magnetic anisotropy energy has the relationship below:[323]

$$E_A = KVsin^2\theta$$

where E_A is the anisotropy energy (i.e., the energy barrier for flipping the magnetic dipoles), K is the magnetocrystalline anisotropy constant, V is the volume of the particle and θ is the angle between the intrinsic easy axis of the magnetic dipole of the materials and the applied magnetic field. When θ=0 or π, the minimum anisotropy energy can be observed, and these two minimum points are symmetrically separated by an energy barrier as high as KV.

Among all the magnetic materials, 3d transition metal oxide-based magnetic nanomaterials with spinel structure, including magnetite (Fe_3O_4), manganese ferrite ($MnFe_2O_4$), cobalt ferrite ($CoFe_2O_4$) and nickel ferrite ($NiFe_2O_4$) have attracted tremendous interest because of their low cost, relatively facile synthetic processes, high chemical, and mechanical stability, as well as tunable magnetic properties by changing the composition and cation distribution among different sites within the crystal lattice.[324-334] Furthermore, those metal oxide nanomaterials are found to be useful for different kinds of applications in various biomedical and technological fields, including biosensor, bio-separation, hyperthermia, catalysis, information storage, etc. due to their unique magnetic, optical, electronic and catalytic properties.[324-329, 335-346] Different magnetic properties are required for different kinds of applications, the capability of tuning the magnetic properties of those metal oxide magnetic nanocrystals therefore becomes one of the focuses of the research.

3d transition metal oxide nanocrystals with spinel ferrites, belonging to Fd3m space group, have a general formula of MFe_2O_4 (M = Mn, Co, Fe, etc.). The cubic unit cell is composed of 56 atoms, containing 32 close-packed oxygen anions, 24 cations occupying 8 (out of 64 in total) tetrahedral site (A-sites), and 16 (out of 32 in total) octahedral sites (B-sites). The unit cell of spinel ferrites is shown in **Figure. 1.17**.[347] The structural formula can also be expressed as below, based on the cation distribution on A-sites and B-sites:

$$[M_{(1-i)}Fe_i]^A[M_iFe_{(2-i)}]^BO_4$$

where the atoms in first brackets represent the average occupancy of A-sites, while the atoms in second brackets represent the average occupancy of B-sites and *i* is the inversion parameter. Based on different kinds of cations distribution, the spinel structure can be further divided into normal spinel, inverse spinel, and mixed spinel structure. In a normal spinel structure, tetrahedral sites (A-sites) are all occupied by 8 bivalent cations (M^{2+}) and octahedral sites (B-sites) are all occupied by

trivalent cations (Fe^{3+} in the case of spinel ferrite). In an inverse spinel structure, all the 8 tetrahedral sites are occupied by trivalent cations, whereas the octahedral sites are occupied by both bivalent cations and trivalent cations. In terms of the inversion parameter (i), $i = 0$ represents the normal spinel structure while $i = 1$ represents the inverse spinel structure. Finally, if the bivalent cations, instead of only present on tetrahedral sites (normal spinel structure) or octahedral sites (inverse spinel structure), present on both 2 sites, then the materials are with mixed spinel structure ($0 < i < 1$).[347-353]

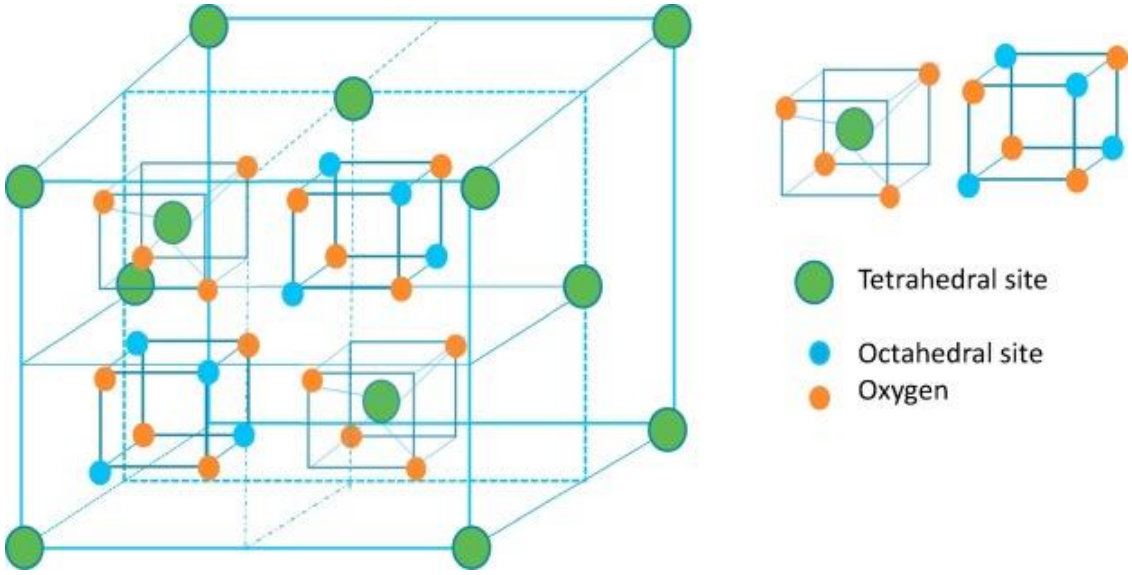

Figure 1.17 Schematic representation of the unit cell of spinel ferrite structure.[347]

Specifically, the normal spinel structure shows the structural formula of $M^{2+}[Fe_2^{3+}]O_4^{2-}$. Zinc ferrite is the typical material that has this kind of structure ($Zn^{2+}[Fe_2^{3+}]O_4^{2-}$). Mixed spinel structure has a more complicated structural formula: $M_{(1-i)}^{2+}\ Fe_i^{3+}\ [M_i^{2+}Fe_{(2-i)}^{3+}]O_4^{2-}$ since both M^{2+} and Fe^{3+} cations are occupying tetrahedral sites and octahedral sites. Manganese ferrite possesses this type of structure and typically has an inversion degree of 0.2. Inverse spinel structure, on the other hand, shows the general structural formula of $Fe^{3+}[M^{2+}Fe^{3+}]O_4^{2-}$ and has the representing materials like

iron oxides, cobalt ferrites, and nickel ferrites. Intriguingly, the inversion degree (i.e., cation distribution, indicating the distribution of 2 different cations on 2 sites) is not a set value even for the same material, it can be altered by lots of synthetic condition, especially the annealing step with various temperatures and time.[288-289, 293-294] And sometimes change in size and shape of the materials can result in different inversion degrees as well. Below shows the schematic illustration of the cation distribution and the corresponding magnetic dipole moment alignment with three different spinel structures (**Figure 1.18**).

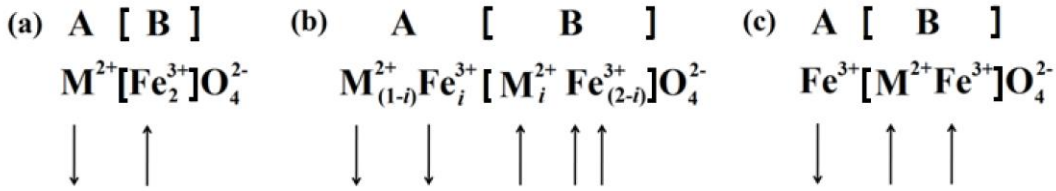

Figure 1.18 Cations distribution with **(a)** normal, **(b)** mixed, and **(c)** inverse spinel ferrites and the corresponding magnetic dipole moment orientation.

1.3.3 Routes to spinel magnetic nanoparticles

Despite relatively well-established dependence of magnetic properties on the size of the magnetic nanomaterials, magnetic behavior is complicated and cannot be predicted simply by one parameter, e.g., the change in shape, composition, and structure of the nanomaterials can have a significant influence on the magnetic properties as well. Size effect even though has been widely discussed, on magnetic properties is relatively clear but some critical parameters still have not reached a consensus.[354-361] For example, as the size of the nanomaterials increases, the materials will show the transition from superparamagnetic, single-domain to multidomain magnetic behavior and M_s will gradually increase and finally reach to a plateau with the value close to that of bulk materials, whereas H_c will reach the maximum value twice at the transition crystal lengths between different magnetic behaviors.[281] However, defining a discrete transition point is challenging since the number varies from different literature. On the other hand, there's relatively less research on the effect of shape on the magnetic properties of nanomaterials, possibly due to less controllability over the shape of the materials. With that being said, there are still some studies on synthesizing unique shapes of magnetic nanocrystals including nanocube, nanorods, nanowires, nanodiscs, tetrapods, etc.[332, 362-368] Some papers attributed the different magnetic properties (coercivity in this case) between different shapes to the different coordination numbers of the oxygen atom on the surface, leading to less surface pinning and eventually different anisotropy constant. In contrast, there is no unifying trend for the correlation between shape and M_s for nanocrystals even though some papers indeed proposed that difference compared between cubic and spherical morphologies resulted from the number of disordered spins. Therefore, it would be helpful to provide more systematic studies on this topic with nanocrystals spanning a larger range of sizes and shapes. Finally, the composition is the most extensively-studied parameter for

determining the magnetic properties of the material. Tuning the composition can render a direct and significant impact on the magnetic properties. An obvious explanation is that different metal ions possess a different number of unpaired electrons. For instance, Fe^{3+} has five unpaired electrons, generating magnetic moment with 8.5 Bohr magnetons in magnitude (estimated based on the magnetic moment of a single electron is around 1.73 Bohr magnetons).[369-371] In addition, the distribution of cations on either octahedral and/or tetrahedral sites, specifically in spinel or inverse spinel structure cases, can have a critical influence on magnetic properties as well. The reason lies in the different alignment of the magnetic moment on different sites, i.e., the cations in the octahedral sites are aligned parallel to the magnetic field, whereas those in the tetrahedral sites are aligned antiparallel. The magnetic moments on 2 sites are canceling out each other, therefore, the net change in magnetic moment depends on how cations (with a varied number of unpaired electrons) present in specific sites.[372-379] More studies are in progress for understanding the impact of the composition by varying the precursor concentration, the synthetic approach, and by controlling post-synthetic cation exchanges.

To elucidate the morphology, composition, and structure effect on magnetic/superparamagnetic behavior of magnetic nanomaterials, how to synthesize magnetic nanocrystals with controllable dimension, shape, and composition thus become crucial. Here, we will focus on the synthesis approaches for magnetic metal oxide nanocrystals with spinel structure. In general, the synthesis of magnetic metal oxides nanocrystals can be conducted both in aqueous and nonaqueous solutions. Disregards of the solvents used, surfactant/ligands as stabilizers are always required for successfully obtaining monodisperse magnetic spinel metal oxides nanocrystals. In terms of the synthesis in aqueous solution, a variety of approaches, including co-precipitation, microemulsion, hydrolysis, sonochemical and hydrothermal reaction, etc., have all

been proposed previously.[380-389] Nanoparticle, among all kinds of nanometer-scaled morphologies, is the most commonly-seen and discussed one. The size of the synthesized nanoparticles typically falls within the range of 5-30 nm. Furthermore, many of these processes can be used for preparing metal oxide nanocrystals with various dopants, providing the possibility to investigate the influence of dopant types and concentration on magnetic properties. Nevertheless, they all have their disadvantages. Take the co-precipitation method as an example, it generally suffers from the necessity of careful adjustment of reaction condition and poor controllability over size, size distribution, and shape of the product. On the other hand, the reverse micelle method (micelles, generated by water-in-oil emulsions, serve as nanoreactors to capture the water-soluble precursors within the micellar cores) provides good controllability of size and shape of as-synthesized nanoparticles, while polymer-template-assisted method provides structural stable magnetic nanoparticles through polymeric supports.

Nonhydrolytic procedures for synthesizing magnetic metal oxide nanocrystals rely on thermal decomposition of suitable precursors in hot surfactants. Metal carbonyl, acetate, acetylacetonate, and carboxylate are some of the commonly-chosen precursors. Magnetic metal oxide nanocrystals with spinel structure synthesized by this pathway generally possess good crystallinity as well as a more uniform size and shape. Li *et al* reported the synthesis of magnetic nanoparticles by employing iron (III) acetylacetonate as the precursor under high-temperature (i.e., refluxing temperature of diphenyl ether) reaction. By introducing oleic acid and oleylamine as surfactants, monodisperse magnetic nanoparticles with a size smaller than 6 nm can be successfully acquired. Moreover, a seeded growth process (two-step synthetic process) had been conducted, and nanoparticles with size up to 16 nm in diameter can be obtained.[287] The synthesis of other magnetic metal oxide nanocrystals can be done by facilely substituting different metal precursors for iron.

For instance, thermal decomposition of $(\eta^5\text{-}C_5H_5)CoFe_2(CO)_9$ with the presence of oleic acid in octyl ether, followed by oxidation by trimethylamine can generate $CoFe_2O_4$ nanocrystals.[390] Furthermore, the size of the cobalt ferrite nanocrystals can be tuned via controlling the molar ratio of precursor to oleic acid and the carbon chain length of carboxylic acids. Besides precisely controlling the size of the magnetic metal oxide nanocrystals with spinel structure, Zhang *et al.* proposed the critical parameter for reversibly interchanging between spherical and cubic morphology was the nanocrystal growth rate, which can be controlled by heating rate during the reaction.[332] By employing nonhydrolytic reaction with a seed-mediated growth approach, high-quality and monodisperse spinel cobalt ferrite with a tunable shape between nearly spherical or almost perfectly cubic morphologies can be obtained and the correlation between nanocrystal shape and magnetic properties was discussed.

1.3.4 Potential applications of magnetic nanoparticles

The usage of magnetic materials can be traced back to ancient china more than two thousand years ago. Nowadays, magnetic materials are indispensable in our daily life in various fields of applications, stimulating research for elucidating the physical or chemical properties to magnetic performance fundamentally. For instance, reliable ultrahigh-density and low-cost magnetic storage devices are in high demand due to the extensively-used computers and a variety of electronic devices. One research focus lies in developing novel possible arrangements for recording besides common recording techniques, i.e., longitudinal, and perpendicular recording, to increase recording media density. In addition, discovering materials with higher anisotropy and coercivity with small material dimensions while maintaining ferromagnetic/ferrimagnetic behavior instead of transition into superparamagnetic behavior (known as the superparamagnetic limitation) is also critical in developing more advanced memory devices.[391-393]

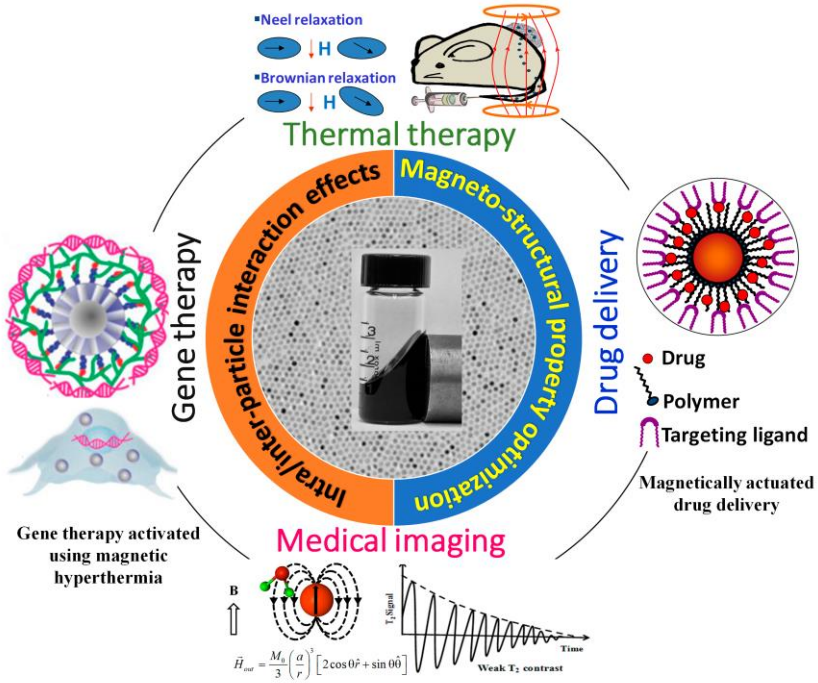

Figure 1.19 Applications of magnetic nanostructures in cancer therapy, drug carrier, and gene therapy because of their heat activation ability.[390]

These magnetic nanocrystals with unique properties can also be applied in various biomedical applications, such as contrast enhancement in magnetic resonance imaging (MRI), nano-sized carriers in drug delivery, mediators in converting electromagnetic energy to heat, targeting and biosensing agents, etc.[394-399] Magnetic nanocrystals with high magnetic moments, small size as well as narrow size distribution are critical properties required in those bio-related applications. Based on those properties, the magnetic nanocrystals can show well-defined and well-controlled physical and chemical properties. Four important areas of cancer theranostics with the employment of magnetic nanomaterials are illustrated in **Figure 1.19**. Localized heat induction, derived from placing magnetic nanocrystals under an alternating magnetic field, is an emerging technique that can be used in cancer treatment, thermally activated drug release, and remote activation of cell functions.[400-405] The induced heat comes from the energy losses during the magnetization reversal of the magnetic nanomaterials, thus depending on a variety of different intrinsic properties of the magnetic nanomaterials including size, magnetization, and magnetic anisotropy as well as extrinsic properties like the amplitude and frequency of the applied alternating magnetic field. To be more specific, the magnetization reversal occurs from two different processes, which are hysteresis loss (happen in ferromagnetic nanocrystals) and susceptibility loss (happen in superparamagnetic nanocrystals). Hysteresis loss is strongly affected by the amplitude of applied magnetic field and magnetic coercive field whereas susceptibility loss is associated with Neel reaction and Brownian rotation of the nanocrystals. The Neel relaxation is controlled by anisotropy energy of the magnetic nanomaterials and the Brownian rotation, on the other hand, is directly related to the hydrodynamic volume of the materials. Research then focuses on improving inductive heating efficiency by modifying the properties of magnetic nanostructures. For instance, hard and soft ferrites with a core-shell structure are proved to demonstrate higher magnetic heating power because of strong

exchange-coupling. Synthesizing nanostructures with various morphologies, such as nanoflowers, nanoclusters, and nanoassemblies had been shown with enhanced heating power as well due to the cooperative magnetism among nanomaterials. In summary, metal oxides with optimized size, shape, and magnetic performance that can render high specific adsorption rate values are demonstrated to be promising materials in the heat-induction biomedical applications. However, some questions still need to be addressed, such as the long-term stability, toxicological impact, site-specific internalization, the metabolism of the magnetic nanomaterials as well as the discovery of large-scale and highly reproducible synthetic approach.[390]

MRI is a noninvasive technology commonly used in clinics for diagnostic imaging. The change in magnetization of protons in a magnetic field after being exposed by a radiofrequency pulse is measured.[401, 406-408] This signal magnitude can not only be affected by the concentration of hydrogen atoms in specific volume, but also the rate of relaxation of the spin of the proton T_1 (in the *z*-axis) and T_2 (in the *xy*-plane).[409] The T_1 relaxation (i.e., spin-lattice) results from the energy loss as heat, while the T_2 relaxation (i.e., spin-spin) comes from the phase coherence or dephasing. By introducing MRI contrast agents, the relaxation time can be reduced, leading to better contrast/signal in MRI images. Both T_1 and T_2 can be tuned by the magnetic contrast enhancers like superparamagnetic metal oxide nanocrystals, while the agents have a stronger effect on T_2. For example, superparamagnetic nanocrystals, magnetically saturated with the applied magnetic field under MRI measurement, provide local variations in the magnetic susceptibility of the system and decrease T_2 while maintaining relaxation time of T_1, finally resulting in enhanced negative contrast. A variety of superparamagnetic contrast agents are commercially available, most of them are based on superparamagnetic iron oxides. The nanocrystals need to be small enough (typically less than 30 nm) to gain high efficiency and a longer lifetime without being trapped in specific

organs. Furthermore, magnetic nanocrystals with different kinds of surface functionalization, such as polymers, liposomes, and proteins, can become target specific for imaging. When the therapeutic drugs or gene vectors are encapsulated in the functionalized magnetic nanocrystals system, diagnostic and therapeutic drug delivery vehicle can be provided.

In addition, significant attention has been directed toward the development of magnetic nanomaterials as sustainable nanocatalysts for specific chemical transformations and photo- and/or electrochemical reaction due to their unique advantages such as efficient activity, low cost, simple synthetic approach, high stability and facile separation by the external magnetic field. In particular, spinel materials have been used as electrode materials in Na-ion, Mg-ion and Zn-ion batteries as well as catalysts for facilitating NO_x reduction, CO oxidation, CO_2 reduction, hydrogen evolution reaction (HER), oxygen reduction reaction (ORR), oxygen evolution reaction (OER), etc.[410-418] Among various catalytic reactions, spinel nanomaterials demonstrate remarkable ORR and OER activity, which are the key process for energy conversion and storage devices. By precisely controlling the structure, composition, phase, valence, morphology, and defect of the as-synthesized spinel nanomaterials, not only spinel catalysts with activities comparable to those of noble metals can be developed, but the correlation between the intrinsic properties and their electrocatalytic performance can be understood fundamentally. Besides optimizing the intrinsic properties of the spinel nanocrystals, thus enabling better affinity with oxygen-containing groups, fabricating spinel/carbon-based hybrids with small particle size, nice dispersion, and increased electrical conductivity as catalysts is also proved to be an effective way to enhance the catalytic activities. Developing porous 3D structures can also be beneficial to facilitate air transport during the ORR/OER reaction. More systematic experiment design and comprehensive understanding can provide guidelines for obtaining spinel catalysts with advanced electrochemical properties.

1.4 Polymeric nanoreactor for synthesis of inorganic nanoparticles

Nano-scaled inorganic colloidal nanoparticles possess many different properties such as high electron density and strong optical absorption (such as metal particles), photoluminescence in the form of fluorescence (semiconductor quantum dots) or magnetic moment (iron oxide or cobalt nanoparticles).[419-424] Proper surface functionalization of such nanoparticles is the prerequisite for every possible application since it can determine the interaction between the particles with the environment. The choice of the right ligand, depending on the materials of nanoparticles and the solvent in which the particles are dispersed, can yield stable particles. One of the commonly-used capping strategies is by attaching small ligands to the surface of nanoparticles via non-covalent binding, which is relatively unstable and can easily desorb and impair the stabilization of the particles. Employing polymer as a ligand is another general approach to stabilize nanocomposites as well as provide access to control the macroscopic alignment of nanoparticles within polymer matrices. Among the polymer-assisted approaches, most of them utilize polymeric micelle as templates for nanoparticle *in-situ* synthesis by self-assembly of linear block copolymers. To obtain fine nanoparticles with this method, optimal conditions need to be precisely tuned and the size and shape of the resulting nanoparticles are highly sensitive to the environment.

A robust and general strategy for synthesizing stable unimolecular micelles with well-defined size and structure, then subsequently served as nanoreactors for a variety of nanoparticle synthesis has been proposed by Lin. For synthesizing star-like nanoreactors for nanoparticle synthesis, 21-arms ß-cyclodextrin (ß-CD) is first brominated, converting hydroxyl groups into bromine. Then resulting brominated ß-CD has been used as the initiator for two- or three-times sequential atom transfer radical polymerization (ATRP). Whether do ATRP twice (diblock nanoreactors) or three times (triblock nanoreactors) depends on the morphologies of particles one would like to obtain in

the end (**Figure 1.20**). By employing diblock star-like copolymers, we can obtain plain nanoparticles with second-block polymer capped on the surface, while utilizing triblock star-like copolymers, we can obtain even more complicated structures, such as core/shell or hollow structures. The mechanism for synthesizing nanoparticles with various nanostructures is by the coordination interaction between precursors and functional groups of polymers.[425]

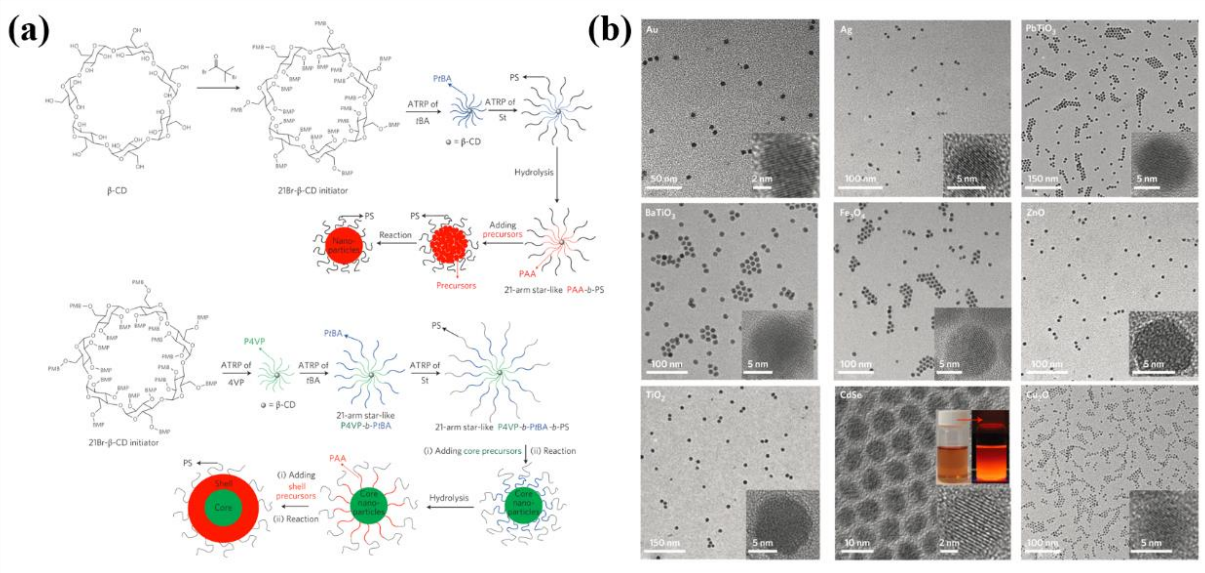

Figure 1.20 (a) Schematic representation of synthetic strategies for nanoparticles with different architectures (plain and core/ shell) using star-like block copolymers **(b)** Representative TEM images of a variety of nanoparticles synthesized using star-like block copolymer.[425]

Take triblock poly(4-vinyl pyridine)-*block*-poly(*tert*-butyl acrylate)-*block*-polystyrene (P4VP-*b*-P*t*BA-*b*-PS) as an example, if we desire to obtain ferromagnetic/ferroelectric Fe_3O_4/$BaTiO_3$ core/shell nanoparticles, we first mix the precursor of Fe_3O_4 with the triblock template. By coordination between Fe_3O_4 precursor and pyridine group of P4VP, the monodispersed Fe_3O_4 core can be formed and confined within the P4VP block area. After hydrolyzing and converting P*t*BA into poly(acrylic acid) (PAA), again we can obtain $BaTiO_3$ shell by coordination between $BaTiO_3$ precursor and carboxylic group of PAA. Eventually, we can get monodispersed, PS-capped Fe_3O_4/ $BaTiO_3$ core/shell nanoparticles. Furthermore, by changing ß-CD into cellulose and applying

similar synthetic procedures (**Figure 1.21**), we can produce nanoreactors for synthesizing rod-like materials, including plain nanorod, core/shell nanorod as well as hollow nanorod, thus proving the versatility of this strategy for fabricating all kinds of materials with various nanostructures.

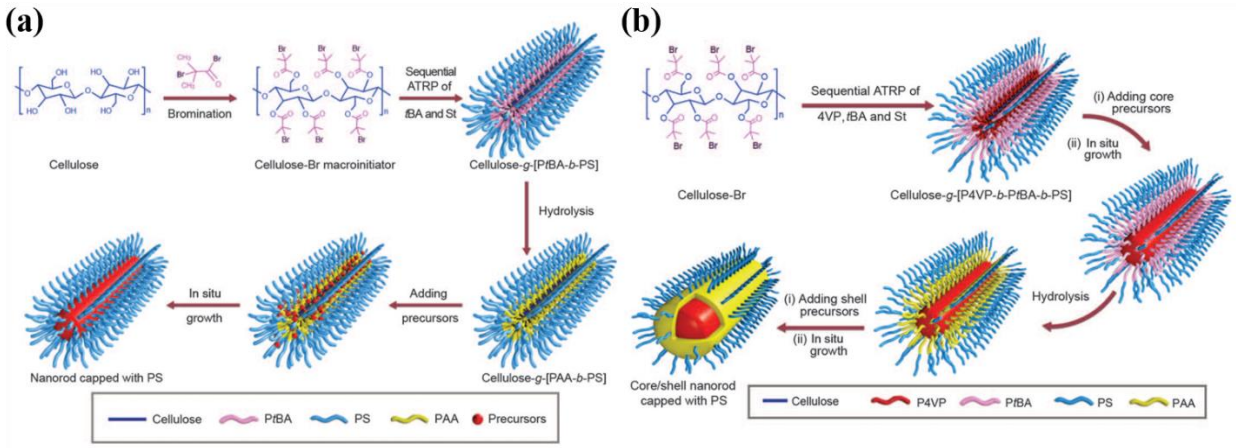

Figure 1.21 Schematic strategies for 1D nanocrystals via employing amphiphilic cylindrical bottlebrush-like block copolymers as nanoreactors: **(a)** Diblock copolymer for synthesizing plain nanorods, and **(b)** triblock copolymer for synthesizing core-shell nanorods.[426]

This nanoreactor-assisted synthetic approach can be capitalized for synthesizing a rich diversity of inorganic nanomaterials, especially with more complicated composition and structure. Taking synthesis of perovskite oxide (i.e., $BaTiO_3$, $PbTiO_3$ or other La-based materials) as an example, the first advantage of this strategy is the capability of acquiring monodisperse perovskite oxide nanoparticles with tailorable dimension, which is rather difficult to achieve since the formation of perovskite materials typically requires high reaction/annealing temperature. And the size of the as-synthesized nanoparticles can be simply modified by changing the molecular weight of the inner block polymer, opening the avenue to investigate the size effect on desired properties. Second, since the outer block is covalently and permanently ligated on the surface of the as-synthesized nanoparticles, the nanoparticles can remain dispersing and stable even after multiple purification steps, which is in opposition to other convention small molecules or ligands. Third,

despite different solubility of precursors (particularly in perovskite oxide synthesis, more than two precursors are normally required) in the reaction solvents, by employing the coordination ability between the functional group and metal moieties within precursors, the optimized stoichiometry of the final product can be tuned by changing the ratio between different precursors accordingly. Finally, by changing the outer block of the nanoreactor, we can modify the surface chemistry of the as-synthesized nanoparticles, leading to excellent dispersity in desired solvents, thus rendering various potential applications in different fields. Consequently, this versatile synthetic strategy for producing monodisperse nanocrystals with the controllable size is essential for a better understanding of the fundamental relationship between material morphologies and the desired properties/optimized performances.

1.5 References

1. Hadjichristidis, N.; Pitsikalis, M.; Pispas, S.; Iatrou, H., Polymers with complex architecture by living anionic polymerization. *Chemical reviews* **2001,** *101* (12), 3747-3792.
2. Hawker, C. J.; Bosman, A. W.; Harth, E., New polymer synthesis by nitroxide mediated living radical polymerizations. *Chemical reviews* **2001,** *101* (12), 3661-3688.
3. Kamigaito, M.; Ando, T.; Sawamoto, M., Metal-catalyzed living radical polymerization. *Chemical Reviews* **2001,** *101* (12), 3689-3746.
4. Matyjaszewski, K.; Xia, J., Atom transfer radical polymerization. *Chemical reviews* **2001,** *101* (9), 2921-2990.
5. Zhao, Y.; Shuai, X.; Chen, C.; Xi, F., Synthesis of star block copolymers from dendrimer initiators by combining ring-opening polymerization and atom transfer radical polymerization. *Macromolecules* **2004,** *37* (24), 8854-8862.
6. Matyjaszewski, K., The synthesis of functional star copolymers as an illustration of the importance of controlling polymer structures in the design of new materials. *Polymer international* **2003,** *52* (10), 1559-1565.
7. Matyjaszewski, K., Atom transfer radical polymerization (ATRP): current status and future perspectives. *Macromolecules* **2012,** *45* (10), 4015-4039.
8. Ribelli, T. G.; Lorandi, F.; Fantin, M.; Matyjaszewski, K., Atom transfer radical polymerization: billion times more active catalysts and new initiation systems. *Macromolecular rapid communications* **2019,** *40* (1), 1800616.
9. Webster, O. W., Living polymerization methods. *Science* **1991,** *251* (4996), 887-893.
10. Grayson, S. M.; Frechet, J. M., Convergent dendrons and dendrimers: from synthesis to applications. *Chemical Reviews* **2001,** *101* (12), 3819-3868.
11. Bosman, d. A.; Janssen, H.; Meijer, E., About dendrimers: structure, physical properties, and applications. *Chemical reviews* **1999,** *99* (7), 1665-1688.
12. Abdouni, Y.; Yilmaz, G.; Becer, C. R., Sequence Controlled Polymers from a Novel β-Cyclodextrin Core. *Macromolecular rapid communications* **2017,** *38* (24), 1700501.
13. Cheng, G.; Böker, A.; Zhang, M.; Krausch, G.; Müller, A. H., Amphiphilic cylindrical core− shell brushes via a "grafting from" process using ATRP. *Macromolecules* **2001,** *34* (20), 6883-6888.
14. Gerle, M.; Fischer, K.; Roos, S.; Müller, A. H.; Schmidt, M.; Sheiko, S. S.; Prokhorova, S.; Möller, M., Main chain conformation and anomalous elution behavior of cylindrical brushes as revealed by GPC/MALLS, light scattering, and SFM. *Macromolecules* **1999,** *32* (8), 2629-2637.
15. Zhang, Z.-X.; Liu, K. L.; Li, J., Self-assembly and micellization of a dual thermoresponsive supramolecular pseudo-block copolymer. *Macromolecules* **2011,** *44* (5), 1182-1193.
16. Zhang, Z.-X.; Liu, X.; Xu, F. J.; Loh, X. J.; Kang, E.-T.; Neoh, K.-G.; Li, J., Pseudo-block copolymer based on star-shaped poly (N-isopropylacrylamide) with a β-cyclodextrin core and guest-bearing PEG: controlling thermoresponsivity through supramolecular self-assembly. *Macromolecules* **2008,** *41* (16), 5967-5970.
17. Zhang, Q.; Su, L.; Collins, J.; Chen, G.; Wallis, R.; Mitchell, D. A.; Haddleton, D. M.; Becer, C. R., Dendritic cell lectin-targeting sentinel-like unimolecular glycoconjugates to release an anti-HIV drug. *Journal of the American Chemical Society* **2014,** *136* (11), 4325-4332.
18. Narrainen, A. P.; Pascual, S.; Haddleton, D. M., Amphiphilic diblock, triblock, and star block copolymers by living radical polymerization: Synthesis and aggregation behavior. *Journal of Polymer Science Part A: Polymer Chemistry* **2002,** *40* (4), 439-450.
19. Iatridi, Z.; Tsitsilianis, C., pH responsive MWCNT–star terpolymer nanohybrids. *Soft Matter* **2013,** *9* (1), 185-193.
20. Heise, A.; Hedrick, J. L.; Frank, C. W.; Miller, R. D., Starlike block copolymers with amphiphilic arms as models for unimolecular micelles. *Journal of the American Chemical Society* **1999,** *121* (37), 8647-8648.

21. Li, F.; Cao, M.; Feng, Y.; Liang, R.; Fu, X.; Zhong, M., Site-Specifically Initiated Controlled/Living Branching Radical Polymerization: A Synthetic Route toward Hierarchically Branched Architectures. *Journal of the American Chemical Society* **2018,** *141* (2), 794-799.
22. Hadjichristidis, N., Synthesis of miktoarm star (μ-star) polymers. *Journal of Polymer Science Part A: Polymer Chemistry* **1999,** *37* (7), 857-871.
23. Liu, Y.; Yang, X.; Zhang, W.; Zheng, S., Star-shaped poly (ε-caprolactone) with polyhedral oligomeric silsesquioxane core. *Polymer* **2006,** *47* (19), 6814-6825.
24. Ueda, J.; Kamigaito, M.; Sawamoto, M., Calixarene-core multifunctional initiators for the ruthenium-mediated living radical polymerization of methacrylates. *Macromolecules* **1998,** *31* (20), 6762-6768.
25. Rempp, P. F.; Franta, E., Macromonomers: Synthesis, characterization and applications. In *Polymerization Reactions*, Springer: 1984; pp 1-53.
26. Chen, L.; Li, P.; Cheng, Y.; Xie, Z.; Wang, L.; Jing, X.; Wang, F., White Electroluminescence from Star-like Single Polymer Systems: 2, 1, 3-Benzothiadiazole Derivatives Dopant as Orange Cores and Polyfluorene Host as Six Blue Arms. *Advanced Materials* **2011,** *23* (26), 2986-2990.
27. Liu, J.; Cheng, Y.; Xie, Z.; Geng, Y.; Wang, L.; Jing, X.; Wang, F., White Electroluminescence from a Star-like Polymer with an Orange Emissive Core and Four Blue Emissive Arms. *Advanced Materials* **2008,** *20* (7), 1357-1362.
28. Lai, W.-Y.; Chen, Q.-Q.; He, Q.-Y.; Fan, Q.-L.; Huang, W., Microwave-enhanced multiple Suzuki couplings toward highly luminescent starburst monodisperse macromolecules. *Chemical communications* **2006,** (18), 1959-1961.
29. Lai, W.-Y.; Zhu, R.; Fan, Q.-L.; Hou, L.-T.; Cao, Y.; Huang, W., Monodisperse six-armed triazatruxenes: microwave-enhanced synthesis and highly efficient pure-deep-blue electroluminescence. *Macromolecules* **2006,** *39* (11), 3707-3709.
30. Kanibolotsky, A. L.; Berridge, R.; Skabara, P. J.; Perepichka, I. F.; Bradley, D. D.; Koeberg, M., Synthesis and properties of monodisperse oligofluorene-functionalized truxenes: highly fluorescent star-shaped architectures. *Journal of the American Chemical Society* **2004,** *126* (42), 13695-13702.
31. Pei, J.; Wang, J.-L.; Cao, X.-Y.; Zhou, X.-H.; Zhang, W.-B., Star-shaped polycyclic aromatics based on oligothiophene-functionalized truxene: synthesis, properties, and facile emissive wavelength tuning. *Journal of the American Chemical Society* **2003,** *125* (33), 9944-9945.
32. Zou, Y.; Zou, J.; Ye, T.; Li, H.; Yang, C.; Wu, H.; Ma, D.; Qin, J.; Cao, Y., Unexpected Propeller-Like Hexakis (fluoren-2-yl) benzene Cores for Six-Arm Star-Shaped Oligofluorenes: Highly Efficient Deep-Blue Fluorescent Emitters and Good Hole-Transporting Materials. *Advanced Functional Materials* **2013,** *23* (14), 1781-1788.
33. Nafee, N.; Hirosue, M.; Loretz, B.; Wenz, G.; Lehr, C.-M., Cyclodextrin-based star polymers as a versatile platform for nanochemotherapeutics: enhanced entrapment and uptake of idarubicin. *Colloids and Surfaces B: Biointerfaces* **2015,** *129*, 30-38.
34. Kuo, C.-Y.; Liu, T.-Y.; Hardiansyah, A.; Lee, C.-F.; Wang, M.-S.; Chiu, W.-Y., Self-assembly behaviors of thermal-and pH-sensitive magnetic nanocarriers for stimuli-triggered release. *Nanoscale research letters* **2014,** *9* (1), 520.
35. Du, H.; Han, R.; Tang, E.; Zhou, J.; Liu, S.; Guo, X.; Wang, R., Synthesis of pH-responsive cellulose-g-P4VP by atom transfer radical polymerization in ionic liquid, loading, and controlled release of aspirin. *Journal of Polymer Research* **2018,** *25* (9), 205.
36. Gao, H.; Matyjaszewski, K., Synthesis of star polymers by a combination of ATRP and the "click" coupling method. *Macromolecules* **2006,** *39* (15), 4960-4965.
37. Whittaker, M. R.; Urbani, C. N.; Monteiro, M. J., Synthesis of 3-miktoarm stars and 1st generation mikto dendritic copolymers by "living" radical polymerization and "click" chemistry. *Journal of the American Chemical Society* **2006,** *128* (35), 11360-11361.
38. Altintas, O.; Hizal, G.; Tunca, U., ABC-type hetero-arm star terpolymers through "Click" chemistry. *Journal of Polymer Science Part A: Polymer Chemistry* **2006,** *44* (19), 5699-5707.

39. Altintas, O.; Yankul, B.; Hizal, G.; Tunca, U., A3-type star polymers via click chemistry. *Journal of Polymer Science Part A: Polymer Chemistry* **2006,** *44* (21), 6458-6465.
40. Mayadunne, R. T.; Jeffery, J.; Moad, G.; Rizzardo, E., Living free radical polymerization with reversible addition− fragmentation chain transfer (raft polymerization): Approaches to star polymers. *Macromolecules* **2003,** *36* (5), 1505-1513.
41. Kanaoka, S.; Sawamoto, M.; Higashimura, T., Star-shaped polymers by living cationic polymerization. 1. Synthesis of star-shaped polymers of alkyl and vinyl ethers. *Macromolecules* **1991,** *24* (9), 2309-2313.
42. Matyjaszewski, K.; Miller, P. J.; Pyun, J.; Kickelbick, G.; Diamanti, S., Synthesis and characterization of star polymers with varying arm number, length, and composition from organic and hybrid inorganic/organic multifunctional initiators. *Macromolecules* **1999,** *32* (20), 6526-6535.
43. Angot, S.; Murthy, K. S.; Taton, D.; Gnanou, Y., Atom transfer radical polymerization of styrene using a novel octafunctional initiator: synthesis of well-defined polystyrene stars. *Macromolecules* **1998,** *31* (21), 7218-7225.
44. Wu, P.; Malkoch, M.; Hunt, J. N.; Vestberg, R.; Kaltgrad, E.; Finn, M.; Fokin, V. V.; Sharpless, K. B.; Hawker, C. J., Multivalent, bifunctional dendrimers prepared by click chemistry. *Chemical communications* **2005,** (46), 5775-5777.
45. Deng, G.; Ma, D.; Xu, Z., Synthesis of ABC-type miktoarm star polymers by "click" chemistry, ATRP and ROP. *European polymer journal* **2007,** *43* (4), 1179-1187.
46. Gao, H.; Matyjaszewski, K., Synthesis of star polymers by a new "core-first" method: sequential polymerization of cross-linker and monomer. *Macromolecules* **2008,** *41* (4), 1118-1125.
47. Xia, J.; Zhang, X.; Matyjaszewski, K., Synthesis of star-shaped polystyrene by atom transfer radical polymerization using an "arm first" approach. *Macromolecules* **1999,** *32* (13), 4482-4484.
48. Zhang, X.; Xia, J.; Matyjaszewski, K., End-functional poly (tert-butyl acrylate) star polymers by controlled radical polymerization. *Macromolecules* **2000,** *33* (7), 2340-2345.
49. Baek, K.-Y.; Kamigaito, M.; Sawamoto, M., Star-shaped polymers by metal-catalyzed living radical polymerization. 1. Design of Ru (II)-based systems and divinyl linking agents. *Macromolecules* **2001,** *34* (2), 215-221.
50. Gao, H.; Tsarevsky, N. V.; Matyjaszewski, K., Synthesis of degradable miktoarm star copolymers via atom transfer radical polymerization. *Macromolecules* **2005,** *38* (14), 5995-6004.
51. Gao, H.; Matyjaszewski, K., Synthesis of Miktoarm star polymers via ATRP using the "in− out" method: determination of initiation efficiency of star macroinitiators. *Macromolecules* **2006,** *39* (21), 7216-7223.
52. Gao, H.; Matyjaszewski, K., Arm-first method as a simple and general method for synthesis of miktoarm star copolymers. *Journal of the American Chemical Society* **2007,** *129* (38), 11828-11834.
53. Gao, H.; Matyjaszewski, K., Structural control in ATRP synthesis of star polymers using the arm-first method. *Macromolecules* **2006,** *39* (9), 3154-3160.
54. Baek, K.; Kamigaito, M.; Sawamoto, M., Polym Sci, Part A: Polym Chem 2002; 40: 633–41;(i) Guo A, Liu GJ, Tao J. *Macromolecules* **1996,** *29*, 2487-93.
55. Hedrick, J. L.; Trollsås, M.; Hawker, C. J.; Atthoff, B.; Claesson, H.; Heise, A.; Miller, R. D.; Mecerreyes, D.; Jérôme, R.; Dubois, P., Dendrimer-like star block and amphiphilic copolymers by combination of ring opening and atom transfer radical polymerization. *Macromolecules* **1998,** *31* (25), 8691-8705.
56. Heise, A.; Trollsås, M.; Magbitang, T.; Hedrick, J. L.; Frank, C. W.; Miller, R. D., Star polymers with alternating arms from miktofunctional μ-initiators using consecutive atom transfer radical polymerization and ring-opening polymerization. *Macromolecules* **2001,** *34* (9), 2798-2804.
57. Dichtel, W. R.; Baek, K. Y.; Fréchet, J. M.; Rietveld, I. B.; Vinogradov, S. A., Amphiphilic diblock star polymer catalysts via atom transfer radical polymerization. *Journal of Polymer Science Part A: Polymer Chemistry* **2006,** *44* (17), 4939-4951.
58. Kennedy, J.; Jacob, S., Cationic polymerization astronomy. Synthesis of polymer stars by cationic means. *Accounts of chemical research* **1998,** *31* (12), 835-841.

59. Quirk, R. P.; Tsai, Y., Trifunctional organolithium initiator based on 1, 3, 5-tris (1-phenylethenyl) benzene. Synthesis of functionalized, three-armed, star-branched polystyrenes. *Macromolecules* **1998,** *31* (23), 8016-8025.
60. Francis, R.; Lepoittevin, B.; Taton, D.; Gnanou, Y., Toward an easy access to asymmetric stars and miktoarm stars by atom transfer radical polymerization. *Macromolecules* **2002,** *35* (24), 9001-9008.
61. Wang, W.; Zhang, J.; Li, C.; Huang, P.; Gao, S.; Han, S.; Dong, A.; Kong, D., Facile access to cytocompatible multicompartment micelles with adjustable Janus-cores from A-block-B-graft-C terpolymers prepared by combination of ROP and ATRP. *Colloids and Surfaces B: Biointerfaces* **2014,** *115*, 302-309.
62. Wu, W.; Wang, W.; Li, J., Star polymers: Advances in biomedical applications. *Progress in Polymer Science* **2015,** *46*, 55-85.
63. Matyjaszewski, K.; Spanswick, J., Controlled/living radical polymerization. *Materials Today* **2005,** *8* (3), 26-33.
64. Wang, J.-S.; Matyjaszewski, K., Controlled/" living" radical polymerization. atom transfer radical polymerization in the presence of transition-metal complexes. *Journal of the American Chemical Society* **1995,** *117* (20), 5614-5615.
65. Patten, T. E.; Xia, J.; Abernathy, T.; Matyjaszewski, K., Polymers with very low polydispersities from atom transfer radical polymerization. *Science* **1996,** *272* (5263), 866-868.
66. Matyjaszewski, K.; Patten, T. E.; Xia, J., Controlled/“living” radical polymerization. Kinetics of the homogeneous atom transfer radical polymerization of styrene. *Journal of the American Chemical Society* **1997,** *119* (4), 674-680.
67. Li, M.; Jahed, N. M.; Min, K.; Matyjaszewski, K., Preparation of linear and star-shaped block copolymers by ATRP using simultaneous reverse and normal initiation process in bulk and miniemulsion. *Macromolecules* **2004,** *37* (7), 2434-2441.
68. Guyot, A.; Chu, F.; Schneider, M.; Graillat, C.; McKenna, T., High solid content latexes. *Progress in Polymer Science* **2002,** *27* (8), 1573-1615.
69. Gromada, J.; Matyjaszewski, K., Simultaneous reverse and normal initiation in atom transfer radical polymerization. *Macromolecules* **2001,** *34* (22), 7664-7671.
70. Patten, T. E.; Matyjaszewski, K., Atom transfer radical polymerization and the synthesis of polymeric materials. *Advanced Materials* **1998,** *10* (12), 901-915.
71. Coessens, V.; Pintauer, T.; Matyjaszewski, K., Functional polymers by atom transfer radical polymerization. *Progress in polymer science* **2001,** *26* (3), 337-377.
72. Pyun, J.; Matyjaszewski, K., Synthesis of nanocomposite organic/inorganic hybrid materials using controlled/“living” radical polymerization. *Chemistry of Materials* **2001,** *13* (10), 3436-3448.
73. Davis, J. H., State Space Realizations. In *Foundations of Deterministic and Stochastic Control*, Springer: 2002; pp 1-69.
74. Chaffey-Millar, H.; Stenzel, M. H.; Davis, T. P.; Coote, M. L.; Barner-Kowollik, C., Design criteria for star polymer formation processes via living free radical polymerization. *Macromolecules* **2006,** *39* (19), 6406-6419.
75. Chong, Y.; Krstina, J.; Le, T. P.; Moad, G.; Postma, A.; Rizzardo, E.; Thang, S. H., Thiocarbonylthio compounds [sc (ph) s− r] in free radical polymerization with reversible addition-fragmentation chain transfer (raft polymerization). Role of the free-radical leaving group (r). *Macromolecules* **2003,** *36* (7), 2256-2272.
76. Calitz, F.; Tonge, M.; Sanderson, R., Kinetic and electron spin resonance analysis of RAFT polymerization of styrene. *Macromolecules* **2003,** *36* (1), 5-8.
77. Chiefari, J.; Mayadunne, R. T.; Moad, C. L.; Moad, G.; Rizzardo, E.; Postma, A.; Skidmore, M. A.; Thang, S. H., Thiocarbonylthio compounds (SC (Z) S− R) in free radical polymerization with reversible addition-fragmentation chain transfer (RAFT polymerization). Effect of the activating group Z. *Macromolecules* **2003,** *36* (7), 2273-2283.

78. Perrier, S.; Takolpuckdee, P., Macromolecular design via reversible addition–fragmentation chain transfer (RAFT)/xanthates (MADIX) polymerization. *Journal of Polymer Science Part A: Polymer Chemistry* **2005,** *43* (22), 5347-5393.
79. Chaffey-Millar, H.; Busch, M.; Davis, T. P.; Stenzel, M. H.; Barner-Kowollik, C., Advanced computational strategies for modelling the evolution of full molecular weight distributions formed during multiarmed (star) polymerisations. *Macromolecular theory and simulations* **2005,** *14* (3), 143-157.
80. Konkolewicz, D.; Magenau, A. J.; Averick, S. E.; Simakova, A.; He, H.; Matyjaszewski, K., ICAR ATRP with ppm Cu Catalyst in Water. *Macromolecules* **2012,** *45* (11), 4461-4468.
81. Kwak, Y.; Magenau, A. J.; Matyjaszewski, K., ARGET ATRP of methyl acrylate with inexpensive ligands and ppm concentrations of catalyst. *Macromolecules* **2011,** *44* (4), 811-819.
82. Wang, Y.; Lorandi, F.; Fantin, M.; Chmielarz, P.; Isse, A. A.; Gennaro, A.; Matyjaszewski, K., Miniemulsion ARGET ATRP via interfacial and ion-pair catalysis: From ppm to ppb of residual copper. *Macromolecules* **2017,** *50* (21), 8417-8425.
83. Wang, G.; Schmitt, M.; Wang, Z.; Lee, B.; Pan, X.; Fu, L.; Yan, J.; Li, S.; Xie, G.; Bockstaller, M. R., Polymerization-induced self-assembly (PISA) using ICAR ATRP at low catalyst concentration. *Macromolecules* **2016,** *49* (22), 8605-8615.
84. Konkolewicz, D.; Schröder, K.; Buback, J.; Bernhard, S.; Matyjaszewski, K., Visible light and sunlight photoinduced ATRP with ppm of Cu catalyst. *ACS Macro Letters* **2012,** *1* (10), 1219-1223.
85. Discekici, E. H.; Pester, C. W.; Treat, N. J.; Lawrence, J.; Mattson, K. M.; Narupai, B.; Toumayan, E. P.; Luo, Y.; McGrath, A. J.; Clark, P. G., Simple benchtop approach to polymer brush nanostructures using visible-light-mediated metal-free atom transfer radical polymerization. *ACS Macro Letters* **2016,** *5* (2), 258-262.
86. Perkowski, A. J.; You, W.; Nicewicz, D. A., Visible light photoinitiated metal-free living cationic polymerization of 4-methoxystyrene. *Journal of the American Chemical Society* **2015,** *137* (24), 7580-7583.
87. Discekici, E. H.; Anastasaki, A.; Read de Alaniz, J.; Hawker, C. J., Evolution and future directions of metal-free atom transfer radical polymerization. *Macromolecules* **2018,** *51* (19), 7421-7434.
88. Pan, X.; Fang, C.; Fantin, M.; Malhotra, N.; So, W. Y.; Peteanu, L. A.; Isse, A. A.; Gennaro, A.; Liu, P.; Matyjaszewski, K., Mechanism of photoinduced metal-free atom transfer radical polymerization: experimental and computational studies. *Journal of the American Chemical Society* **2016,** *138* (7), 2411-2425.
89. Aydogan, C.; Yilmaz, G.; Yagci, Y., Synthesis of hyperbranched polymers by photoinduced metal-free ATRP. *Macromolecules* **2017,** *50* (23), 9115-9120.
90. Inoue, K., Functional dendrimers, hyperbranched and star polymers. *Progress in Polymer Science* **2000,** *25* (4), 453-571.
91. Hirao, A.; Hayashi, M.; Loykulnant, S.; Sugiyama, K.; Ryu, S. W.; Haraguchi, N.; Matsuo, A.; Higashihara, T., Precise syntheses of chain-multi-functionalized polymers, star-branched polymers, star-linear block polymers, densely branched polymers, and dendritic branched polymers based on iterative approach using functionalized 1, 1-diphenylethylene derivatives. *Progress in polymer science* **2005,** *30* (2), 111-182.
92. Yang, X.; Shang, H.; Ding, C.; Li, J., Recent developments and applications of bioinspired dendritic polymers. *Polymer Chemistry* **2015,** *6* (5), 668-680.
93. Pearson, D. S.; Helfand, E., Viscoelastic properties of star-shaped polymers. *Macromolecules* **1984,** *17* (4), 888-895.
94. Roovers, J., Concentration dependence of the relative viscosity of star polymers. *Macromolecules* **1994,** *27* (19), 5359-5364.
95. Lee, V. Y.; Havenstrite, K.; Tjio, M.; McNeil, M.; Blau, H. M.; Miller, R. D.; Sly, J., Nanogel Star Polymer Architectures: A Nanoparticle Platform for Modular Programmable Macromolecular Self-Assembly, Intercellular Transport, and Dual-Mode Cargo Delivery. *Advanced materials* **2011,** *23* (39), 4509-4515.

96. Ahmad Fuaad, A. A.; Jia, Z.; Zaman, M.; Hartas, J.; Ziora, Z. M.; Lin, I.-C.; Moyle, P. M.; Batzloff, M. R.; Good, M. F.; Monteiro, M. J., Polymer–peptide hybrids as a highly immunogenic single-dose nanovaccine. *Nanomedicine* **2014,** *9* (1), 35-43.
97. Li, J.; Guo, Z.; Xin, J.; Zhao, G.; Xiao, H., 21-Arm star polymers with different cationic groups based on cyclodextrin core for DNA delivery. *Carbohydrate Polymers* **2010,** *79* (2), 277-283.
98. Xiu, K.; Yang, J.; Zhao, N.; Li, J.; Xu, F., Multiarm cationic star polymers by atom transfer radical polymerization from β-cyclodextrin cores: Influence of arm number and length on gene delivery. *Acta biomaterialia* **2013,** *9* (1), 4726-4733.
99. Boyer, C.; Teo, J.; Phillips, P.; Erlich, R. B.; Sagnella, S.; Sharbeen, G.; Dwarte, T.; Duong, H. T.; Goldstein, D.; Davis, T. P., Effective delivery of siRNA into cancer cells and tumors using well-defined biodegradable cationic star polymers. *Molecular pharmaceutics* **2013,** *10* (6), 2435-2444.
100. Shi, C.; Guo, X.; Qu, Q.; Tang, Z.; Wang, Y.; Zhou, S., Actively targeted delivery of anticancer drug to tumor cells by redox-responsive star-shaped micelles. *Biomaterials* **2014,** *35* (30), 8711-8722.
101. Zhao, F.; Yin, H.; Li, J., Supramolecular self-assembly forming a multifunctional synergistic system for targeted co-delivery of gene and drug. *Biomaterials* **2014,** *35* (3), 1050-1062.
102. Chen, H.; Li, G.; Chi, H.; Wang, D.; Tu, C.; Pan, L.; Zhu, L.; Qiu, F.; Guo, F.; Zhu, X., Alendronate-conjugated amphiphilic hyperbranched polymer based on Boltorn H40 and poly (ethylene glycol) for bone-targeted drug delivery. *Bioconjugate chemistry* **2012,** *23* (9), 1915-1924.
103. Zhao, F.; Yin, H.; Zhang, Z.; Li, J., Folic acid modified cationic γ-cyclodextrin-oligoethylenimine star polymer with bioreducible disulfide linker for efficient targeted gene delivery. *Biomacromolecules* **2013,** *14* (2), 476-484.
104. Mizrahi, B.; Khoo, X.; Chiang, H. H.; Sher, K. J.; Feldman, R. G.; Lee, J.-J.; Irusta, S.; Kohane, D. S., Long-lasting antifouling coating from multi-armed polymer. *Langmuir* **2013,** *29* (32), 10087-10094.
105. Schulte, V. A.; Diez, M.; Hu, Y.; Möller, M.; Lensen, M. C., Combined influence of substrate stiffness and surface topography on the antiadhesive properties of Acr-sP (EO-stat-PO) hydrogels. *Biomacromolecules* **2010,** *11* (12), 3375-3383.
106. Alonso-Cristobal, P.; Laurenti, M.; Sanchez-Muniz, F.; López-Cabarcos, E.; Rubio-Retama, J., Polymeric nanoparticles with tunable architecture formed by biocompatible star shaped block copolymer. *Polymer* **2012,** *53* (21), 4569-4578.
107. Cho, H. Y.; Srinivasan, A.; Hong, J.; Hsu, E.; Liu, S.; Shrivats, A.; Kwak, D.; Bohaty, A. K.; Paik, H.-j.; Hollinger, J. O., Synthesis of biocompatible PEG-based star polymers with cationic and degradable core for siRNA delivery. *Biomacromolecules* **2011,** *12* (10), 3478-3486.
108. Li, J.; Xu, S.; Zheng, J.; Pan, Y.; Wang, J.; Zhang, L.; He, X.; Liu, D., Polypeptide-based star-block quadripolymers as unimolecular nanocarriers for the simultaneous encapsulation of hydrophobic and hydrophilic guests. *European polymer journal* **2012,** *48* (10), 1696-1708.
109. Liu, F.; Eisenberg, A., Preparation and pH triggered inversion of vesicles from poly (acrylic acid)-b lock-polystyrene-b lock-Poly (4-vinyl pyridine). *Journal of the American Chemical Society* **2003,** *125* (49), 15059-15064.
110. Zhang, W.; Shi, L.; Ma, R.; An, Y.; Xu, Y.; Wu, K., Micellization of thermo-and pH-responsive triblock copolymer of poly (ethylene glycol)-b-poly (4-vinylpyridine)-b-poly (N-isopropylacrylamide). *Macromolecules* **2005,** *38* (21), 8850-8852.
111. Yin, M. J.; Yao, M.; Gao, S.; Zhang, A. P.; Tam, H. Y.; Wai, P. K. A., Rapid 3D patterning of poly (acrylic acid) ionic hydrogel for miniature pH sensors. *Advanced Materials* **2016,** *28* (7), 1394-1399.
112. Li, G.; Shi, L.; Ma, R.; An, Y.; Huang, N., Formation of complex micelles with double-responsive channels from self-assembly of two diblock copolymers. *Angewandte Chemie International Edition* **2006,** *45* (30), 4959-4962.
113. Prabaharan, M.; Grailer, J. J.; Pilla, S.; Steeber, D. A.; Gong, S., Amphiphilic multi-arm-block copolymer conjugated with doxorubicin via pH-sensitive hydrazone bond for tumor-targeted drug delivery. *Biomaterials* **2009,** *30* (29), 5757-5766.
114. Wang, Y.; Zhong, W. H., Development of Electrolytes towards Achieving Safe and High-Performance Energy-Storage Devices: A Review. *ChemElectroChem* **2015,** *2* (1), 22-36.

115. Stephan, A. M., Review on gel polymer electrolytes for lithium batteries. *European polymer journal* **2006,** *42* (1), 21-42.
116. Song, J.; Wang, Y.; Wan, C. C., Review of gel-type polymer electrolytes for lithium-ion batteries. *Journal of power sources* **1999,** *77* (2), 183-197.
117. Jow, T. R.; Xu, K.; Borodin, O.; Ue, M., *Electrolytes for lithium and lithium-ion batteries*. Springer: 2014; Vol. 58.
118. Deng, F.; Wang, X.; He, D.; Hu, J.; Gong, C.; Ye, Y. S.; Xie, X.; Xue, Z., Microporous polymer electrolyte based on PVDF/PEO star polymer blends for lithium ion batteries. *Journal of membrane science* **2015,** *491*, 82-89.
119. de Bettignies, R.; Nicolas, Y.; Blanchard, P.; Levillain, E.; Nunzi, J. M.; Roncali, J., Planarized star-shaped oligothiophenes as a new class of organic semiconductors for heterojunction solar cells. *Advanced Materials* **2003,** *15* (22), 1939-1943.
120. Ponomarenko, S. A.; Kirchmeyer, S.; Elschner, A.; Huisman, B. H.; Karbach, A.; Drechsler, D., Star-Shaped Oligothiophenes for Solution-Processible Organic Field-Effect Transistors. *Advanced Functional Materials* **2003,** *13* (8), 591-596.
121. Chakraborty, C.; Layek, A.; Ray, P. P.; Malik, S., Star-shaped polyfluorene: Design, synthesis, characterization and application towards solar cells. *European polymer journal* **2014,** *52*, 181-192.
122. Smith, D. S.; Ghayoub, N.; Charissou, I.; Bellon, O.; Abélard, P.; Edwards, A. H., Transient thermal gradients in barium titanate positive temperature coefficient (PTC) thermistors. *Journal of the American ceramic Society* **1998,** *81* (7), 1789-1796.
123. Shut, V.; Kostomarov, S.; Gavrilov, A., PTCR ceramics produced from oxalate-derived barium titanate. *Inorganic Materials* **2008,** *44* (8), 905.
124. Cai, Q. J.; Gan, Y.; Chan-Park, M. B.; Yang, H. B.; Lu, Z. S.; Li, C. M.; Guo, J.; Dong, Z. L., Solution-processable barium titanate and strontium titanate nanoparticle dielectrics for low-voltage organic thin-film transistors. *Chemistry of Materials* **2009,** *21* (14), 3153-3161.
125. Jang, Y.; Lee, W. H.; Park, Y. D.; Kwak, D.; Cho, J. H.; Cho, K., High field-effect mobility pentacene thin-film transistors with nanoparticle polymer composite/polymer bilayer insulators. *Applied Physics Letters* **2009,** *94* (18), 125.
126. Yeh, M.; Liu, Y.; Liu, K.; Lin, I.; Lee, J.; Cheng, H., Electrical characteristics of barium titanate films prepared by laser ablation. *Journal of applied physics* **1993,** *74* (3), 2143-2145.
127. Jin, H.; Zhu, J., Size effect and fatigue mechanism in ferroelectric thin films. *Journal of applied physics* **2002,** *92* (8), 4594-4598.
128. Ruglovsky, J. L.; Li, J.; Bhattacharya, K.; Atwater, H. A., The effect of biaxial texture on the effective electromechanical constants of polycrystalline barium titanate and lead titanate thin films. *Acta materialia* **2006,** *54* (14), 3657-3663.
129. Maranganti, R.; Sharma, P., Atomistic determination of flexoelectric properties of crystalline dielectrics. *Physical Review B* **2009,** *80* (5), 054109.
130. Marx, J.; Eknoyan, O.; Taylor, H.; Tang, Z.; Neurgaonkar, R., Electro-optic modulation and self-poling in strain-induced waveguides in barium strontium titanate niobate. *Applied physics letters* **1995,** *67* (10), 1381-1383.
131. Dent, A.; Bowen, C.; Stevens, R.; Cain, M.; Stewart, M., Effective elastic properties for unpoled barium titanate. *Journal of the European Ceramic Society* **2007,** *27* (13-15), 3739-3743.
132. Meyer, R. J.; Newnham, R. E.; Amin, A.; Kulwicki, B. M., Flextensional barium strontium titanate actuators. *Journal of the American Ceramic Society* **2003,** *86* (6), 934-938.
133. Hueter, T.; Dozois, E., The frequency response of barium titanate transducers. *The Journal of the acoustical Society of America* **1952,** *24* (1), 85-86.
134. Haertling, G. H.; LAND, C. E., Hot-pressed (Pb, La)(Zr, Ti) O3 ferroelectric ceramics for electrooptic applications. *Journal of the American Ceramic Society* **1971,** *54* (1), 1-11.
135. Haertling, G. H., Ferroelectric ceramics: history and technology. *Journal of the American Ceramic Society* **1999,** *82* (4), 797-818.

136. Azough, F.; Al-Saffar, R.; Freer, R., A transmission electron microscope study of commercial X7R-type multilayer ceramic capacitors. *Journal of the European Ceramic Society* **1998,** *18* (7), 751-758.
137. Suntivich, J.; May, K. J.; Gasteiger, H. A.; Goodenough, J. B.; Shao-Horn, Y., A perovskite oxide optimized for oxygen evolution catalysis from molecular orbital principles. *Science* **2011,** *334* (6061), 1383-1385.
138. Huang, X.; Zhao, G.; Wang, G.; Irvine, J. T., Synthesis and applications of nanoporous perovskite metal oxides. *Chemical science* **2018,** *9* (15), 3623-3637.
139. Maeno, Y.; Hashimoto, H.; Yoshida, K.; Nishizaki, S.; Fujita, T.; Bednorz, J.; Lichtenberg, F., Superconductivity in a layered perovskite without copper. *Nature* **1994,** *372* (6506), 532-534.
140. Huang, Y.-H.; Dass, R. I.; Xing, Z.-L.; Goodenough, J. B., Double perovskites as anode materials for solid-oxide fuel cells. *Science* **2006,** *312* (5771), 254-257.
141. Kobayashi, K.-I.; Kimura, T.; Sawada, H.; Terakura, K.; Tokura, Y., Room-temperature magnetoresistance in an oxide material with an ordered double-perovskite structure. *Nature* **1998,** *395* (6703), 677-680.
142. Pena, M.; Fierro, J., Chemical structures and performance of perovskite oxides. *Chemical reviews* **2001,** *101* (7), 1981-2018.
143. Jiang, B.; Iocozzia, J.; Zhao, L.; Zhang, H.; Harn, Y.-W.; Chen, Y.; Lin, Z., Barium titanate at the nanoscale: controlled synthesis and dielectric and ferroelectric properties. *Chemical Society Reviews* **2019,** *48* (4), 1194-1228.
144. Zhao, Q.; Yan, Z.; Chen, C.; Chen, J., Spinels: controlled preparation, oxygen reduction/evolution reaction application, and beyond. *Chemical reviews* **2017,** *117* (15), 10121-10211.
145. Yamaguchi, Y.; Fukushima, M.; Ito, S.; Fujimoto, K., Low-temperature Solid-state Synthesis of Perovskite Oxides under 50° C. *Chemistry Letters* **2016,** *45* (2), 226-228.
146. Yamaguchi, Y.; Hamamoto, K.; Hamao, N.; Shimada, H.; Sumi, H.; Nomura, K.; Fujishiro, Y., Near room temperature synthesis of perovskite oxides. *Ceramics International* **2019,** *45* (18), 24936-24940.
147. Bartel, C. J.; Sutton, C.; Goldsmith, B. R.; Ouyang, R.; Musgrave, C. B.; Ghiringhelli, L. M.; Scheffler, M., New tolerance factor to predict the stability of perovskite oxides and halides. *Science advances* **2019,** *5* (2), eaav0693.
148. Li, Z.; Yang, M.; Park, J.-S.; Wei, S.-H.; Berry, J. J.; Zhu, K., Stabilizing perovskite structures by tuning tolerance factor: formation of formamidinium and cesium lead iodide solid-state alloys. *Chemistry of Materials* **2016,** *28* (1), 284-292.
149. Shi, C.; Yu, C. H.; Zhang, W., Predicting and screening dielectric transitions in a series of hybrid organic–inorganic double perovskites via an extended tolerance factor approach. *Angewandte Chemie International Edition* **2016,** *55* (19), 5798-5802.
150. Kieslich, G.; Sun, S.; Cheetham, A. K., An extended tolerance factor approach for organic–inorganic perovskites. *Chemical science* **2015,** *6* (6), 3430-3433.
151. Sato, T.; Takagi, S.; Deledda, S.; Hauback, B. C.; Orimo, S.-i., Extending the applicability of the Goldschmidt tolerance factor to arbitrary ionic compounds. *Scientific reports* **2016,** *6*, 23592.
152. Dutta, P. K.; Gregg, J., Hydrothermal synthesis of tetragonal barium titanate (BaTiO3). *Chemistry of materials* **1992,** *4* (4), 843-846.
153. Lu, S. W.; Lee, B. I.; Wang, Z. L.; Samuels, W. D., Hydrothermal synthesis and structural characterization of BaTiO3 nanocrystals. *Journal of Crystal Growth* **2000,** *219* (3), 269-276.
154. Ma, Y.; Vileno, E.; Suib, S. L.; Dutta, P. K., Synthesis of tetragonal BaTiO3 by microwave heating and conventional heating. *Chemistry of materials* **1997,** *9* (12), 3023-3031.
155. O'Brien, S.; Brus, L.; Murray, C. B., Synthesis of monodisperse nanoparticles of barium titanate: toward a generalized strategy of oxide nanoparticle synthesis. *Journal of the American Chemical Society* **2001,** *123* (48), 12085-12086.
156. Kessler, V. G.; Hubert-Pfalzgraf, L. G.; Daniele, S.; Gleizes, A., Single-source Precursors for BaTiO3: Synthesis and Characterization of. beta.-Diketonato Alkoxides and Molecular Structure of Ba2Ti2 (thd) 4 (. mu. 3-OEt) 2 (. mu.-OEt) 4 (OEt) 2 (EtOH) 2. *Chemistry of materials* **1994,** *6* (12), 2336-2342.

157. Wang, X.; Lee, B.; Hu, M.; Payzant, E.; Blom, D., Synthesis of nanocrystalline BaTiO3 by solvent refluxing method. *Journal of materials science letters* **2003,** *22* (7), 557-559.
158. Hernandez, B. A.; Chang, K.-S.; Fisher, E. R.; Dorhout, P. K., Sol− gel template synthesis and characterization of BaTiO3 and PbTiO3 nanotubes. *Chemistry of Materials* **2002,** *14* (2), 480-482.
159. Niederberger, M.; Pinna, N.; Polleux, J.; Antonietti, M., A general soft-chemistry route to perovskites and related materials: synthesis of BaTiO3, BaZrO3, and LiNbO3 nanoparticles. *Angewandte Chemie International Edition* **2004,** *43* (17), 2270-2273.
160. Komarneni, S.; Roy, R.; Li, Q., Microwave-hydrothermal synthesis of ceramic powders. *Materials Research Bulletin* **1992,** *27* (12), 1393-1405.
161. Smith, M. B.; Page, K.; Siegrist, T.; Redmond, P. L.; Walter, E. C.; Seshadri, R.; Brus, L. E.; Steigerwald, M. L., Crystal structure and the paraelectric-to-ferroelectric phase transition of nanoscale BaTiO3. *Journal of the American Chemical Society* **2008,** *130* (22), 6955-6963.
162. Schlag, S.; Eicke, H.-F., Size driven phase transition in nanocrystalline BaTiO3. *Solid state communications* **1994,** *91* (11), 883-887.
163. Jung, Y.-S.; Na, E.-S.; Paik, U.; Lee, J.; Kim, J., A study on the phase transition and characteristics of rare earth elements doped BaTiO3. *Materials research bulletin* **2002,** *37* (9), 1633-1640.
164. Dobal, P.; Dixit, A.; Katiyar, R.; Yu, Z.; Guo, R.; Bhalla, A., Micro-Raman scattering and dielectric investigations of phase transition behavior in the BaTiO 3–BaZrO 3 system. *Journal of Applied Physics* **2001,** *89* (12), 8085-8091.
165. Viswanath, R.; Ramasamy, S., Preparation and ferroelectric phase transition studies of nanocrystalline BaTiO3. *Nanostructured materials* **1997,** *8* (2), 155-162.
166. Kolhatkar, A. G.; Jamison, A. C.; Litvinov, D.; Willson, R. C.; Lee, T. R., Tuning the magnetic properties of nanoparticles. *International journal of molecular sciences* **2013,** *14* (8), 15977-16009.
167. Tsunekawa, S.; Ito, S.; Mori, T.; Ishikawa, K.; Li, Z.-Q.; Kawazoe, Y., Critical size and anomalous lattice expansion in nanocrystalline BaTiO 3 particles. *Physical Review B* **2000,** *62* (5), 3065.
168. Shaw, T.; Trolier-McKinstry, S.; McIntyre, P., The properties of ferroelectric films at small dimensions. *Annual Review of Materials Science* **2000,** *30* (1), 263-298.
169. Wang, Y.; Zhong, W.; Zhang, P., Size driven phase transition in ferroelectric particles. *Solid state communications* **1994,** *90* (5), 329-332.
170. Kanata, T.; Yoshikawa, T.; Kubota, K., Grain-size effects on dielectric phase transition of BaTiO3 ceramics. *Solid state communications* **1987,** *62* (11), 765-767.
171. Zheng, P.; Zhang, J.; Tan, Y.; Wang, C., Grain-size effects on dielectric and piezoelectric properties of poled BaTiO3 ceramics. *Acta Materialia* **2012,** *60* (13-14), 5022-5030.
172. Takeuchi, T.; Tabuchi, M.; Ado, K.; Honjo, K.; Nakamura, O.; Kageyama, H.; Suyama, Y.; Ohtori, N.; Nagasawa, M., Grain size dependence of dielectric properties of ultrafine BaTiO3 prepared by a sol-crystal method. *Journal of materials science* **1997,** *32* (15), 4053-4060.
173. Fang, C.; Chen, L.; Zhou, D., Influence of domain on grain size effects of the dielectric properties of BaTiO3 nanoceramics and nanoparticles. *Physica B: Condensed Matter* **2013,** *409*, 83-86.
174. Trasatti, S., Electrocatalysis by oxides-attempt at a unifying approach. **1980**.
175. Chen, D.; Chen, C.; Baiyee, Z. M.; Shao, Z.; Ciucci, F., Nonstoichiometric oxides as low-cost and highly-efficient oxygen reduction/evolution catalysts for low-temperature electrochemical devices. *Chemical reviews* **2015,** *115* (18), 9869-9921.
176. Liu, S.; Luo, H.; Li, Y.; Liu, Q.; Luo, J.-L., Structure-engineered electrocatalyst enables highly active and stable oxygen evolution reaction over layered perovskite LaSr3Co1. 5Fe1. 5O10-δ. *Nano Energy* **2017,** *40*, 115-121.
177. Takeguchi, T.; Yamanaka, T.; Takahashi, H.; Watanabe, H.; Kuroki, T.; Nakanishi, H.; Orikasa, Y.; Uchimoto, Y.; Takano, H.; Ohguri, N., Layered perovskite oxide: a reversible air electrode for oxygen evolution/reduction in rechargeable metal-air batteries. *Journal of the American Chemical Society* **2013,** *135* (30), 11125-11130.

178. Jung, K.-N.; Lee, J.-I.; Im, W. B.; Yoon, S.; Shin, K.-H.; Lee, J.-W., Promoting Li 2 O 2 oxidation by an La 1.7 Ca 0.3 Ni 0.75 Cu 0.25 O 4 layered perovskite in lithium–oxygen batteries. *Chemical Communications* **2012,** *48* (75), 9406-9408.
179. Ortatatlı, Ş.; Ternieden, J.; Weidenthaler, C., Low Temperature Formation of Ruddlesden–Popper-Type Layered La2CoO4±δ Perovskite Monitored via In Situ X-ray Powder Diffraction. *European Journal of Inorganic Chemistry* **2018,** *2018* (48), 5238-5245.
180. Amow, G.; Davidson, I.; Skinner, S., A comparative study of the Ruddlesden-Popper series, Lan+ 1NinO3n+ 1 (n= 1, 2 and 3), for solid-oxide fuel-cell cathode applications. *Solid State Ionics* **2006,** *177* (13-14), 1205-1210.
181. Le Dréau, L. Phase transitions and oxygen ordering in La2CoO4+ δ and (T, T')-La2CuO4: single crystal growth and structural studies using synchrotron and neutron diffraction methods. 2011.
182. Madelung, O.; Rössler, U.; Schulz, M., Ternary Compounds, Organic Semiconductors. *Landolt-Bornstein− Group III Condensed Matter* **2000**.
183. Tokura, Y.; Takagi, H.; Uchida, S., A superconducting copper oxide compound with electrons as the charge carriers. *nature* **1989,** *337* (6205), 345-347.
184. Chen, B.-H., Introduction of a tolerance factor for the Nd2CuO4 (T′)-type structure. *Journal of Solid State Chemistry* **1996,** *125* (1), 63-66.
185. Boehm, E.; Bassat, J.-M.; Dordor, P.; Mauvy, F.; Grenier, J.-C.; Stevens, P., Oxygen diffusion and transport properties in non-stoichiometric Ln2− xNiO4+ δ oxides. *Solid State Ionics* **2005,** *176* (37-38), 2717-2725.
186. Tarancón, A.; Burriel, M.; Santiso, J.; Skinner, S. J.; Kilner, J. A., Advances in layered oxide cathodes for intermediate temperature solid oxide fuel cells. *Journal of Materials chemistry* **2010,** *20* (19), 3799-3813.
187. Kim, J.; Sengodan, S.; Kwon, G.; Ding, D.; Shin, J.; Liu, M.; Kim, G., Triple-conducting layered perovskites as cathode materials for proton-conducting solid oxide fuel cells. *ChemSusChem* **2014,** *7* (10), 2811-2815.
188. Xie, W.; Lee, Y.-L.; Shao-Horn, Y.; Morgan, D., Oxygen Point Defect Chemistry in Ruddlesden–Popper Oxides (La1–x Sr x) 2MO4±δ (M= Co, Ni, Cu). *The journal of physical chemistry letters* **2016,** *7* (10), 1939-1944.
189. Centi, G.; Perathoner, S., Catalysis by layered materials: A review. *Microporous and mesoporous materials* **2008,** *107* (1-2), 3-15.
190. Gómez, S.; Gurauskis, J.; Øygarden, V.; Hotza, D.; Grande, T.; Wiik, K., Synthesis and oxygen transport properties of La2− ySryNi1− xMoxO4+ δ. *Solid State Ionics* **2016,** *292*, 38-44.
191. Munnings, C.; Skinner, S.; Amow, G.; Whitfield, P.; Davidson, I., Oxygen transport in the La2Ni1− xCoxO4+ δ system. *Solid State Ionics* **2005,** *176* (23-24), 1895-1901.
192. Woolley, R.; Ryan, M.; Skinner, S., In Situ Measurements on Solid Oxide Fuel Cell Cathodes–Simultaneous X-Ray Absorption and AC Impedance Spectroscopy on Symmetrical Cells. *Fuel Cells* **2013,** *13* (6), 1080-1087.
193. Sayers, R.; Skinner, S., Evidence for the catalytic oxidation of La 2 NiO 4+ δ. *Journal of materials chemistry* **2011,** *21* (2), 414-419.
194. Kim, S. J.; Kim, K. J.; Dayaghi, A. M.; Choi, G. M., Polarization and stability of La2NiO4+ δ in comparison with La0. 6Sr0. 4Co0. 2Fe0. 8O3− δ as air electrode of solid oxide electrolysis cell. *International Journal of Hydrogen Energy* **2016,** *41* (33), 14498-14506.
195. Sharma, R. K.; Burriel, M.; Dessemond, L.; Martin, V.; Bassat, J.-M.; Djurado, E., An innovative architectural design to enhance the electrochemical performance of La2NiO4+ δ cathodes for solid oxide fuel cell applications. *Journal of Power Sources* **2016,** *316*, 17-28.
196. Tong, X.; Zhou, F.; Yang, S.; Zhong, S.; Wei, M.; Liu, Y., Performance and stability of Ruddlesden-Popper La2NiO4+ δ oxygen electrodes under solid oxide electrolysis cell operation conditions. *Ceramics International* **2017,** *43* (14), 10927-10933.

197. Huan, Y.; Chen, S.; Zeng, R.; Wei, T.; Dong, D.; Hu, X.; Huang, Y., Intrinsic Effects of Ruddlesden-Popper-Based Bifunctional Catalysts for High-Temperature Oxygen Reduction and Evolution. *Advanced Energy Materials* **2019,** *9* (29), 1901573.
198. Jung, K.-N.; Jung, J.-H.; Im, W. B.; Yoon, S.; Shin, K.-H.; Lee, J.-W., Doped lanthanum nickelates with a layered perovskite structure as bifunctional cathode catalysts for rechargeable metal–air batteries. *ACS applied materials & interfaces* **2013,** *5* (20), 9902-9907.
199. Tsai, H.; Nie, W.; Blancon, J.-C.; Stoumpos, C. C.; Asadpour, R.; Harutyunyan, B.; Neukirch, A. J.; Verduzco, R.; Crochet, J. J.; Tretiak, S., High-efficiency two-dimensional Ruddlesden–Popper perovskite solar cells. *Nature* **2016,** *536* (7616), 312-316.
200. Kharton, V.; Viskup, A.; Kovalevsky, A.; Naumovich, E.; Marques, F., Ionic transport in oxygen-hyperstoichiometric phases with K2NiF4-type structure. *Solid State Ionics* **2001,** *143* (3-4), 337-353.
201. Kanade, K.; Baeg, J.-O.; Kong, K.-j.; Kale, B.; Lee, S. M.; Moon, S.-J.; Lee, C. W.; Yoon, S., A new layer perovskites Pb2Ga2Nb2O10 and RbPb2Nb2O7: An efficient visible light driven photocatalysts to hydrogen generation. *International journal of hydrogen energy* **2008,** *33* (23), 6904-6912.
202. Li, Y.; Chen, G.; Zhang, H.; Li, Z.; Sun, J., Electronic structure and photocatalytic properties of ABi2Ta2O9 (A= Ca, Sr, Ba). *Journal of Solid State Chemistry* **2008,** *181* (10), 2653-2659.
203. Ko, Y.-G.; Lee, W. Y., Effects of nickel-loading method on the water-splitting activity of a layered NiO x/Sr 4 Ti 3 O 10 photocatalyst. *Catalysis letters* **2002,** *83* (3-4), 157-160.
204. Zhao, Z.; Yang, X.; Wu, Y., Comparative study of nickel-based perovskite-like mixed oxide catalysts for direct decomposition of NO. *Applied Catalysis B: Environmental* **1996,** *8* (3), 281-297.
205. Ramesh, S.; Hegde, M. S., New uniform solid catalyst for the low-temperature oxidation of carbon monoxide: A triple-layered rare earth perovskite containing Co and Cu ions. *The Journal of Physical Chemistry* **1996,** *100* (20), 8443-8447.
206. Hu, M. Z.-C.; Kurian, V.; Payzant, E. A.; Rawn, C. J.; Hunt, R. D., Wet-chemical synthesis of monodispersed barium titanate particles—hydrothermal conversion of TiO2 microspheres to nanocrystalline BaTiO3. *Powder Technology* **2000,** *110* (1-2), 2-14.
207. Slamovich, E. B.; Aksay, I. A., Structure evolution in hydrothermally processed (< 100 C) BaTiO3 films. *Journal of the American Ceramic Society* **1996,** *79* (1), 239-247.
208. Ciftci, E.; Rahaman, M.; Shumsky, M., Hydrothermal precipitation and characterization of nanocrystalline BaTiO3 particles. *Journal of materials science* **2001,** *36* (20), 4875-4882.
209. Feng, Q.; Hirasawa, M.; Yanagisawa, K., Synthesis of crystal-axis-oriented BaTiO3 and anatase platelike particles by a hydrothermal soft chemical process. *Chemistry of materials* **2001,** *13* (2), 290-296.
210. Frey, M.; Payne, D., Nanocrystalline barium titanate: evidence for the absence of ferroelectricity in sol-gel derived thin-layer capacitors. *Applied physics letters* **1993,** *63* (20), 2753-2755.
211. Limmer, S. J.; Seraji, S.; Wu, Y.; Chou, T. P.; Nguyen, C.; Cao, G. Z., Template-Based Growth of Various Oxide Nanorods by Sol–Gel Electrophoresis. *Advanced Functional Materials* **2002,** *12* (1), 59-64.
212. Kamalasanan, M.; Chandra, S.; Joshi, P.; Mansingh, A., Structural and optical properties of sol-gel-processed BaTiO3 ferroelectric thin films. *Applied physics letters* **1991,** *59* (27), 3547-3549.
213. Lee, B.; Zhang, J., Preparation, structure evolution and dielectric properties of BaTiO3 thin films and powders by an aqueous sol–gel process. *Thin solid films* **2001,** *388* (1-2), 107-113.
214. Yoko, T.; Kamiya, K.; Tanaka, K., Preparation of multiple oxide BaTiO 3 fibres by the sol-gel method. *Journal of materials science* **1990,** *25* (9), 3922-3929.
215. Shimooka, H.; Kuwabara, M., Preparation of Dense BaTiO3 Ceramics from Sol-Gel-Derived Monolithic Gels. *Journal of the American Ceramic Society* **1995,** *78* (10), 2849-2852.
216. Cheung, M.; Chan, H.; Choy, C., Study on barium titanate ceramics prepared by various methods. *Journal of materials science* **2001,** *36* (2), 381-387.
217. Simon-Seveyrat, L.; Hajjaji, A.; Emziane, Y.; Guiffard, B.; Guyomar, D., Re-investigation of synthesis of BaTiO3 by conventional solid-state reaction and oxalate coprecipitation route for piezoelectric applications. *Ceramics international* **2007,** *33* (1), 35-40.
218. Potdar, H.; Deshpande, S.; Date, S., Chemical coprecipitation of mixed (Ba+ Ti) oxalates precursor leading to BaTiO3 powders. *Materials chemistry and physics* **1999,** *58* (2), 121-127.

219. Lee, S.; Park, T.; Choi, G.; Koo, K.; Kim, S. W., Effects of KOH/BaTi and Ba/Ti ratios on synthesis of BaTiO3 powder by coprecipitation/hydrothermal reaction. *Materials chemistry and physics* **2003,** *82* (3), 742-749.
220. Choi, G. J.; Lee, S. K.; Woo, K. J.; Koo, K. K.; Cho, Y. S., Characteristics of BaTiO3 Particles Prepared by Spray− Coprecipitation Method Using Titanium Acylate-Based Precursors. *Chemistry of materials* **1998,** *10* (12), 4104-4113.
221. Brutchey, R. L.; Morse, D. E., Template-free, low-temperature synthesis of crystalline barium titanate nanoparticles under bio-inspired conditions. *Angewandte Chemie International Edition* **2006,** *45* (39), 6564-6566.
222. Urban, J. J.; Spanier, J. E.; Ouyang, L.; Yun, W. S.; Park, H., Single-crystalline barium titanate nanowires. *Advanced Materials* **2003,** *15* (5), 423-426.
223. Berweger, S.; Neacsu, C. C.; Mao, Y.; Zhou, H.; Wong, S. S.; Raschke, M. B., Optical nanocrystallography with tip-enhanced phonon Raman spectroscopy. *Nature nanotechnology* **2009,** *4* (8), 496.
224. Žagar, K.; Rečnik, A.; Šturm, S.; Gajović, A.; Čeh, M., Structural and chemical characterization of BaTiO3 nanorods. *Materials Research Bulletin* **2011,** *46* (3), 366-371.
225. Son, J. Y.; Lee, J.-H.; Song, S.; Shin, Y.-H.; Jang, H. M., Four-states multiferroic memory embodied using Mn-doped BaTiO3 nanorods. *ACS nano* **2013,** *7* (6), 5522-5529.
226. Gajović, A.; Pleština, J. V.; Žagar, K.; Plodinec, M.; Šturm, S.; Čeh, M., Temperature-dependent Raman spectroscopy of BaTiO3 nanorods synthesized by using a template-assisted sol–gel procedure. *Journal of Raman Spectroscopy* **2013,** *44* (3), 412-420.
227. Hou, B.; Li, Z.; Xu, Y.; Wu, D.; Sun, Y., Solvothermal synthesis of single-crystalline BaTiO3 nanocubes in a mixed solution. *Chemistry letters* **2005,** *34* (7), 1040-1041.
228. Alluri, N. R.; Chandrasekhar, A.; Vivekananthan, V.; Purusothaman, Y.; Selvarajan, S.; Jeong, J. H.; Kim, S.-J., Scavenging biomechanical energy using high-performance, flexible BaTiO3 nanocube/PDMS composite films. *ACS Sustainable Chemistry & Engineering* **2017,** *5* (6), 4730-4738.
229. Mimura, K.; Kato, K.; Imai, H.; Wada, S.; Haneda, H.; Kuwabara, M., Piezoresponse properties of orderly assemblies of BaTiO3 and SrTiO3 nanocube single crystals. *Applied Physics Letters* **2012,** *101* (1), 012901.
230. Miao, J.; Hu, C.; Liu, H.; Xiong, Y., BaTiO3 nanocubes: Size-selective formation and structure analysis. *Materials letters* **2008,** *62* (2), 235-238.
231. Swaminathan, V.; Pramana, S. S.; White, T.; Chen, L.; Chukka, R.; Ramanujan, R., Microwave synthesis of noncentrosymmetric BaTiO3 truncated nanocubes for charge storage applications. *ACS applied materials & interfaces* **2010,** *2* (11), 3037-3042.
232. Babkevich, P.; Prabhakaran, D.; Frost, C.; Boothroyd, A., Magnetic spectrum of the two-dimensional antiferromagnet La 2 CoO 4 studied by inelastic neutron scattering. *Physical Review B* **2010,** *82* (18), 184425.
233. Le Dreau, L.; Prestipino, C.; Hernandez, O.; Schefer, J. r.; Vaughan, G.; Paofai, S.; Perez-Mato, J. M.; Hosoya, S.; Paulus, W., Structural modulation and phase transitions in La2CoO4. 14 investigated by synchrotron x-ray and neutron single-crystal diffraction. *Inorganic chemistry* **2012,** *51* (18), 9789-9798.
234. Midouni, A.; Houchati, M. I.; Othman, W. B.; Chniba-Boudjada, N.; Ceretti, M.; Paulus, W.; Jaouadi, M.; Hamzaoui, A. H., Influence of nickel doping on oxygen-ionic conductivity of the n= 1 Ruddlesden-Popper Phases La1. 85Ca0. 15 (Cu1− xNix) O4− δ (δ= 0.0905). *Journal of Solid State Chemistry* **2016,** *240*, 101-108.
235. Nemudry, A.; Rudolf, P.; Schöllhorn, R., Room temperature topotactic oxidation of lanthanum cobalt oxide La2CoO4. 0. *Solid State Ionics* **1998,** *109* (3-4), 213-222.
236. Guo, J.; Lou, H.; Zhu, Y.; Zheng, X., La-based perovskite precursors preparation and its catalytic activity for CO2 reforming of CH4. *Materials Letters* **2003,** *57* (28), 4450-4455.
237. Jeon, S.-Y.; Choi, M.-B.; Im, H.-N.; Hwang, J.-H.; Song, S.-J., Oxygen ionic conductivity of La2NiO4+ δ via interstitial oxygen defect. *Journal of Physics and Chemistry of Solids* **2012,** *73* (5), 656-660.

238. Jeong, C.; Lee, J.-H.; Park, M.; Hong, J.; Kim, H.; Son, J.-W.; Lee, J.-H.; Kim, B.-K.; Yoon, K. J., Design and processing parameters of La2NiO4+ δ-based cathode for anode-supported planar solid oxide fuel cells (SOFCs). *Journal of Power Sources* **2015,** *297*, 370-378.
239. Stephens, I. E.; Bondarenko, A. S.; Grønbjerg, U.; Rossmeisl, J.; Chorkendorff, I., Understanding the electrocatalysis of oxygen reduction on platinum and its alloys. *Energy & Environmental Science* **2012,** *5* (5), 6744-6762.
240. Zhu, H.; Zhang, P.; Dai, S., Recent advances of lanthanum-based perovskite oxides for catalysis. *ACS Catalysis* **2015,** *5* (11), 6370-6385.
241. Liang, Y.; Li, Y.; Wang, H.; Zhou, J.; Wang, J.; Regier, T.; Dai, H., Co 3 O 4 nanocrystals on graphene as a synergistic catalyst for oxygen reduction reaction. *Nature materials* **2011,** *10* (10), 780-786.
242. Suntivich, J.; Gasteiger, H. A.; Yabuuchi, N.; Nakanishi, H.; Goodenough, J. B.; Shao-Horn, Y., Design principles for oxygen-reduction activity on perovskite oxide catalysts for fuel cells and metal–air batteries. *Nature chemistry* **2011,** *3* (7), 546-550.
243. Tong, Y.; Guo, Y.; Chen, P.; Liu, H.; Zhang, M.; Zhang, L.; Yan, W.; Chu, W.; Wu, C.; Xie, Y., Spin-state regulation of perovskite cobaltite to realize enhanced oxygen evolution activity. *Chem* **2017,** *3* (5), 812-821.
244. Liu, R.; Liang, F.; Zhou, W.; Yang, Y.; Zhu, Z., Calcium-doped lanthanum nickelate layered perovskite and nickel oxide nano-hybrid for highly efficient water oxidation. *Nano Energy* **2015,** *12*, 115-122.
245. May, K. J.; Carlton, C. E.; Stoerzinger, K. A.; Risch, M.; Suntivich, J.; Lee, Y.-L.; Grimaud, A.; Shao-Horn, Y., Influence of oxygen evolution during water oxidation on the surface of perovskite oxide catalysts. *The journal of physical chemistry letters* **2012,** *3* (22), 3264-3270.
246. Grimaud, A.; May, K. J.; Carlton, C. E.; Lee, Y.-L.; Risch, M.; Hong, W. T.; Zhou, J.; Shao-Horn, Y., Double perovskites as a family of highly active catalysts for oxygen evolution in alkaline solution. *Nature communications* **2013,** *4*, 2439.
247. Mefford, J. T.; Rong, X.; Abakumov, A. M.; Hardin, W. G.; Dai, S.; Kolpak, A. M.; Johnston, K. P.; Stevenson, K. J., Water electrolysis on La 1− x Sr x CoO 3− δ perovskite electrocatalysts. *Nature communications* **2016,** *7* (1), 1-11.
248. Xu, J.; Chen, C.; Han, Z.; Yang, Y.; Li, J.; Deng, Q., Recent Advances in Oxygen Electrocatalysts Based on Perovskite Oxides. *Nanomaterials* **2019,** *9* (8), 1161.
249. Matsumoto, Y.; Yoneyama, H.; Tamura, H., Catalytic activity for electrochemical reduction of oxygen of lanthanum nickel oxide and related oxides. *Journal of Electroanalytical Chemistry and Interfacial Electrochemistry* **1977,** *79* (2), 319-326.
250. Hardin, W. G.; Mefford, J. T.; Slanac, D. A.; Patel, B. B.; Wang, X.; Dai, S.; Zhao, X.; Ruoff, R. S.; Johnston, K. P.; Stevenson, K. J., Tuning the electrocatalytic activity of perovskites through active site variation and support interactions. *Chemistry of Materials* **2014,** *26* (11), 3368-3376.
251. Zhu, Y.; Zhou, W.; Yu, J.; Chen, Y.; Liu, M.; Shao, Z., Enhancing electrocatalytic activity of perovskite oxides by tuning cation deficiency for oxygen reduction and evolution reactions. *Chemistry of Materials* **2016,** *28* (6), 1691-1697.
252. Jung, J. I.; Jeong, H. Y.; Lee, J. S.; Kim, M. G.; Cho, J., A bifunctional perovskite catalyst for oxygen reduction and evolution. *Angewandte Chemie International Edition* **2014,** *53* (18), 4582-4586.
253. Grimaud, A.; Diaz-Morales, O.; Han, B.; Hong, W. T.; Lee, Y.-L.; Giordano, L.; Stoerzinger, K. A.; Koper, M. T.; Shao-Horn, Y., Activating lattice oxygen redox reactions in metal oxides to catalyse oxygen evolution. *Nature chemistry* **2017,** *9* (5), 457.
254. Sathiya, M.; Rousse, G.; Ramesha, K.; Laisa, C.; Vezin, H.; Sougrati, M. T.; Doublet, M.-L.; Foix, D.; Gonbeau, D.; Walker, W., Reversible anionic redox chemistry in high-capacity layered-oxide electrodes. *Nature materials* **2013,** *12* (9), 827-835.
255. Cheng, X.; Fabbri, E.; Nachtegaal, M.; Castelli, I. E.; El Kazzi, M.; Haumont, R.; Marzari, N.; Schmidt, T. J., Oxygen evolution reaction on La1–x Sr x CoO3 perovskites: a combined experimental and theoretical study of their structural, electronic, and electrochemical properties. *Chemistry of Materials* **2015,** *27* (22), 7662-7672.

256. Shin, B.; Choi, S.; Tak, Y., Electrocatalytic activity of Co-based perovskite oxides for oxygen reduction and evolution reactions. *Int. J. Electrochem. Sci* **2016,** *11*, 5900-5908.
257. Retuerto, M.; Pascual, L.; Calle-Vallejo, F.; Ferrer, P.; Gianolio, D.; Pereira, A. G.; García, Á.; Torrero, J.; Fernández-Díaz, M. T.; Bencok, P., Na-doped ruthenium perovskite electrocatalysts with improved oxygen evolution activity and durability in acidic media. *Nature communications* **2019,** *10* (1), 1-9.
258. Celorrio, V.; Tiwari, D.; Fermin, D. J., Composition-Dependent Reactivity of Ba0. 5Sr0. 5Co x Fe1–x O3− δ toward the Oxygen Reduction Reaction. *The Journal of Physical Chemistry C* **2016,** *120* (39), 22291-22297.
259. Sun, N.; Liu, H.; Yu, Z.; Zheng, Z.; Shao, C., The electrochemical performance of La 0. 6 Sr 0. 4 Co 1-x Ni x O 3 perovskite catalysts for Li-O 2 batteries. *Ionics* **2016,** *22* (6), 869-876.
260. Zhang, D.; Song, Y.; Du, Z.; Wang, L.; Li, Y.; Goodenough, J. B., Active LaNi 1− x Fe x O 3 bifunctional catalysts for air cathodes in alkaline media. *Journal of Materials Chemistry A* **2015,** *3* (18), 9421-9426.
261. Su, C.; Wang, W.; Chen, Y.; Yang, G.; Xu, X.; Tadé, M. O.; Shao, Z., SrCo0. 9Ti0. 1O3− δ as a new electrocatalyst for the oxygen evolution reaction in alkaline electrolyte with stable performance. *ACS applied materials & interfaces* **2015,** *7* (32), 17663-17670.
262. Wang, H.; Xu, W.; Richins, S.; Liaw, K.; Yan, L.; Zhou, M.; Luo, H., Polymer-assisted approach to LaCo1-xNixO3 network nanostructures as bifunctional oxygen electrocatalysts. *Electrochimica Acta* **2019,** *296*, 945-953.
263. Zhu, Y.; Zhou, W.; Chen, Y.; Yu, J.; Xu, X.; Su, C.; Tadé, M. O.; Shao, Z., Boosting oxygen reduction reaction activity of palladium by stabilizing its unusual oxidation states in perovskite. *Chemistry of Materials* **2015,** *27* (8), 3048-3054.
264. Li, Z.; Lv, L.; Wang, J.; Ao, X.; Ruan, Y.; Zha, D.; Hong, G.; Wu, Q.; Lan, Y.; Wang, C., Engineering phosphorus-doped LaFeO3-δ perovskite oxide as robust bifunctional oxygen electrocatalysts in alkaline solutions. *Nano Energy* **2018,** *47*, 199-209.
265. Zhu, Y.; Zhou, W.; Sunarso, J.; Zhong, Y.; Shao, Z., Phosphorus-Doped Perovskite Oxide as Highly Efficient Water Oxidation Electrocatalyst in Alkaline Solution. *Advanced Functional Materials* **2016,** *26* (32), 5862-5872.
266. Zhou, W.; Zhao, M.; Liang, F.; Smith, S. C.; Zhu, Z., High activity and durability of novel perovskite electrocatalysts for water oxidation. *Materials Horizons* **2015,** *2* (5), 495-501.
267. Velraj, S.; Zhu, J., Sm0. 5Sr0. 5CoO3− δ–A new bi-functional catalyst for rechargeable metal-air battery applications. *Journal of power sources* **2013,** *227*, 48-52.
268. Jiang, Y.; Geng, Z.; Yuan, L.; Sun, Y.; Cong, Y.; Huang, K.; Wang, L.; Zhang, W., Nanoscale Architecture of RuO2/La0. 9Fe0. 92Ru0. 08–x O3− δ Composite via Manipulating the Exsolution of Low Ru-Substituted A-Site Deficient Perovskite. *ACS Sustainable Chemistry & Engineering* **2018,** *6* (9), 11999-12005.
269. Kim, J.; Yin, X.; Tsao, K.-C.; Fang, S.; Yang, H., Ca2Mn2O5 as oxygen-deficient perovskite electrocatalyst for oxygen evolution reaction. *Journal of the American Chemical Society* **2014,** *136* (42), 14646-14649.
270. Chen, C.-F.; King, G.; Dickerson, R. M.; Papin, P. A.; Gupta, S.; Kellogg, W. R.; Wu, G., Oxygen-deficient BaTiO3− x perovskite as an efficient bifunctional oxygen electrocatalyst. *Nano Energy* **2015,** *13*, 423-432.
271. Zhou, W.; Sunarso, J., Enhancing bi-functional electrocatalytic activity of perovskite by temperature shock: A case study of LaNiO3− δ. *The journal of physical chemistry letters* **2013,** *4* (17), 2982-2988.
272. Menzel, N.; Ortel, E.; Kraehnert, R.; Strasser, P., Electrocatalysis using porous nanostructured materials. *ChemPhysChem* **2012,** *13* (6), 1385-1394.
273. Zhu, C.; Li, H.; Fu, S.; Du, D.; Lin, Y., Highly efficient nonprecious metal catalysts towards oxygen reduction reaction based on three-dimensional porous carbon nanostructures. *Chemical Society Reviews* **2016,** *45* (3), 517-531.

274. Mattick, V. F.; Jin, X.; White, R. E.; Huang, K., Understanding the role of carbon in alkaline oxygen electrocatalysis: A case study on La0. 6Sr0. 4CoO3-δ/Vulcan carbon composite electrocatalyst. *International Journal of Hydrogen Energy* **2019,** *44* (5), 2760-2769.
275. Hu, J.; Liu, Q.; Shi, Z.; Zhang, L.; Huang, H., LaNiO 3-nanorod/graphene composite as an efficient bi-functional catalyst for zinc–air batteries. *RSC advances* **2016,** *6* (89), 86386-86394.
276. Kittel, C., Introduction to Solid State Physics, (Wiley, New York, 1996). *K. Balasubramanian, Chem. Rev* **1990,** *35*, 90-93.
277. Bertotti, G., *Hysteresis in magnetism: for physicists, materials scientists, and engineers*. Academic press: 1998.
278. Jiles, D., *Introduction to magnetism and magnetic materials*. CRC press: 2015.
279. Morrish, A., "The Physical Principles of Magnetism"(John Wiley and Sons., Inc., New York, 1965).
280. Song, Q. Size and shape controlled synthesis and superparamagnetic properties of spinel ferrites nanocrystals. Georgia Institute of Technology, 2005.
281. Jeong, U.; Teng, X.; Wang, Y.; Yang, H.; Xia, Y., Superparamagnetic colloids: controlled synthesis and niche applications. *Advanced Materials* **2007,** *19* (1), 33-60.
282. Frey, N. A.; Peng, S.; Cheng, K.; Sun, S., Magnetic nanoparticles: synthesis, functionalization, and applications in bioimaging and magnetic energy storage. *Chemical Society Reviews* **2009,** *38* (9), 2532-2542.
283. López-Ortega, A.; Estrader, M.; Salazar-Alvarez, G.; Roca, A. G.; Nogués, J., Applications of exchange coupled bi-magnetic hard/soft and soft/hard magnetic core/shell nanoparticles. *Physics Reports* **2015,** *553*, 1-32.
284. Vestal, C. R.; Zhang, Z. J., Effects of surface coordination chemistry on the magnetic properties of MnFe2O4 spinel ferrite nanoparticles. *Journal of the American Chemical Society* **2003,** *125* (32), 9828-9833.
285. Pereira, C.; Pereira, A. M.; Fernandes, C.; Rocha, M.; Mendes, R.; Fernández-García, M. P.; Guedes, A.; Tavares, P. B.; Grenèche, J.-M.; Araújo, J. o. P., Superparamagnetic MFe2O4 (M= Fe, Co, Mn) nanoparticles: tuning the particle size and magnetic properties through a novel one-step coprecipitation route. *Chemistry of Materials* **2012,** *24* (8), 1496-1504.
286. Liu, C.; Zou, B.; Rondinone, A. J.; Zhang, Z. J., Reverse micelle synthesis and characterization of superparamagnetic MnFe2O4 spinel ferrite nanocrystallites. *The Journal of Physical Chemistry B* **2000,** *104* (6), 1141-1145.
287. Sun, S.; Zeng, H.; Robinson, D. B.; Raoux, S.; Rice, P. M.; Wang, S. X.; Li, G., Monodisperse mfe2o4 (m= fe, co, mn) nanoparticles. *Journal of the American Chemical Society* **2004,** *126* (1), 273-279.
288. Long, X.-Y.; Li, J.-Y.; Sheng, D.; Lian, H.-Z., Spinel-type manganese ferrite (MnFe2O4) microspheres: A novel affinity probe for selective and fast enrichment of phosphopeptides. *Talanta* **2017,** *166*, 36-45.
289. Naseri, M. G.; Saion, E. B., Crystalization in spinel ferrite nanoparticles. *Advances in Crystallization Processes* **2012**, 349-380.
290. Pradhan, P.; Giri, J.; Samanta, G.; Sarma, H. D.; Mishra, K. P.; Bellare, J.; Banerjee, R.; Bahadur, D., Comparative evaluation of heating ability and biocompatibility of different ferrite-based magnetic fluids for hyperthermia application. *Journal of Biomedical Materials Research Part B: Applied Biomaterials: An Official Journal of The Society for Biomaterials, The Japanese Society for Biomaterials, and The Australian Society for Biomaterials and the Korean Society for Biomaterials* **2007,** *81* (1), 12-22.
291. Aghavnian, T.; Moussy, J.-B.; Stanescu, D.; Belkhou, R.; Jedrecy, N.; Magnan, H.; Ohresser, P.; Arrio, M.-A.; Sainctavit, P.; Barbier, A., Determination of the cation site distribution of the spinel in multiferroic CoFe2O4/BaTiO3 layers by X-ray photoelectron spectroscopy. *Journal of Electron Spectroscopy and Related Phenomena* **2015,** *202*, 16-21.
292. Nguyen, L. H., INFLUENCE OF SATURATION MAGNETIZATION AND VISCOSITY ON SPECIFIC LOSS POWER FOR CoFe2O4 AND MnFe2O4 MAGNETIC NANOPARTICLES. *Vietnam Journal of Science and Technology* **2016,** *54* (1A), 33.

293. Andersen, H. L.; Saura-Múzquiz, M.; Granados-Miralles, C.; Canévet, E.; Lock, N.; Christensen, M., Crystalline and magnetic structure–property relationship in spinel ferrite nanoparticles. *Nanoscale* **2018,** *10* (31), 14902-14914.
294. Goodarz Naseri, M.; Saion, E. B.; Kamali, A., An overview on nanocrystalline ZnFe 2 O 4, MnFe 2 O 4, and CoFe 2 O 4 synthesized by a thermal treatment method. *ISRN Nanotechnology* **2012,** *2012*.
295. Xu, Y.; Sherwood, J.; Qin, Y.; Holler, R. A.; Bao, Y., A general approach to the synthesis and detailed characterization of magnetic ferrite nanocubes. *Nanoscale* **2015,** *7* (29), 12641-12649.
296. Bruno, P., Magnetic surface anisotropy of cobalt and surface roughness effects within Neel's model. *Journal of Physics F: Metal Physics* **1988,** *18* (6), 1291.
297. Garanin, D.; Kachkachi, H., Surface contribution to the anisotropy of magnetic nanoparticles. *Physical review letters* **2003,** *90* (6), 065504.
298. Bruno, P.; Renard, J.-P., Magnetic surface anisotropy of transition metal ultrathin films. *Applied Physics A* **1989,** *49* (5), 499-506.
299. Lu, Y.; Altman, R.; Marley, A.; Rishton, S.; Trouilloud, P.; Xiao, G.; Gallagher, W.; Parkin, S., Shape-anisotropy-controlled magnetoresistive response in magnetic tunnel junctions. *Applied physics letters* **1997,** *70* (19), 2610-2612.
300. Grimsditch, M.; Jaccard, Y.; Schuller, I. K., Magnetic anisotropies in dot arrays: Shape anisotropy versus coupling. *Physical Review B* **1998,** *58* (17), 11539.
301. Dubowik, J., Shape anisotropy of magnetic heterostructures. *Physical Review B* **1996,** *54* (2), 1088.
302. Daalderop, G.; Kelly, P.; Schuurmans, M., First-principles calculation of the magnetocrystalline anisotropy energy of iron, cobalt, and nickel. *Physical Review B* **1990,** *41* (17), 11919.
303. Daalderop, G.; Kelly, P.; Schuurmans, M., Magnetocrystalline anisotropy and orbital moments in transition-metal compounds. *Physical Review B* **1991,** *44* (21), 12054.
304. Katter, M.; Wecker, J.; Schultz, L.; Grössinger, R., Magnetocrystalline anisotropy of Sm2Fe17N2. *Journal of magnetism and magnetic materials* **1990,** *92* (1), L14-L18.
305. Bruno, P., Tight-binding approach to the orbital magnetic moment and magnetocrystalline anisotropy of transition-metal monolayers. *Physical Review B* **1989,** *39* (1), 865.
306. Berger, L.; Labaye, Y.; Tamine, M.; Coey, J., Ferromagnetic nanoparticles with strong surface anisotropy: Spin structures and magnetization processes. *Physical Review B* **2008,** *77* (10), 104431.
307. Skomski, R., Exact nucleation modes in arrays of magnetic particles. *Journal of applied physics* **2002,** *91* (10), 7053-7055.
308. Pujada, B.; Sinnecker, E.; Rossi, A.; Guimaraes, A., Enhanced magnetic anisotropy in granular cobalt–copper alloys. *Journal of applied physics* **2003,** *93* (10), 7217-7219.
309. Luis, F.; Torres, J.; García, L.; Bartolomé, J.; Stankiewicz, J.; Petroff, F.; Fettar, F.; Maurice, J.-L.; Vaures, A., Enhancement of the magnetic anisotropy of nanometer-sized Co clusters: Influence of the surface and of interparticle interactions. *Physical Review B* **2002,** *65* (9), 094409.
310. Gurgel, A. L.; Martinelli, A. E.; de Aquino Conceição, O. L.; Xavier Jr, M. M.; Torres, M. A. M.; de Araújo Melo, D. M., Microwave-assisted hydrothermal synthesis and magnetic properties of nanostructured cobalt ferrite. *Journal of Alloys and Compounds* **2019,** *799*, 36-42.
311. Ortiz-Quiñonez, J.-L.; Pal, U.; Villanueva, M. S., Structural, magnetic, and catalytic evaluation of spinel Co, Ni, and Co–Ni ferrite nanoparticles fabricated by low-temperature solution combustion process. *ACS omega* **2018,** *3* (11), 14986-15001.
312. Kumar, Y.; Shirage, P. M., Highest coercivity and considerable saturation magnetization of CoFe 2 O 4 nanoparticles with tunable band gap prepared by thermal decomposition approach. *Journal of Materials Science* **2017,** *52* (9), 4840-4851.
313. Liu, F.; Laurent, S.; Roch, A.; Vander Elst, L.; Muller, R. N., Size-controlled synthesis of CoFe2O4 nanoparticles potential contrast agent for MRI and investigation on their size-dependent magnetic properties. *Journal of Nanomaterials* **2013,** *2013*.
314. Artus, M.; Tahar, L. B.; Herbst, F.; Smiri, L.; Villain, F.; Yaacoub, N.; Grenèche, J.-M.; Ammar, S.; Fiévet, F., Size-dependent magnetic properties of CoFe2O4 nanoparticles prepared in polyol. *Journal of Physics: Condensed Matter* **2011,** *23* (50), 506001.

315. Goodarz Naseri, M.; Saion, E. B.; Abbastabar Ahangar, H.; Shaari, A. H.; Hashim, M., Simple synthesis and characterization of cobalt ferrite nanoparticles by a thermal treatment method. *Journal of Nanomaterials* **2010,** *2010*.
316. Maaz, K.; Mumtaz, A.; Hasanain, S.; Ceylan, A., Synthesis and magnetic properties of cobalt ferrite (CoFe2O4) nanoparticles prepared by wet chemical route. *Journal of magnetism and magnetic materials* **2007,** *308* (2), 289-295.
317. George, M.; John, A. M.; Nair, S. S.; Joy, P.; Anantharaman, M., Finite size effects on the structural and magnetic properties of sol–gel synthesized NiFe2O4 powders. *Journal of Magnetism and Magnetic Materials* **2006,** *302* (1), 190-195.
318. Ge, J.; Hu, Y.; Biasini, M.; Beyermann, W. P.; Yin, Y., Superparamagnetic magnetite colloidal nanocrystal clusters. *Angewandte Chemie International Edition* **2007,** *46* (23), 4342-4345.
319. Weissleder, R. a.; Stark, D. D.; Engelstad, B. L.; Bacon, B. R.; Compton, C. C.; White, D. L.; Jacobs, P.; Lewis, J., Superparamagnetic iron oxide: pharmacokinetics and toxicity. *American Journal of Roentgenology* **1989,** *152* (1), 167-173.
320. Mørup, S.; Tronc, E., Superparamagnetic relaxation of weakly interacting particles. *Physical Review Letters* **1994,** *72* (20), 3278.
321. Bean, C.; Livingston, u. D., Superparamagnetism. *Journal of Applied Physics* **1959,** *30* (4), S120-S129.
322. Bean, C.; Jacobs, I., Magnetic granulometry and super-paramagnetism. *Journal of applied Physics* **1956,** *27* (12), 1448-1452.
323. Stoner, E. C.; Wohlfarth, E., A mechanism of magnetic hysteresis in heterogeneous alloys. *Philosophical Transactions of the Royal Society of London. Series A, Mathematical and Physical Sciences* **1948,** *240* (826), 599-642.
324. Cannas, C.; Musinu, A.; Ardu, A.; Orru, F.; Peddis, D.; Casu, M.; Sanna, R.; Angius, F.; Diaz, G.; Piccaluga, G., CoFe2O4 and CoFe2O4/SiO2 core/shell nanoparticles: magnetic and spectroscopic study. *Chemistry of Materials* **2010,** *22* (11), 3353-3361.
325. Shafi, K. V.; Gedanken, A.; Prozorov, R.; Balogh, J., Sonochemical preparation and size-dependent properties of nanostructured CoFe2O4 particles. *Chemistry of Materials* **1998,** *10* (11), 3445-3450.
326. Sawatzky, G.; Van Der Woude, F.; Morrish, A., Cation distributions in octahedral and tetrahedral sites of the ferrimagnetic spinel CoFe2O4. *Journal of Applied Physics* **1968,** *39* (2), 1204-1205.
327. Haneda, K.; Morrish, A., Noncollinear magnetic structure of CoFe2O4 small particles. *Journal of Applied Physics* **1988,** *63* (8), 4258-4260.
328. Zheng, H.; Straub, F.; Zhan, Q.; Yang, P. L.; Hsieh, W. K.; Zavaliche, F.; Chu, Y. H.; Dahmen, U.; Ramesh, R., Self-assembled growth of BiFeO3–CoFe2O4 nanostructures. *Advanced Materials* **2006,** *18* (20), 2747-2752.
329. Zheng, H.; Wang, J.; Lofland, S.; Ma, Z.; Mohaddes-Ardabili, L.; Zhao, T.; Salamanca-Riba, L.; Shinde, S.; Ogale, S.; Bai, F., Multiferroic batio3-cofe2o4 nanostructures. *Science* **2004,** *303* (5658), 661-663.
330. Torres, T.; Lima Jr, E.; Mayoral, A.; Ibarra, A.; Marquina, C.; Ibarra, M. R.; Goya, G. F., Validity of the Néel-Arrhenius model for highly anisotropic CoxFe3− xO4 nanoparticles. *Journal of Applied Physics* **2015,** *118* (18), 183902.
331. Stingaciu, M.; Andersen, H. L.; Granados-Miralles, C.; Mamakhel, A.; Christensen, M., Magnetism in CoFe 2 O 4 nanoparticles produced at sub-and near-supercritical conditions of water. *CrystEngComm* **2017,** *19* (28), 3986-3996.
332. Song, Q.; Zhang, Z. J., Shape control and associated magnetic properties of spinel cobalt ferrite nanocrystals. *Journal of the American Chemical Society* **2004,** *126* (19), 6164-6168.
333. Kang, Y. S.; Risbud, S.; Rabolt, J. F.; Stroeve, P., Synthesis and characterization of nanometer-size Fe3O4 and γ-Fe2O3 particles. *Chemistry of Materials* **1996,** *8* (9), 2209-2211.
334. Peng, S.; Sun, S., Synthesis and characterization of monodisperse hollow Fe3O4 nanoparticles. *Angewandte Chemie International Edition* **2007,** *46* (22), 4155-4158.

335. Liu, B.; Li, Q.; Zhang, B.; Cui, Y.; Chen, H.; Chen, G.; Tang, D., Synthesis of patterned nanogold and mesoporous CoFe2O4 nanoparticle assemblies and their application in clinical immunoassays. *Nanoscale* **2011,** *3* (5), 2220-2226.
336. Maleki, A.; Aghaei, M.; Hafizi-Atabak, H. R.; Ferdowsi, M., Ultrasonic treatment of CoFe2O4@ B2O3-SiO2 as a new hybrid magnetic composite nanostructure and catalytic application in the synthesis of dihydroquinazolinones. *Ultrasonics sonochemistry* **2017,** *37*, 260-266.
337. Ren, S.; Zhao, X.; Chen, R.; Fichtner, M., A facile synthesis of encapsulated CoFe2O4 into carbon nanofibres and its application as conversion anodes for lithium ion batteries. *Journal of Power Sources* **2014,** *260*, 205-210.
338. Bi, Z.; Zhu, J.; Batey, J., CoFe2O4 spinel protection coating thermally converted from the electroplated Co–Fe alloy for solid oxide fuel cell interconnect application. *Journal of Power Sources* **2010,** *195* (11), 3605-3611.
339. Saffari, J.; Ghanbari, D.; Mir, N.; Khandan-Barani, K., Sonochemical synthesis of CoFe2O4 nanoparticles and their application in magnetic polystyrene nanocomposites. *Journal of Industrial and Engineering Chemistry* **2014,** *20* (6), 4119-4123.
340. Kim, C. H.; Myung, Y.; Cho, Y. J.; Kim, H. S.; Park, S.-H.; Park, J.; Kim, J.-Y.; Kim, B., Electronic structure of vertically aligned Mn-doped CoFe2O4 nanowires and their application as humidity sensors and photodetectors. *The Journal of Physical Chemistry C* **2009,** *113* (17), 7085-7090.
341. Kumbhar, V.; Jagadale, A.; Shinde, N.; Lokhande, C., Chemical synthesis of spinel cobalt ferrite (CoFe2O4) nano-flakes for supercapacitor application. *Applied Surface Science* **2012,** *259*, 39-43.
342. Liu, Z.; Wang, J.; Xie, D.; Chen, G., Polyaniline-coated Fe3O4 nanoparticle–carbon-nanotube composite and its application in electrochemical biosensing. *Small* **2008,** *4* (4), 462-466.
343. Zhu, M.; Diao, G., Synthesis of porous Fe3O4 nanospheres and its application for the catalytic degradation of xylenol orange. *The Journal of Physical Chemistry C* **2011,** *115* (39), 18923-18934.
344. Cao, S.-W.; Zhu, Y.-J.; Ma, M.-Y.; Li, L.; Zhang, L., Hierarchically nanostructured magnetic hollow spheres of Fe3O4 and γ-Fe2O3: preparation and potential application in drug delivery. *The Journal of Physical Chemistry C* **2008,** *112* (6), 1851-1856.
345. Hong, R.; Feng, B.; Chen, L.; Liu, G.; Li, H.; Zheng, Y.; Wei, D., Synthesis, characterization and MRI application of dextran-coated Fe3O4 magnetic nanoparticles. *Biochemical Engineering Journal* **2008,** *42* (3), 290-300.
346. Shen, Y.; Tang, J.; Nie, Z.; Wang, Y.; Ren, Y.; Zuo, L., Preparation and application of magnetic Fe3O4 nanoparticles for wastewater purification. *Separation and Purification Technology* **2009,** *68* (3), 312-319.
347. Kefeni, K. K.; Mamba, B. B.; Msagati, T. A., Application of spinel ferrite nanoparticles in water and wastewater treatment: a review. *Separation and Purification Technology* **2017,** *188*, 399-422.
348. Yao, J.; Li, X.; Li, Y.; Le, S., Density functional theory investigations on the structure and electronic properties of normal spinel ZnFe2O4. *Integrated Ferroelectrics* **2013,** *145* (1), 17-23.
349. Prim, S.; Garcia, A.; Galindo, R.; Cerro, S.; Llusar, M.; Folgueras, M.; Monros, G., Pink ceramic pigments based on chromium doped M (Al2− xCrx) O4, M= Mg, Zn, normal spinel. *Ceramics International* **2013,** *39* (6), 6981-6989.
350. Liu, X.; Prewitt, C. T., High-temperature X-ray diffraction study of Co 3 O 4: Transition from normal to disordered spinel. *Physics and Chemistry of Minerals* **1990,** *17* (2), 168-172.
351. Rozenberg, G. K.; Amiel, Y.; Xu, W.; Pasternak, M.; Jeanloz, R.; Hanfland, M.; Taylor, R., Structural characterization of temperature-and pressure-induced inverse↔ normal spinel transformation in magnetite. *Physical Review B* **2007,** *75* (2), 020102.
352. Szotek, Z.; Temmerman, W.; Ködderitzsch, D.; Svane, A.; Petit, L.; Winter, H., Electronic structures of normal and inverse spinel ferrites from first principles. *Physical Review B* **2006,** *74* (17), 174431.
353. Thomas, M.; David, W.; Goodenough, J. B.; Groves, P., Synthesis and structural characterization of the normal spinel Li [Ni2] O4. *Materials research bulletin* **1985,** *20* (10), 1137-1146.

354. Darbandi, M.; Stromberg, F.; Landers, J.; Reckers, N.; Sanyal, B.; Keune, W.; Wende, H., Nanoscale size effect on surface spin canting in iron oxide nanoparticles synthesized by the microemulsion method. *Journal of Physics D: Applied Physics* **2012,** *45* (19), 195001.
355. Chen, D.; Tang, X.; Wu, J.; Zhang, W.; Liu, Q.; Jiang, Y., Effect of grain size on the magnetic properties of superparamagnetic Ni0. 5Zn0. 5Fe2O4 nanoparticles by co-precipitation process. *Journal of magnetism and magnetic materials* **2011,** *323* (12), 1717-1721.
356. He, L.; Chen, C.; Wang, N.; Zhou, W.; Guo, L., Finite size effect on Néel temperature with Co 3 O 4 nanoparticles. *Journal of Applied Physics* **2007,** *102* (10), 103911.
357. Qu, Y.; Yang, H.; Yang, N.; Fan, Y.; Zhu, H.; Zou, G., The effect of reaction temperature on the particle size, structure and magnetic properties of coprecipitated CoFe2O4 nanoparticles. *Materials Letters* **2006,** *60* (29-30), 3548-3552.
358. Liu, C.; Zhang, Z. J., Size-dependent superparamagnetic properties of Mn spinel ferrite nanoparticles synthesized from reverse micelles. *Chemistry of Materials* **2001,** *13* (6), 2092-2096.
359. Liu, C.; Rondinone, A. J.; Zhang, Z. J., Synthesis of magnetic spinel ferrite CoFe2O4 nanoparticles from ferric salt and characterization of the size-dependent superparamagnetic properties. *Pure and applied chemistry* **2000,** *72* (1-2), 37-45.
360. Belle, C. J.; Bonamin, A.; Simon, U.; Santoyo-Salazar, J.; Pauly, M.; Bégin-Colin, S.; Pourroy, G., Size dependent gas sensing properties of spinel iron oxide nanoparticles. *Sensors and Actuators B: Chemical* **2011,** *160* (1), 942-950.
361. Mathew, D. S.; Juang, R.-S., An overview of the structure and magnetism of spinel ferrite nanoparticles and their synthesis in microemulsions. *Chemical engineering journal* **2007,** *129* (1-3), 51-65.
362. Ngo, A.; Pileni, M., Cigar-shaped ferrite nanocrystals: Orientation of the easy magnetic axes. *Journal of applied physics* **2002,** *92* (8), 4649-4652.
363. Cao, H.; Wang, G.; Zhang, L.; Liang, Y.; Zhang, S.; Zhang, X., Shape and magnetic properties of single-crystalline hematite (α-Fe2O3) nanocrystals. *ChemPhysChem* **2006,** *7* (9), 1897-1901.
364. Bao, N.; Shen, L.; An, W.; Padhan, P.; Heath Turner, C.; Gupta, A., Formation mechanism and shape control of monodisperse magnetic CoFe2O4 nanocrystals. *Chemistry of Materials* **2009,** *21* (14), 3458-3468.
365. Cozzoli, P. D.; Snoeck, E.; Garcia, M. A.; Giannini, C.; Guagliardi, A.; Cervellino, A.; Gozzo, F.; Hernando, A.; Achterhold, K.; Ciobanu, N., Colloidal synthesis and characterization of tetrapod-shaped magnetic nanocrystals. *Nano letters* **2006,** *6* (9), 1966-1972.
366. Sun, S.; Wang, Z. L., Shapes, multiple twins and surface structures of monodisperse FePt magnetic nanocrystals. *Surface Science* **2002,** *505*, 325-335.
367. Jana, N. R.; Chen, Y.; Peng, X., Size-and shape-controlled magnetic (Cr, Mn, Fe, Co, Ni) oxide nanocrystals via a simple and general approach. *Chemistry of materials* **2004,** *16* (20), 3931-3935.
368. Puntes, V. F.; Krishnan, K. M.; Alivisatos, A. P., Colloidal nanocrystal shape and size control: the case of cobalt. *Science* **2001,** *291* (5511), 2115-2117.
369. Begum, S. M.; Rao, M.; Aparna, Y.; Rao, P.; Ravikumar, R., Spectroscopic investigations of Fe3+ doped poly vinyl alcohol (PVA) capped ZnSe nanoparticles. *Spectrochimica Acta Part A: Molecular and Biomolecular Spectroscopy* **2012,** *98*, 100-104.
370. Tucker, W. F.; Asplund, R. O.; Holt, S. L., Preparation and properties of Fe3+-amino acid complexes: Crystalline complexes with aliphatic amino acids. *Archives of biochemistry and biophysics* **1975,** *166* (2), 433-438.
371. Morre, P. B., Octahedral tetramer in the crystal structure of leucophosphite, K2 [Fe3+ 4 (OH) 2 (H2O) 2 (PO4) 4]. 2H2O. *American Mineralogist: Journal of Earth and Planetary Materials* **1972,** *57* (3-4_Part_1), 397-410.
372. Cormack, A.; Lewis, G.; Parker, S.; Catlow, C., On the cation distribution of spinels. *Journal of Physics and Chemistry of Solids* **1988,** *49* (1), 53-57.
373. Chandramohan, P.; Srinivasan, M.; Velmurugan, S.; Narasimhan, S., Cation distribution and particle size effect on Raman spectrum of CoFe2O4. *Journal of Solid State Chemistry* **2011,** *184* (1), 89-96.

374. COOLEY, R. F.; REED, J. S., Equilibrium cation distribution in NiAl2O4, CuAl2O4, and ZnAl2O4 spinels. *Journal of the American Ceramic Society* **1972,** *55* (8), 395-398.
375. Lavina, B.; Salviulo, G.; Della Giusta, A., Cation distribution and structure modelling of spinel solid solutions. *Physics and Chemistry of Minerals* **2002,** *29* (1), 10-18.
376. Marco, J. F.; Gancedo, J. R.; Gracia, M.; Gautier, J. L.; Ríos, E. I.; Palmer, H. M.; Greaves, C.; Berry, F. J., Cation distribution and magnetic structure of the ferrimagnetic spinel NiCo2O4. *Journal of Materials Chemistry* **2001,** *11* (12), 3087-3093.
377. O'Neil, H. S. C.; Navrotsky, A., Cation distributions and thermodynamic properties of binary spinel solid solutions. *American Mineralogist* **1984,** *69* (7-8), 733-753.
378. O'Neill, H. S. C.; Navrotsky, A., Simple spinels; crystallographic parameters, cation radii, lattice energies, and cation distribution. *American Mineralogist* **1983,** *68* (1-2), 181-194.
379. Navrotsky, A.; Kleppa, O., The thermodynamics of cation distributions in simple spinels. *Journal of Inorganic and nuclear Chemistry* **1967,** *29* (11), 2701-2714.
380. Lu, J.; Jiao, X.; Chen, D.; Li, W., Solvothermal synthesis and characterization of Fe3O4 and γ-Fe2O3 nanoplates. *The Journal of Physical Chemistry C* **2009,** *113* (10), 4012-4017.
381. Yan, A.; Liu, X.; Qiu, G.; Wu, H.; Yi, R.; Zhang, N.; Xu, J., Solvothermal synthesis and characterization of size-controlled Fe3O4 nanoparticles. *Journal of Alloys and Compounds* **2008,** *458* (1-2), 487-491.
382. Deng, J.; Wen, X.; Wang, Q., Solvothermal in situ synthesis of Fe3O4-multi-walled carbon nanotubes with enhanced heterogeneous Fenton-like activity. *Materials Research Bulletin* **2012,** *47* (11), 3369-3376.
383. Zhan, Y.; Meng, F.; Lei, Y.; Zhao, R.; Zhong, J.; Liu, X., One-pot solvothermal synthesis of sandwich-like graphene nanosheets/Fe3O4 hybrid material and its microwave electromagnetic properties. *Materials Letters* **2011,** *65* (11), 1737-1740.
384. Zhang, J.; Yao, Y.; Huang, T.; Yu, A., Uniform hollow Fe3O4 spheres prepared by template-free solvothermal method as anode material for lithium-ion batteries. *Electrochimica acta* **2012,** *78*, 502-507.
385. Zhou, L.; Deng, H.; Wan, J.; Shi, J.; Su, T., A solvothermal method to produce RGO-Fe3O4 hybrid composite for fast chromium removal from aqueous solution. *Applied Surface Science* **2013,** *283*, 1024-1031.
386. Bretcanu, O.; Spriano, S.; Verne, E.; Cöisson, M.; Tiberto, P.; Allia, P., The influence of crystallised Fe3O4 on the magnetic properties of coprecipitation-derived ferrimagnetic glass–ceramics. *Acta biomaterialia* **2005,** *1* (4), 421-429.
387. Meng, H.; Zhang, Z.; Zhao, F.; Qiu, T.; Yang, J., Orthogonal optimization design for preparation of Fe3O4 nanoparticles via chemical coprecipitation. *Applied Surface Science* **2013,** *280*, 679-685.
388. Xia, T.; Xu, X.; Wang, J.; Xu, C.; Meng, F.; Shi, Z.; Lian, J.; Bassat, J.-M., Facile complex-coprecipitation synthesis of mesoporous Fe3O4 nanocages and their high lithium storage capacity as anode material for lithium-ion batteries. *Electrochimica Acta* **2015,** *160*, 114-122.
389. Xu, C.; Ouyang, C.; Jia, R.; Li, Y.; Wang, X., Magnetic and optical properties of poly (vinylidene difluoride)/Fe3O4 nanocomposite prepared by coprecipitation approach. *Journal of applied polymer science* **2009,** *111* (4), 1763-1768.
390. Mohapatra, J.; Xing, M.; Liu, J. P., Inductive Thermal Effect of Ferrite Magnetic Nanoparticles. *Materials* **2019,** *12* (19), 3208.
391. Peng, H.; Wu, T., Nonvolatile resistive switching in spinel ZnMn 2 O 4 and ilmenite ZnMnO 3. *Applied Physics Letters* **2009,** *95* (15), 152106.
392. Chen, X.; Wu, G.; Jiang, P.; Liu, W.; Bao, D., Colossal resistance switching effect in Pt/spinel-MgZnO/Pt devices for nonvolatile memory applications. *Applied Physics Letters* **2009,** *94* (3), 033501.
393. Hu, W.; Qin, N.; Wu, G.; Lin, Y.; Li, S.; Bao, D., Opportunity of spinel ferrite materials in nonvolatile memory device applications based on their resistive switching performances. *Journal of the American Chemical Society* **2012,** *134* (36), 14658-14661.

394. Phadatare, M.; Khot, V.; Salunkhe, A.; Thorat, N.; Pawar, S., Studies on polyethylene glycol coating on NiFe2O4 nanoparticles for biomedical applications. *Journal of Magnetism and Magnetic Materials* **2012,** *324* (5), 770-772.
395. Humbe, A. V.; Birajdar, S. D.; Bhandari, J.; Waghule, N.; Bhagwat, V.; Jadhav, K. In *Polyethylene glycol coated CoFe2O4 nanoparticles: A potential spinel ferrite for biomedical applications*, AIP Conference Proceedings, AIP Publishing LLC: 2015; p 050138.
396. Kefeni, K. K.; Msagati, T. A.; Nkambule, T. T.; Mamba, B. B., Spinel ferrite nanoparticles and nanocomposites for biomedical applications and their toxicity. *Materials Science and Engineering: C* **2020,** *107*, 110314.
397. Sanpo, N.; Berndt, C.; Wen, C.; Wang, J., New approaches to the study of spinel ferrite nanoparticles for biomedical applications. **2015**.
398. Amiri, M.; Salavati-Niasari, M.; Akbari, A., Magnetic nanocarriers: evolution of spinel ferrites for medical applications. *Advances in colloid and interface science* **2019**.
399. Galvão, W. S.; Neto, D.; Freire, R. M.; Fechine, P. B. In *Super-paramagnetic nanoparticles with spinel structure: a review of synthesis and biomedical applications*, solid state phenomena, Trans Tech Publ: 2016; pp 139-176.
400. Jaiswal, M. K.; Gogoi, M.; Sarma, H. D.; Banerjee, R.; Bahadur, D., Biocompatibility, biodistribution and efficacy of magnetic nanohydrogels in inhibiting growth of tumors in experimental mice models. *Biomaterials Science* **2014,** *2* (3), 370-380.
401. Gupta, J.; Mohapatra, J.; Bhargava, P.; Bahadur, D., A pH-responsive folate conjugated magnetic nanoparticle for targeted chemo-thermal therapy and MRI diagnosis. *Dalton Transactions* **2016,** *45* (6), 2454-2461.
402. Calatayud, M. P.; Soler, E.; Torres, T. E.; Campos-Gonzalez, E.; Junquera, C.; Ibarra, M. R.; Goya, G. F., Cell damage produced by magnetic fluid hyperthermia on microglial BV2 cells. *Scientific reports* **2017,** *7* (1), 1-16.
403. Moise, S.; Byrne, J. M.; El Haj, A. J.; Telling, N. D., The potential of magnetic hyperthermia for triggering the differentiation of cancer cells. *Nanoscale* **2018,** *10* (44), 20519-20525.
404. Di Corato, R.; Espinosa, A.; Lartigue, L.; Tharaud, M.; Chat, S.; Pellegrino, T.; Ménager, C.; Gazeau, F.; Wilhelm, C., Magnetic hyperthermia efficiency in the cellular environment for different nanoparticle designs. *Biomaterials* **2014,** *35* (24), 6400-6411.
405. Lee, J.-H.; Jang, J.-t.; Choi, J.-s.; Moon, S. H.; Noh, S.-h.; Kim, J.-w.; Kim, J.-G.; Kim, I.-S.; Park, K. I.; Cheon, J., Exchange-coupled magnetic nanoparticles for efficient heat induction. *Nature nanotechnology* **2011,** *6* (7), 418.
406. Joshi, H. M.; Lin, Y. P.; Aslam, M.; Prasad, P.; Schultz-Sikma, E. A.; Edelman, R.; Meade, T.; Dravid, V. P., Effects of shape and size of cobalt ferrite nanostructures on their MRI contrast and thermal activation. *The Journal of Physical Chemistry C* **2009,** *113* (41), 17761-17767.
407. Lartigue, L.; Hugounenq, P.; Alloyeau, D.; Clarke, S. P.; Levy, M.; Bacri, J.-C.; Bazzi, R.; Brougham, D. F.; Wilhelm, C.; Gazeau, F., Cooperative organization in iron oxide multi-core nanoparticles potentiates their efficiency as heating mediators and MRI contrast agents. *ACS nano* **2012,** *6* (12), 10935-10949.
408. Barick, K.; Singh, S.; Bahadur, D.; Lawande, M. A.; Patkar, D. P.; Hassan, P., Carboxyl decorated Fe3O4 nanoparticles for MRI diagnosis and localized hyperthermia. *Journal of colloid and interface science* **2014,** *418*, 120-125.
409. Weishaupt, D.; Köchli, V. D.; Marincek, B., *How does MRI work?: an introduction to the physics and function of magnetic resonance imaging*. Springer Science & Business Media: 2008.
410. Serov, A.; Andersen, N. I.; Roy, A. J.; Matanovic, I.; Artyushkova, K.; Atanassov, P., CuCo2O4 ORR/OER bi-functional catalyst: influence of synthetic approach on performance. *Journal of The Electrochemical Society* **2015,** *162* (4), F449-F454.
411. Su, Y.-Z.; Xu, Q.-Z.; Chen, G.-F.; Cheng, H.; Li, N.; Liu, Z.-Q., One dimensionally spinel NiCo2O4 nanowire arrays: facile synthesis, water oxidation, and magnetic properties. *Electrochimica Acta* **2015,** *174*, 1216-1224.

412. Jin, C.; Lu, F.; Cao, X.; Yang, Z.; Yang, R., Facile synthesis and excellent electrochemical properties of NiCo 2 O 4 spinel nanowire arrays as a bifunctional catalyst for the oxygen reduction and evolution reaction. *Journal of Materials Chemistry A* **2013,** *1* (39), 12170-12177.
413. Tan, Y.; Wu, C.; Lin, H.; Li, J.; Chi, B.; Pu, J.; Jian, L., Insight the effect of surface Co cations on the electrocatalytic oxygen evolution properties of cobaltite spinels. *Electrochimica Acta* **2014,** *121*, 183-187.
414. Wang, L.; Zhao, X.; Lu, Y.; Xu, M.; Zhang, D.; Ruoff, R. S.; Stevenson, K. J.; Goodenough, J. B., CoMn2O4 spinel nanoparticles grown on graphene as bifunctional catalyst for lithium-air batteries. *Journal of The Electrochemical Society* **2011,** *158* (12), A1379-A1382.
415. Abidat, I.; Bouchenafa-Saib, N.; Habrioux, A.; Comminges, C.; Canaff, C.; Rousseau, J.; Napporn, T.; Dambournet, D.; Borkiewicz, O.; Kokoh, K., Electrochemically induced surface modifications of mesoporous spinels (Co 3 O 4− δ, MnCo 2 O 4− δ, NiCo 2 O 4− δ) as the origin of the OER activity and stability in alkaline medium. *Journal of Materials Chemistry A* **2015,** *3* (33), 17433-17444.
416. Hamdani, M.; Singh, R.; Chartier, P., Co3O4 and Co-based spinel oxides bifunctional oxygen electrodes. *Int. J. Electrochem. Sci* **2010,** *5* (4), 556-577.
417. Maiyalagan, T.; Jarvis, K. A.; Therese, S.; Ferreira, P. J.; Manthiram, A., Spinel-type lithium cobalt oxide as a bifunctional electrocatalyst for the oxygen evolution and oxygen reduction reactions. *Nature communications* **2014,** *5* (1), 1-8.
418. Cheng, F.; Shen, J.; Peng, B.; Pan, Y.; Tao, Z.; Chen, J., Rapid room-temperature synthesis of nanocrystalline spinels as oxygen reduction and evolution electrocatalysts. *Nature chemistry* **2011,** *3* (1), 79.
419. Ovais, M.; Khalil, A. T.; Raza, A.; Islam, N. U.; Ayaz, M.; Saravanan, M.; Ali, M.; Ahmad, I.; Shahid, M.; Shinwari, Z. K., Multifunctional theranostic applications of biocompatible green-synthesized colloidal nanoparticles. *Applied microbiology and biotechnology* **2018,** *102* (10), 4393-4408.
420. Lohse, S. E.; Murphy, C. J., Applications of colloidal inorganic nanoparticles: from medicine to energy. *Journal of the American Chemical Society* **2012,** *134* (38), 15607-15620.
421. Elaissari, A., *Colloidal nanoparticles in biotechnology*. John Wiley & Sons: 2008; Vol. 2.
422. Sperling, R. A.; Gil, P. R.; Zhang, F.; Zanella, M.; Parak, W. J., Biological applications of gold nanoparticles. *Chemical Society Reviews* **2008,** *37* (9), 1896-1908.
423. Howes, P. D.; Chandrawati, R.; Stevens, M. M., Colloidal nanoparticles as advanced biological sensors. *Science* **2014,** *346* (6205), 1247390.
424. Pellegrino, T.; Kudera, S.; Liedl, T.; Muñoz Javier, A.; Manna, L.; Parak, W. J., On the development of colloidal nanoparticles towards multifunctional structures and their possible use for biological applications. *small* **2005,** *1* (1), 48-63.
425. Pang, X.; Zhao, L.; Han, W.; Xin, X.; Lin, Z., A general and robust strategy for the synthesis of nearly monodisperse colloidal nanocrystals. *Nature nanotechnology* **2013,** *8* (6), 426.
426. Pang, X.; He, Y.; Jung, J.; Lin, Z., 1D nanocrystals with precisely controlled dimensions, compositions, and architectures. *Science* **2016,** *353* (6305), 1268-1272.

CHAPTER 2. RESEARCH GOALS, OBJECTIVES, AND OVERVIEW

2.1 Goals

The goals of this research are to (1) develop a robust approach for synthesizing both star-like diblock and triblock copolymers with controlled molecular weight of each block, respectively and narrow molecular weight distribution serving as nanoreactors for subsequent *in-situ* synthesis of inorganic nanoparticles with tailorable size, architecture and surface chemistry; (2) craft perovskite oxide nanoparticle ($BaTiO_3$, $PbTiO_3$, $LaFeO_3$, and $LaMnO_3$) and layered perovskite oxide nanoparticle ($LaCo_2O_4$) with uniform morphology, tunable size, excellent dispersity in various organic solvents as well as controllable composition (i.e., introducing dopants with pre-determined concentration) via employing star-like diblock copolymer as nanoreactors for use as promising electrocatalysts and scrutinize the size-, dopant- and structure-dependent oxygen reduction reaction (ORR) and oxygen evolution reaction activity; (3) synthesize spinel ferrite nanoparticles with tunable composition and dimension via polymer-assisted approach for elucidation on composition and size effects on magnetic properties. The overall goal for this study is to synthesize star-like diblock and triblock copolymers with controlled molecular weight and narrow molecular weight distribution and use those polymers as nanoreactors of a versatile method for obtaining diverse inorganic nanoparticles with tailorable dimension, crystallinity, composition and surface functionality for electrocatalytic and magnetic properties investigation.

Several critical factors can significantly affect the desired properties of the as-synthesized nanoparticles. First, in terms of the star-like polymer nanoreactors, the architecture, the molecular weight of each block, the polydispersity, the functional groups as well as the outer block can all play important roles in determining the properties and thus the performance for specific applications of the nanoparticles. Second, during the nanoparticle synthesis, type of the precursor

chosen, speed of raising temperature, reaction temperature, and reaction time can also result in nanoparticles with distinct features. Therefore, by understanding the interaction between nanoreactors and inorganic nanoparticles and how the change in polymeric nanoreactors can affect the growth of the inorganic nanoparticles, nanoparticle with controllable morphology, composition and crystallinity change can be rendered and systematic study on the correlation between the changes with those as-synthesized nanoparticles with their properties and performance can be achieved.

There are several advantages for synthesizing inorganic nanoparticles by this robust nanoreactor-assisted approach. First, by exploiting the coordination interaction between the functional group of the star-like polymer with the metal moieties of the precursor, the precursor can be confined within the specific compartment, yielding highly uniform nanoparticles. Furthermore, the size of the as-synthesized nanoparticles can be tailored by simply changing the molecular weight of the polymer. Second, since the outer block polymers are covalently ligated on the surface of the nanoparticles, nanoparticles are highly stable even after multiple purification steps and can be well-disperse in good solvents of the outer block polymers. Third, the inorganic materials synthesized in this study (i.e., perovskite oxide and spinel ferrite) typically required higher synthetic temperature, resulting in aggregation and irregular morphology, while using star-like polymers as nanoreactors, the as-synthesized particles can be within nanometer regime. Forth, simply by introducing different precursors with pre-determined concentration, doped nanoparticles can be formed with excellent morphology and dispersity. Finally, the synthetic procedure for nanoparticles is versatile, relatively easy, and straightforward. The capability to synthesize nanoparticles with precisely controllable dimension, morphology, crystallinity, and surface

chemistry opens an avenue for elucidating fundamental science questions and possibly provide guidelines for designing materials in various application fields.

2.2 Objectives

Below are the specific research objectives based on the goal noted above.

Study 1: Synthesis of amphiphilic and double hydrophilic star-like block copolymers and the dual pH-responsiveness of unimolecular micelle

(a) Synthesizing star-like diblock copolymers (P4VP-*b*-PAA) and triblock copolymers (P4VP-*b*-PAA-*b*-varied outer block) with controllable molecular weight of each block and narrow polydispersity, which can possibly serve as polymeric template for subsequent inorganic nanoparticle synthesis.

(b) Adding linear initiator when polymerizing the star-like second and the third block was found to be beneficial to control the molecular weight distribution, especially in the case when pyridine-containing polymers are involved within non-linear polymer architecture.

(c) The capability of tailoring the surface chemistry (i.e., the third block) of the star-like polymer by simply changing the monomer from styrene, methyl(methacrylate) and ethylene oxide and reaction (i.e., ATRP and click reaction) had been demonstrated, leading to possibilities in various kind of applications.

(d) Dual pH-responsive behaviors of double hydrophilic star-like P4VP-*b*-PAA diblock copolymer had been demonstrated and the discussion on the possible morphology evolution under different pH environments had been provided.

Study 2: Tailoring electrocatalytic activity of in-situ crafted perovskite oxide nanocrystals via precise size and dopant

(a) By employing star-like PAA-*b*-PS diblock copolymers as nanoreactors, *in-situ* synthesis of various monodisperse, PS-capped perovskite oxide nanoparticles (i.e., $BaTiO_3$ and $PbTiO_3$) with controllable dimension and high purity can be successfully acquired, which is generally difficult due to high formation energy required for synthesizing perovskite oxides.

(b) Meticulous characterization of the as-synthesized perovskite oxide nanoparticles had been provided, and the relationship between composition (especially by doping), size, and electrocatalytic performance (i.e., oxygen reduction reaction (ORR) performance) had been exhibited, leading to guidelines for optimizing the desired properties of electrocatalysts.

(c) To better understand the mechanism of the enhanced electrocatalytic performance after doping, DFT calculation had been conducted and mechanisms for the phenomenon had been proposed. This versatile polymer-assisted approach together with as-synthesized perovskite oxide nanoparticles provided an excellent platform for elucidating doping and size effect on electronic structure, adsorption energy/Gibb's free energy difference and thus electrocatalytic performance.

Study 3: Electrocatalytic activity of monodisperse, Ruddlesden-Popper layered perovskite nanocatalysts for oxygen reduction and evolution reactions

(a) Successfully synthesizing three kinds of La-based nanoparticles (i.e., $LaFeO_3$, $LaMnO_3$, and La_2CoO_4) with perovskite and Ruddlesden-Popper layered perovskite structure by employing star-like PAA-*b*-PS diblock copolymer as nanoreactors. In particular, the synthetic temperature for acquiring Ruddlesden-Popper layered perovskite nanoparticle can be significantly reduced

based on this synthetic strategy, possibly resulting from nanometer-scaled products and different surface chemistries.

(b) Similarly, the size of the as-synthesized nanoparticles can be tailored by modifying the molecular weight of the inner PAA block due to the strong coordination interaction between the precursors and the functional group within PAA block, enabling the investigation of the dependency of size on electrocatalytic activities.

(c) Ruddlesden-Popper layered La_2CoO_4 perovskite nanoparticles, *for the first time*, have been demonstrated as a promising candidate for bifunctional electrocatalysts for both ORR and oxygen evolution reaction (OER) at low temperature. Furthermore, the performance was superior to other La-based perovskite nanoparticles as well as some previously reported perovskite-based catalysts. The remarkable performance can be originated from highly-active lattice oxygen and an increased amount of hydroxyl groups.

Study 4: Facile manipulation of magnetic properties of spinel MFe_2O_4 (M = Co, Ni, Mn) nanoparticles via robust size and composition engineering

(a) Three kinds of magnetic spinel ferrite nanoparticles have been synthesized by utilizing star-like PAA-*b*-PSAN diblock copolymer as nanoreactors. Similarly, dispersity in various organic solvents and the controllability of the dimension can be rendered by this robust synthetic approach.

(b) Composition and structure (mixed spinel structure) had been scrutinized by detailed characterizations.

(c) Investigation of the dependency of magnetic properties on composition (i.e., $CoFe_2O_4$, $NiFe_2O_4$, and $MnFe_2O_4$) and size was exhibited and discussion between the mechanism for the

difference was provided.

2.3 Organization and composition of the dissertation

Chapter 1 is a brief review on several topics, including the introduction on (1) non-linear polymer, (2) perovskite-based materials, and (3) magnetic materials, related to this dissertation. First, in terms of non-linear polymer, the examples of non-linear polymer structure with varied topologies, compositions, and functionalities are demonstrated, followed by a general introduction on three categories for synthesizing non-linear polymers, which are "core-first", "arm-first" and "coupling onto". Star-shaped polymer, having the simplest structure among all the non-linear polymer, is specifically discussed with their classifications. To obtain a well-defined structure regarding composition and molecular architecture of star-shaped polymers, living/controlled radical polymerization was identified as a robust synthetic approach because of their mild reaction conditions and can be applied to polymerize a rich diversity of monomers. In particular, the mechanism of both reversible addition-fragmentation chain transfer (RAFT) and atom transfer radical polymerization (ATRP) are discussed. Finally, the distinct features and applications of non-linear polymers are exhibited. Second, we put our focus on perovskite oxide and their applications as electrocatalysts. In this part, a brief introduction to the structure of perovskite oxides and derivatives of perovskite oxides (by changing the intergrowths layer and tuning the oxygen content, especially layered perovskite with Ruddlesden-Popper structure) is first given. Among all, intriguing dielectric, ferroelectric, and size effects on domain configuration of $BaTiO_3$ are specifically discussed. The common synthetic approaches for preparing perovskite oxides are then listed and compared. Finally, basic mechanisms for ORR and OER are proposed, followed by some studies of capitalizing perovskite oxide as electrocatalysts for these reactions. The last part

of the introduction focuses on magnetic materials. We first discuss different magnetic behaviors and typical features as indicators for magnetic properties. Then the structure of spinel magnetic materials, especially the emergence of superparamagnetic behavior when the size of the materials is reduced under specific critical numbers is discussed. Approaches for obtaining those spinel magnetic materials are then proposed. Finally, some examples of potential applications with those magnetic materials are discussed.

Chapter 2 describes the scientific goals and objectives of the work presented in this dissertation. First is the synthesis of star-like diblock and triblock copolymer that consists of pyridine-group polymer as the first block, with tailorable molecular weight, narrow molecular weight distribution, and the dual pH-responsive behavior of star-like hydrophilic diblock copolymer. Second is the synthesis of perovskite oxide nanoparticles with tunable size and dopant type as promising catalysts for ORR. Third is the synthesis of three kinds of La-based nanoparticles with both perovskite and layered perovskite structure and their electrocatalytic performance for both ORR and OER. Last is the synthesis of spinel magnetic nanoparticles with tunable size, composition, and the dependency of magnetic properties on these factors.

Chapter 3 presents the experimental condition as well as characterizations that are crucial for the studies in this dissertation. Material synthesis includes synthesizing star-like diblock and triblock copolymers (with 21-arms macroinitiator), star-like diblock copolymer with 8-arms macroinitiator, and synthesis of different kinds of inorganic nanoparticles (i.e., $BaTiO_3$, $PbTiO_3$, La-based perovskite and layered perovskite nanoparticles and spinel ferrite nanoparticles). Material characterization techniques include gel permeation chromatography (GPC), proton NMR (^{1}H NMR), Fourier transform infrared spectroscopy (FTIR), dynamic light scattering (DLS), X-ray diffraction (XRD), Raman spectroscopy, X-ray photoelectron spectroscopy (XPS), and

transmission electron microscopy (TEM). Materials property measurements include piezoresponse force microscopy (PFM) and electrochemical characterization station.

Chapter 4 reports the synthesis of star-like diblock and triblock copolymers, containing poly(4-vinyl pyridine) (P4VP) as the first block. Normally, synthesis of star-like polymer consisting of pyridine-containing (in this case, P4VP) with ATRP is difficult due to the easy occurrence of the coupling reaction, and the influence of pyridine group remains when polymerizing the second block and the third block. Herein, we find that by introducing additional linear initiator when conducting the second poly(*tert*-butyl acrylate) (P*t*BA) block polymerization, the ratio between total initiate sites to metal moieties can be increased to around 1 to 1, which can prevent the coupling reaction from happening and thus acquiring star-like diblock copolymer with narrow molecular weight distribution. In addition, various kinds of monomers are used for the third block polymerization, corroborating the flexibility of changing the surface chemistry of this star-like polymer. Finally, by hydrolyzing second P*t*BA block into poly(acrylic acid) (PAA) of the star-like diblock copolymer, the dual pH-responsive behavior can be observed because of different protonation/deprotonation properties of PAA and P4VP under varied pH environments, rendering the possibility for drug delivery carriers, sensors and/or tunable templates for nanomaterials.

Chapter 5 reports the nanoreactor-templated *in-situ* synthesis of perovskite oxide nanoparticles with well-controlled dimensions and dopant types by capitalizing the star-like PAA-*b*-PS diblock copolymer as nanoreactor. By the strong coordination interaction between the metal moieties of the precursor and the functional group of inner PAA block of the star-like diblock copolymer nanoreactor, precursors can occupy the compartment of inner PAA block exclusively, yielding monodisperse nanoparticles with tailorable size. Therefore, perovskite oxide nanoparticles with controllable dimensions, uniformity, composition, and enhanced dispersity in

various kinds of organic solvents can be obtained by this unimolecular nanoreactor synthetic strategy. Furthermore, by dispersing as-synthesized nanoparticles onto graphene oxide before annealing, the crystallinity of the nanoparticles can be improved, whereas the morphology can be maintained. ORR activity is then measured and the correlation between varied nanoparticle size, dopant types, doping concentration, and electrocatalytic performance is demonstrated and elucidated. In particular, the enhancement of oxygen reduction reaction activity when doping with different elements is explained by computational results with DFT calculation.

Chapter 6 proposes La-based perovskite and layered perovskite oxide nanoparticles can similarly be obtained by employing the star-like diblock copolymer as nanoreactors. By using this synthetic strategy, not only the size of the as-synthesized nanoparticle can be modified, but the synthetic temperature required can be significantly reduced. Intriguing, in addition to simple perovskite structure (with a general formula of ABO_3), the product with Ruddlesden-Popper layered structure (with a general formula of $A_{n+1}B_nO_{3n+1}$) can be rendered, suggesting the high flexibility of this synthetic strategy for tuning the crystal structure, composition, and dimension of the product. The electrocatalytic performance of three La-based nanoparticles (i.e., $LaFeO_3$, $LaMnO_3$, and La_2CoO_4) for both ORR and OER is then demonstrated. Layered La_2CoO_4 perovskite nanoparticles, *to our surprise*, exhibit the best bifunctional catalytic activity among the three, as well as being superior to many previously reported perovskite-based catalysts, which may result from highly active lattice oxygen and increased amount of hydroxyl groups on the surface.

Chapter 7 reports the nanoreactor-assisted approach for synthesizing spinel ferrites nanoparticles with varied compositions (i.e. $CoFe_2O_4$, $MnFe_2O_4$, and $NiFe_2O_4$) and varied size (i.e., 4, 7, 11 nm). By using PAA-*b*-poly(styrene-co-acrylonitrile) (PAA-*b*-PSAN) as nanoreactor, the size of the as-synthesized nanoparticles can be facilely-tuned by changing the molecular weight of

the inner PAA block. This robust synthetic approach can thus enable the investigation of the correlation of size, composition, and magnetic properties. In particular, the saturation magnetization between different compositions can be heavily influenced by the type of transition metal and cation distribution, while the decreased saturation magnetization with decreased nanoparticle size can be attributed to an increased ratio of the surface-spin-disordered layer as size decreases. Such an understanding of the morphology-composition-property relationship can potentially provide guidelines for designing materials used in catalysis, magnetic storage, and biotechnology.

Chapter 8 describes the general discussion and conclusion of the overall research. The significance of this dissertation, which can be divided into three parts, are listed. First, the capability of synthesizing a large variety of inorganic nanoparticles with controllable size and composition, rendering the possibility to investigate the size, composition, dopants, crystal structures, and surface chemistry effect on electrocatalytic, including both oxygen reduction reaction and oxygen evolution reaction activity. Second, the identification of promising materials that can serve as electrocatalysts, which have been rarely studied before. In particular, $BaTiO_3$ nanoparticles doped with La and Co with small doping concentration are demonstrated to be a highly active catalyst for oxygen reduction reaction, while layered perovskite La_2CoO_4 nanoparticles are found to outperform electrocatalyst for both oxygen reduction reaction and oxygen evolution reaction compared to $LaFeO_3$ and $LaMnO_3$, which can be employed for advanced energy-related applications, such as fuel cells and metal-air batteries. Finally, the mechanism for the enhanced oxygen reduction reaction activity after doping La and Co with $BaTiO_3$ nanoparticles is explained by computational results, which are the reduced free energy barrier during oxygen reduction reaction as well as increased conductivity. This result proves that

doping, even with small doping concentration, can be effective in changing the electrocatalytic activity, and materials with further improved or optimized performance are expected to be synthesized if the dopant type and doping concentration are chosen judiciously.

CHAPTER 3. EXPERIMENTAL METHODS

3.1 Synthesis of star-like polymer nanoreactors

3.1.1 Synthesis of star-like diblock copolymer nanoreactors with 21-arm initiator (ß-cyclodextrin, ß-CD)

We have successfully synthesized PAA-*b*-PS diblock nanoreactors by following the procedure shown in **Figure 3.1**. Below are the descriptions of detailed synthetic steps:

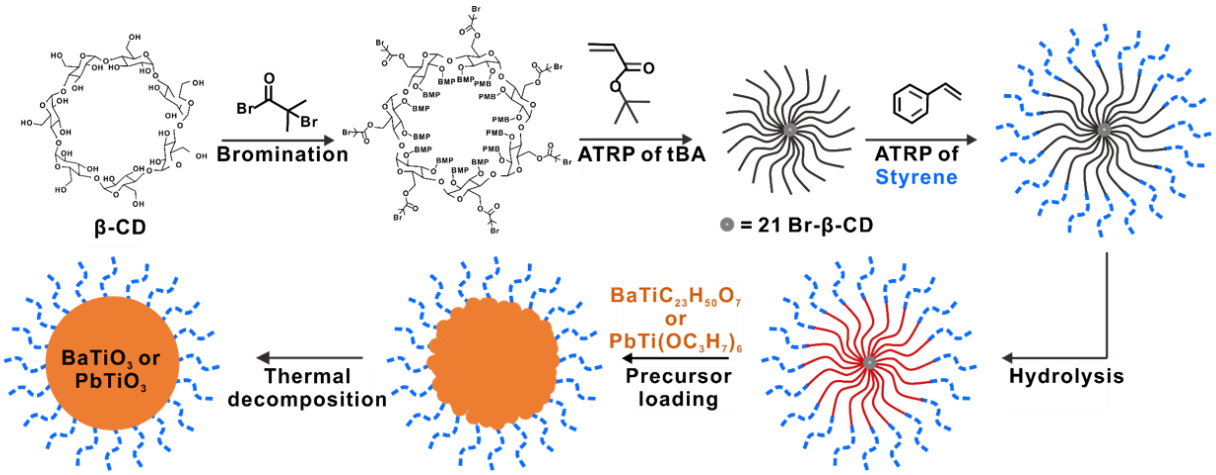

Figure 3.1 Scheme for synthesizing star-like PAA-*b*-PS diblock copolymer as nanoreactor for subsequent synthesis of inorganic nanoparticles (perovskite oxide in this case).

(1) Synthesis of brominated ß-CD (denote 21-Br-ß-CD, as 21-arms initiator): ß-CD was first dissolved in anhydrous 1-methyl-2-pyrrolidone (NMP). After cooling the solution to 0 ^{o}C, 2-bromoisobytyryl bromide was added into the solution dropwise. The bromination reaction was left under vigorous stirring for 24 h (2 h under 0 ^{o}C and 22 h under room temperature). The crude solution was washed with $NaHCO_3$ saturated aqueous solution and DI water several times sequentially, removing acid generated during the reaction (by $NaHCO_3$) and salt generated during washing (by DI water). After washing, the product was then precipitated in water and dried in the vacuum oven.

(2) Synthesis of star-like poly(*tert*-butyl acrylate) (P*t*BA) homopolymer by ATRP using 21-Br-β-CD as macroinitiator: by employing atom transfer radical polymerization (ATRP), we utilized Br-ß-CD as the microinitiator, methyl ethyl ketone (MEK) as the solvent; CuBr as the catalyst; PMDETA as ligand and *tert*-butyl acrylate (*t*BA) as the monomer for growing first P*t*BA block. All the reactants were mixed in a pressure vessel and degassed by N_2 bubbling, followed by stirring at 60 ^oC in the oil bath. Polymerization time determines the desired molecular weight of the synthesized polymer. After a specific reaction time, the reaction was terminated by immersing the vessel into liquid N_2. The reacting solvent was then diluted and passed through an aluminum oxide column to remove copper salt. After concentrating the solution by the rotary evaporator, the product is precipitated in methanol/water (1:1) mixture and dried in vacuum oven.

(3) Synthesis of star-like P*t*BA-*b*-polystyrene (denote P*t*BA-*b*-PS) diblock copolymer using star-like P*t*BA homopolymer in 3.1.1 (2) as macroinitiator: following the similar procedure as the previous step, we were again growing PS as the second-block polymer by ATRP. Compared to growing the first block, in this step, we used star-like P*t*BA as macroinitiator, anisole as the solvent and styrene as the monomer. After mixing all the precursors and degassing with N_2 bubbling, we put the vessel into the oil bath and let it react at 90 ^oC for a specific time. The reaction was terminated by immersing in liquid N_2. The solution was then again passed through an aluminum oxide column and precipitated in methanol. The product can be collected after vacuum dried in the oven.

(4) Hydrolyzing star-like P*t*BA-*b*-PS diblock copolymer: star-like P*t*BA-*b*-PS was dissolved in dichloromethane, then a certain amount of trifluoroacetic acid (TFA) was added. After stirring at room temperature for 24 h, the product was first precipitated in methanol and further purified

by dissolving in DMF and precipitating in methanol repeatedly for several times, then dried in vacuum oven.

3.1.2 Synthesis of star-like diblock copolymer nanoreactors with 8-arm initiator (4-tert-butylcalix[8]arene)

To synthesize 8-arms nanoreactors, we substitute ß-CD with 4-tert-butylcalix[8]arene, which possesses eight hydroxyl groups that can be further brominated then serve as polymerization sites. The synthetic scheme for plain nanoparticles with 8-arms nanoreactors (as well as 16 arms and 42 arms that we are planning to do) is shown in **Figure 3.2**. The following are the detailed synthesis procedures:

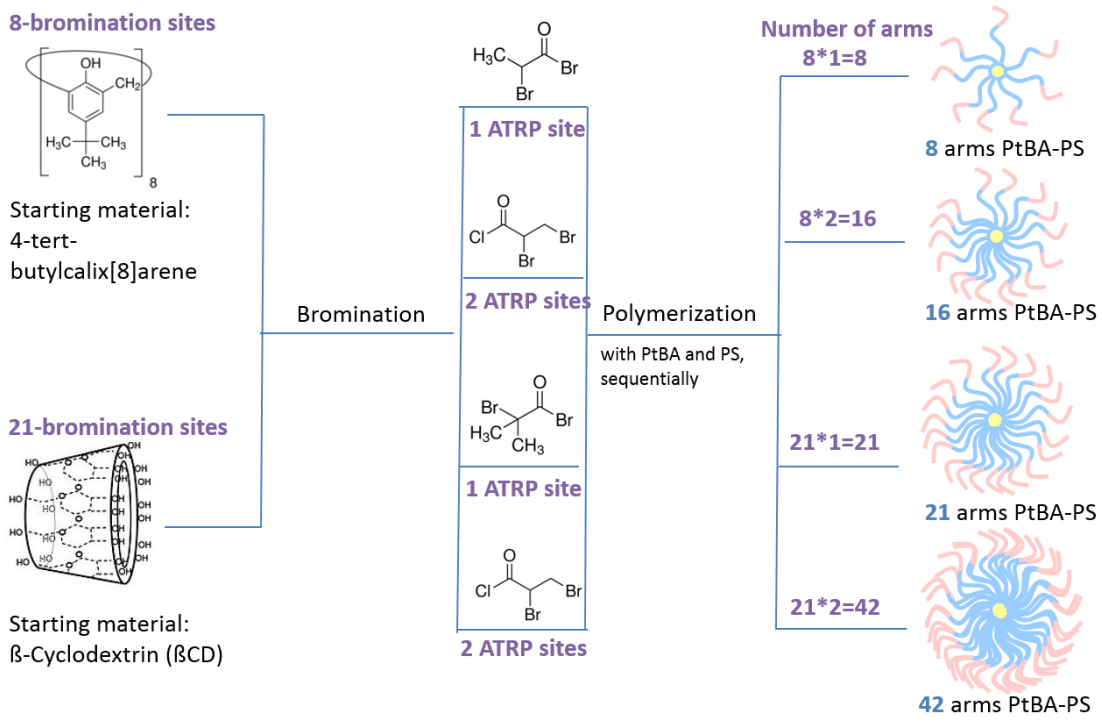

Figure 3.2 Crafting of ferroelectric $BaTiO_3$ nanoparticles using amphiphilic star-like PAA-*b*-PS diblock copolymer with different initiators and bromination agents as nanoreactors.

(1) Synthesis of brominated 4-tert-butylcalix[8]arene: before starting the reaction, we needed to distill both tetrahydrofuran (THF) and triethylamine (TEA) to make sure they are both dry.

First, 4-tert-butylcalix[8]arene was dissolved in anhydrous THF under vigorous stirring. Then a specific amount of TEA was added, and the mixture became homogeneous upon continue stirring. The solution was then cooled to 0 ^{o}C, followed by adding 2-bromopropionyl bromide dropwise. The reaction was continued for 48 h under room temperature. The crude solution is concentrated and precipitated in cold water. The product was then purified by the dissolution-precipitation method (dissolved in acetone and precipitated in water) and dried in vacuum oven for further polymerization.

(2) Synthesis of star-like P*t*BA homopolymer by ATRP using brominated 4-tert-butylcalix[8]arene as macroinitiator: similar to that in the ß-CD case, we first dissolved 8-arms initiators in MEK, then added CuBr, PMDETA, tert-butyl acrylate (*t*BA) with specific ratio into the solution. After all the reactants were added into the pressure vessel, the vessel was immediately closed and degassed by N_2 bubbling. The vessel was then put into the oil bath and reacted under 60 ^{o}C for different periods, depending on the final desired molecular weight. The reaction was then terminated by immersing in liquid N_2. The crude solution was first diluted with acetone, passed through an aluminum oxide column then precipitated in methanol/water mixture solvent. Fractional precipitation, conducted by dissolving polymers in a great amount of good solvent, then gradually adding poor solvent into the solution until the turbid point appeared, was needed to remove linear polymers if the percentage of linear polymer is too high. After washing by the dissolution-precipitation method and fractional precipitation repeatedly, ensuring all the precursors; linear polymers as well as impurities were removed, the product was collected after dried in the vacuum oven overnight.

(3) Synthesis of star-like P*t*BA-*b*-PS diblock copolymer using star-like P*t*BA homopolymer in 3.1.2 (2) as macroinitiator: star-like P*t*BA polymer was first dissolved in styrene, CuBr and

PMDETA were added into the vessel, sequentially. The vessel was closed and degassed with N_2 bubbling. After bubbling for sufficient time, the reaction was initiated by vigorously stirring at 90 ^oC for a specific time. Polymerization was again terminated by immersing the vessel in liquid N_2. The product was collected after completing all the purification steps, including passing through an aluminum oxide column, precipitating in methanol/dissolve in THF, and drying in the vacuum oven.

(4) Synthesis of PAA-*b*-PS star-like diblock copolymers: the product from 3.1.2 (3) was dissolved in DCM, followed by adding a certain amount of TFA dropwise under stirring. The reaction was kept under 0 ^oC for the first 2 h then kept at room temperature for another 22 h. After the reaction was terminated, the solvent was first evaporated by the rotary evaporator. The product was further washed by dissolving in DMF and precipitated in methanol for at least three times before it can be used as nanoreactors for nanoparticle synthesis.

3.1.3 Synthesis of star-like triblock copolymer nanoreactors with 21-arm initiator (β-CD) via addition of linear initiator

(1) Synthesis of Br-β-CD: the process to brominate β-CD was the same as described in 3.1.1 (1).

(2) Synthesis of star-like P4VP by ATRP using 21-Br-β-CD as macroinitiator: all polymerization of 4VP was conducted using 21-Br-β-CD as macroinitiator. An ampoule with the reaction solution containing 21-Br-β-CD, 2-propanol, distilled 4VP monomer, CuCl, CuCl2, and Me_6TREN was purged with N_2 for 3 h then placed in an oil bath at 40 ^oC. The reaction was terminated by dipping the ampoule in liquid N_2 at various reaction times to control the molecular weight of the synthesized star-like P4VP homopolymer. The solution was then diluted with DCM and stirred with basic alumina to remove the catalyst. After that, the solution

was first concentrated by rotary evaporator, then precipitate in cold hexane. After centrifugation, the final product was purified by the dissolution-precipitation process three times with DCM and cold hexane; dried at room temperature in vacuum overnight and finally stored in the refrigerator before growing the second block.

(3) Synthesis of star-like P4VP-*b*-P*t*BA by ATRP using star-like P4VP homopolymer in 3.1.3 (2) as macroinitiator: all polymerization of *t*BA was conducted in the flask using star-like P4VP as the macroinitiator. The reaction solution containing star-like P4VP homopolymer, CuCl, $CuCl_2$, Me_6TREN, and EBiB in DMF were purged by N_2 for 2 h and then placed in the oil bath maintained at 60 ^oC prior to polymerization. Experiments with a varied amount of EBiB, $CuCl_2$, and *t*BA were performed to elucidate the effect of these precursors on molecular weight and polydispersity of the final star-like diblock copolymers. After the desired polymerization time, the reaction was terminated by dipping the flask into liquid N_2. The mixture was stirred with basic alumina to remove the copper salt, followed by concentrated via rotary evaporator and dissolution-precipitation with methanol: water = 1:1 and acetone for three times. The final product (*i.e.* star-like P4VP-*b*-P*t*BA diblock copolymer) was dried under vacuum overnight and stored in the refrigerator before the growth of the third block. The kinetic studies of growing second P*t*BA block with and without adding EBiB were carried out as follows: (1) The flask containing reaction solution was purged and placed in an oil bath as mentioned previously. (2) At a specific time interval (typically every 20-30 minutes), about 0.5 ml of solution was withdrawn with the long syringe in the glove box (exchanging gas within syringe in the glove box for several times before needling into the flask) to measure the monomer conversion. The withdrawn solution dried and dissolved in DMF, followed by injection into gel permeation chromatography (GPC) for molecular weight and polydispersity at each time

interval. Furthermore, 20 μl of the reaction solution was diluted with d-chloroform for nuclear magnetic resonance measurement for calculating the conversion.

(4) Synthesis of star-like P4VP-*b*-P*t*BA-*b*-PS by ATRP using star-like P4VP-*b*-PtBA diblock copolymer in 3.1.3 (3) as macroinitiator: all polymerizations of styrene were conducted in the ampule. The reaction mixtures consist of star-like diblock copolymer initiator, CuCl, and PMDETA in DMF were purged by N_2 for 2 h then placed in the oil bath that maintained at 70 ^oC/80 ^oC prior to polymerization. The mixture was dipped in liquid N_2 to terminate the reaction after a specific reaction time. Copper salt was removed by mixing the reaction solution with basic alumina or passing an aluminum oxide column. The reaction solution was then concentrated and precipitated in cold solvent consist of methanol: water = 1: 1. The final product was collected by centrifugation, dried under vacuum, and stored under ambient condition.

(5) Synthesis of star-like P4VP-*b*-P*t*BA-*b*-poly(methyl methacrylate) (PMMA) by ATRP using star-like P4VP-*b*-P*t*BA diblock copolymer in 3.1.3 (3) as macroinitiator: Similar to the synthesis of star-like P4VP-*b*-P*t*BA-*b*-PS, star-like P4VP-*b*-P*t*BA-*b*-PMMA were synthesized via ATRP except for substituting styrene monomer with MMA monomer (other synthetic parameters are kept the same).

(6) Synthesis of 21-arm, star-like azide-terminated P4VP-*b*-P*t*BA diblock copolymer (star-like P4VP-*b*-P*t*BA-N_3): the star-like P4VP-*b*-P*t*BA diblock copolymers obtained in the previous step was dissolved in DMF, followed by addition of sodium azide (Br in star-like P4VP-*b*-P*t*BA: sodium azide= 1: 10 in molar ratio). The reaction solution was stirred for 24 h at room temperature, under N_2 protection. The reaction solution was then precipitated in the solvent of methanol: water= 1: 5 for several times. The final product, star-like azide-functionalized

P4VP-*b*-P*t*BA diblock copolymer (i.e., P4VP-*b*-P*t*BA-N_3 diblock copolymer) was collected and dried at room temperature in the vacuum oven overnight.

(7) Synthesis of alkyne-terminated poly(ethylene oxide) methyl ether (mPEO) (i.e, mPEO-propargyl): alkyne-terminated mPEO was obtained by nucleophilic substitution of the hydroxyl group on mPEO into the alkyne group. Typically, mPEO-OH was dissolved in 60 ml of THF under Ar purging. The DPMK solution was added into the solution until the solution turned reddish-brown. Propargyl bromide was added dropwise into the solution during 2 h at 0 ^oC, followed by continuing stirring for 24 h at room temperature. The product was precipitated in diethyl ether twice and dried under vacuum at 40 ^oC until constant weight.

(8) Synthesis of star-like P4VP-*b*-P*t*BA-*b*-PEO by click reaction: star-like P4VP-*b*-P*t*BA-N_3 and alkyne-terminated mPEO were dissolved in DMF in the ampule. CuCl and Me_6TREN were then added into the solution (molar ratio of mPEO-alkyne: star-like P4VP-*b*-P*t*BA-N_3: CuCl: Me_6TREN = 1: 0.1: 20: 20). The reaction solution was degassed by purging with N_2 for 2 h and placed in the oil bath at 90 ^oC for more than a day. The reaction was terminated by immersing the ampule in liquid N_2. Finally, after the removal of copper salt, the product was precipitated in cold hexane (with the addition of DCM) and dried in the vacuum oven at 40 ^oC overnight.

(9) Synthesis of star-like P4VP-*b*-PAA by thermolysis of *tert*-butyl ester groups within P*t*BA block in star-like P4VP-*b*-P*t*BA diblock copolymer: star-like P4VP-*b*-P*t*BA was first dissolved in DMF, then the reaction solution was stirred at refluxing temperature for 4 h. After the reaction was completed, the resulting star-like P4VP-*b*-PAA diblock copolymer was precipitated in cold methanol. Finally, thorough drying under vacuum at 40 ^oC for 24 h was conducted.

3.2 Synthesis of inorganic nanoparticles with star-like block copolymer nanoreactors

3.2.1 Synthesis of pristine and doped-perovskite oxide ($BaTiO_3$ and $PbTiO_3$) nanoparticles via star-like diblock copolymer nanoreactor

(a) Synthesis of perovskite oxide nanoparticles by a bimetallic precursor (with star-like PAA-*b*-PS diblock copolymer as nanoreactor): the synthesis of PS-capped perovskite oxide nanoparticles was performed in a standard schlenk line. In a typical synthesis of perovskite oxide nanoparticles with star-like diblock copolymers nanoreactors, 10 mg of star-like PAA-*b*-PS diblock copolymers were dissolved in 9 ml DPE. After purging the solution with Ar in three-neck flask at 130 °C to remove residual water in the system, a specific amount of bimetallic precursor (i.e., barium titanium ethyl hexano-isopropoxide ($BaTi(O_2CC_7H_{15})[OCH(CH_3)_2]_5$); 1.3 ml) was added. By using a single precursor containing two metals at the same time, the stoichiometry of the resulting $BaTiO_3$ nanoparticles can be ensured. The precursor was gradually dissolved while the isopropanol (solvent of precursor) was removed at 130 °C. After the isopropanol was completely removed, the solution was kept at the same temperature under Ar and stirring overnight, providing enough time for the precursor to coordinate with the inner PAA block of the star-like diblock nanoreactors. Then 1 ml of benzyl alcohol was added to enhance the solubility of the inner PAA block. The reaction started with the addition of 0.3 ml of 30 wt% hydrogen peroxide at 130 °C and lasted for 2 days to facilitate hydrolysis of alkoxide precursors. The crude solution was purified by ultracentrifugation for several times to separate the product from impurities and residual precursors by using toluene as good solvent and methanol as the precipitator, Finally, $BaTiO_3$ nanoparticles were re-dispersed and stored in toluene for further characterizations. Synthesis

of $PbTiO_3$ nanoparticles followed similar experimental procedures except employing lead titanium isopropoxide ($PbTi(OC_3H_7)_6$, 1.3 ml) as the precursor.

(b) Synthesis of lanthanum (La) and cobalt (Co) doped PS-capped $BaTiO_3$ nanoparticles (with star-like PAA-*b*-PS diblock copolymer as nanoreactor): After dissolving 10 mg of precursor in 9 ml DPE, and purging the solution at 130 °C to remove residual water, corresponding amount of lanthanum (III) isopropoxide ($LaC_9H_{21}O_3$, 5 mol% to $BaTiO_3$ precursor) and cobalt (II) acetate tetrahydrate ($Co(CH_3COO)_2 \cdot 4H_2O$, 1, 5, 10 mol% to $BaTiO_3$ precursor) were added for the synthesis of La-doped and Co-doped $BaTiO_3$, respectively. After the precursors were completely dissolved, the precursor of $BaTiO_3$ with a specific amount was added, and the isopropanol was purged and removed at 130 °C. 0.3 ml of H_2O_2 was then added and the reaction started and last for 2 days. The final product was collected following a similar purification process for obtaining $BaTiO_3$ nanoparticles: by employing toluene as solvent and methanol as precipitator, the product can be well-separated from other impurities (product formed outside the template) and residual precursors. Finally, the product was re-dispersed and store in toluene for further characterizations.

(c) Synthesis of perovskite oxide nanoparticles by chloride-based precursor and base (with star-like PAA-*b*-PEO diblock copolymer as nanoreactor): 10 mg of star-like PAA-*b*-PEO copolymers was first dissolved in ethylene glycol/water mixture solution (v/v = 9:1), followed by the addition of a specific amount of precursor (0.244 g $BaCl_2 \cdot 2H_2O$, 0.24 g NaOH, typically molar ratio between precursors to nanoreactor is 10 to 1). By strong coordination between carboxyl groups of PAA and metal moieties of the precursor, the precursor was expected to selectively incorporate into the space of the inner PAA block. After mixing the precursor with nanoreactors for sufficient time by sonicating, we then transferred the solution into a three-

neck flask, followed by vigorous stirring at elevated temperature (i.e., 60 ^{o}C) overnight. Before starting the reaction by refluxing the solution under 180 ^{o}C for 6 h, 0.11 ml $TiCl_4$ is quickly injected into the solution. After the reaction, the solution was then purified by both ultracentrifugation-only method (i.e., simply by tuning the centrifugation speed) and dissolution-precipitation method (with ethanol and DMF as poor and good solvent). The final product was dissolved and kept in DMF.

3.2.2 Synthesis of pristine/layered perovskite oxide (La-based) nanoparticles via star-like diblock copolymer nanoreactor

10 mg of star-like PAA-*b*-PS diblock copolymers were first dissolved in 9 ml DPE, followed by the addition of La precursor (lanthanum acetylacetonate hydrate) and various precursors for divalent metal (Cobalt (III) acetylacetonate as the precursor for Co^{3+}, iron (III) 2,4-pentanedionate as the precursor for Fe^{3+} and manganese (III) 2, 4-pentanedionate as the precursor for Mn^{3+}). The molar ratio between precursor to the functional group within star-like nanoreactors was 10 to 1, ensuring the inner block compartment was fully occupied. Furthermore, the molar ratio between two precursors might not necessarily be 1 to 1, possibly due to different solubility between the precursors and different coordination interactions between precursors and the functional group. Therefore, tuning the ratio between the two in order to obtain the product with a pure phase was required. The reaction solution was then transferred into three-neck-flask with continuous stirring at 60 ^{o}C under Ar purging overnight. After the addition of 1 ml benzyl alcohol, the temperature was then gradually (2 ^{o}C/ min) raised to the refluxing temperature of the solution (~250 ^{o}C) for 12 h. After the reaction finished, the product was purified by the precipitation-dissolution process (i.e., precipitate the polymer-capped nanoparticles by methanol then dissolve

the precipitant with toluene and repeat this process for several times) to remove residual precursors as well as those grown outside of the template. Finally, the as-synthesized nanoparticles were dissolved and stored in DMF. To increase the crystallinity of these nanoparticles, annealing was required. Before putting into furnace, DMF solution, containing both nanoparticles and graphene oxide, was sonicated for more than a day, followed by removing the solvent with the rotary evaporator. The dried composite (in powder form) was then going through a two-step anneal, i.e., annealing in air at 350 ^{o}C for 5 h then annealing in N_2 at 600 ^{o}C for 2 h. Mixing the as-synthesized nanoparticles with graphene oxide can ensure the size and morphology remain similar to that before annealing.

3.2.3 Synthesis of magnetic spinel ferrite nanoparticles via star-like diblock copolymer nanoreactor

MFe_2O_4 (M = Mn, Co, Ni) nanoparticles were synthesized by capitalizing on star-like PAA-*b*-PSAN diblock copolymers as nanoreactors. The strong coordination between the carboxyl groups and metal moieties leads to selective absorption of metal precursors (e.g. $Co(acac)_2$, $Fe(acac)_3$) onto the PAA core. Moreover, the organometallic precursors were pushed into the more polar PAA domain due to the poor solubility of precursors in DPE as a result of its low polarity. After thermolysis, PSAN capped MFe_2O_4 nanoparticles of different sizes were formed effectively with star-like PAA-*b*-PSAN diblock copolymer nanoreactors of different molecular weights. In a typical procedure (taken $CoFe_2O_4$ as an example), star-like PAA-*b*-PSAN (10 mg) was dissolved in mixed solvents of DPE (9 ml) and BA (1 ml) under 50 ^{o}C, followed by the addition of $Co(acac)_2$ (76 mg) and $Fe(acac)_3$ (216 mg) and stirred overnight under Ar atmosphere. As mentioned above, the metal precursors tended to dominate the swelled PAA core because of polarity preference. The

addition of BA led to the nucleation and growth of more spherical nanoparticles. The reaction was heated to refluxing temperature (about 258 ºC) of the solvent for 12 h under stirring with Ar protection, yielding a dark black solution. The nanoparticles were precipitated and washed with ethanol 4 times and dried under vacuum overnight.

3.3 Characterization

3.3.1 Gel permeation chromatography (GPC)

The molecular weight as well as the molecular weight distribution of the as-synthesized star-like polymers were measured by gel permeation chromatography (GPC), equipped with an Agilent1100 with a G1310A pump, a G1362A refractive detector, and a G1314A variable wavelength detector. THF was used as the eluent at 1.0 ml/min at 35 °C. One 5 μm LP gel column (500 Å, molecular range: 500-2 ×104 g/ mol) and two 5 μm LP gel mixed bed columns (molecular range: 200-3 ×106 g/mol) were calibrated with PS standard samples.

3.3.2 Proton NMR (^{1}H NMR)

Proton nuclear magnetic resonance (^{1}H NMR) results were measured by Varian VXR-300 spectroscope with the solvent resonances as the internal standard. Deuterated chloroform was used as the solvent for NMR measurement. The efficiency of esterification of the initiators as well as the molecular weight (per polymeric arm) after polymerization can be obtained by the ratio of the integral area between the newly-emerged functional group and the originally-existing functional group.

3.3.3 Fourier transform infrared spectroscopy (FTIR)

For characterizing the star-like P*t*BA-*b*-PEO diblock copolymers, successful azidation, as well as click reaction, can be corroborated by the emergence and disappearance of the characteristic stretching of -N_3 at ~2112 cm^{-1} from the FTIR studies.

3.3.4 Dynamic light scattering (DLS)

The average size and size distribution of both star-like diblock copolymer nanoreactors as well as the polymer-capped nanoparticles can be acquired by laser light-scattering spectrometer (Wyatt DyanoPro DLS) which measures the hydrodynamic volume of the material.

3.3.5 X-ray diffraction (XRD)

By analyzing the characteristic peaks from XRD (Alpha 1) results, the crystal structures and the crystallinity of the as-synthesized inorganic nanoparticles can be understood. Furthermore, the purity of the as-synthesized materials (i.e., any emerging peaks don't belong to the desired product) and the phase (typically in $BaTiO_3$ case, splitting peaks can be observed due to the distortion of the crystal) can also be understood.

3.3.6 Raman spectroscopy

Particularly, Raman (Renishaw, equipped with a 785 nm laser) result is also required for identifying the phase of the as-synthesized $BaTiO_3$ nanoparticles, which provides microscopically/local distortion of the crystal instead of the long-range distortion in XRD case.

3.3.7 X-ray photoelectron spectroscopy (XPS)

The identification of chemical states for the elements in the pure and doped perovskite oxide nanoparticles as well as element within as-synthesized magnetic spinel ferrite nanoparticles was obtained by X-ray photoelectron spectroscopy (XPS, Thermo K-alpha XPS).

3.3.8 Transmission electron microscopy (TEM)

The morphology of all the nanoparticles synthesized in this study, including perovskite oxide, layered-perovskite oxide, and spinel ferrite nanoparticles as well as the composition of nanoparticles dispersed on reduced graphene oxide after annealing were characterized by TEM (JEOL 100, operated at 100 kV). HRTEM was employed especially for the morphology and composition for pristine and doped-perovskite oxide nanoparticles.

3.3.9 Piezoresponse force microscopy (PFM)

PFM (atomic force microscopy in PFM mode with conductive tip) was used for measuring the ferroelectric behavior that might exist in the as-synthesized $BaTiO_3$ and $PbTiO_3$ nanoparticles. By employing different nanoreactors for making those nanoparticles (i.e., 21-arms and 8-arms star-like nanoreactors), we're planning to investigate the interaction between organic polymeric chain with inorganic nanoparticles and how this interaction influences the domain distribution and ferroelectric properties. Typical butterfly loop (amplitude) and hysteresis loop (phase) were observed with the thin film sample we made by spin coating (on both silicon and FTO substrates). Further clarification on whether this signal indeed came from the sample itself or other contributions need to be conducted.

3.3.10 Electrochemical characterization

(1) Cyclic voltammetry (CV) and rotating disk electrode (RDE) measurement: the working electrode was prepared by loading catalyst sample film of 0.136 mg on 5.0 mm-diameter glassy carbon electrode. First, the ink was prepared by dispersing 1 mg of catalyst and 10 μl of 5 wt % Nafion solution in 0.1 ml of 1:1 v/v water/ethanol mixed solvent by 30 min sonication to form a homogeneous dispersion. Next, 15 μl of the catalyst ink (containing 1 mg of catalyst)

was loaded onto a glassy carbon electrode of 5 mm in diameter by dropping 5 μl at a time and repeating for three times (loading ~ 0.136 mg). The ink was dried slowly in air, and a uniform catalyst film deposited on the electrode surface was obtained. CV and RDE were conducted in a three-electrode electrochemical cell at room temperature using a saturated Ag/AgCl electrode as the reference electrode, and a graphite rod as the counter electrode. The electrolyte for the measurement is 0.1 M KOH, which was saturated with oxygen by bubbling O_2 prior to the start of each experiment. A flow of O_2 was maintained over the electrolyte during the recording of CVs to ensure the saturated O_2 environment. The working electrode was cycled at least 5 times before data were recorded at a scan rate of 10 mV/s. In control experiments, CV and RDE measurements were performed in N_2 saturated environment by switching to N_2 flow through the electrochemical cell.

(2) Oxygen electrode activities on glassy carbon electrode: for measurements of oxygen reduction reaction (ORR) activity at room temperature in 0.1 M KOH, working electrode was prepared by the same method above. It was cycled at least 10 times between 100 mV and -1 V vs. Ag/ AgCl before data were recorded. Steady-state polarization plots were recorded in a potential of the same range at a scan rate of 5 mV/s. A continuous O_2 flow was supplied to the measurement setup. The disk rotation rates for the ORR ranged from 400 to 2500 rpm. For measurements of oxygen evolution reaction (OER) activity at room temperature in 0.1 M KOH and 1 M KOH, the experimental conditions were the same with the ORR measurement except the scanning range was between 100 mV and 1 V vs. Ag/ AgCl. The ORR stability in O_2-saturated 0.1 M KOH was performed by chronoamperometry (i-t) at the 0.7 V (around the half-wave potential obtained from the LSV curve at 1600 rpm). In this work, all the potentials vs. Ag/AgCl were converted to the reversible hydrogen electrode (RHE) by the equation:

$E(RHE) = E(Ag/AgCl) + 0.059 \times pH + E^0(Ag/AgCl)\,V$. Specifically, with 0.1 M KOH as the electrolyte, the reaction can be converted into $E(RHE) = E(Ag/AgCl) + 0.9646\,V$. Koutechy-Levich plots (J^{-1} vs. ω^{-1}) were analyzed at various electrode potentials. The slopes of their best linear fit lines were used to calculate the number of electrons transferred (*n*) based on the equation below:

$$\frac{1}{J} = \frac{1}{J_L} + \frac{1}{J_K} = \frac{1}{B\omega^{\frac{1}{2}}} + \frac{1}{J_K}$$

$$B = 0.62nFC_0(D_0)^{\frac{2}{3}}\nu^{\frac{-1}{6}}$$

$$J_K = nFkC_0$$

, where J is the measured current density, whereas J_K and J_L are the kinetic- and diffusion-limiting current density, ω is the angular velocity, n is the transferred electron number, F is the Faraday constant, C_o is the bulk concentration of O_2, ν is the kinematic viscosity of the electrolyte and k is the electron-transfer rate constant. The OER stability tests were carried out by recording the corresponding LSVs before and after 1500 cycles of CV measurements ranging from 100 mV to 0.9 V vs. Ag/AgCl at the scanning rate of 200 mV/s^{-1}. The polarization curves were replotted as applied potential (V) vs. log current (log *j*) to get Tafel plots for quantification of the OER activities of all the La-based perovskite NPs

(3) Computational methods: to understand the effects of doping by Co or La atoms, we performed first-principles calculations based on density functional theory (DFT) as implemented in the Vienna Ab initio Simulation Package (VASP). In the simulations, we adopted an energy cutoff of 600 eV for plane waves, and the Perdew–Burke–Ernzerhof (PBE) exchange correlation energy functional together with the PAW pseudopotentials. The energy tolerance for self-

consistency was set to 10^{-6} eV. The force tolerance for atomic relaxation was set to 0.001 eV/Å. The reciprocal space of BTO bulk (slab) was sampled by an 8×8×8 (3×3×1) Monkhorst-Pack k-grid during atomic relaxation. For calculating the projected density of states (PDOS) of the BTO slab, we used a denser k-grid of 5×5×1.

The overall oxygen reduction is:

$$O_2 + 2H_2O + 4e^- \rightarrow 4OH^- \quad (1)$$

Previous studies suggested the following four-step reaction pathway:

$$OH^* + O_2 + e^- \rightarrow OO^* + OH^- \quad (2)$$

$$OO^* + H_2O + e^- \rightarrow OOH^* + OH^- \quad (3)$$

$$OOH^* + e^- \rightarrow O^* + OH^- \quad (4)$$

$$O^* + H_2O + e^- \rightarrow OH^* + OH^- \quad (5)$$

The superscript of * indicates that each intermediate is a substrate-adsorbate hybrid system, not merely the adsorbate. The free energy change for each step:

$$\Delta G = \Delta E + \Delta \mathrm{ZPE} - T\Delta S + e\Phi, \quad (6)$$

, where E is the static DFT energy, ZPE is the zero-point energy, T is temperature, S is entropy, e is the unit charge, and Φ is the potential difference between the cathode and the anode. For small molecules, we obtain the entropy and the vibrational frequencies from the NIST database. For the substrate-adsorbate hybrid systems, we obtain the ZPE and the phonon entropy from the vibrational frequencies as calculated by DFT. Following a previous study, we approximate the free energy difference $G(OH^-)$-$G(e^-)$ at 300 K and 1 atmosphere by

$$G(\mathrm{H_2O}_g, 300\ \mathrm{K}, 0.0349\ \mathrm{atm}) - 0.5 \times G(\mathrm{H}_2, 300\ K, 1\ atm) \quad (7)$$

Here, the subscript g indicates that the water is in the gas phase. We have also included solvation correction energies of −0.32, −0.47, −0.75, and −0.54 eV for OO*, O*, HO*, and HOO* intermediates, respectively. With these approximations, all terms in equation (6) can be found while the potential difference Φ remains adjustable. The equilibrium potential Φ_{eq} is defined such that the net free energy change vanishes, i.e. $\sum_{i=1}^{4} \Delta G_i = 0$. It follows that -2e$\Phi_{eq}$ equals the formation free energy of water from H_2 and $1/2O_2$, which is about -2.46 eV experimentally.

In addition, we calculate the adsorption energy via the equation:

$$E_{ads} = E_{subtrate-adsorbate} - E_{subtrate} - E_{adsorbate}. \quad (8)$$

CHAPTER 4. SNTHESIS OF AMPHIPHILIC AND DOUBLE HYDROPHILIC STAR-LIKE BLOCK COPOLYMERS AND THE DUAL PH-RESPONSIVENESS OF UNIMOLECULAR MICELLE

Yeu-Wei Harn *et al. Macromolecule* (under review)

4.1 Introduction

The past several decades has witnessed significant advances in synthesis of polymers with tailorable compositions, structures and functionalities.[1] Among them, a rich diversity of polymers with nonlinear molecular architectures (e.g., cyclic,[2] dendritic, brush,[3] star-like,[4-5] and hyperbranched[6]) have been extensively studied due to their unique physicochemical,[7] mechanical,[8] photonic,[9-10] and electrical[11] properties for potential applications in molecular recognition,[12] catalysis,[13] drug delivery,[14] etc. Star-like polymer represents one of the simplest nonlinear polymers, containing multiple linear arms covalently linked to a core. In general, the method for synthesizing star polymers can be categorized into two strategies, namely the "core-first"[3, 5, 15] and "arm-first"[16] methods. The former strategy uses pre-synthesized multifunctional initiator as a core, from which subsequent polymerization of monomers produces the multi-arms. On the other hand, the latter involves the preparation of linear arms first, followed by grafting them onto the multifunctional coupling agent, yielding star-like polymers. Clearly, the "core-first" approach provides an better control over the architecture of star-like polymer as the number of arms can be easily tailored by the number of initiate sites of initiators, whereas the "arm-first" route often results in a broad distribution of the number of arms per star-like polymer. Controlled radical polymerizations (CRP), including atom transfer radical polymerization (ATRP) and reversible addition fragmentation chain transfer (RAFT) polymerization, have been proven to be robust

techniques for synthesizing well-defined star-like polymers due to their site-specific initiation as well as efficient reversible deactivation. In addition to various initiators as the core, a variety of monomers[17] can be utilized for growing polymeric arms with CRP.

It is widely recognized that synthesizing pyridine-containing polymer with controlled molecular weight (MW) distribution via ATRP remains challenging, especially with increased initiating sites per core, for the following reasons. First, the pyridine group can strongly coordinate with the metal catalysts in the systems, leading to possible formation of pyridine-coordinated metal complexes, which are verified to be non-effective catalysts for ATRP reaction, thereby greatly reducing the polymerization rate or even rendering uncontrollable polymerization. Second, owing to the ability of halogen atom (especially Br) as the leaving group to nucleophilically attack the pyridal moiety of pyridine-containing polymer, a significant amount of termination and coupling reactions (i.e., between two star-like polymers as well as polymer arms within a star-like polymer), and thus a sharp increase in polydispersity occurs. Furthermore, this phenomenon would become more severe when the number of initiating sites per core increases because of higher tendency of arm-arm coupling within one star-like polymer due to the closer proximity between initiating sites.[18-19]

On the other hand, stimuli-responsive polymers represent an intriguing class of materials as their physical and chemical properties can be conveniently tuned upon exposure to external stimuli (e.g., temperature, pH, and electric fields).[9, 20] Among them, poly(4-vinylpyridine) (P4VP) has been extensively studied owing to its good pH-sensitivity, biocompatibility and hydrophilicity.[21-22] Notably, P4VP has often been exploited as drug carrier due to its enhanced solubility (i.e., fully stretched P4VP chain) under lower pH value, resulting in the release of drug locally (e.g., in the acid environment of tumors).

Herein, we report a route to synthesize a set of star-like homopolymer, diblock and triblock copolymer, containing P4VP as the first block, with low polydispersity by addition of linear initiator (EBiB), followed by investigating the dual pH-responsive behavior of star-like poly(4-vinyl pyridine)-*block*-poly(acrylic acid) (P4VP-*b*-PAA) diblock copolymer. The star-like triblock copolymers comprise poly(4-vinyl pyridine) (P4VP) as the first block, poly(*tert*-butyl acrylate) (P*t*BA) as the second block, and either polystyrene (PS), poly(methyl methacrylate) (PMMA) or poly(ethylene oxide) (PEO) as the third block (denoted P4VP-*b*-P*t*BA-*b*-PS, P4VP-*b*-P*t*BA-*b*-PMMA, and P4VP-*b*-P*t*BA-*b*-PEO, respectively). Specifically, the initiator for ATRP with 21 initiating sites is first formed via bromination of β-cyclodextrin. After successful synthesis of the first P4VP block with tailorable MW and narrow polydispersity, star-like P4VP-*block*-poly(*tert*-butyl acrylate) (P4VP-*b*-P*t*BA) diblock copolymers with controlled MW distribution can be prepared by deliberate addition of an optimal amount of linear initiator of ethyl α-bromoisobutyrate (EBiB) to prevent the coupling reaction between two star-like polymers as well as polymer arms within a star-like polymer . When the molar ratio between initiate site (including sites from both star-like P4VP homopolymer terminated with X (X = Cl and Br) and linear initiator of EBiB) to metal catalysts of CuCl is increased to 1 to 1, suppressed tendency of the coupling between the arms of star-like diblock copolymer as well as between adjacent star-like diblock copolymers and thus narrow polydispersity are achieved. The polymerization kinetics of the second P*t*BA block with and without the addition of linear initiator of EBiB is scrutinized. The linear relationship of $\ln([M]_0/[M])$ ($[M]_0$ and $[M]$ are the monomer concentrations at t_0 and t, respectively) vs. time can only be attained when linear initiator of EBiB is present, indicating the number of propagating species remains constant during the polymerization. As a result, this synthetic approach can facilitate the preparation of multi-arm polymer with controlled MW

distribution, generally below 1.2. Moreover, as-synthesized star-like P4VP-*b*-P*t*BA diblock copolymer terminated with X (X = Cl and Br) could continue serving as macroinitiator for the third polymerization, yielding star-like triblock copolymers. Successful synthesis of star-like P4VP-*b*-P*t*BA-*b*-PS and P4VP-*b*-P*t*BA-*b*-PMMA triblock copolymers by ATRP as well as P4VP-*b*-P*t*BA-*b*-PEO by click reaction demonstrates the versatility of this synthetic strategy. Furthermore, the dual pH change-induced responsive behavior of star-like P4VP-*b*-PAA diblock copolymer obtained via thermolysis of P*t*BA of star-like P4VP-*b*-P*t*BA into PAA is examined via dynamic light scattering and UV-vis studies under various pH environment, and the possible morphological change is proposed. Taken together, the results suggest the promising potential of as-synthesized star-like diblock copolymer as polymeric nanocarriers for controlled release of drugs.

4.2 Experiment Details

The detailed synthesis of star-like P4VP homopolymer, star-like P4VP-*b*-P*t*BA diblock copolymers and star-like P4VP-*b*-P*t*BA-b-PS, P4VP-*b*-P*t*BA-*b*-PMMA and P4VP-*b*-P*t*BA-*b*-PEO triblock copolymers have been rendered in Chapter 3, *3.1*. Below we just specified the procedure for measuring the dual-pH responsive behavior of star-like P4VP-*b*-PAA diblock copolymers and the characterization used in this study:

4.2.1 Stimuli-responsive of star-like P4VP-b-PAA diblock copolymers

(1) Turbidity measurement. The aggregation behavior of star-like P4VP-*b*-PAA in the aqueous solution under different pH value was measured by UV-vis spectrophotometer. Briefly, the aqueous solution containing P4VP-*b*-PAA diblock copolymers (1 mg/ml) was dissolved and placed inside the disposable cuvette. The transmittance of the polymer solutions was monitored between 200 nm to 700 nm with various pH value. The transmittance value at 450 nm was picked and the plot of transmittance to pH value was provided.

(2) Size distribution by DLS. Star-like P4VP-*b*-PAA samples were dissolve in neutral aqueous solution (pH~7, 1 mg/ ml) and stir for more than a day to make sure the star-like diblock copolymer become stable within the solution. Before starting DLS measurement, specific amount of HCl solution (pH = 1) or NaOH solution (pH = 13) were added into the solution to reach desired final pH value. Samples were then stirred for 10 min and placed into cuvette for measurement. Each measurement was repeated for three times, and the average result was used as the final hydrodynamic diameter (D_h).

4.2.2 Characterization

The molecular weight and PDI of polymers were measured by gel permeation chromatography (GPC), equipped with an Agilent1100 with a G1310A pump, a G1362A refractive detector and a G1314A variable wavelength detector. DMF was used as the eluent at 1.0 ml/ min at 35 ^{o}C. Two columns were calibrated with PS standard samples. Proton nuclear magnetic resonance (^{1}H NMR) with Varian VXR-300 spectroscope with the solvent resonances as the internal standard, was capitalized for measuring the conversion during the polymer synthesis as well as MW per polymeric arm. Deuterated chloroform was used as the solvent for NMR measurement. Size distribution of unimolecular star-like micelles with homo-, diblock, triblock copolymers and diblock P4VP-*b*-PAA diblock copolymers under varied pH value were characterized by dynamic light scattering (DLS, Wyatt DyanoPro NanoStar Dynamic Light Scattering). The aggregation behavior of the polymer in the aqueous solutions was measured by a UV-Vis spectrophotometer (UV-2600, Shimadzu). The morphologies of the star-like homopolymer, diblock copolymer and triblock copolymer were characterized by atomic force microscopy (Bruker Dimension Icon). Successful azidation of star-like P4VP-b-PtBA diblock copolymer was confirmed by Fourier-transform infrared spectroscopy (FT-IR, Shimadzu Prestige 21 Infrared Spectrometer (FT-IR)).

4.3 Results and Discussion

Synthesis of initiator with 21 initiate sites for subsequent ATRP reaction. A facile synthesis approach based on previous literature[5, 23] to modify the end hydroxyl groups of β-cyclodextrin (β-CD) by capitalizing on 2-bromoisobutyl bromide was conducted. After mixing β-CD with esterification agent (i.e., α-bromoisobutyryl bromide) for one day under room temperature, the outer hydroxyl groups can be substituted by the bromoisobutyryl units, yielding 21-Br-β-CD (left panel in **Figure 4.1 (a)**). 1-methyl-2-pyrrolidione (NMP) was identified as the suitable solvent for esterification due to its compatibility with the esterification agent and a small amount of HBr byproduct. The successful esterification of β-CD was corroborated by ^{1}H NMR (**Figure 4.2**), where the methyl protons of 21-Br-β-CD (assigned to δ = 1.8-2.2) were seen. The conversion efficiency of the end hydroxyl group can be calculated by the equation:

$$E_T = \frac{A_b}{18A_a} \times 100\%$$

where E_T is the conversion efficiency of hydroxyl groups, A_a (δ = 5.2-5.3) and A_b are the integral areas of the part of the residual protons on β-CD and the methyl protons, respectively. Based on the calculation, as-synthesized 21-Br-β-CD showed a conversion as high as 95%, indicating the successful substitution of hydroxyl groups into bromoisobutyryl units, yielding the initiator for the subsequent ATRP.

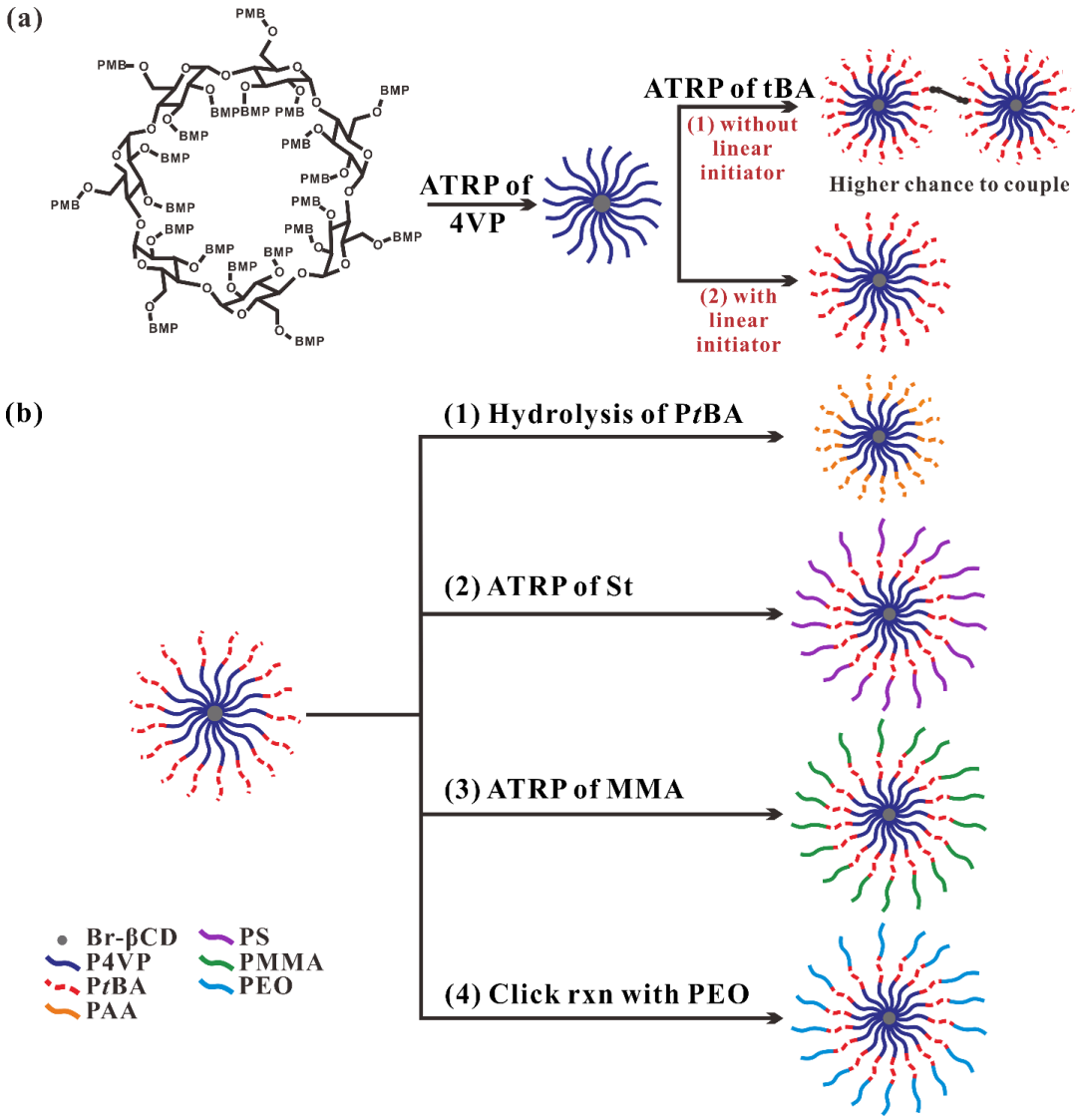

Figure 4.1 (a) Schematic illustration of synthetic route to star-like P4VP-*b*-P*t*BA diblock copolymer (1) without and (2) with the addition of linear initiator EBiB, where BMP is 2-bromo-2-methylpropionate. **(b)** Schematic representation of synthetic strategies for (1) star-like P4VP-*b*-PAA diblock copolymer via hydrolysis of inner P*t*BA block, (2-3) star-like P4VP-*b*-P*t*BA-*b*-PS and P4VP-*b*-P*t*BA-*b*-PMMA triblock copolymers by using star-like P4VP-*b*-P*t*BA diblock copolymer as macroinitiator for ATRP of styrene and methyl methacrylate, respectively, and (4) P4VP-*b*-P*t*BA-*b*-PEO via click reaction of star-like P4VP-*b*-P*t*BA and linear poly(ethylene oxide) (PEO).

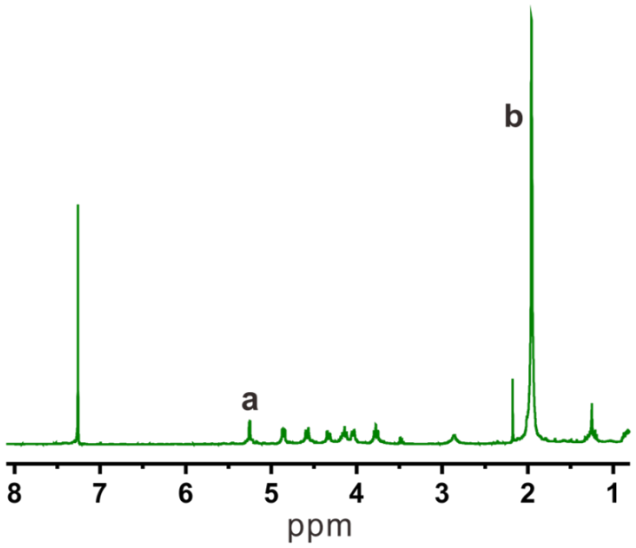

Figure 4.2 ^{1}H NMR spectrum of the macroinitiator, 21-Br-β-CD.

Synthesis of star-like P4VP homopolymer via the first ATRP. By using the 21-Br-β-CD as the initiator and CuCl/Me_6TREN as the cocatalyst (see *Experimental Section* in Supporting Information), ATRP of 4-vinyl pyridine (4VP) was successfully conducted in 2-propanol at 40 ^{o}C. As reported in the literature, polymerization of 4VP via ATRP can be difficult due mainly to (1) the coordination between metal catalysts (i.e., CuCl) and pyridal groups of 4VP/P4VP in the system and (2) the coupling between halide group at polymer chain end of each star-like polymer and pyridal group of 4VP and P4VP,[24] both resulting in the occurrence of termination and/or coupling reaction, and thus broadened the MW distribution. In order to obtain star-like P4VP with tailorable MW and controlled polydispersity, several experimental parameters were tailored. First, instead of CuBr/PMDETA, CuCl/Me_6TREN as cocatalysts was used. It is notable that CuCl was chosen as metal catalyst because of the weak ability of chlorine atom as the leaving group, thereby resulting in less susceptibility to nucleophilically attack pyridal groups of P4VP and thus reduced side reaction in the system. In sharp contrast, a significant termination reaction can be observed,

represented by the appearance of the shoulder peak or broad polydispersity from GPC result, when CuBr was used as metal catalyst for polymerizing 4VP via ATRP. Furthermore, due to the lower activation/deactivation equilibrium constant of alkyl chloride, Me_6TREN was selected as ligand to increase polymerization speed. Moreover, the strong coordination between CuCl and Me_6TREN ligand can facilitate the removal of the catalyst by passing the polymer solution through an alumina column or directly stirring alumina in the product solution, as verified by color change from green to colorless or pale-yellow after the abovementioned treatments. In addition to changing cocatalysts (i.e., CuCl and Me_6TREN), reducing reaction temperature and reaction time were found to be helpful for suppressing the occurrence of the coupling reaction.

Three star-like P4VP homopolymers with different MW and narrow MW distribution (typically lower than 1.1) were synthesized. Monomodal peaks can be observed from the GPC results (**Figure 4.3** and **Figure 4.4**), and the MW can be easily tuned by changing the polymerization time. The molecular weights of all the as-synthesized star-like polymers were summarized in **Table 4.1**. Notably, low polydispersity index (PDI) and no obvious shoulder peak appeared in the high MW range indicated that there were no intermacromolecular coupling reactions. Very little linear P4VP homopolymer appeared suggested the suitable condition chosen for ATRP of 4VP with star-like Br-β-CD as initiator. Representative ^{1}H NMR spectrum of star-like P4VP homopolymer obtained after reacting for 6 h is shown in **Figure 4.5 (a)**. The characteristic chemical shifts of ^{1}H NMR at $\delta = 6.6$ (marked as b in **Figure 4.5 (a)**) and $\delta = 8.3$ (marked as c in **Figure 4.5 (a)**) corresponded to the protons of pyridal group, indicating successful synthesis of P4VP block.

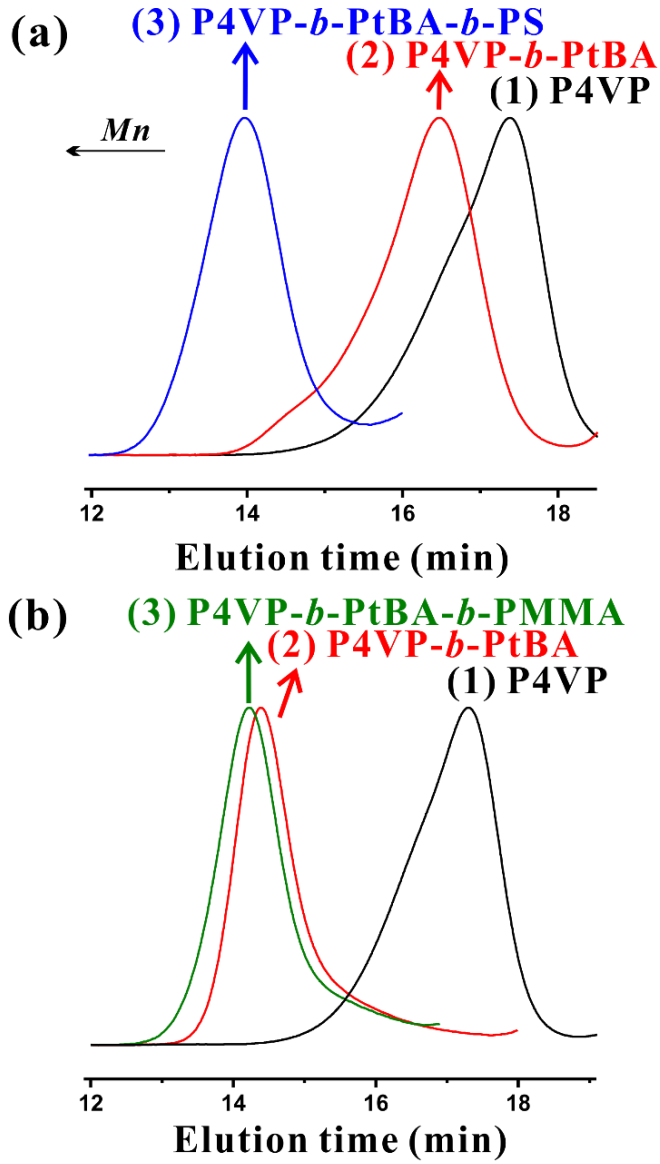

Figure 4.3 (a) GPC traces of (1) star-like P4VP homopolymer, (2) P4VP-*b*-P*t*BA diblock copolymer and (3) P4VP-*b*-P*t*BA-*b*-PS triblock copolymer. **(b)** GPC traces of (1) star-like P4VP homopolymer, (2) P4VP-*b*-P*t*BA diblock copolymer and (3) P4VP-*b*-P*t*BA-*b*-PMMA triblock copolymer.

Table 4.1 Summary of the molecular weight of star-like P4VP-*b*-P*t*BA-*b*-PS (**Sample 1** to **Sample 3**), P4VP-*b*-P*t*BA-*b*-PMMA (**Sample 4**) and P4VP-*b*-P*t*BA-*b*-PEO (**Samples 5-6**) triblock copolymers. All the molecular weights were determined by gel permeation chromatography (GPC) calibrated with polystyrene standards with known molecular weights.

Sample #	**MW of P4VP block**	**MW of P4VP-*b*-P*t*BA block**	**MW of P4VP-*b*-P*t*BA-poly(third block)**
Sample 1	90K	160K	614K (PS)
Sample 2	90K	260K	415K (PS)
Sample 3	90K	476K	685K (PS)
Sample 4	90K	414K	500K (PMMA)
Sample 5	80K	145K	197K (PEO)
Sample 6	90K	130K	170K (PEO)

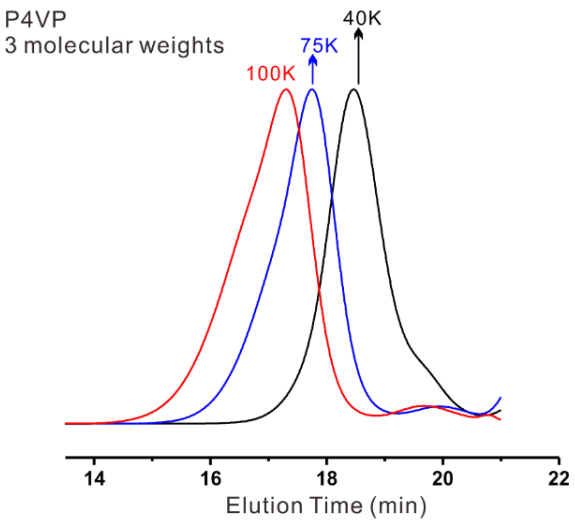

Figure 4.4 GPC traces of star-like P4VP homopolymer with three different molecular weights.

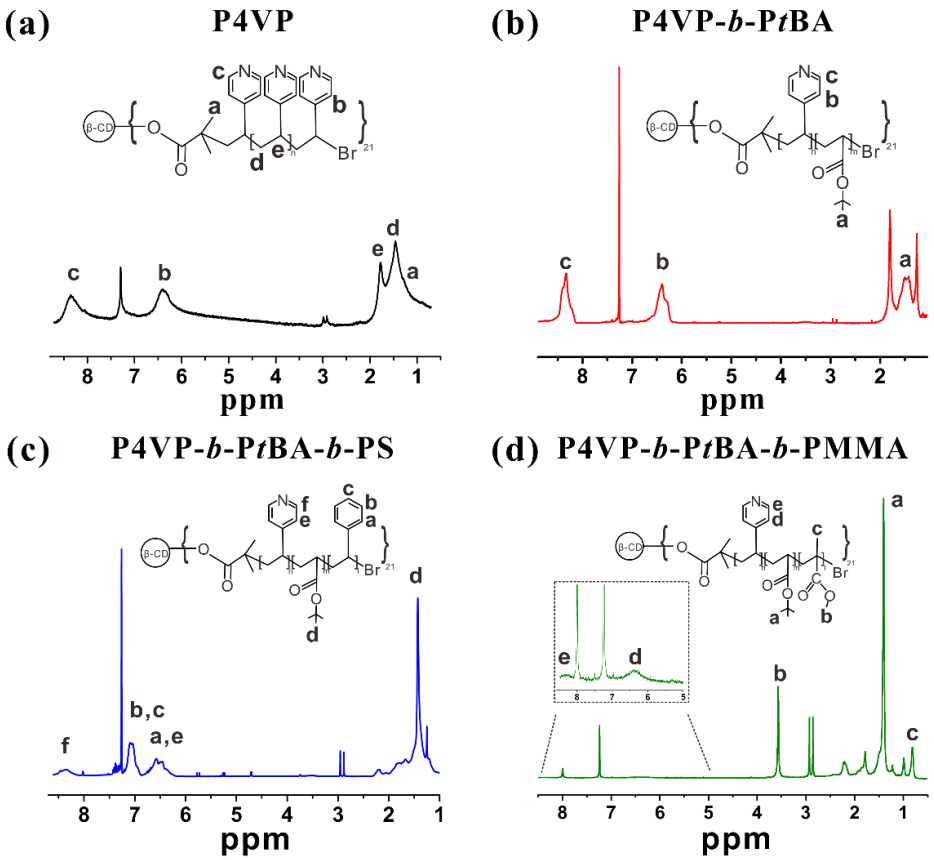

Figure 4.5 ^{1}H NMR spectra for **(a)** star-like P4VP homopolymer, **(b)** star-like P4VP-*b*-P*t*BA diblock copolymer, **(c)** star-like P4VP-*b*-P*t*BA-*b*-PS triblock copolymer and **(d)** star-like P4VP-*b*-P*t*BA-*b*-PMMA triblock copolymer. All the samples are measured in $CDCl_3$.

Synthesis of star-like P4VP-*b*-P*t*BA diblock copolymers with low polydispersity via the second ATRP. A series of star-like P4VP-*b*-P*t*BA diblock copolymers with different MWs and controlled PDI were subsequently synthesized via ATRP using the as-synthesized star-like P4VP homopolymer as macroinitiator (central panel in **Figure 4.1 (a)**). The effect of addition of linear initiator EBiB on MW distribution was scrutinized. This was motivated by the observation of broad peak and/or shoulder in GPC traces during the synthesis of the second star-like P*t*BA block. Notably, we tried to reduce the influence of partially oxidized metal catalyst (i.e., CuCl; it has been difficult to estimate the extent of oxidation as it varied as time went by, even stored the metal catalysts inside the glove box) by keeping the metal catalyst amount no less than 10 mg at each ATRP. A small amount of attainable star-like P4VP block and constant amount of metal catalyst (typically ~10 mg) resulted in low ratio of initiator to metal catalyst. We thus speculate the irregular peak shape of GPC trace may be due to the synergic effect of the use of highly-active ligand,[25] small molar ratio (i.e., 0.02) of the initiation sites from star-like P4VP homopolymer to metal catalyst, and the architecture of star-like polymer (i.e., closer distance between radical within one star-like polymer), thereby generating radical (i.e., active species during ATRP) with higher concentration and increasing the occurrence of termination and/or coupling reaction, which is often seen in surface-initiated living radical polymerization.[26-27] Based on the solutions reported previously with surface-initiated polymerization, we deliberately added predetermined amount of linear initiator EBiB with 1:1 molar ratio of EBiB to metal catalyst to the reaction mixture. Consequently, the addition of linear initiator rendered an appropriate ratio of initiator sites (i.e., halide groups from both star-like P4VP-*b*-P*t*BA diblock copolymer and linear EBiB initiators) to metal catalyst CuCl. Thus, the concentration of Cu^{2+} was increased, ensuring a fast deactivation process and suppressing further termination reactions from radical coupling (see equation below)

in the system and leading to a better control over the chain growth of the star-like diblock copolymer.

$$P - X + Cu^{I}Cl/\ Me_6TREN \leftrightarrow P^{*} + Cu^{II}Cl_2/\ Me_6TREN$$

As a result, by employing the strategy described above, star-like P4VP-*b*-P*t*BA diblock copolymer with monomodal GPC traces was obtained (**Figure 4.6**), and the MW of the resulting star-like P4VP-*b*-P*t*BA can be readily controlled by tuning the reaction time. **Figure 4.5 (b)** shows the ^{1}H NMR spectrum of as-obtained star-like P4VP-*b*-P*t*BA diblock copolymer. The appearance of the strong characteristic peak at δ = 1.45 (marked as a in **Figure 4.5 (b)**), corresponding to the methyl protons in tert-butyl group (-C(CH$_3$)$_3$, confirmed the success in growing P*t*BA onto star-like P4VP block.

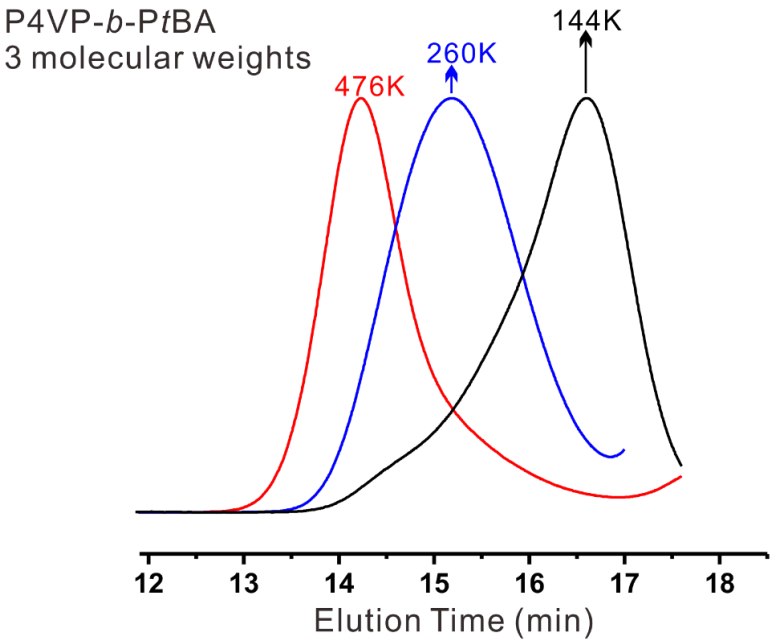

Figure 4.6 GPC traces of star-like P4VP-*b*-P*t*BA diblock copolymer with three different molecular weights.

The polymerization kinetics with and without addition of linear initiator EBiB was then studied (**Tables 4.2** and **Table 4.3**). **Figure 4.7 (a)** displays a linear relationship of semilogarithmic kinetic plot when linear initiator was added, suggesting the radical concentration was constant during the polymerization. Conversely, a nonlinearity was seen in the absence of linear initiator, signifying possible occurrence of termination and/or coupling reactions due to the competing side reactions, that is, termination reactions from radical (i.e., active species within ATRP) coupling and/or coupling between halide groups of star-like polymer chain end and pyridal group within the first star-like P4VP block. Clearly, the addition of linear initiator was thus proven to be effective in reducing the side reaction by decreasing the concentration of active species in the ATRP system. A linear increase of number average molecular weight (M_n) of the second P*t*BA block vs. *t*BA monomer conversion was identified when growing the second P*t*BA block with the presence of EBiB (**Figure 4.7 (b)**). Both linear kinetic plot of $\ln([M]_0/[M])$ vs. time and linear relationship between M_n and monomer conversion corroborated that the successful polymerization of the second P*t*BA block, using the first star-like P4VP block as macroinitiator with addition of linear initiator, is controlled/living radical polymerization with a negligible amount of transfer and termination reaction. Furthermore, the PDI can be significantly suppressed with the presence of linear initiator (as shown in **Figure 4.8**). The PDI remained lower than 1.15 after polymerization for 210 min with the addition of EBiB, while it increased to 1.35 with a similar reaction time in the absence of EBiB. With no EBiB in the system, the shoulder peak started to appear due to the intra- and intermolecular coupling reaction even with only 10 min polymerization time, and the PDI continued increasing with the prolonged reaction time. **Figure 4.8 (c)** compares the PDI when growing the second P*t*BA block from star-like P4VP homopolymer in the presence and absence of linear initiator EBiB.

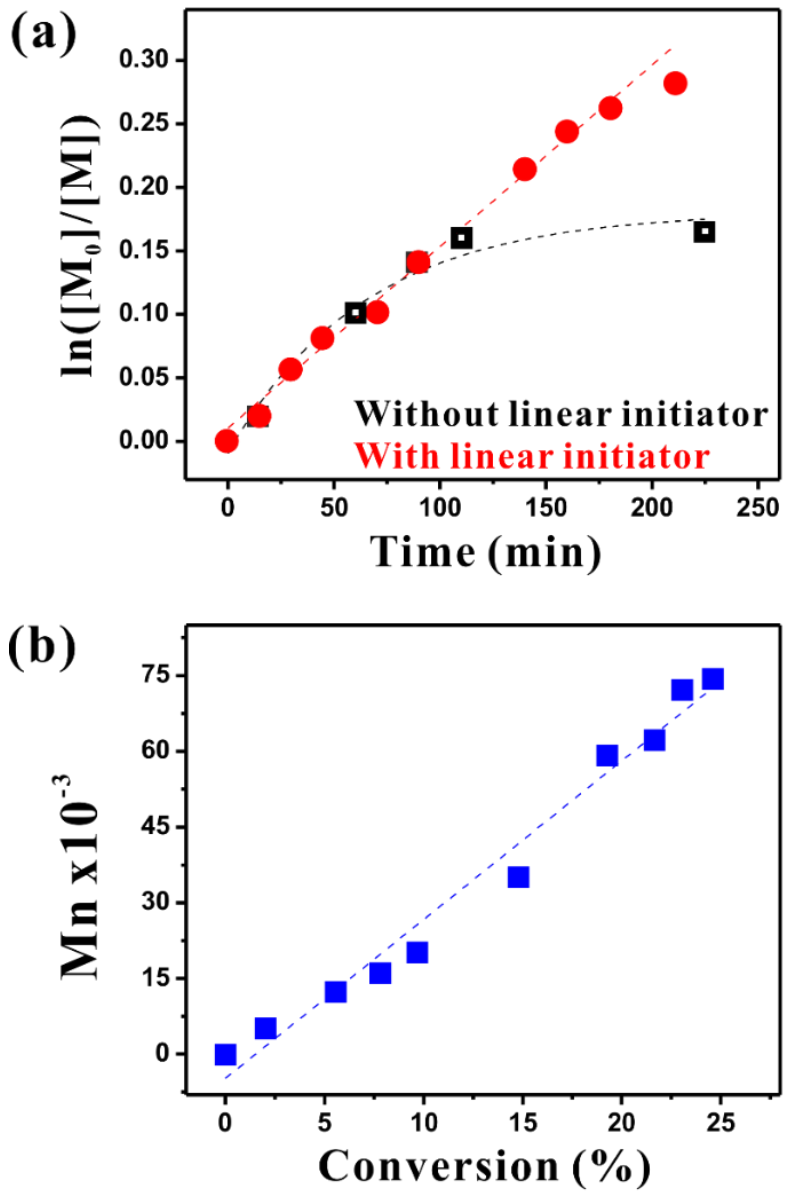

Figure 4.7 (a) Kinetic plot for the copper-mediated ATRP of second P*t*BA block with and without addition of linear initiator EBiB, employing star-like P4VP homopolymer as macroinitiator and DMF as reaction solvent. [M_0] and [M] are the concentration of *t*BA monomer at time 0 an t, respectively. **(b)** Dependence of number-average molecular weight (M_n) of the second P*t*BA block on the *t*BA monomer conversion.

Table 4.2 Results of the polymerization of the second P*t*BA block with the addition of linear initiator EBiB by using star-like P4VP homopolymer as macroinitiator with various reaction times[a].

Run	$[M]_0/[I]_0/[Cu]_0/[L]_0$[b]	Time (min)	conversion (%)[c]	Mn, GPC-all (K)[d]	PDI[f]
1	520/1.02/1/1	0	0	79.8	1.12
2	520/1.02/1/1	15	2.03	85	1.1
3	520/1.02/1/1	30	5.53	92	1.09
4	520/1.02/1/1	45	7.84	95.9	1.1
5	520/1.02/1/1	70	9.7	100	1.1
6	520/1.02/1/1	90	14.83	115	1.12
7	520/1.02/1/1	140	19.3	139	1.12
8	520/1.02/1/1	160	21.69	142	1.13
9	520/1.02/1/1	180	23.08	152	1.13
10	520/1.02/1/1	210	24.62	154	1.14

[a] DMF was used as the solvent for the polymerization. The reactions were carried out at 60 °C.

[b] $[M]_0$, $[I]_0$, $[Cu]_0$ and $[L]_0$ represent initial concentration of monomer, total initiation sites (from both star-like P4VP homopolymer and linear initiator), Cu(I)Br, and ligand (Me_6Tren), respectively.

[c] Calculated from the ratio of integrated area of solvent to residual monomer.

[d, f] Obtained by GPC.

Table 4.3 Results of the polymerization of second P*t*BA block without the addition of linear initiator by using star-like P4VP homopolymer as macroinitiator with various reaction time[a].

Run	$[M]_0/[I]_0/[Cu]_0/[L]_0$[b]	Time (min)	conversion (%)	Mn, GPC-all (K)[c]	PDI[d]
1	520/0.02/1/1	0	0	79.8	1.12
2	520/0.02/1/1	10	8.7	166	1.29
3	520/0.02/1/1	25	10.66	198	1.29
4	520/0.02/1/1	30	14.588	252	1.29
5	520/0.02/1/1	60	14.8	258	1.31
6	520/0.02/1/1	105	15.3	267	1.34
7	520/0.02/1/1	225	18.36	287	1.35

[a] Polymerization condition is the same except no linear initiator was added.

[b] Keep all the experimental condition same except without the addition of linear initiator, thus the initial concentration of initiation sites only came from star-like P4VP homopolymer.

[c, d] Obtained by GPC.

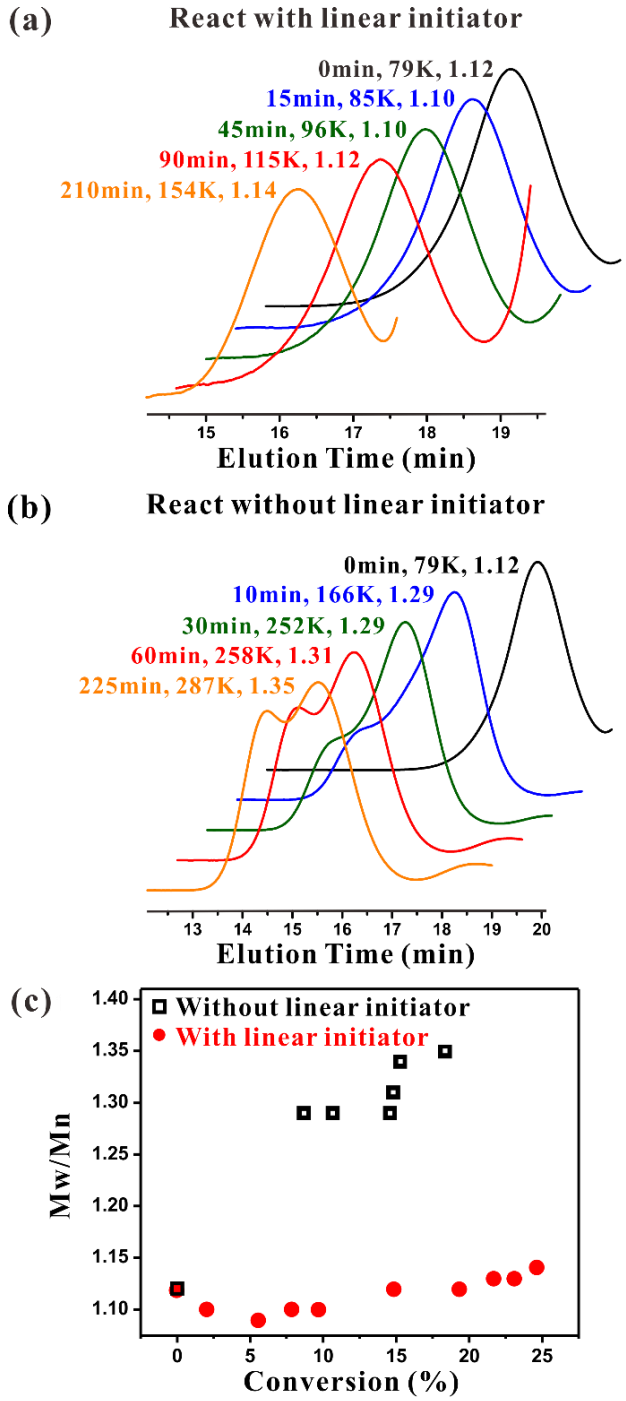

Figure 4.8 GPC chromatograms of star-like P4VP-*b*-P*t*BA diblock copolymer prepared using ATRP **(a)** with and **(b)** without the addition of linear initiator, and **(c)** dependence of polydispersity (M_w/M_n) on monomer conversion of star-like P4VP-*b*-P*t*BA diblock copolymer.

On the basis of the results described above, by employing the additional linear initiator, its effect in suppressing the occurrence of coupling and/or termination reaction, resulting from increasing concentration of Cu^{2+} and in turn faster deactivation process can thus be substantiated. Furthermore, this approach by judiciously introducing linear initiator is particularly beneficial when synthesizing star-like, pyridine-containing polymers due to closer proximity between radicals within each star-like polymer and using more active ligand (i.e., Me_6TREN). The addition of linear initiator can thus lead to markedly improved controllability of the growth of polymer chains (i.e., narrow polydispersity).

Moreover, the appropriate amount of linear initiator (EBiB) added was also investigated. **Figure 4.9** compares the GPC traces of the growth of the second P*t*BA block with various amounts of linear initiator added yet with the same reaction time. The optimal amount was found when the ratio of linear initiator to metal catalyst (CuCl) is 1 to 1 (central panel; **Figure 4.9**). At low amount of linear initiator (i.e., molar ratio of EBiB/CuCl is 0.5 to 1), the peak still broadened with increased PDI (upper panel; **Figure 4.9**). The peak broadening became even more obvious with a prolong polymerization time (**Figure 4.10**). On the other hand, with an excess amount of EBiB added (i.e., molar ratio of EBiB/CuCl is 1 to 1.5), the polymerization speed decreased (lower panel; **Figure 4.9**) possibly because both star-like P4VP and linear initiator competed for reacting with *t*BA monomers.

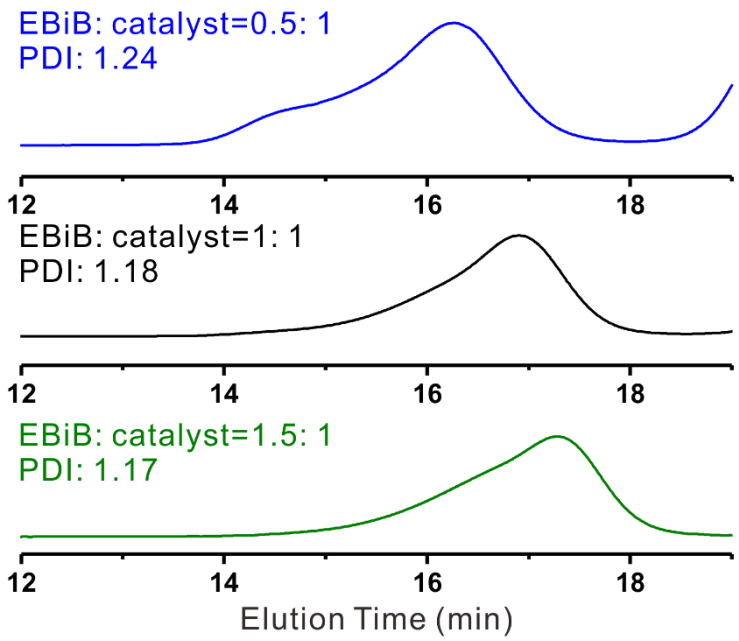

Figure 4.9 GPC traces of star-like P4VP-*b*-P*t*BA diblock copolymer with different amount of additional linear initiator during polymerization. Numbers marked as molar ratio between linear initiator (EBiB) to metal catalyst (CuCl).

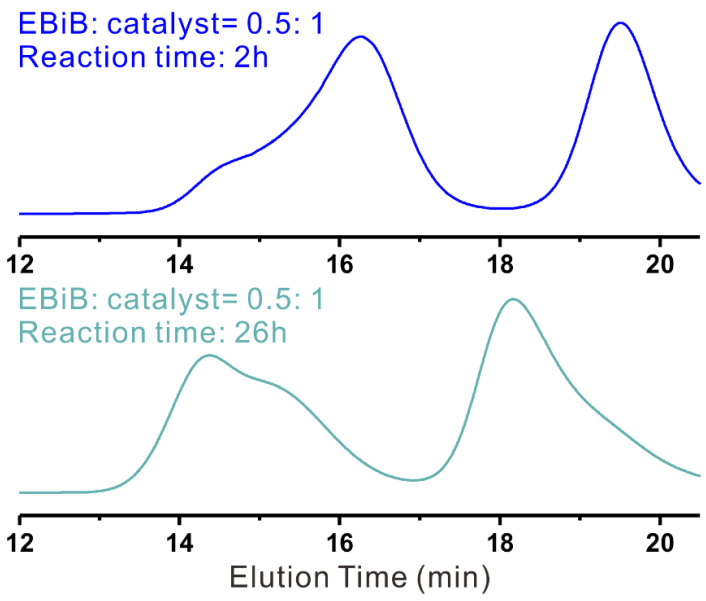

Figure 4.10 GPC traces of star-like P4VP-*b*-P*t*BA diblock copolymer with insufficient linear initiator under various polymerization time. Numbers marked as molar ratio between linear initiator (EBiB) to metal catalyst (CuCl).

We note that another possibility to reduce the polymerization speed for better control over PDI is to introduce additional $CuCl_2$, as reported in literature. To this end, $CuCl_2$ with varied amounts (i.e., the molar ratios of $CuCl_2$ to CuCl are 0, 0.27 and 0.54) was added to elucidate the effect of $CuCl_2$ on polymerization. From the GPC traces shown in **Figure 4.11**, broad peak can be observed in all cases regardless of the amount of $CuCl_2$ added. This may be because even with the presence of $CuCl_2$ (especially within the range tried), the ratio between metal catalyst to initiating sites of star-like P4VP homopolymer may still remain high, suggesting the approach to decrease coupling and/or termination reactions via adding $CuCl_2$ was not effective in this system.

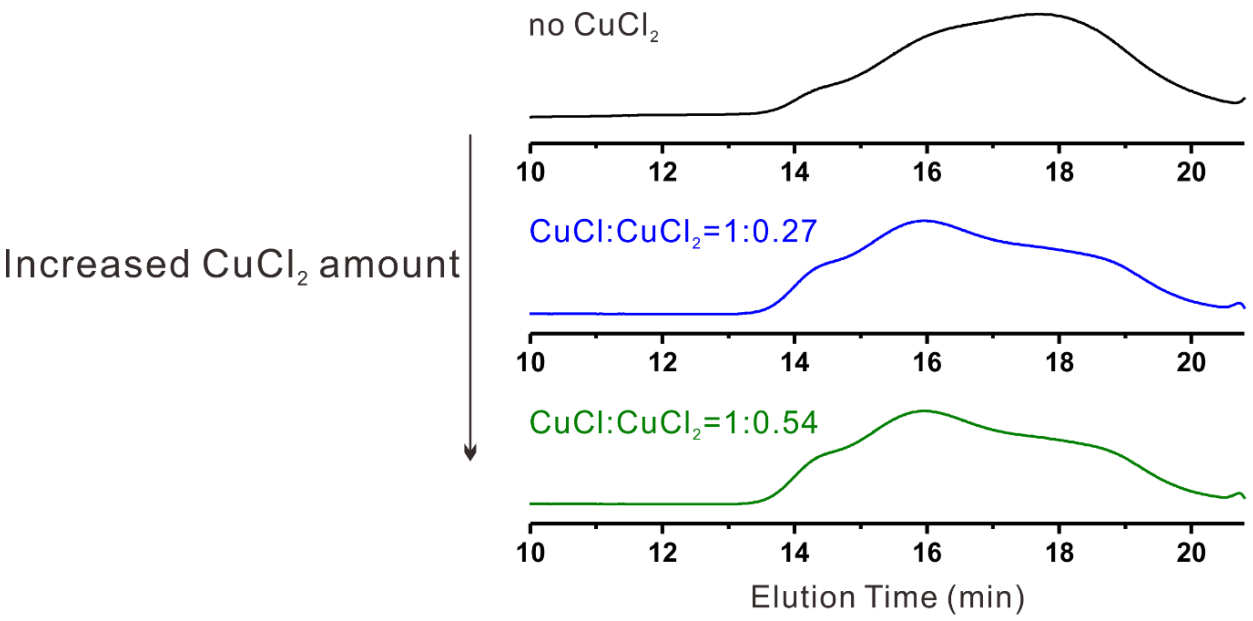

Figure 4.11 GPC traces of star-like P4VP-*b*-P*t*BA diblock copolymer with different amount of $CuCl_2$ during polymerization. Numbers marked as molar ratio between CuCl to $CuCl_2$.

Initially, the polymerization of the second P*t*BA block was carried out with an $[M]_0/[I]_0$ ratio of 520 as shown in **Table 4.2**, where $[M]_0$ and $[I]_0$ are the initial concentrations of monomer and overall initiation sites from both star-like P4VP and linear initiators. Star-like P4VP-*b*-P*t*BA

diblock copolymer with narrow MW distribution can be synthesized with monomer conversion up to 25% after 3-4 h. When conversion was larger than 25-30%, the polymerization speed gradually decreased with prolong reaction time (**Figure 4.12**). To further increase the MW of the second P*t*BA block, we raised the molar ratio of $[M]_0/[I]_0$ from 520 to 780. The MW of P*t*BA block was enlarged when *t*BA monomer amount was increased while keeping other experimental conditions the same. The GPC traces of ATRP of the second P*t*BA block with different amounts of monomer are shown in **Figure 4.13**. Compared to employing the ratio of 520 at specific reaction time (marked as a-1 and a-2 in **Figure 4.13**, respectively), P*t*BA with larger MW can be acquired when the ratio increased to 780, as marked as b-1 and b-2 in **Figure 4.13**, at both reaction times. Remarkably, the PDI can still be maintained less than 1.2. The molecular weight of the second P*t*BA block can thus be increased simply by increasing the *t*BA monomer amount even with the monomer conversion still lower than 30%.

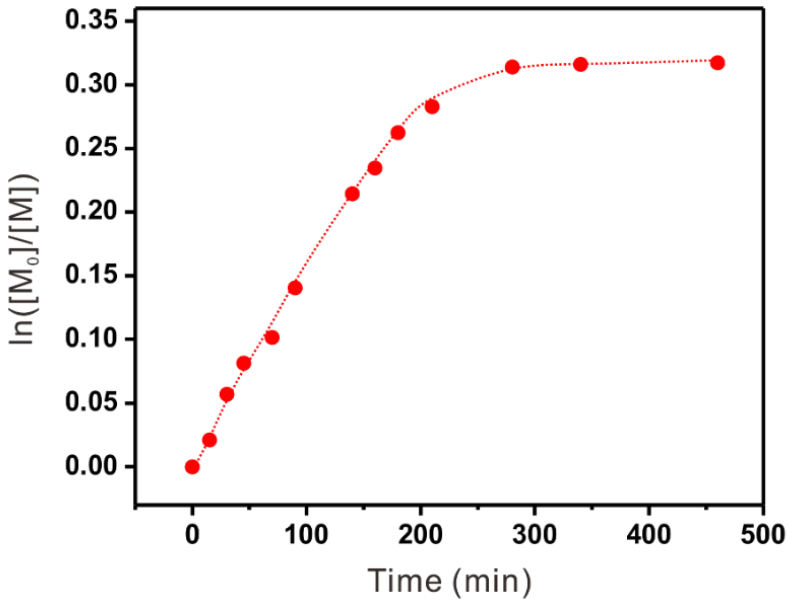

Figure 4.12 Kinetic plot for the copper-mediated ATRP of second P*t*BA block with addition of linear initiator and prolonged reaction time, employing star-like P4VP homopolymer as initiator in DMF.

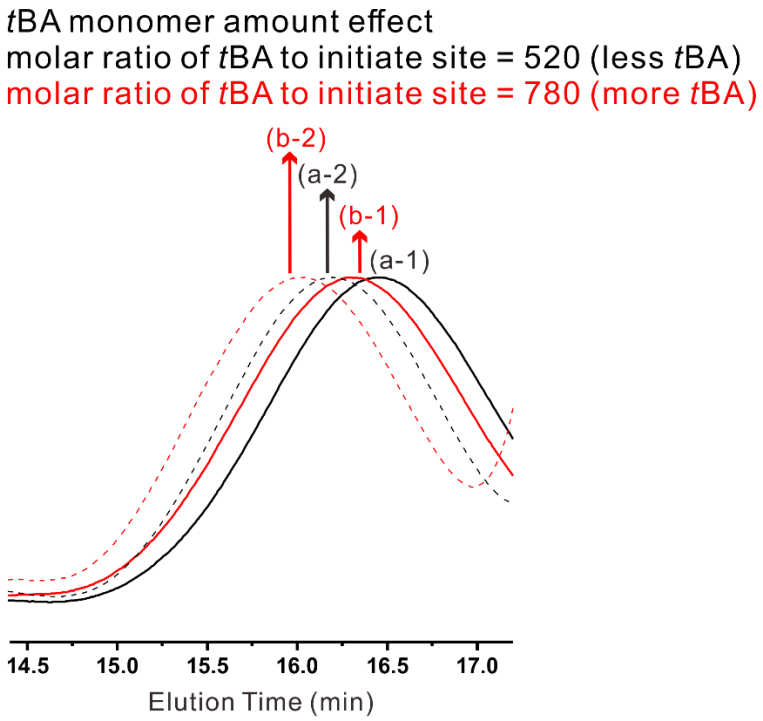

Figure 4.13 GPC traces of star-like P4VP-*b*-P*t*BA diblock copolymer with different amount of *t*BA monomer: (a-1) and (a-2) use ratio of tBA: initiator= 520: 1.02 with polymerization time of 90 min and 150 min, respectively. (b-1) and (b-2) use ratio of tBA: initiator= 780: 1.02 with polymerization time of 90 min and 150 min, respectively.

Despite good controllability in PDI by adding linear initiator during reaction, the appearance of linear P*t*BA block was inevitable. Typically, fractional precipitation can be utilized to remove the undesired linear polymer, that is, by the fact that polymer with larger MW would precipitate out first when dissolving polymer in good solvent with the gradual addition of poor solvent. In this case, the difficulty of conducting fractional precipitation lies in identifying good solvent and poor solvent for both P4VP and P*t*BA block at the same time. Intriguingly, we found the linear P*t*BA can be easily removed by washing the product with hexane (**Figure S9**). Employing the solubility difference of P4VP and P*t*BA in hexane (good solubility for P*t*BA and poor solubility for P4VP), linear P*t*BA is soluble in hexane whereas star-like P4VP-*b*-P*t*BA diblock copolymer cannot be well dissolved in hexane, resulting in easy separation of the two parts

via washing the product, followed by centrifuging and collecting the precipitant. Notably, the larger the MW of the outer P*t*BA block, the higher tendency for dissolving the star-like diblock copolymer in hexane at the same time, eventually leading to more losses during this washing process.

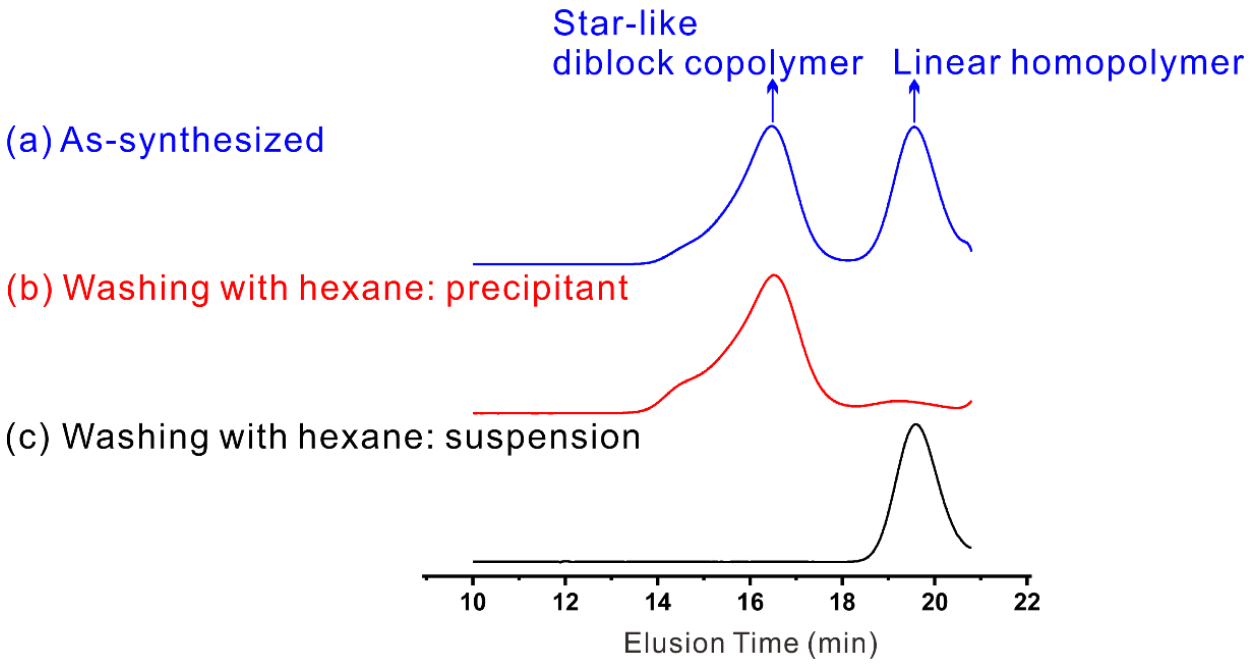

Figure 4.14 Removal of linear PtBA by washing with hexane: **(a)** as-synthesized star-like P4VP-*b*-P*t*BA diblock copolymer before washing, **(b)** precipitant of star-like P4VP-*b*-P*t*BA diblock copolymer after washing with hexane and centrifuging, and **(c)** suspension of star-like P4VP-*b*-P*t*BA diblock copolymer after washing with hexane and centrifuging.

Synthesis of star-like P4VP-*b*-P*t*BA-*b*-PS and P4VP-*b*-PtBA-*b*-PMMA triblock copolymers via the third ATRP. A series of star-like P4VP-*b*-P*t*BA-*b*-PS and P4VP-*b*-P*t*BA-*b*-PMMA triblock copolymers with different MWs were successfully prepared by conducting third ATRP using star-like P4VP-*b*-P*t*BA diblock copolymer as macroinitiator (**Figure 4.1 (b-2)** and **(b-3)**, respectively). The absence of intermacromolecular coupling was verified by the GPC traces of star-like P4VP-*b*-P*t*BA-*b*-PS and P4VP-*b*-P*t*BA-*b*-PMMA triblock copolymers (**Figure 4.3** and

Figure 4.15). **Figure 4.5 (c-d)** show the representative ^{1}H NMR spectra of star-like P4VP-*b*-P*t*BA-*b*-PS and P4VP-*b*-P*t*BA-*b*-PMMA triblock copolymers, respectively. In **Figure 4.5 (c)**, except for those characteristic chemical shifts from pervious blocks, the peaks at δ = 6.33-7.31 ppm can be assigned to the protons on phenyl ring of the third PS block, indicating the successful growth of PS onto the star-like P4VP-*b*-P*t*BA macroinitiator. On the other hand, the chemical shift in **Figure 4.5 (d)** at δ = 0.8-1.12 can be ascribed to methyl groups of the third PMMA block. The weak signal at δ = 6.6 and 8.3 from the pyridine group of the first star-like P4VP block might be due to the small ratio of molecular weight between P4VP and the subsequent P*t*BA and PMMA block.

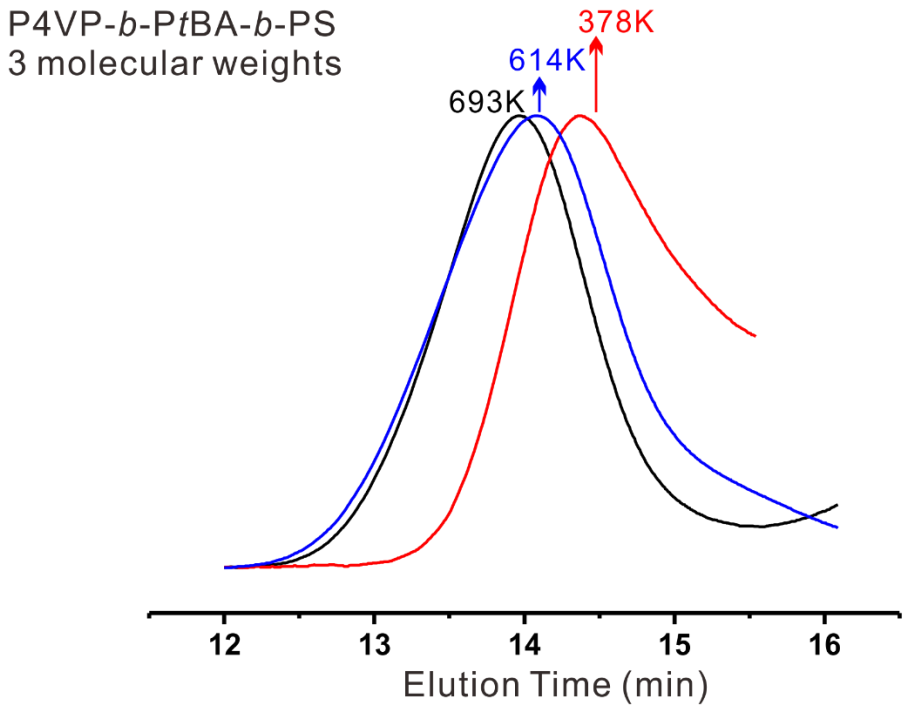

Figure 4.15 GPC traces of star-like P4VP-*b*-P*t*BA-*b*-PS triblock copolymer with three different molecular weights.

It is notable that when performing ATRP for the second (*t*BA) or third block (styrene and methyl methacrylate, respectively), even though the macroinitiator (e.g., X-terminated (X = Cl and Br) star-like P4VP in the case of grafting second P*t*BA block) was dissolved in good solvent at the beginning, the addition of *t*BA monomers may still cause turbidity or precipitation because *t*BA was the poor solvent for star-like P4VP homopolymer. As a result, the molar ratio of solvent to monomer was an important parameter that we paid attention to and the speed of adding *t*BA monomers should be controlled, that is, a dropwise injection was preferred to prevent the precipitation of the macroinitiator.

The hydrodynamic diameters D_h of the star-like P4VP homopolymer, star-like P4VP-*b*-P*t*BA diblock copolymer and star-like P4VP-*b*-P*t*BA-*b*-PS triblock copolymer were measured by dynamic light scattering (DLS) (**Figure 4.16 (a)).** Clearly, the D_h of the polymer increased from 24 nm, 33 nm to 65 nm when an additional block was polymerized, suggesting each block was successfully grown from the previous star-like initiator. AFM measurements were conducted to distinguish the structure of unimolecular star-like polymer. A DMF solution containing star-like P4VP, P4VP-*b*-P*t*BA and P4VP-*b*-P*t*BA-*b*-PS (Sample 1; **Table 4.1**) was spin-coated on the pre-cleaned Si substrate and the results are shown in **Figure 4.16 (b-d)**, respectively. The spherical unimolecular nanoparticulates are clearly evident with an average diameter of 19.9 ± 3.4 nm, 29.1 ± 4.5 nm and 59.7 ± 5.9 nm for star-like P4VP homopolymer, star-like P4VP-*b*-P*t*BA diblock copolymer and star-like P4VP-*b*-P*t*BA-*b*-PS triblock copolymer (**Figure 4.17**), correlating well with the D_h results from the DLS measurements.

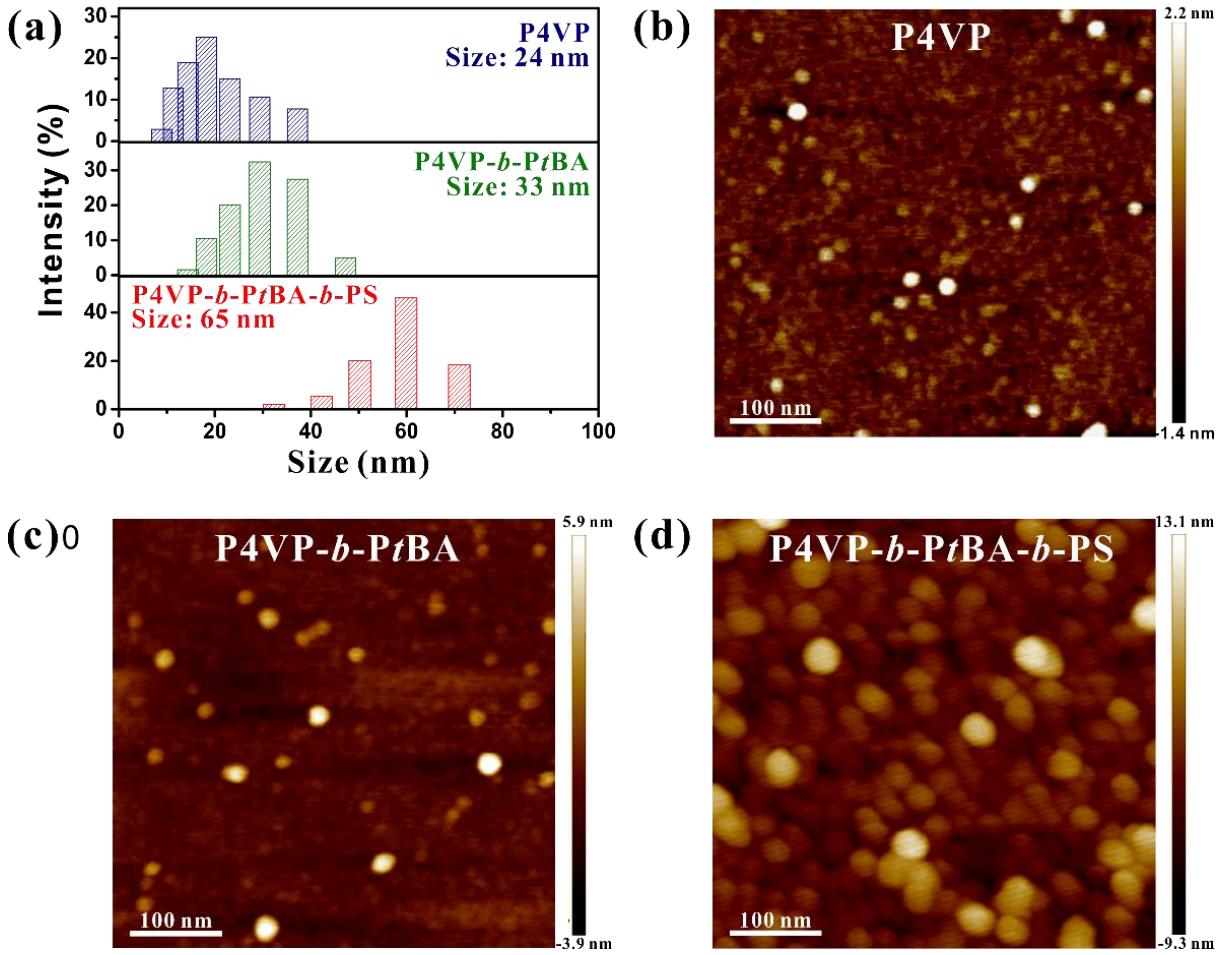

Figure 4.16 (a) Size change from star-like P4VP homopolymer, P4VP-*b*-P*t*BA diblock copolymer to P4VP-*b*-P*t*BA-*b*-PS triblock copolymer at 25 °C as measured by dynamic light scattering (DLS). **(b-d)** AFM height images of the corresponding star-like **(b)** P4VP, **(c)** P4VP-*b*-P*t*BA and **(d)** P4VP-*b*-P*t*BA-*b*-PS. Image size = 0.5 μm x 0.5 μm.

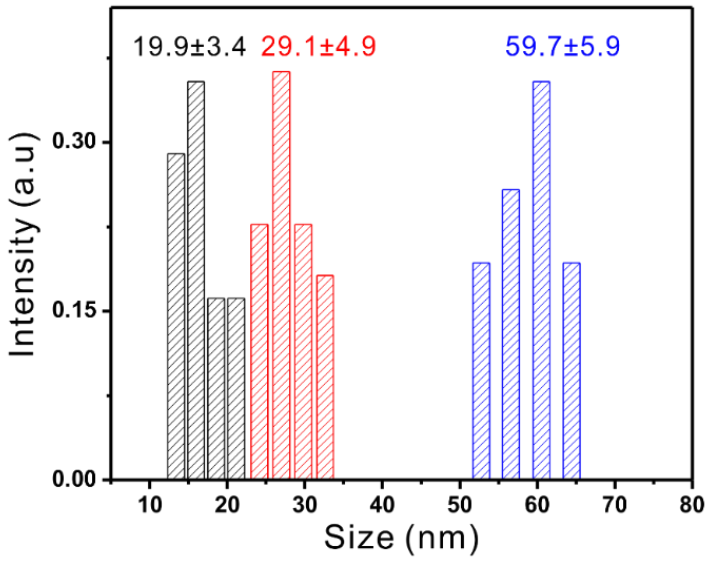

Figure 4.17 Statistic size distribution from star-like homopolymer (P4VP), diblock copolymer (P4VP-*b*-P*t*BA) to triblock copolymer (P4VP-*b*-P*t*BA-*b*-PS), measured by *ImageJ* with 100 nanoparticles in corresponding AFM height images.

Synthesis of star-like P4VP-*b*-P*t*BA-*b*-PEO via click reaction. In addition to using ATRP for the growth of the third block of star-like triblock copolymer, hydrophilic PEO can be grafted onto star-like P4VP-*b*-P*t*BA diblock copolymer via click reaction, suggesting the capability of tailoring surface chemistry in this star-like polymer system. To proceed the reaction, the halogen end groups (i.e., Cl and Br) on star-like P4VP-*b*-P*t*BA diblock copolymer were first transformed into azide functionalities through nucleophilic substitution reaction with NaN_3 in DMF. Successful azidation can be confirmed by the appearance of the stretching of $-N_3$ at 2112 cm^{-1} in FTIR result (**Figure 4.18 (a)**, indicating by the black arrow). Subsequently, the click reaction between star-like P4VP-*b*-P*t*BA-N_3 and alkyne-terminated PEO was performed. During the click reaction, excess amount of alkyne-terminated PEO was added into the system to ensure all the star-like P4VP-*b*-P*t*BA arms were clicked with linear PEO. The unreacted linear alkyne-terminated PEO can be removed facilely by precipitating the reaction solvent in cold methanol for

several times. The successful click reaction can be verified by GPC traces with a significant peak shift (**Figure 4.18 (b)**), signifying the effective grafting of linear PEO onto star-like P4VP-*b*-P*t*BA diblock copolymer.

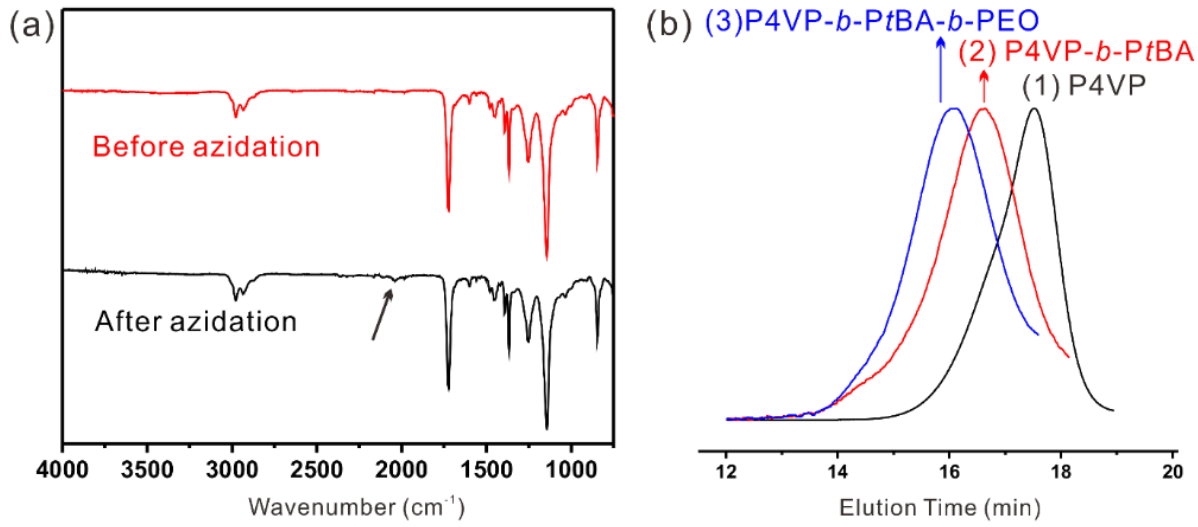

Figure 4.18 (a) FTIR spectra of star-like P4VP-*b*-P*t*BA diblock copolymer before and after azidation, i.e., P4VP-*b*-P*t*BA (red curve) and P4VP-*b*-P*t*BA-N_3 (black curve) and **(b)** GPC traces of star-like P4VP-*b*-P*t*BA-*b*-PEO triblock copolymer with (1) first P4VP block, (2) P4VP-*b*-P*t*BA diblock and (3) P4VP-*b*-P*t*BA-*b*-PEO triblock copolymer.

Dual pH-responsive star-like P4VP-*b*-PAA diblock copolymer. Both hydrophilic P4VP and PAA are weak polyelectrolytes that the degree of ionization is governed by pH and ionic strength of aqueous solution. At higher pH (basic medium), PAA chains are deprotonated and fully stretched due to the repulsion of negatively charged PAA chains, whereas at lower pH (acid medium), P4VP chains can be fully stretched due to the repulsion of positively charged P4VP chains. Moreover, the strong ionization on either P4VP or PAA block can facilitate the re-dissolution of the star-like diblock copolymer.[28] Before investigating the pH-responsive behaviors of star-like P4VP-*b*-PAA diblock copolymers, we first looked into the pH-responsive behaviors of star-like P4VP and star-like PAA homopolymer, respectively. The UV-Vis transmittance and DLS

results of star-like P4VP homopolymer (MW from GPC = 75K, blue curve in **Figure 4.4**) and star-like PAA homopolymer (MW from GPC = 290K) under different pH values in aqueous solution were obtained to indirectly characterize the associated morphological change of star-like polymer under different pH environment. Size and transmittance change of star-like P4VP homopolymer under varied pH values are shown in **Figure 4.20**. The hydrodynamic diameter of the P4VP remained a similar size at pH = 1 and 2, slightly decreased when pH increased to 3, followed by continuously increased at pH value higher than 5. The size distribution and size change at different pH values are shown in **Figure 4.20 (a)** and **Figure 4.20 (b)**, respectively. At pH ≤ 2, star-like P4VP homopolymer was fully dissolved and polymer chains were fully stretched, yielding a transparent solution (**Figure 4.19**). With increased pH, the deprotonation of the P4VP side chains and side chain aggregation toward to the core occurred, resulting in slight decrease in size (at pH=3). With further increased pH, the dispersed star-like P4VP started to form large intermolecular aggregates, leading to sharp increase of polymer size (inset in **Figure 4.20 (b)**).

In addition to the pH-dependent size change measured by DLS, the transmittance of solution containing star-like P4VP homopolymer provided a further support on the proposed morphological change under different pH environment (**Figure 4.20 (c)**). At pH > 2, the solution transmittance gradually decreased, resulting from the deprotonation of P4VP side chains and reduced electrostatic repulsion between star-like P4VP homopolymers. At pH > 3, the transmittance rapidly dropped due to the occurrence of the collapse of the deprotonated side chains and intermolecular aggregation.

On the other hand, the size and transmittance variations of star-like PAA homopolymer under various pH were also measured and summarized in **Figure 4.21**. Similar to the size change trend of star-like P4VP except that PAA dissolved better at higher pH due to the deprotonated

polymer chains, in star-like PAA homopolymer case, with decreasing pH, the polymer size first slightly reduced with partially collapsed polymer chains, followed by continuous increase in size because of intermolecular aggregation between star-like PAA homopolymers. Moreover, UV-vis measurement of star-like PAA showed consistent result with continuous increase in transmittance with increasing pH. Taken together, both star-like P4VP and star-like PAA were thus demonstrated to be pH-responsive with opposite size change under varied pH condition. Given the pH responses of star-like P4VP and PAA homopolymer, respectively, a dual pH response of star-like P4VP-*b*-PAA diblock copolymer may thus be expected.

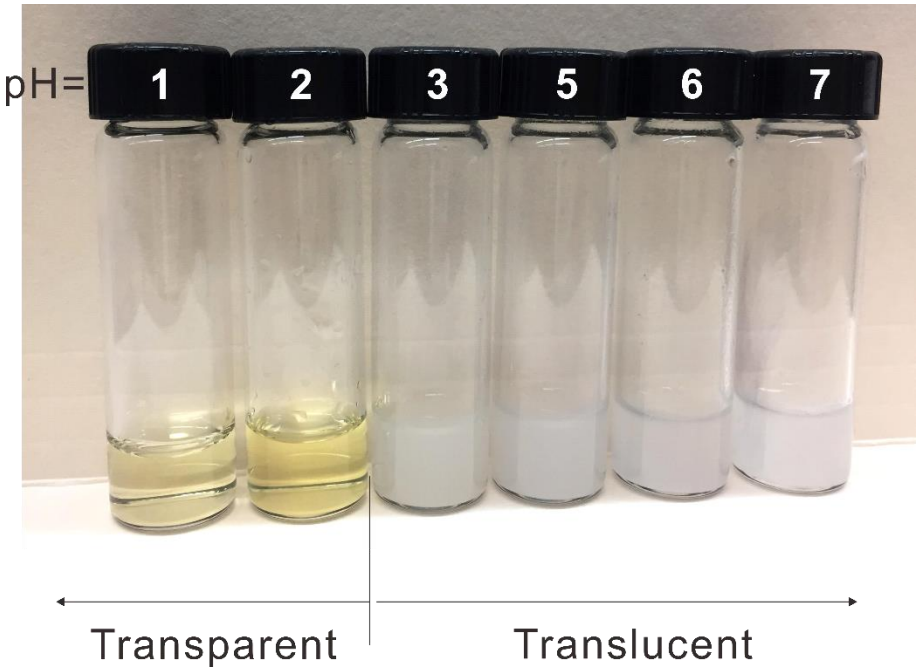

Figure 4.19 Digital image of star-like P4VP homopolymer under various pH value.

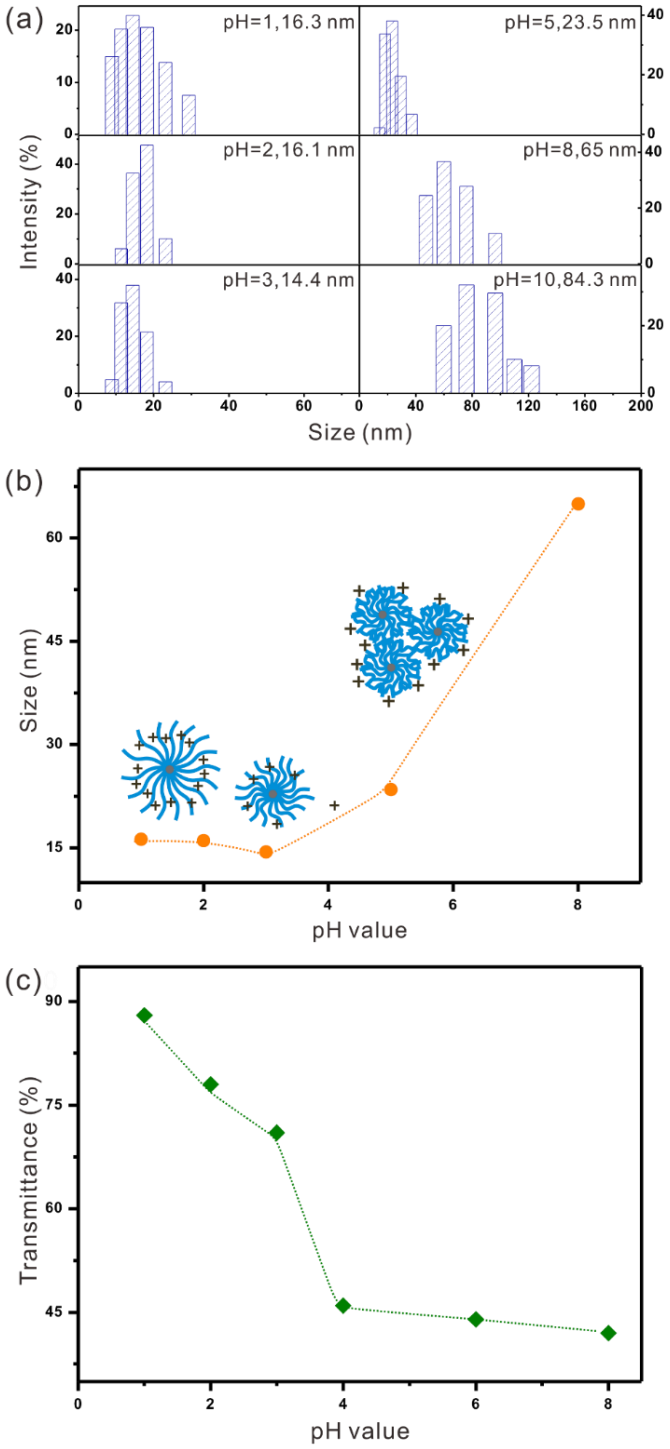

Figure 4.20 (a) Size change of star-like P4VP homopolymer at different pH value (in water) at 25 °C as measured by DLS, **(b)** the relationship between average hydrodynamic diameter of star-like P4VP homopolymer and pH value, summarized from DLS data in **(a)**, and **(c)** UV-vis transmittance at 450 nm of star-like P4VP homopolymer as a function of pH value. The inset scheme in **(b)** shows the proposed morphological change of star-like P4VP homopolymer under varied pH environment. The concentration of the sample is 1 mg/ml.

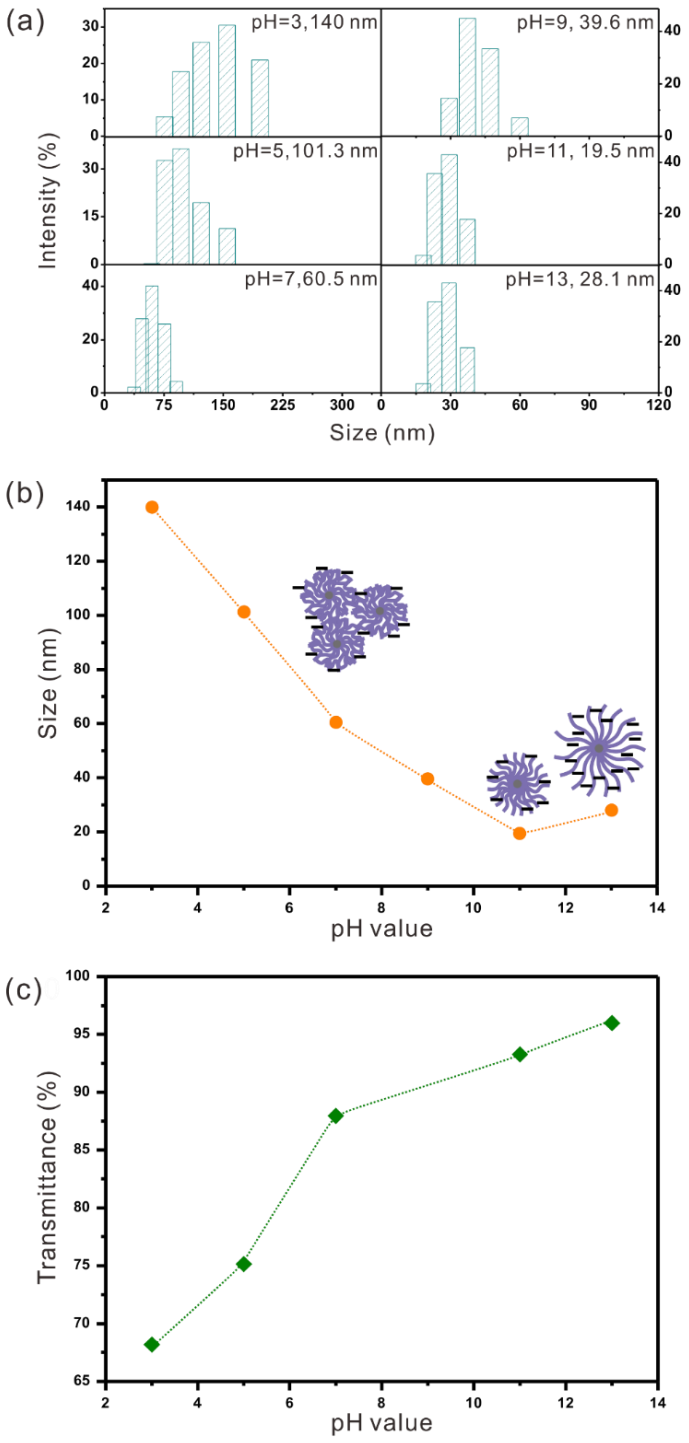

Figure 4.21 (a) Size change of star-like PAA homopolymer at different pH value (in water) at 25 ºC as measured by DLS, **(b)** the relation between average hydrodynamic diameter of star-like PAA homopolymer and pH value, summarized from DLS data in **(a),** and **(c)** UV-vis transmittance at 450 nm of star-like PAA homopolymer as a function of pH value. The inset scheme in **(b)** shows the proposed morphological change of star-like PAA homopolymer under varied pH environment. The concentration of the sample is 1 mg/ml.

To obtain star-like P4VP-*b*-PAA diblock copolymer, star-like P4VP-*b*-P*t*BA diblock copolymers with narrow PDI (sample 1 without growing third PS block; **Table 4.1**) were first dissolved in DMF, followed by raising to refluxing temperature and reacting for 4 h. *Tert*-butyl substituent of P*t*BA block can then be thermolyzed selectively and efficiently, yielding star-like P4VP-*b*-PAA diblock copolymer for pH-responsive behavior study. **Figure 4.22** depicts the size (**Figure 4.22 (a-b)**) and transmittance changes (**Figure 4.22 (c)**) of star-like P4VP-*b*-PAA diblock copolymer under different pH environment. Surprisingly, by monitoring the appearance of the solution under different pH value, we found the solutions were turbid despite dissolved in acid or basic environment, due possibly to the interference of the insolubility of the other different block in the star-like P4VP-*b*-PAA system. For instance, P4VP dissolved well in acid condition whereas PAA had low solubility in acid condition, thus still leading to slight aggregation, as confirmed by only slight increase in size. The similar behavior was observed in basic environment. Intriguingly, a continuous size increase from pH=5 to pH=8 was found with the most significant increase occurred at pH = 8 (**Figure 4.22 (b)**). We speculated that for the pH value in this range, the positively charged pyridine groups and negatively charged carboxyl groups in the star-like P4VP-*b*-PAA diblock copolymer may compensate their opposite charges that diminish the electrostatic repulsion, thereby leading to aggregation between star-like P4VP-*b*-PAA.

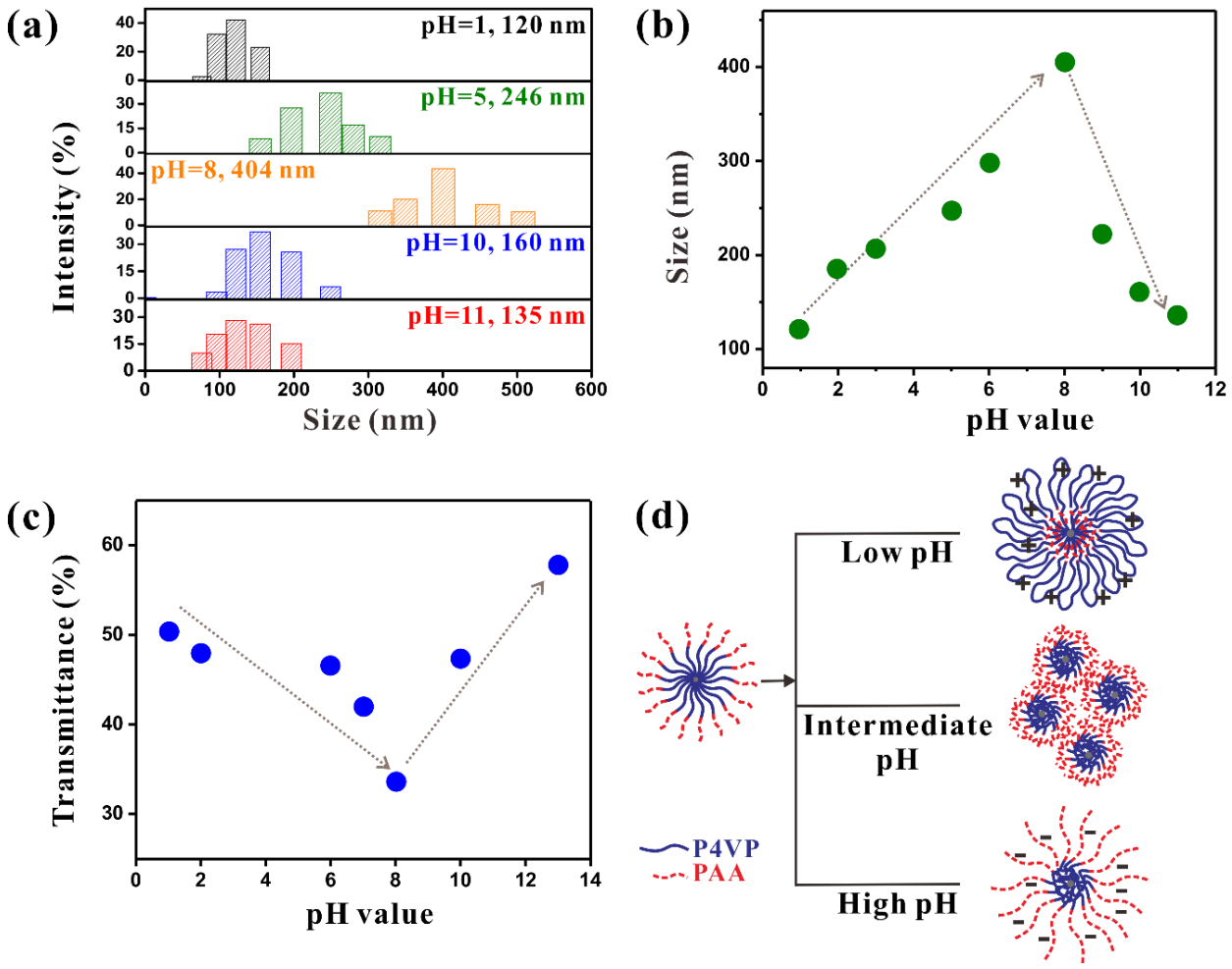

Figure 4.22 (a) Size change of double hydrophilic star-like P4VP-*b*-PAA diblock copolymer at different pH values at 25 °C as measured by DLS. **(b)** The relation between average hydrodynamic diameter of P4VP-*b*-PAA diblock copolymer and pH value, summarized from DLS data in **(a)**. **(c)** UV-vis transmittance of star-like P4VP-*b*-PAA diblock copolymer at 450 nm as a function of pH. The sample concentration is 1 mg/ml. **(d)** The proposed morphological change of star-like P4VP-*b*-PAA under various pH environment.

The possible mechanism accounting for the size change under different pH values is schematically illustrated in **Figure 4.22 (d)**. In basic environment (i.e., a good solvent for PAA block yet a poor solvent for P4VP block), the outer deprotonated PAA block could be fully stretched because of the electrostatic repulsion, whereas the inner P4VP block would be collapsed, thus resulting in stabilization of the star-like P4VP-*b*-PAA diblock copolymer to some extent. On

the other hand, under acid condition (i.e., a good solvent for P4VP block yet a poor solvent for PAA block), the shrunk PAA chains would collapse onto the core, and meanwhile the P4VP block would extend into the acidic solution, forming the inversed unimolecular micellar structure. This observation is similar to the results from previous literature.[21, 29] Again, due to the electrostatic repulsion between P4VP chains, star-like P4VP-*b*-PAA diblock copolymer could still be stabilized in acid solution. Interestingly, at the intermediate pH, because of the deprotonation of P4VP (less positively charged) and protonation of PAA (less negatively charged) as well as the charge balance between the two blocks, obvious aggregation between star-like diblock copolymer was found, representing as increased hydrodynamic size from the DLS measurements and lowered transmission in UV-vis studies. Furthermore, we note that the pH range for achieving fully-stretched P4VP block and fully-stretched PAA block (i.e., the solubility of the star-like diblock copolymer) may be readily tuned by different molar ratio between the two blocks. On the basis of the dual-pH responsive behavior discussed above, a class of double hydrophilic star-like diblock copolymers could be rationally designed, synthesized, and exploited as polymer nanocarriers, encapsulating different kinds of drugs that are released under varied pH range. For instance, drug for oral administration should be released with increased pH while the anticancer drugs should be released at decreased pH (at tumor tissues or the endosomal and lysosomal compartments of cells).

4.4 Conclusion

In summary, we developed an approach to prepare star-like triblock copolymers consisting of P4VP and P*t*BA as the first and second blocks with narrow molecular weight distribution via addition of a linear initiator during the second ATRP for the polymerization of P*t*BA block. The advantages of this approach are manifested in the tailorability of the molecular weight of each

block as well as the excellent control over the molecular weight distribution (typically lower than 1.2). The kinetics of growing the second P*t*BA block by ATRP with and without the addition of linear initiator are scrutinized. The linear relationship in both semilogarithmic kinetic plot and molecular weight vs. monomer conversion plot with the presence of linear initiator during the polymerization substantiate the suppressed termination and coupling reaction between polymer chains and the nature of living radical polymerization, respectively. The method via the deliberate introduction of linear initiator can thus resolve the coupling/termination issue during the growth of the second and third blocks with non-linear macroinitiator via ATRP, especially when pyridine-containing polymers are involved. Finally, after hydrolyzing P*t*BA block within star-like P4VP-*b*-P*t*BA diblock copolymer, the resulting star-like P4VP-*b*-PAA diblock copolymer displays an intriguing dual pH-responsive behavior, signifying its potential application as polymer nanocarriers for drug delivery. By extension, unimolecular star-like diblock or triblock copolymers composed of dissimilar stimuli-responsive blocks (e.g., pH-responsive, thermo-responsive, or photo-responsive) could also be rationally designed and synthesized via sequential ATRP from brominated cyclodextrins (i.e., α-, β-, γ-CD) as initiators. They may render a set of investigation into their appealing dual and triple stimuli-responsive properties triggered by different stimuli individually or concurrently for use in controlled delivery, sensors, nanotechnology, biotechnology, among other areas.

4.5 References

1. Matyjaszewski, K.; Tsarevsky, N. V., Nanostructured functional materials prepared by atom transfer radical polymerization. *Nature chemistry* **2009,** *1* (4), 276.
2. Bielawski, C. W.; Benitez, D.; Grubbs, R. H., An" endless" route to cyclic polymers. *Science* **2002,** *297* (5589), 2041-2044.
3. Pang, X.; He, Y.; Jung, J.; Lin, Z., 1D nanocrystals with precisely controlled dimensions, compositions, and architectures. *Science* **2016,** *353* (6305), 1268-1272.
4. Zhang, Q.; Su, L.; Collins, J.; Chen, G.; Wallis, R.; Mitchell, D. A.; Haddleton, D. M.; Becer, C. R., Dendritic cell lectin-targeting sentinel-like unimolecular glycoconjugates to release an anti-HIV drug. *Journal of the American Chemical Society* **2014,** *136* (11), 4325-4332.
5. Pang, X.; Zhao, L.; Han, W.; Xin, X.; Lin, Z., A general and robust strategy for the synthesis of nearly monodisperse colloidal nanocrystals. *Nature nanotechnology* **2013,** *8* (6), 426.
6. Li, F.; Cao, M.; Feng, Y.; Liang, R.; Fu, X.; Zhong, M., Site-Specifically Initiated Controlled/Living Branching Radical Polymerization: A Synthetic Route toward Hierarchically Branched Architectures. *Journal of the American Chemical Society* **2018,** *141* (2), 794-799.
7. Zhao, Y.; Shuai, X.; Chen, C.; Xi, F., Synthesis of star block copolymers from dendrimer initiators by combining ring-opening polymerization and atom transfer radical polymerization. *Macromolecules* **2004,** *37* (24), 8854-8862.
8. Daniel, W. F.; Burdyńska, J.; Vatankhah-Varnoosfaderani, M.; Matyjaszewski, K.; Paturej, J.; Rubinstein, M.; Dobrynin, A. V.; Sheiko, S. S., Solvent-free, supersoft and superelastic bottlebrush melts and networks. *Nature materials* **2016,** *15* (2), 183.
9. Chen, Y.; Yang, D.; Yoon, Y. J.; Pang, X.; Wang, Z.; Jung, J.; He, Y.; Harn, Y. W.; He, M.; Zhang, S., Hairy uniform permanently ligated hollow nanoparticles with precise dimension control and tunable optical properties. *Journal of the American Chemical Society* **2017,** *139* (37), 12956-12967.
10. He, Y.; Pang, X.; Jiang, B.; Feng, C.; Harn, Y. W.; Chen, Y.; Yoon, Y. J.; Pan, S.; Lu, C. H.; Chang, Y., Unconventional Route to Uniform Hollow Semiconducting Nanoparticles with Tailorable Dimensions, Compositions, Surface Chemistry, and Near-Infrared Absorption. *Angewandte Chemie* **2017,** *129* (42), 13126-13131.
11. Li, S.; Mohamed, A. I.; Pande, V.; Wang, H.; Cuthbert, J.; Pan, X.; He, H.; Wang, Z.; Viswanathan, V.; Whitacre, J. F., Single-ion homopolymer electrolytes with high transference number prepared by click chemistry and photoinduced metal-free atom-transfer radical polymerization. *ACS Energy Letters* **2017,** *3* (1), 20-27.
12. Koda, Y.; Terashima, T.; Nomura, A.; Ouchi, M.; Sawamoto, M., Fluorinated microgel-core star polymers as fluorous compartments for molecular recognition. *Macromolecules* **2011,** *44* (12), 4574-4578.
13. Terashima, T.; Kamigaito, M.; Baek, K.-Y.; Ando, T.; Sawamoto, M., Polymer catalysts from polymerization catalysts: direct encapsulation of metal catalyst into star polymer core during metal-catalyzed living radical polymerization. *Journal of the American Chemical Society* **2003,** *125* (18), 5288-5289.
14. Du, H.; Han, R.; Tang, E.; Zhou, J.; Liu, S.; Guo, X.; Wang, R., Synthesis of pH-responsive cellulose-g-P4VP by atom transfer radical polymerization in ionic liquid, loading, and controlled release of aspirin. *Journal of Polymer Research* **2018,** *25* (9), 205.
15. Matyjaszewski, K.; Miller, P. J.; Pyun, J.; Kickelbick, G.; Diamanti, S., Synthesis and characterization of star polymers with varying arm number, length, and composition from organic and hybrid inorganic/organic multifunctional initiators. *Macromolecules* **1999,** *32* (20), 6526-6535.
16. Mayadunne, R. T.; Jeffery, J.; Moad, G.; Rizzardo, E., Living free radical polymerization with reversible addition− fragmentation chain transfer (raft polymerization): Approaches to star polymers. *Macromolecules* **2003,** *36* (5), 1505-1513.

17. Matyjaszewski, K.; Patten, T. E.; Xia, J., Controlled/"living" radical polymerization. Kinetics of the homogeneous atom transfer radical polymerization of styrene. *Journal of the American Chemical Society* **1997,** *119* (4), 674-680.
18. Angot, S.; Murthy, K. S.; Taton, D.; Gnanou, Y., Scope of the copper halide/bipyridyl system associated with calixarene-based multihalides for the synthesis of well-defined polystyrene and poly (meth) acrylate stars. *Macromolecules* **2000,** *33* (20), 7261-7274.
19. Cheng, G.; Böker, A.; Zhang, M.; Krausch, G.; Müller, A. H., Amphiphilic cylindrical core− shell brushes via a "grafting from" process using ATRP. *Macromolecules* **2001,** *34* (20), 6883-6888.
20. Yin, M. J.; Yao, M.; Gao, S.; Zhang, A. P.; Tam, H. Y.; Wai, P. K. A., Rapid 3D patterning of poly (acrylic acid) ionic hydrogel for miniature pH sensors. *Advanced Materials* **2016,** *28* (7), 1394-1399.
21. Xiong, D. a.; He, Z.; An, Y.; Li, Z.; Wang, H.; Chen, X.; Shi, L., Temperature-responsive multilayered micelles formed from the complexation of PNIPAM-b-P4VP block-copolymer and PS-b-PAA core–shell micelles. *Polymer* **2008,** *49* (10), 2548-2552.
22. Li, D.; He, Q.; Cui, Y.; Li, J., Fabrication of pH-responsive nanocomposites of gold nanoparticles/poly (4-vinylpyridine). *Chemistry of materials* **2007,** *19* (3), 412-417.
23. Pang, X.; Zhao, L.; Feng, C.; Lin, Z., Novel amphiphilic multiarm, starlike coil–Rod diblock copolymers via a combination of click chemistry with living polymerization. *Macromolecules* **2011,** *44* (18), 7176-7183.
24. Yang, R.; Wang, Y.; Wang, X.; He, W.; Pan, C., Synthesis of poly (4-vinylpyridine) and block copoly (4-vinylpyridine–b-styrene) by atom transfer radical polymerization using 5, 5, 7, 12, 12, 14-hexamethyl-1, 4, 8, 11-tetraazamacrocyclotetradecane as ligand. *European polymer journal* **2003,** *39* (10), 2029-2033.
25. Liu, T.; Casado-Portilla, R.; Belmont, J.; Matyjaszewski, K., ATRP of butyl acrylates from functionalized carbon black surfaces. *Journal of Polymer Science Part A: Polymer Chemistry* **2005,** *43* (20), 4695-4709.
26. Couet, J.; Biesalski, M., Surface-initiated ATRP of N-isopropylacrylamide from initiator-modified self-assembled peptide nanotubes. *Macromolecules* **2006,** *39* (21), 7258-7268.
27. Ejaz, M.; Ohno, K.; Tsujii, Y.; Fukuda, T., Controlled grafting of a well-defined glycopolymer on a solid surface by surface-initiated atom transfer radical polymerization. *Macromolecules* **2000,** *33* (8), 2870-2874.
28. Houbenov, N.; Minko, S.; Stamm, M., Mixed polyelectrolyte brush from oppositely charged polymers for switching of surface charge and composition in aqueous environment. *Macromolecules* **2003,** *36* (16), 5897-5901.
29. Iatridi, Z.; Tsitsilianis, C., pH responsive MWCNT–star terpolymer nanohybrids. *Soft Matter* **2013,** *9* (1), 185-193.

CHAPTER 5. TAILORING ELECTROCATALYTIC ACTIVITY OF IN-SITU CRAFTED PEROVSKITE OXIDE NANOCRYSTALS VIA PRECISE SIZE AND DOPANT CONTROL

Yeu-Wei Harn *et al.* submitted to *Proceedings of the National Academy of Sciences of the United States of America*

5.1 Introduction

The slow kinetics of oxygen reduction reaction (ORR) represents one of the key challenges in fuel cells. In this context, the ability to develop highly active catalysts is vital for efficient electrochemical energy conversion and storage.[1-3] Despite superior catalytic activity and good chemical stability, noble metal (e.g., Pt and Ir) catalysts are widely viewed as unsustainable materials as they are scarce and expensive. Clearly, it is highly desirable to develop low-cost noble-metal-free alternatives with high catalytic performance. Among various non-noble metal catalysts investigated over the past decades, perovskite oxides (hereafter referred to as perovskites) with a generic chemical formula ABO_3 have been regarded as potential candidates due to their unique compositional versatility and structural stability as a rich diversity of cations for A (rare-earth or alkaline-earth metal) and B (transition metal) sites can be chosen. As such, they render fundamental exploration of the substitution effect of A and/or B sites on electronic structures and catalytic properties of perovskites.[4,5] For instance, by substituting the B site cations, ORR performance of $LaCrO_3$, $LaFeO_3$ and $LaMnO_3$ can be readily compared, and more importantly, e_g filling, which leads to change in the B-O_2 bonding strength, has been identified as a descriptor for the ORR activity.[5,6] It is noteworthy that investigation into the size effect of perovskite nanomaterials on electrocatalytic performance remains very limited, due highly likely to the

incapability of precisely tuning their sizes. Particularly, the dependence of $BaTiO_3$ nanoparticle size on ORR properties has yet to be explored.

In addition to catalytic property noted above, perovskites also possess intriguing oxygen-transport, ferroelectric, piezoelectric and dielectric characteristics.[4,7-12] Notably, all these properties depend heavily on the size, defects, and surface properties of perovskite crystals.[13-15] Thus, the ability to produce homogeneous and stoichiometric perovskites with controlled size and shape enables the study of their dimension-dependent properties for designing perovskite nanomaterials and devices with desired functionalities. Conventionally, perovskites are yielded by solid-state reaction.[16] For instance, bulk $BaTiO_3$ are often synthesized at high temperature (> 1000°C) by calcinating a mixture of TiO_2 and $BaCO_3$ powders. Yet, such a high-reaction-temperature approach has limited control over size and shape of $BaTiO_3$ (i.e., forming large crystalline grains with a wide range of size). To this end, several wet chemistry methods (e.g., co-precipitation process,[17] pyrolysis,[18] sol-gel,[19] hydrothermal[20] and metal-organic decomposition[21-23]) conducted at much lower temperature have been employed to offer better control over composition and homogeneity of perovskites particles.[16,21-23] Notably, some approaches noted above require strong alkaline condition and yield relatively large, nonuniform particle sizes (several hundred nm);[20] and the others produce finer particle size (a few tens of nm),[19] yet the size of $BaTiO_3$ nanoparticles cannot be easily tailored.[23] As a result, the understanding on size-dependent properties remains comparatively elusive.

Herein, we develop a robust amphiphilic star-like block copolymer nanoreactor strategy for crafting a set of monodisperse $BaTiO_3$ and La- and Co-doped $BaTiO_3$ NPs and scrutinize, *for the first time*, their size- and dopant-dependent ORR activities. A series of amphiphilic star-like poly(acrylic acid)-*block*-polystyrene (denoted PAA-*b*-PS) diblock copolymers with varied

molecular weight of each block are synthesized by atom transfer radical polymerization (i.e., a living polymerization technique that affords the synthesis of polymer with well-defined molecular weight and low polydispersity). They are then employed as nanoreactors to guide *in-situ* growth of perovskite NPs via strong coordination between the bimetallic precursors and the carboxylic acid groups of inner PAA blocks of star-like PAA-*b*-PS at relatively low temperature (100 ^{o}C). Interestingly, the study of NP growth kinetics manifests that NPs are clearly templated by star-like PAA-*b*-PS diblock copolymer. Notably, star-like PAA-*b*-PS nanoreactors also render the synthesis of uniform $PbTiO_3$ NPs with different sizes, as well as La- and Co-doped $BaTiO_3$ NPs in which La and Co are chosen as dopants, demonstrating the effectiveness of nanoreactor in yielding NPs with tunable compositions. Subsequently, by dispersing pristine and doped $BaTiO_3$ NPs on reduced graphene oxide (rGO) as electrocatalysts, the correlations between the NP size and ORR activity, as well as between the dopant type (La and Co) and concentration ($\leq$ 10 mol%) and ORR performance, are elucidated. Quite intriguingly, the ORR activities progressively weaken as the size of $BaTiO_3$ NP increases. Moreover, La- and Co-doped $BaTiO_3$ NPs carry a significantly improved ORR performance over the pristine counterpart. Our first-principles calculations density functional theory (DFT) reveals that such enhanced ORR properties of doped $BaTiO_3$ NPs can be attributed to reduced free energy barrier of ORR reaction because of the enhanced adsorption energy of intermediates and increased conductivity due to the modification of the electronic structure. By extension, amphiphilic star-like block copolymer nanoreactor strategy may enable the crafting of a large variety of other functional nanomaterials with tailored sizes and compositions, including metal chalcogenides, carbides, phosphates and nitrides. As such, they may open up new avenues for judicious design of high-activity electrocatalysts for ORR, oxygen

evolution reaction (OER), and concurrent ORR/OER for advanced energy conversion and storage devices (e.g., rechargeable metal-air batteries and regenerative fuel cells).

5.2 Experiment Details

The detailed synthetic processes of star-like PAA-*b*-PS diblock copolymer nanoreactor as well as perovskite and doped perovskite oxide nanoparticles ($BaTiO_3$, $PbTiO_3$ and La-doped, Co-doped $BaTiO_3$ nanoparticles) have been described in Chapter 3, *3.1* and *3.2*, respectively. Below we just specified the procedure for preparing annealed composite of $BaTiO_3$ nanoparticles and reduced graphene oxide (rGO).

5.2.1 Annealing of composites consisting of $BaTiO_3$ NPs and reduced graphene oxide

Graphene oxide was first prepared by Hummer's method and stored in DMF, forming well-dispersed graphene oxide DMF solution. After perovskite $BaTiO_3$ NPs were synthesized, purified, and stored in toluene solution, graphene DMF solution was added at a 1:1 weight ratio of as-synthesized perovskite NPs to graphene oxide. Sonication and stirring of the solution for more than one day were conducted to ensure good dispersion of as-synthesized NPs on graphene. Then the whole solution was dried out by rotary evaporator and the composite in powder form was obtained. Finally, the powder was placed in furnace tube and ready to be annealed. Prior to raise the temperature, purging the tube with N_2 for more than 30 min is required to ensure the N_2 atmosphere during annealing. Temperature was raised to 600 ^oC for 2 h at a heating rate of 3^o/min. The furnace was opened, and the product was retrieved after the furnace was cooled down to room temperature naturally. The graphene oxide in the composite was believed to be partially reduced into reduced graphene oxide after high-temperature-annealing treatment.

On the other hand, the annealing of composites consisting of $PbTiO_3$ NPs and graphene oxide was also conducted. In this case, the impurity peaks (possibly from single oxide) cannot be completely removed after the annealing condition used. Therefore, we decided to focus on $BaTiO_3$ NPs for the following doping and electrocatalytic property investigations.

Likewise, La- and Co-doped $BaTiO_3$ NPs were also deposited on graphene oxide and undergone the same treatments as discussed above. To further improve both ORR and OER performance by introducing oxygen vacancies into the sample (i.e., Co-doped $BaTiO_3$ NPs), after annealing at 600 ^oC in N_2 for 2 h to ensure good crystallinity, the samples were then reduced at 350 ^oC with forming gas of 5% H_2 in N_2 for 3 h.

5.2.2 Characterization

Molecular weights of polymers were measured by gel permeation chromatography (GPC), equipped with an Agilent1100 with a G1310A pump, a G1362A refractive detector and a G1314A variable wavelength detector. THF was used as the eluent at 1.0 ml/min at 35 °C. One 5 μm LP gel column (500 Å, molecular range: 500-2 $\times 10^4$ g/ mol) and two 5 μm LP gel mixed bed columns (molecular range: 200-3 $\times 10^6$ g/ mol) were calibrated using PS standard samples. Proton nuclear magnetic resonance (^{1}H NMR) measurements were conducted on Varian VXR-300 spectroscope with the solvent resonances as the internal standard. Deuterated chloroform was used as the solvent for NMR measurement. The morphologies and the size distribution of perovskite NPs were characterized by transmission electron microscopy (TEM) (JOEL TEM 100CX; operated at 100 kV) and HRTEM (zzJEOL 4000EX TEM, operated at 300 kV). Atomic structure, lattice constant and energy dispersive X-Ray spectroscopy analysis (EDX) were examined by HRTEM (zzJEOL 4000EX TEM, operated at 300 kV). TEM samples were prepared by applying several drops of

diluted solution (with toluene as solvent) onto a carbon-coated copper TEM grid (300 mesh) and allowing the solvent to evaporate under ambient condition. Size distribution of diblock copolymer nanoreactors was acquired by laser light-scattering spectrometer (DLS, Wyatt DyanoPro). The synthesized NPs were annealed in furnace at 600 °C for 2 h to improve the crystallinity. The crystalline structures of perovskite NPs were measured by X-ray powder diffraction (XRD, Pananlytic XPert PRO Alpha-1 XRD, Cu Kα radiation (λ = 0.154 nm)). Raman studies were performed using the 785 nm exciting line of a Nd:YAG laser (Renishaw, U.K.). The identification of chemical states for the elements in the pristine and doped perovskite NPs was obtained by X-ray photoelectron spectroscopy (XPS, Thermo K-alpha XPS).

5.3 Results and Discussion

Figure 5.1 (a) depicts the synthetic procedure towards monodisperse perovskite NP via capitalizing on amphiphilic star-like PAA-*b*-PS diblock copolymer as nanoreactor (see *Experimental Section* in *Supplementary Information*). First, the esterification of 21 hydroxyl groups (-OH) on β-cyclodextrin (β-CD) with 2-bromoisobytyryl bromide yields heptakis[2,3,6-tri-O-(2-bromo-2-methylpropionyl]-ß-cyclodextrin) (denoted 21Br-ß-CD; upper second panel, **Figure 5.1 (a)**). By employing 21-Br-β-CD as a macroinitiator and performing sequential atom transfer radical polymerization (ATRP) of *tert*-butyl acrylate (*t*BA) and styrene, respectively (upper third and fourth panels; **Figure 5.1 (a)**), star-like poly(*tert*-butyl acrylate)-*block*-polystyrene (P*t*BA-*b*-PS) diblock copolymers with well-defined molecular weight of each block are thus synthesized because of living free radical polymerization characteristic of ATRP.[24,25] The hydrolysis is then conducted to convert P*t*BA blocks into poly(acrylic acid) (PAA; lower right panel, **Figure 5.1 (a)**) by using trifluoroacetic acid (TFA), yielding star-like PAA-*b*-PS diblock copolymers.

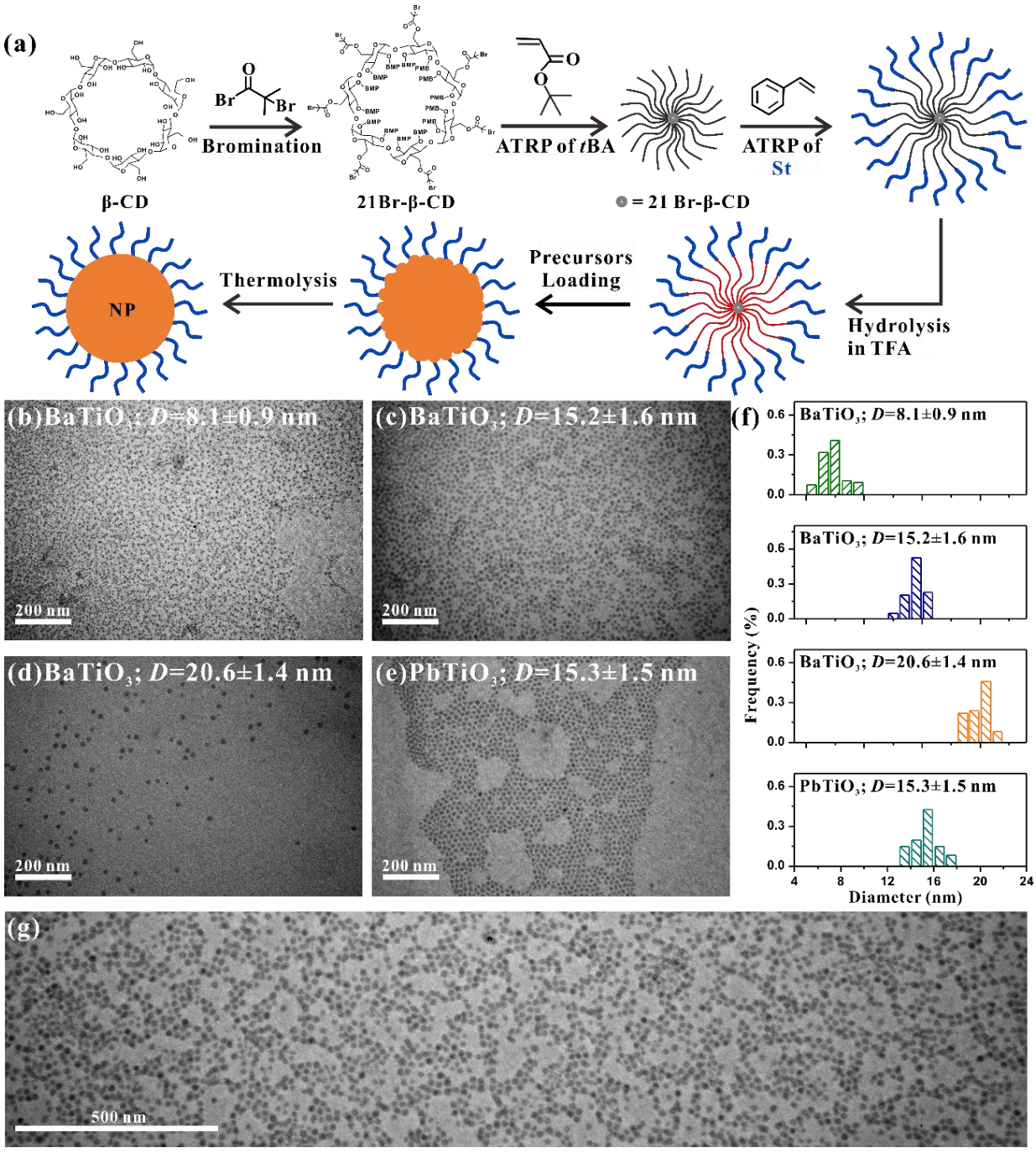

Figure 5.1 (a) Stepwise representation of synthesis of perovskite NPs by capitalizing on star-like PAA-*b*-PS diblock copolymer as nanoreactor. **(b-e)** Representative TEM images of monodispersed PS-ligated perovskite NPs (i.e., $BaTiO_3$ and $PbTiO_3$) with diameters of **(b)** 8.1 nm **(c)** 15.2 nm, **(d)** 20.6 nm, and **(e)** 15.3 nm, yielded by utilizing respective star-like PAA-*b*-PS nanoreactors (i.e., Samples 1-3 in **Table 5.1**). **(f)** Statistics of size distribution of as-synthesized NPs. **(g)** A large-area TEM image of monodispersed $BaTiO_3$ NPs (D = 15.2 nm) synthesized using Sample 2 as nanoreactor (**Table 5.1**).

Table 5.1 Summary of star-like P*t*BA (and PAA) homopolymers, star-like P*t*BA-*b*-PS diblock copolymers and the $BaTiO_3$ nanoparticle (NP) sizes synthesized by using the corresponding star-like PAA-*b*-PS diblock copolymers as nanoreactors

Sample #	$M_{n,\ GPC}$ of star-like P*t*BA (PAA) block[a]	$M_{n,\ NMR}$ of P*t*BA block[b]	$M_{n,\ GPC}$ of star-like P*t*BA-*b*-PS diblock copolymer[c]	$M_{n,\ NMR}$ of PS block[d]	Size of PS-ligated $BaTiO_3$ NPs[e]
Sample 1	95K (53K)	5,500	281K	4,500	8.1 ± 0.9 nm
Sample 2	160K (90K)	5,900	340K	4,440	15.2 ± 1.6 nm
Sample 3	216K (122K)	6,300	400K	4,480	20.6 ± 1.4 nm

Notes: [a] Number-average molecular weight, $M_{n,\ GPC}$ of star-like P*t*BA homopolymer determined by GPC, calibrated by PS standards. The $M_{n,\ GPC}$ of star-like PAA calculated by multiply the molecular weight ratio between *t*BA monomer and AA monomer. [b] M_n of each P*t*BA arm calculated from ^{1}H NMR data (**Figure S2**) based on the following equation:

$$M_{n,\ PtBA} = \frac{A_b/9}{A_a/6} \times 128.17$$

where A_b and A_a are the integral area of the methyl protons in *tert*-butyl group of P*t*BA chains and the integral area of methyl protons at the α-end of P*t*BA chains, respectively, and 128.17 is the molecular weight of the *t*BA monomer. [c] Number-average molecular weight, $M_{n,\ GPC}$ of star-like P*t*BA-*b*-PS diblock copolymer determined by GPC. [d] M_n of each PS arm calculated from ^{1}H NMR data (**Figure S3**) based on the following equation:

$$M_{n,\ PS} = \frac{A_g/5}{A_a/6} \times 104.15$$

where A_g and A_a are the integral area of phenyl protons on the PS block and the integral area of methyl protons at the α-end of the diblock arm, respectively, and 104.15 is the molecular weight of St monomer. [e] The size of NPs is statistically averaged over with 100 NPs in a TEM image by using *ImageJ* software.

Three star-like PAA-*b*-PS diblock copolymers were successfully synthesized (see *Experimental Section*). The detailed characterizations on each step of reaction are shown in **Figures 5.2-5.6**. The as-synthesized star-like PAA-*b*-PS diblock copolymers were then employed as nanoreactors for crafting perovskite NPs intimately ligated by outer PS blocks (lower central

and left panels, **Figure 5.1 (a)**), including $BaTiO_3$, $PbTiO_3$, and doped $BaTiO_3$ NPs as sequentially discussed below (see *Experimental Section* for more details). Notably, single bimetallic alkoxide was chosen as precursor for perovskite NP synthesis as it can simultaneously ensure the hydrolysis and correct stoichiometry of the final product.[23] For synthesis of $BaTiO_3$ NP, the metal moieties of precursors (i.e., $BaTi(O_2CC_7H_{15})[OCH(CH_3)_2]_5$) were selectively and strongly coordinated with the functional groups (-COOH) of PAA blocks (lower central panel; **Figure 5.1 (a)**), eventually leading to the formation of perovskite NP within the compartment occupied by PAA blocks via thermolysis (lower left panel; **Figure 5.1 (a)**). Particularly, as noted above, the surface of as-synthesized perovskite NP was intimately capped by the outer PS blocks (i.e., forming PS-ligated NP) as the outer PS chains were originally covalently bonded to the inner PAA chains, thereby preventing NPs from aggregation and facilitating their solubility in various organic solvents. It is notable that the diameter of as-synthesized $BaTiO_3$ NPs can be easily altered by capitalizing on star-like PAA-*b*-PS diblock copolymers with different molecular weights of the inner PAA blocks at nearly same molecular weight of the outer PS blocks. **Tables 5.1**-**5.2** summarize the molecular weight of each block and the average diameter of the resulting NPs template-grown using the respective PAA-*b*-PS diblock copolymer nanoreactors.

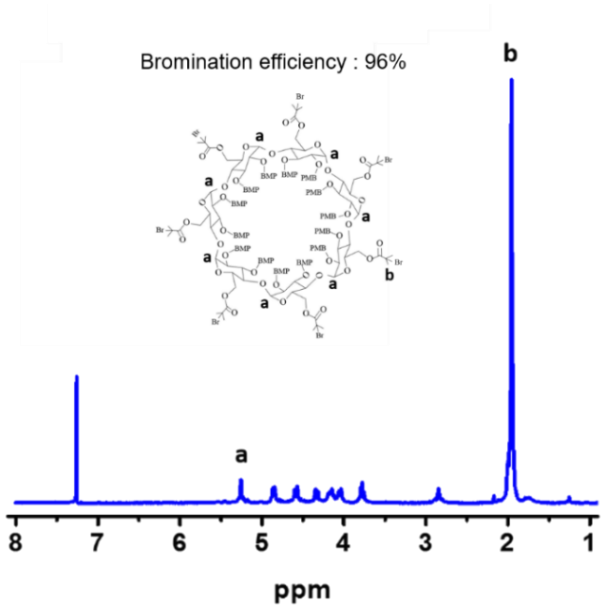

Figure 5.2 ^{1}H-NMR spectrum of brominated β-cyclodextrin (denoted 21 Br-β-CD) macroinitiator, with $CDCl_3$ used as solvent.

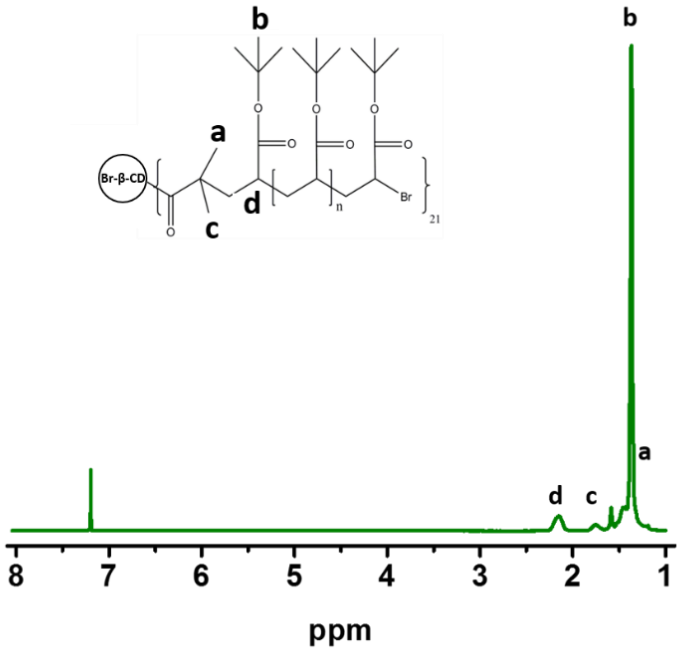

Figure 5.3 ^{1}H-NMR spectrum of star-like poly(*tert*-butyl acrylate) (P*t*BA), with $CDCl_3$ used as solvent.

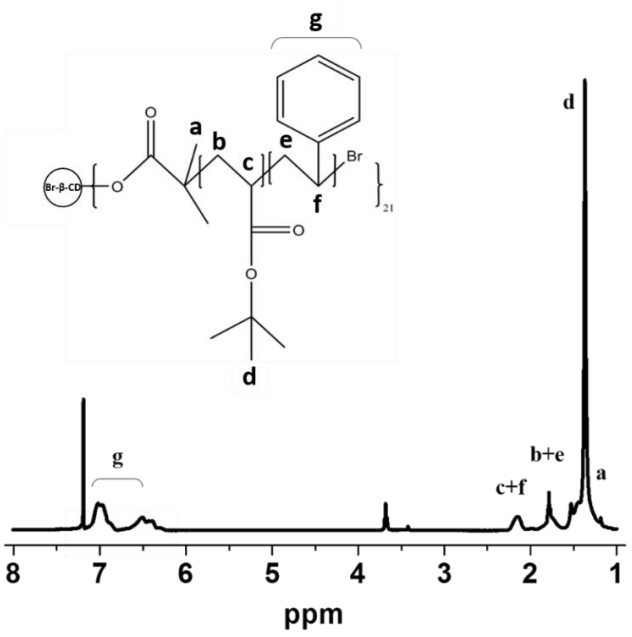

Figure 5.4 ^{1}H-NMR spectrum of star-like poly(*tert*-butyl acrylate)-*block*-polystyrene (denoted P*t*BA-*b*-PS), with $CDCl_3$ used as solvent.

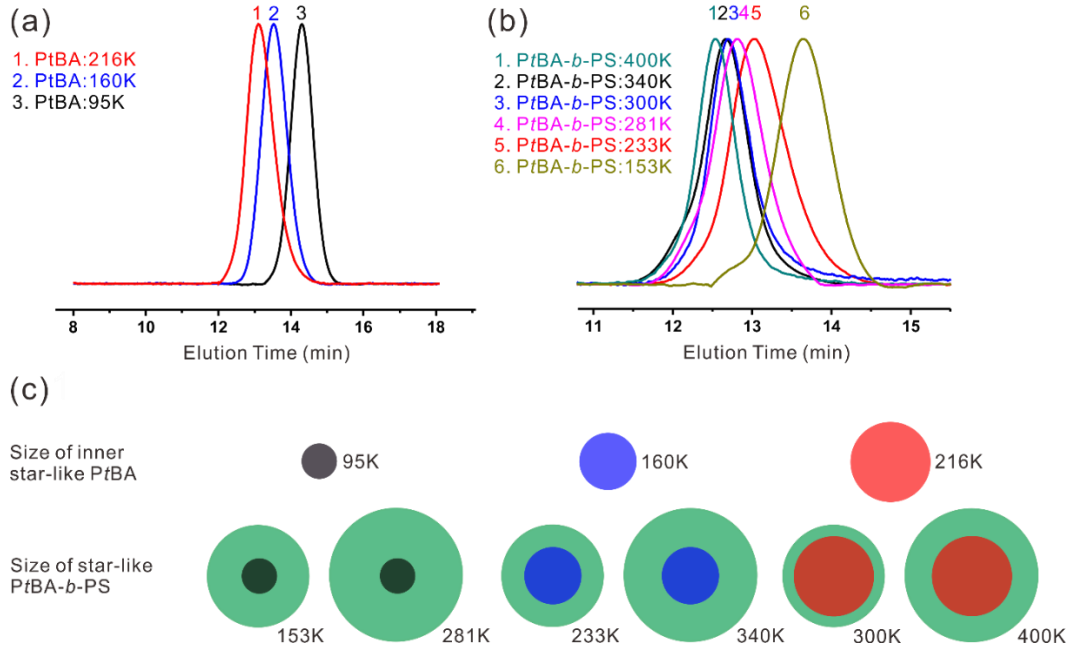

Figure 5.5 (a) GPC traces of three star-like P*t*BA homopolymers. **(b)** GPC traces of six star-like P*t*BA-*b*-PS diblock copolymers. **(c)** Schematic of six star-like P*t*BA-*b*-PS diblock copolymers with varied molecular weights of inner P*t*BA block (MW= 95K, 160K and 216K), representing the possible dimension of each star-like P*t*BA-*b*-PS diblock copolymer based on the molecular weight of star-like P*t*BA block and total molecular weight of star-like P*t*BA-*b*-PS shown in **(a)** and **(b)**.

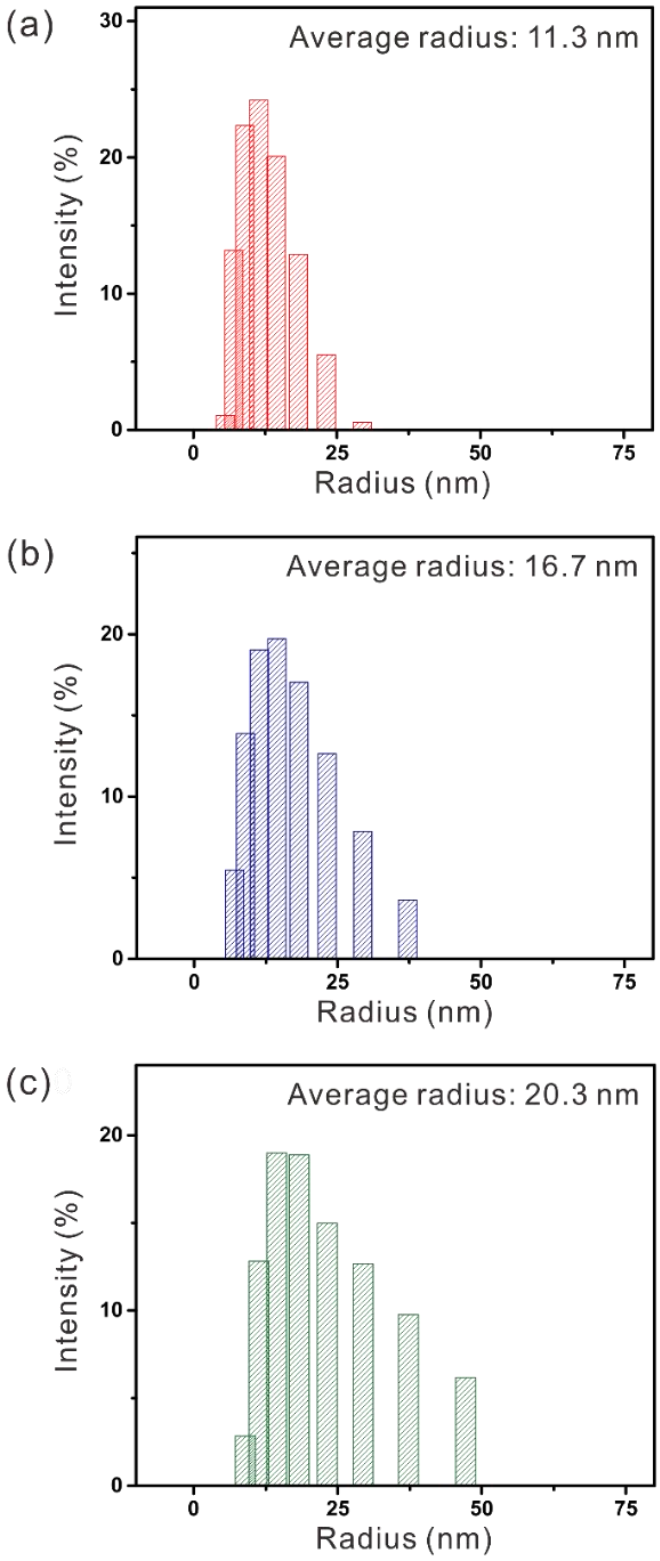

Figure 5.6 Hydrodynamic radii for star-like PAA-*b*-PS diblock copolymer nanoreactors with different molecular weights in diphenyl ether (DPE).

Table 5.2 Summary of star-like P*t*BA (and PAA) homopolymers and the size of $BaTiO_3$ and $PbTiO_3$ nanoparticle (NP) synthesized using the corresponding star-like PAA-*b*-PS as nanoreactors

Sample #	MW of P*t*BA[a]	MW of PAA[b]	Size of $BaTiO_3$ (nm)[c]	Size of $PbTiO_3$ (nm)[d]
Sample 1	95K	50.6K	8.1	8.0
Sample 2	160K	90K	15.2	15.3
Sample 3	216K	122K	20.6	20.7

[a] Number-average molecular weight, $M_{n,\,GPC}$ of star-like P*t*BA homopolymer determined by GPC and [b] the corresponding molecular weight of PAA after hydrolysis. [c] and [d] are the average size of the $BaTiO_3$, and $PbTiO_3$ NPs synthesized using the corresponding star-like PAA-*b*-PS nanoreactors, calculated by *ImageJ* software by averaging over 100 nanoparticles in a TEM image.

Figure 5.1 (b-d) show representative transmission electron microscope (TEM) images of three different-sized PS-ligated $BaTiO_3$ NPs synthesized by employing three respective star-like PAA-*b*-PS diblock copolymers as nanoreactors (i.e., Samples 1-3 in **Table 5.1**). Their average diameters are 8.1 ± 0.9 nm (**Figure 5.1 (b)**; from Sample 1 nanoreactor), 15.2 ± 1.6 nm (**Figure 5.1 (c)**, from Sample 2 nanoreactor) and 20.6 ± 1.4 nm (**Figure 5.1 (d)**, from Sample 3 nanoreactor). The statistics of the NP size distribution are shown in **Figure 5.1 (f)**, suggesting these NPs are uniform. All PS-ligated $BaTiO_3$ NPs can be well-dispersed in good solvents of PS and easily purified (**Figure 5.1 (g)** and **Figures 5.7-5.10**; see *Experimental Section* for more details). Remarkably, all the TEM images shown are free of NP aggregation and impurities, signifying great feasibility and reproducibility of the nanoreactor approach.

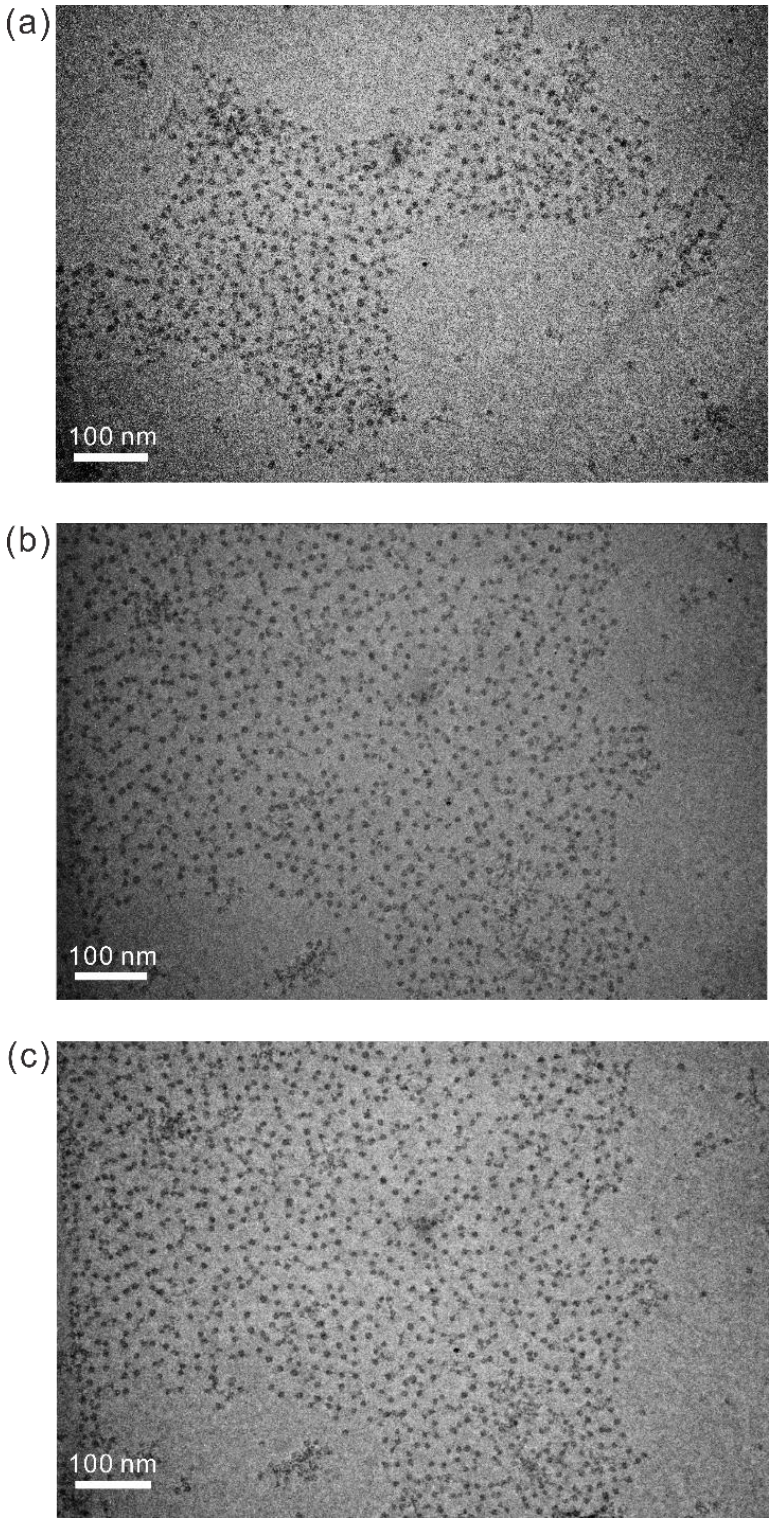

Figure 5.7 Representative TEM images of uniform PS-ligated $BaTiO_3$ nanoparticles with an average diameter of 8.1 nm obtained by utilizing star-like PAA-*b*-PS diblock copolymer (Sample 1 in **Table 5.1**) as nanoreactor.

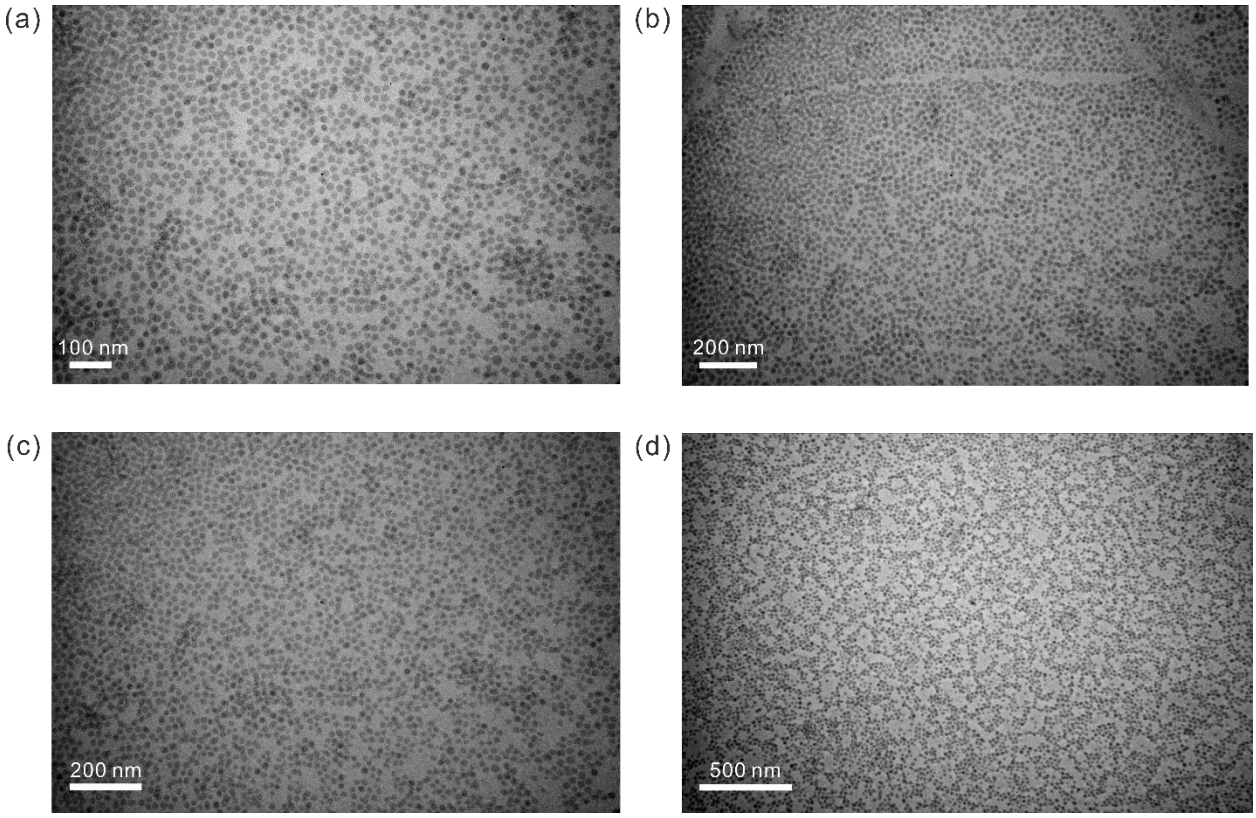

Figure 5.8 Representative TEM images of uniform PS-ligated $BaTiO_3$ nanoparticles with an average diameter of 15.2 nm under different magnifications. They were obtained by utilizing star-like PAA-*b*-PS diblock copolymer (Sample 2 in **Table 5.1**) as nanoreactor.

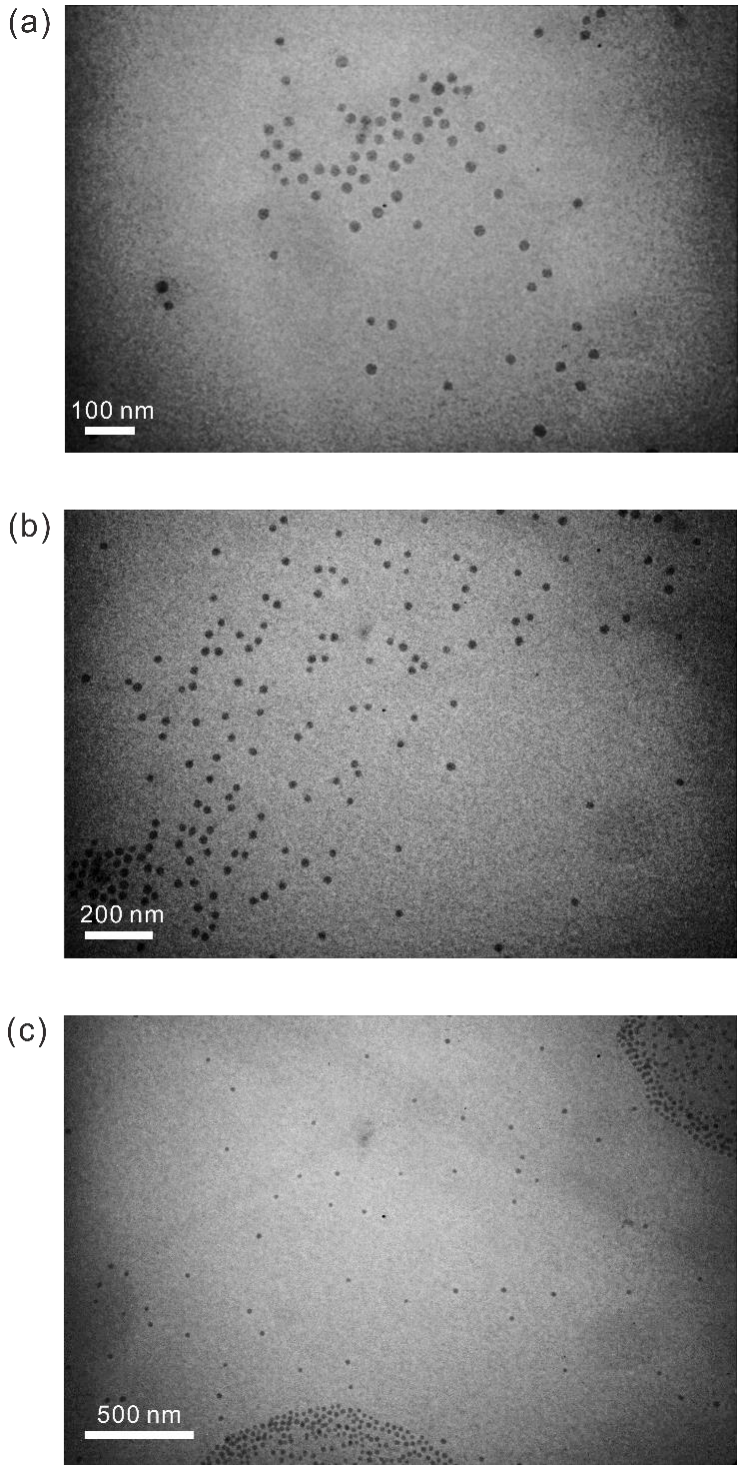

Figure 5.9 Representative TEM images of uniform PS-ligated $BaTiO_3$ nanoparticles with an average diameter of 20.6 nm under different magnifications. They were obtained by utilizing star-like PAA-*b*-PS diblock copolymer (Sample 3 in **Table 5.1**) as nanoreactor.

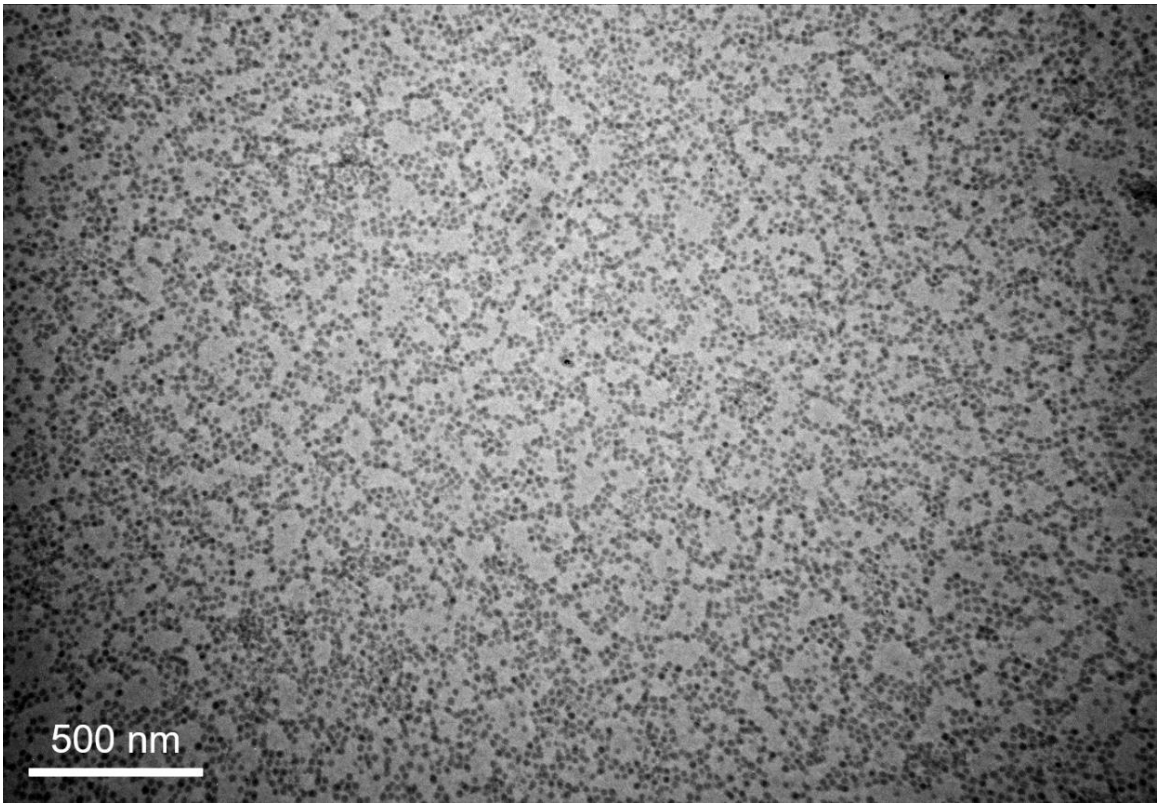

Figure 5.10 Close-up TEM image of monodispersed PS-ligated $BaTiO_3$ nanoparticles (D = 15.2 nm) synthesized using star-like PAA-*b*-PS diblock copolymer (Sample 2 in **Table 5.1)** as nanoreactor.

It is interesting to note that the growth of $BaTiO_3$ NP within inner hydrophilic PAA blocks of star-like PAA-*b*-PS nanoreactor was monitored by ex-situ TEM study at different reaction times (**Figure 5.11**). Shortly after the bimetallic precursors were added into the solution, no obvious structures were observed (**Figure 5.11 (a)**). Clear NPs of with an average size of 5.9 nm can be seen after a short reaction time (3 min, **Figure 5.11 (b)**), indicating a fast reaction speed to synthesize perovskite NPs with this approach. Intriguingly, as reaction time increased from 5 min (10.3 nm, **Figure 5.11 (c)**) to 30 min (14.5 nm, **Figure 5.11 (d)**), as-formed NPs were progressively grown and the NP sizes maintained uniform, as corroborated by low variation in the statistics of size distribution of NPs. When the average NP size reached 15 nm, their growth

virtually finished, as shown in **Figure 5.11 (e-f)**, where the NP size remained unchanged with the prolonged reaction time (from 200 min to 1020 min). This is likely because the inner PAA compartment of star-like PAA-*b*-PS nanoreactor was fully taken up and the continuous growth of NP was restricted by the outer hydrophobic PS blocks. Notably, the formed NPs can be well-dispersed in the solution even when the reaction time was prolonged to 1020 min (**Figure 5.11 (e)**), further confirming the effectiveness of the presence of outer PS blocks on the surface of NPs in stabilizing the NPs in common organic solvents (e.g., toluene) without aggregation.

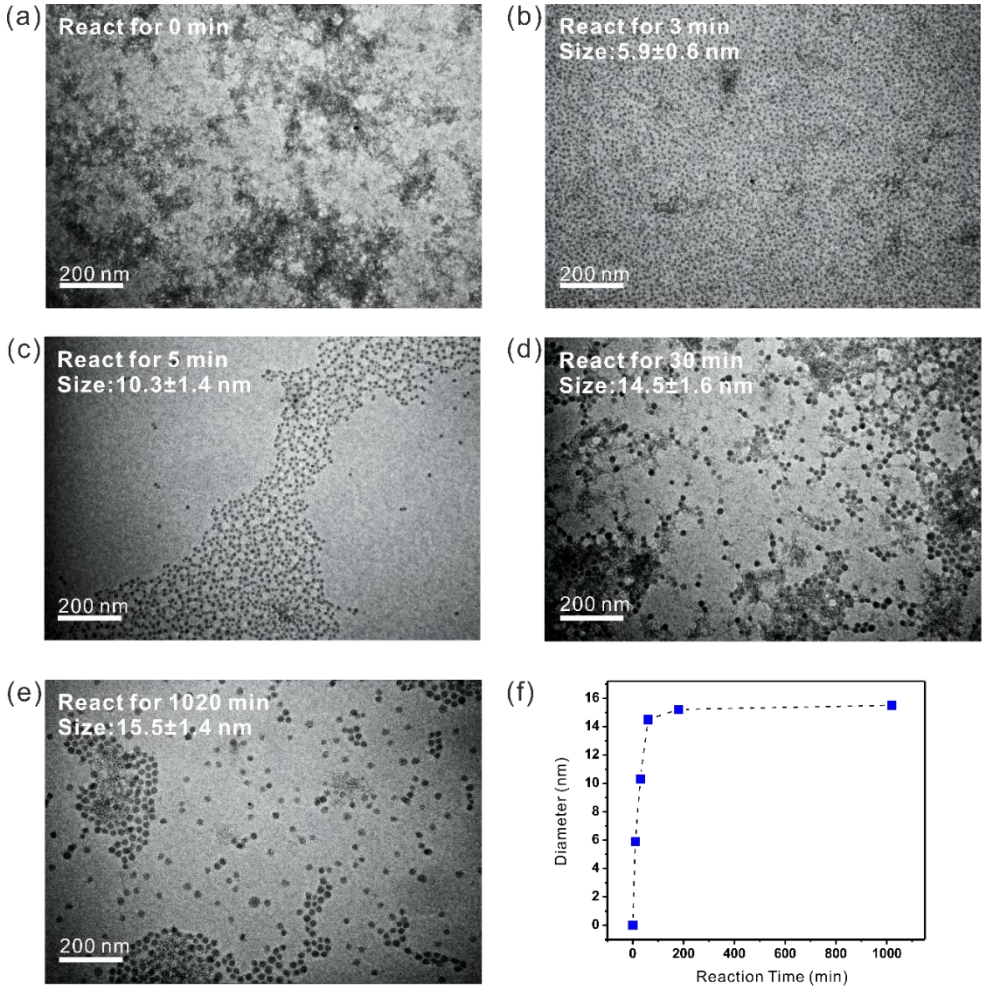

Figure 5.11 (a-e) TEM images of PS-ligated $BaTiO_3$ nanoparticles synthesized by employing star-like PAA-*b*-PS diblock copolymer (**Sample 2** in **Table S1**) as nanoreactor at different reaction times. **(a)** 0 min **(b)** 3 min **(c)** 5 min **(d)** 30 min and **(e)** 1020 min. **(f)** Plot of the relation between the diameter of as-synthesized $BaTiO_3$ nanoparticles and reaction time.

Furthermore, in order to verify that the formation of $BaTiO_3$ NPs was indeed structure-directed by the inner PAA blocks of star-like PAA-*b*-PS, control experiments were conducted for several times under the same experimental conditions except no star-like nanoreactors were introduced into the system (**Figure 5.12**). Clearly, most of the products had matrix-like structures (**Figure 5.12 (a)**), possibly resulting from the unreacted precursors or the aggregated products due to lack of surface ligands. Big aggregates with irregular size of a few hundred of nanometers can also be found (**Figure 5.12 (b)**). Thus, control experiment further substantiated the key importance of star-like diblock copolymers in directing the growth and stabilizing the resulting NPs without aggregation.

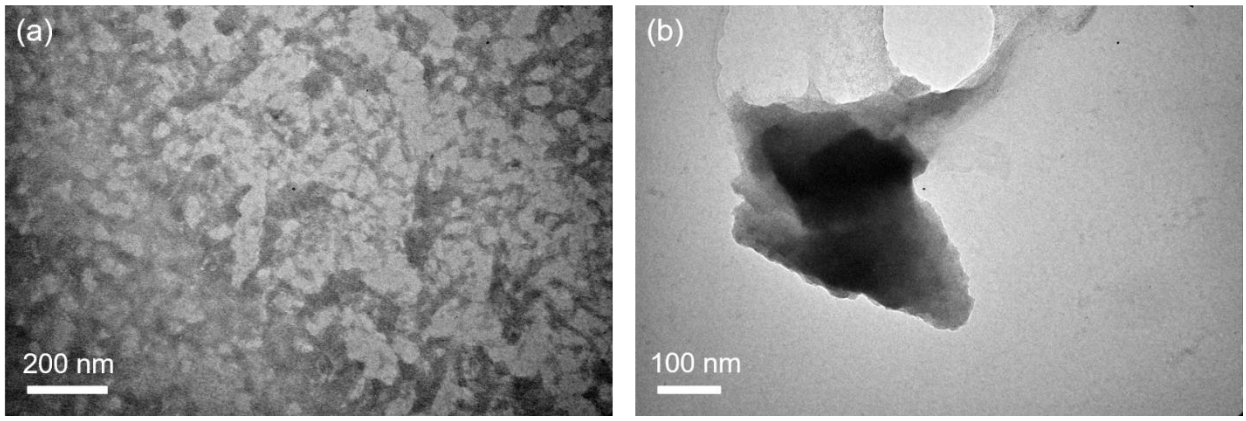

Figure 5.12 TEM images of the control sample, that is, $BaTiO_3$ synthesized under the same experimental condition yet without adding star-like diblock copolymer nanoreactor.

It is worth noting that in addition to $BaTiO_3$ NPs, the star-like diblock copolymer nanoreactor strategy is versatile in yielding other perovskite NPs. To this end, PS-ligated $PbTiO_3$ NPs were synthesized using star-like PAA-*b*-PS as nanoreactor and lead titanium isopropoxide [$PbTi(OCH(CH_3)_2)_6$] as precursor (a bimetallic alkoxide as well). Notably, the sizes of $PbTiO_3$ NPs were nearly identical to that of $BaTiO_3$ NPs synthesized using the same series of nanoreactors

(**Table 5.2**; **Figure 5.13-5.14**). TEM images of the as-synthesized $PbTiO_3$ NPs of three different sizes show they are well-dispersed and uniform without any aggregation or impurities after simple purification (**Figure 5.14 (a, c, e)**), where the corresponding statistics of size distribution are depicted in **Figure 5.14 (b, d, f)**. Furthermore, a representative TEM image of PS-ligated $PbTiO_3$ NPs with an average diameter of 15.3 ± 1.5 nm, synthesized by employing Sample 2 as nanoreactor, is shown in **Figure 5.1 (e-f)**.

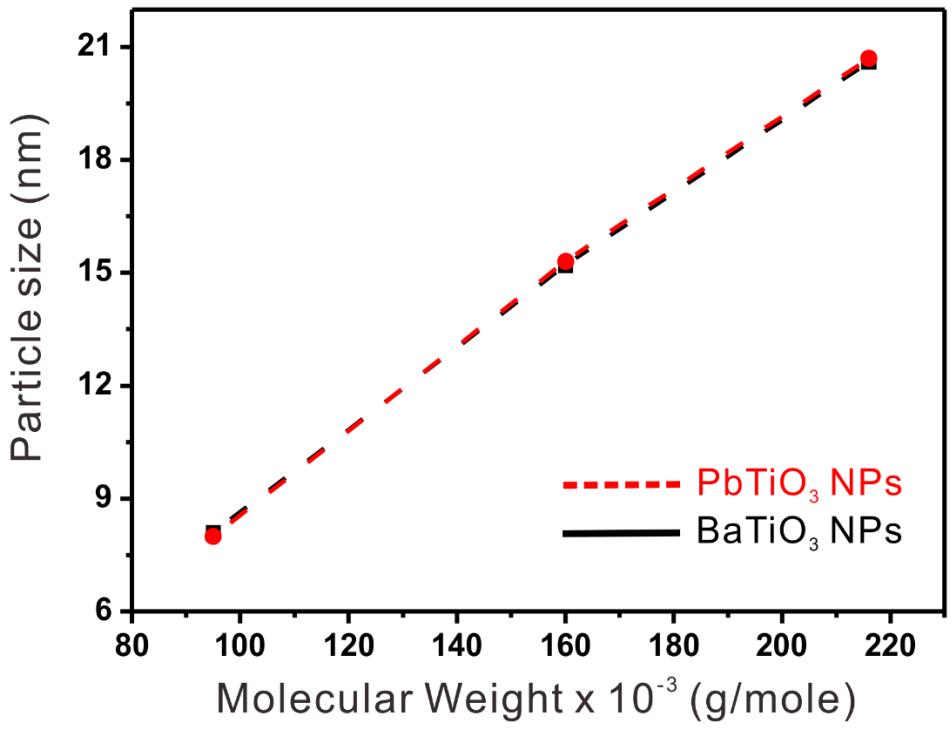

Figure 5.13 Plot of the correlation between as-synthesized $BaTiO_3$ nanoparticle size and molecular weights of the inner P*t*BA block of nanoreactors that were used as nanoreactor for nanoparticle synthesis.

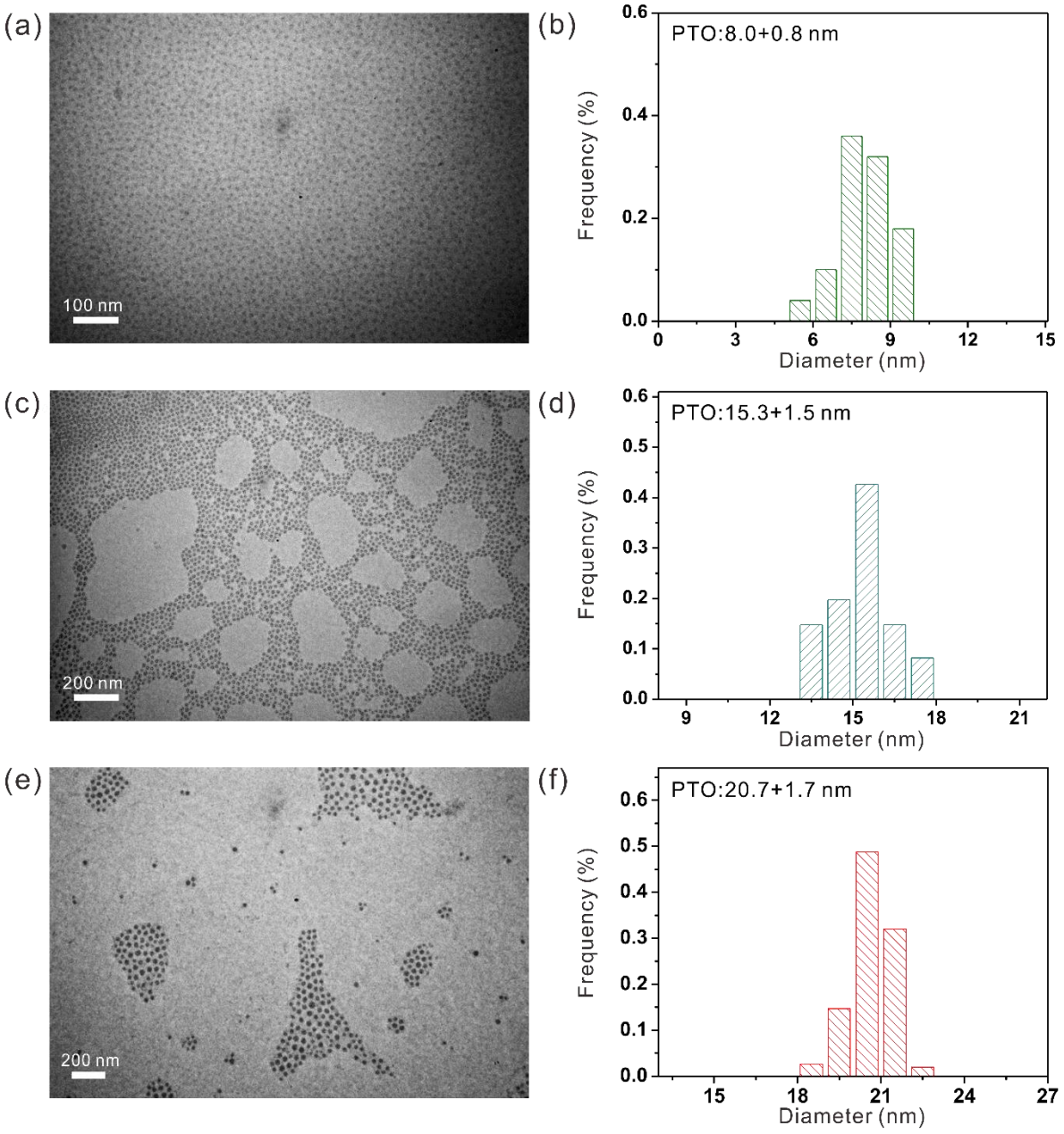

Figure 5.14 (a-c) TEM images of PS-ligated $PbTiO_3$ nanoparticles synthesized by utilizing star-like PAA-*b*-PS diblock copolymers (Samples 1-3 shown in **Table 5.1**, respectively) as nanoreactors with varied nanoparticle sizes and **(d-f)** their corresponding statistics of nanoparticle size distribution.

Figure 5.15 (a) displays the representative X-ray diffraction (XRD) profile of PS-capped $BaTiO_3$ NPs before (upper panel) and after (lower panel) annealing in a N_2-filled furnace at 600 ^oC. Clearly, as-synthesized $BaTiO_3$ NPs had low crystallinity, only the strongest peak (indexed to

(110) facet at 2θ = 31.6° appeared. We speculated the low crystallinity of the as-synthesized perovskite NPs may be due to incomplete thermolysis of bimetallic alkoxide precursors due to relatively low reaction temperature (100 °C). Nevertheless, the signals of Ba, Ti and O were observed from the energy-dispersive X-ray spectroscopy of as-synthesized $BaTiO_3$ NPs (**Figure 5.16**). After annealing PS-ligated $BaTiO_3$ NPs dispersed on graphene oxide (GO) in furnace at 600 ^oC (i.e., forming $BaTiO_3$ NPs/rGO composites after annealing; see *Experimental Section*), the diffraction peaks appeared and can be indexed to cubic phase of $BaTiO_3$ (lower panel, **Figure 5.15 (a)**). In addition, Raman spectroscopy characterization was also conducted to detect the composition and local structure of PS-capped $BaTiO_3$ NPs after annealing in N_2-filled furnace at 600 ^oC, substantiating the product was $BaTiO_3$ with some local tetragonal distortions after annealing (**Figure 5.17**).

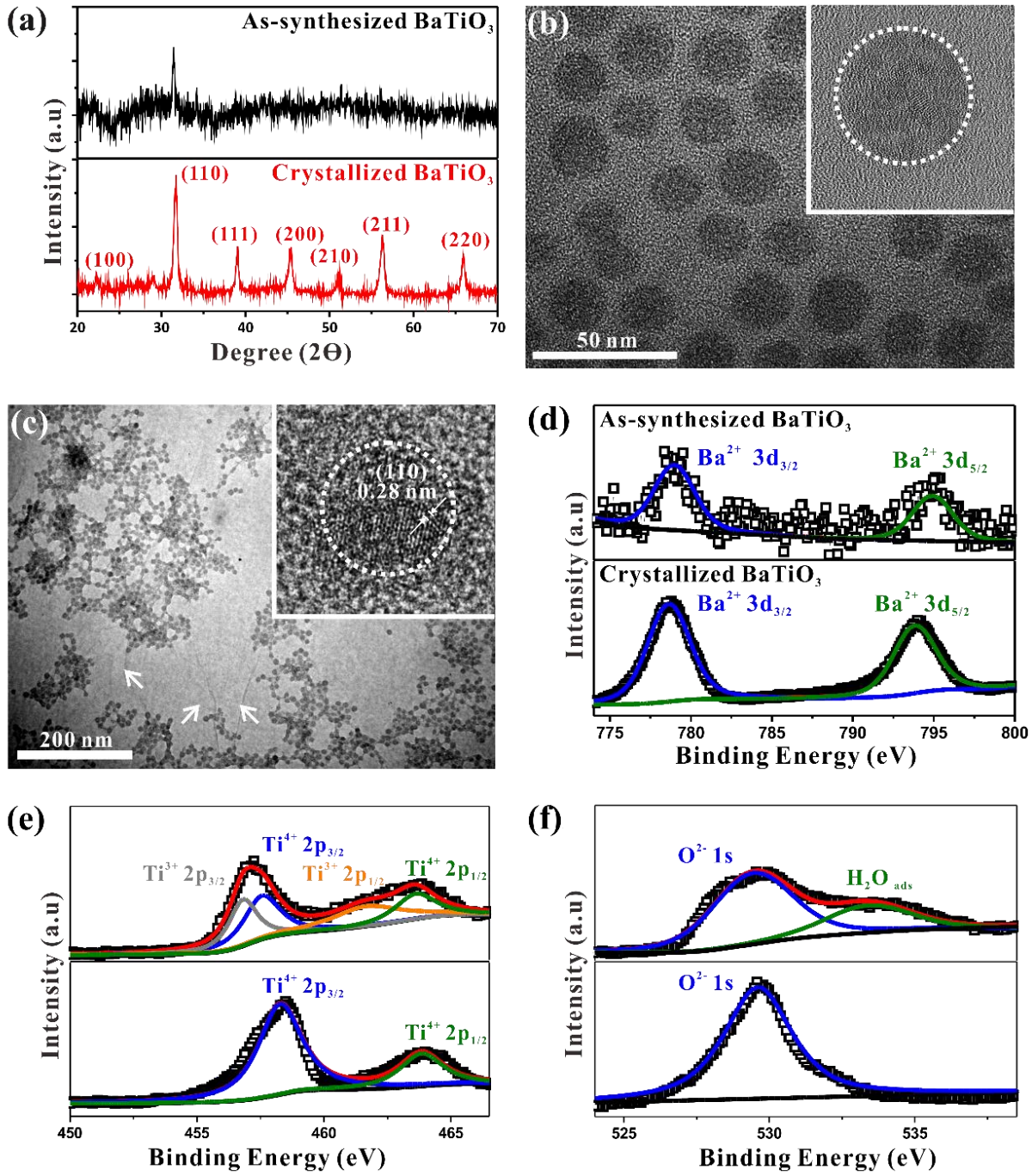

Figure 5.15 (a) Representative XRD patterns of as-synthesized and crystallized $BaTiO_3$ nanoparticles (NPs). **(b-c)** TEM of **(b)** as-synthesized $BaTiO_3$ NPs and **(c)** crystallized $BaTiO_3$ NPs dispersed on reduced graphene oxide sheets (indicated with white arrows). Both NPs were yielded by utilizing star-like PAA-*b*-PS nanoreactors (i.e., Samples 2 in **Table 5.1**). **(d-f)** Representative XPS spectra of as-synthesized $BaTiO_3$ NPs (upper panel) and crystallized $BaTiO_3$ NPs (lower panel) of **(d)** barium (Ba), **(e)** titanium (Ti) and **(f)** oxygen (O). Insets in **(b)** and **(c)** are the HRTEM images of as-synthesized and crystallized $BaTiO_3$ NPs.

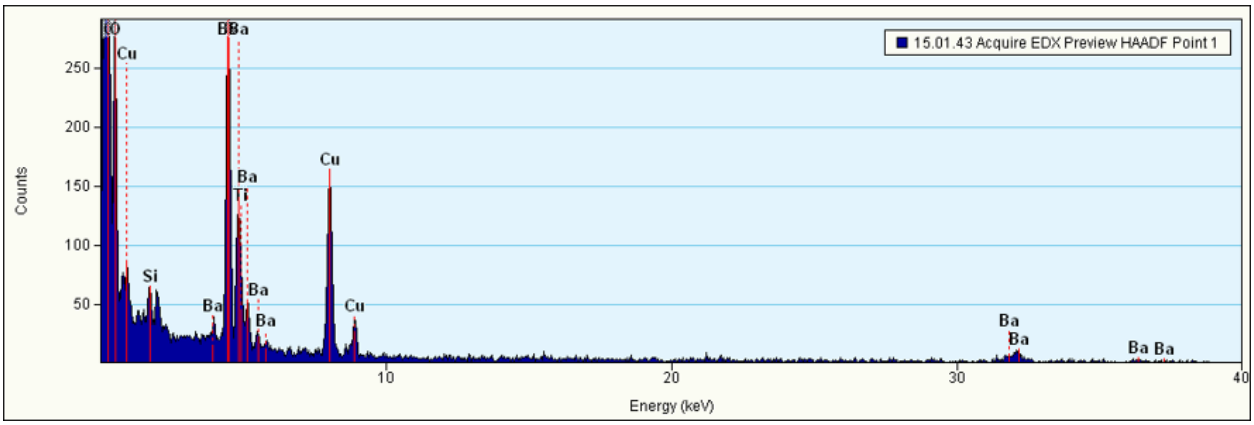

Figure 5.16 Energy dispersive X-Ray spectroscopy analysis of as-synthesized $BaTiO_3$ nanoparticles.

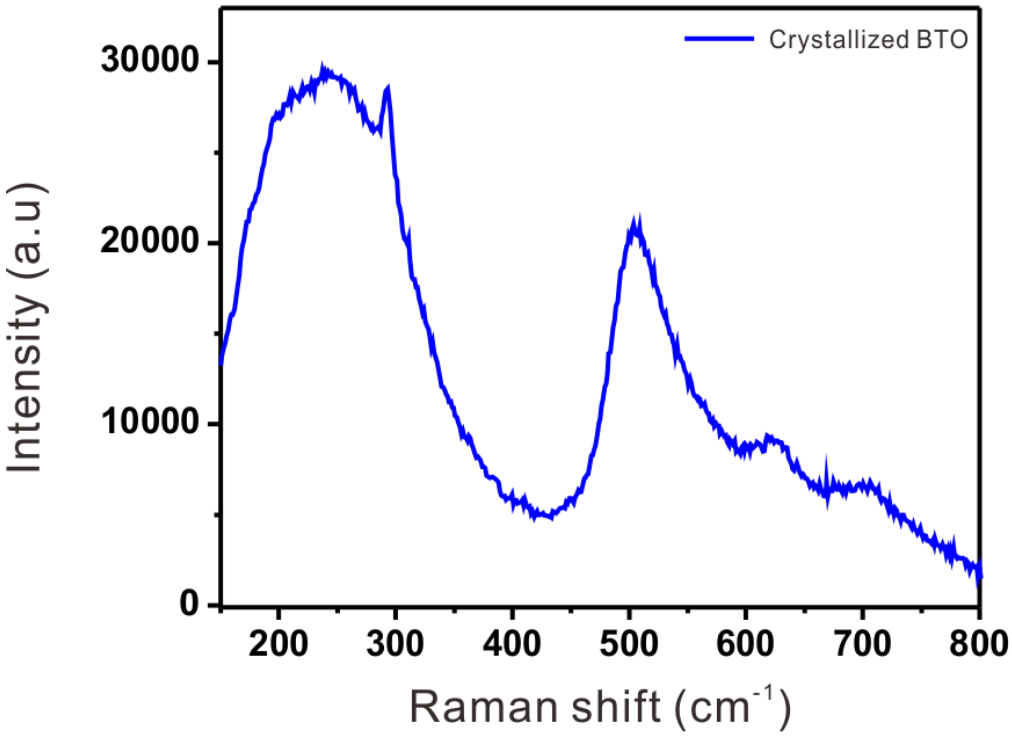

Figure 5.17 Raman spectrum from PS-ligated $BaTiO_3$ nanoparticles after annealing at 600 ^oC in N_2 atmosphere.

Raman spectroscopy measurement is widely employed for detecting the composition and local structure of $BaTiO_3$, especially when the sample amount is small. **Figure 5.17** presents the room-temperature Raman spectrum (150 cm^{-1} to 800 cm^{-1}) of PS-capped $BaTiO_3$ nanoparticles after annealing in N_2-filled furnace at 600 ^oC. The bands located at 515 and 260 cm^{-1} can be assigned to the transverse optical (TO) modes of A1 symmetry. The band at 715 cm^{-1} is related to the highest frequency longitudinal optical

mode (LO) with A1 symmetry, while the band around 305 cm^{-1} associated with the B1 mode. The peaks at 305 cm^{-1} and at 715 cm^{-1} are generally considered as the signature of the ferroelectric (tetragonal) phase of $BaTiO_3$. The presence of the two peaks at 305 and 715 cm^{-1} indicated that there are local tetragonal distortions in the $BaTiO_3$ nanoparticles after annealing. We note the assignments discussed above are consistent with those reported in the literature. Compared to Raman profile, XRD data suggested the annealed $BaTiO_3$ NPs were in cubic phase. This discrepancy may due to the following two reasons. First, the distortion detected by Raman may be only local distortion. For XRD, it measured the bulk behavior and thus local tetragonal signals, if any, would not be reflected in the XRD profile. Second, because XRD peaks are broadened as the particle sizes decrease, the splitting of peaks, which serves as an indicator of tetragonal phase, may be difficult to be observed clearly.

Figure 5.15 (b) shows a representative TEM image of PS-ligated $BaTiO_3$ NPs (a high-resolution TEM (HRETM) image of a single NP) before annealing with unclear crystalline structure and lattice spacing, which is consistent with the XRD profile (upper panel, **Figure 5.15 (a)**). As noted above, to retain the NP size and prevent them from aggregation after annealing, as-synthesized NPs were first deposited on GO (TEM of pure GO is shown in **Figure 5.18 (a)**) and annealed, during which GO was converted into rGO (see *Experimental Section*). The TEM images revealed that $BaTiO_3$ NPs possessed similar size and remained separately after annealing (**Figure 5.15 (c)** and **Figure 5.18 (b)**), where the fold of rGO is indicated by white arrows in both images, verifying the presence of rGO either above or under the NPs. The HRTEM image of a $BaTiO_3$ NP after annealing (inset of **Figure 5.15 (c)**) clearly showed crystalline lattices and characteristic d spacing of (110) plane of $BaTiO_3$. In contrast, control experiment on annealing $BaTiO_3$ NPs without introduction of graphene is demonstrated in **Figure 5.19** with the NPs aggregated into larger size and irregular shape.

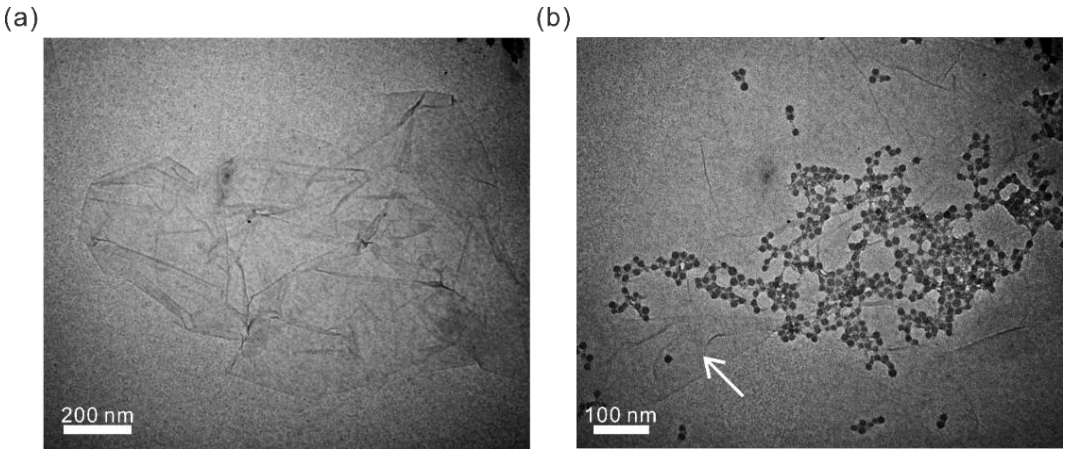

Figure 5.18 TEM image of **(a)** pristine graphene oxide (GO) before annealing and **(b)** composite of $BaTiO_3$ nanoparticles deposited on reduced graphene oxide (rGO) after annealing at 600 ^oC in N_2. The white arrow in **(b)** indicates the underlying rGO sheet.

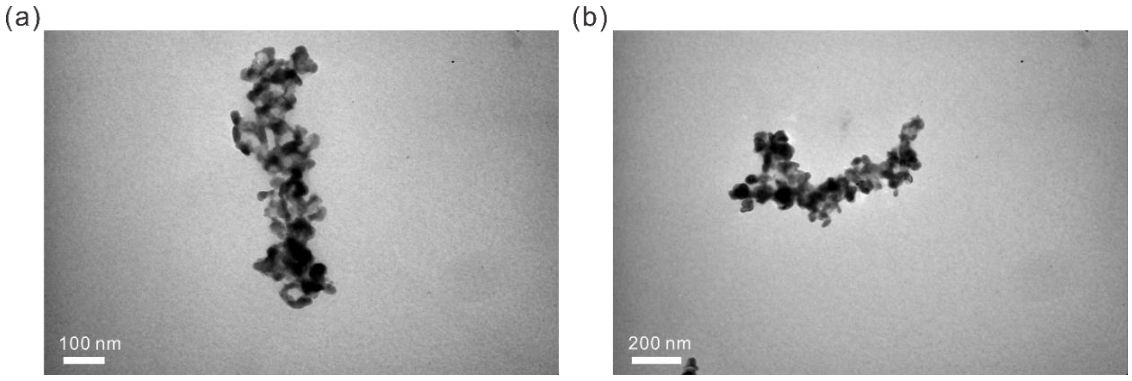

Figure 5.19 TEM images of $BaTiO_3$ nanoparticles after annealing at 600 ^oC without mixing with graphene oxide (GO).

The X-ray photoelectron spectroscopy (XPS) survey spectra of $BaTiO_3$ NPs and high-resolution spectra of individual elements, Ba 3d, Ti 2p and O 1s are presented in **Figure 5.20** and **Figure 5.15 (d-f)**, respectively. The Ba^{2+} $3d_{3/2}$ and Ba^{2+} $3d_{5/2}$ peak positions centered at 779.7 and 795 eV (upper panel, **Figure 5.15 (d)**; before annealing (as-synthesized)) are slightly higher than those in crystallized $BaTiO_3$ NPs (779 and 793.8; lower panel, **Figure 5.15 (d)**; after annealing). The shift to slightly higher binding energy may be a result of different chemical environment of

Ba in the non-crystalline phase as compared to the crystalline phase.[26,27] The Ti 2p peak of as-synthesized $BaTiO_3$ NPs can be resolved into two components (Ti $2p_{3/2}$ and Ti $2p_{1/2}$), which can further be deconvoluted into four peaks (upper panel, **Figure 5.15 (e)**). Among them, the peaks at 458.2 eV and 463.7 eV can be assigned to Ti $2p_{3/2}$ and Ti $2p_{1/2}$ peaks of Ti^{4+} in the TiO_6 octahedra,[28] whereas the peaks located at 456.8 eV and 461.6 eV are consistent with Ti $2p_{3/2}$ and Ti $2p_{1/2}$ peaks of reduced Ti,[29] often described as Ti^{3+}. The appearance of a low-binding-energy component suggested there were some structural defects in as-synthesized $BaTiO_3$ NPs due possibly to low reaction temperature (100 °C). However, no observable shift in the main peak of Ti between as-synthesized and crystallized $BaTiO_3$ NPs (lower panel, **Figure 5.15 (e)**) indicated that the structure of TiO_6 octahedra was largely chemically unchanged. For the O 1s peak of as-synthesized $BaTiO_3$ NPs (**Figure 5.15 (f)**), the main peak positioned at 529.5 eV can be assigned to oxygen in the $BaTiO_3$ lattice, whereas the shoulder peak at higher binding energy can be attributed to physisorbed molecular water, both consistent with previous XPS studies of bulk and single-crystal $BaTiO_3$.[20] Furthermore, the greatly-suppressed shoulder peak after annealing the sample under 600 ^oC (lower panel, **Figure 5.15 (f)**) indirectly supported the origin of the shoulder peak was actually physisorbed molecular water.

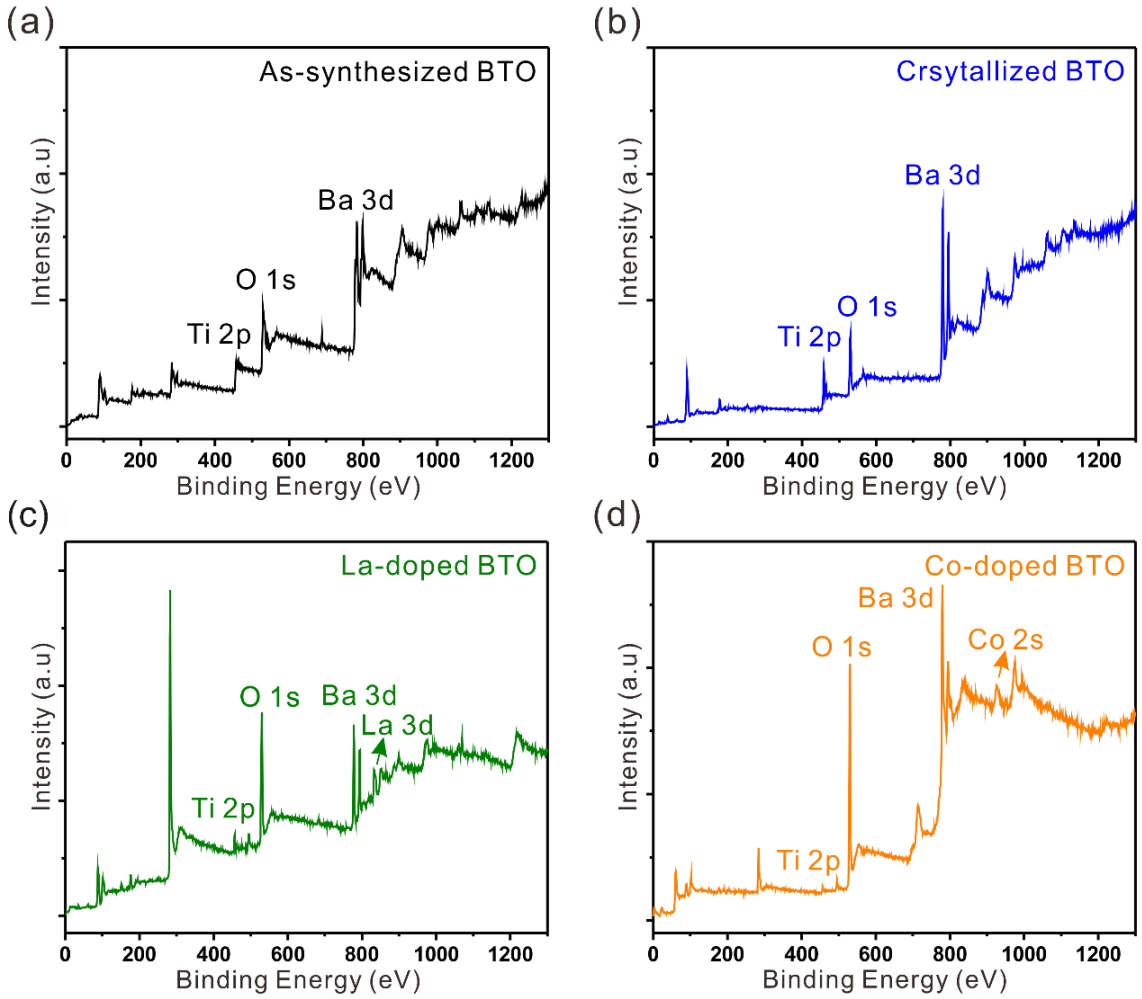

Figure 5.20 XPS full spectra of **(a)** as-synthesized, **(b)** crystallized, **(c)** La-doped and **(d)** Co-doped $BaTiO_3$ nanoparticles, respectively.

As a semiconducting material with a large bandgap (~3.1 eV), the structural, chemical, optical and electrical properties of $BaTiO_3$ are known to depend heavily on the purity of the starting materials, annealing conditions, and dopant types.[30] In the latter context, doping a low concentration of lanthanum (La) in $BaTiO_3$ has been shown to increase grain growth and decrease Curie temperature.[31] On the other hand, doping with cobalt (Co) could induce lattice strain, leading to increased piezoelectric and magnetostrictive strains and thus enhanced magnetoelectric coupling.[32] Notably, pristine and doped perovskite oxides are widely recognized as promising

electrocatalysts owing to their appealing attributes including low cost, facile synthesis, high stability in alkaline solution, and composition flexibility (a large variety of A and B cations can be chosen and substituted),[4,33] as noted above. Importantly, such composition tunability renders tailored electrocatalytic behaviors by varying oxidation states and coordination environments.[15,34] To this end, as La-based and Co-based materials are known as good electrocatalysts for ORR, La and Co were thus chosen as dopants to yield La-doped and Co-doped $BaTiO_3$ NPs for scrutinizing the composition-dependent electrocatalytic properties of $BaTiO_3$ NPs (i.e., pristine, La-doped, and Co-doped $BaTiO_3$ NPs), in addition to the size-dependent electrocatalysis.

PS-ligated La-doped and Co-doped $BaTiO_3$ NPs were first synthesized by exploiting the same nanoreactor strategy as PS-ligated $BaTiO_3$ NPs except a certain amount of dopant precursors (lanthanum isopropoxide for La^{3+} doping, and cobalt acetate for Co^{2+} doping) were added at the same time when dissolving and coordinating bimetallic precursors of $BaTiO_3$ with -COOH groups of inner PAA blocks (see *Experimental Section*). The proposed formation mechanism for both La-doped $BaTiO_3$ NPs and Co-doped $BaTiO_3$ NPs with star-like diblock copolymer nanoreactors[35] can be referred to the *Experimental Section*. **Figure 5.21 (a-b)** show the representative TEM images of as-synthesized (i.e., before annealing) La-doped and Co-doped $BaTiO_3$ NPs with 5 mol% of dopants, both synthesized using star-like PAA-*b*-PS nanoreactor (Sample 2 in **Table 5.1**). It is clear that they are uniform with the size of 15.4 ± 1.2 nm for La-doped $BaTiO_3$ NPs (**Figure 5.22)** and 15.6 ± 1.5 nm for Co-doped $BaTiO_3$ NPs (**Figure 5.23**), close to that without doping (15.2 ± 1.2 nm; i.e., pristine $BaTiO_3$ NPs in **Figure 5.1 (f)**). Clearly, the success in producing doped $BaTiO_3$ NPs further demonstrated the robustness of our nanoreactor strategy in effectively crafting a large variety of uniform perovskite NPs of tailored compositions.

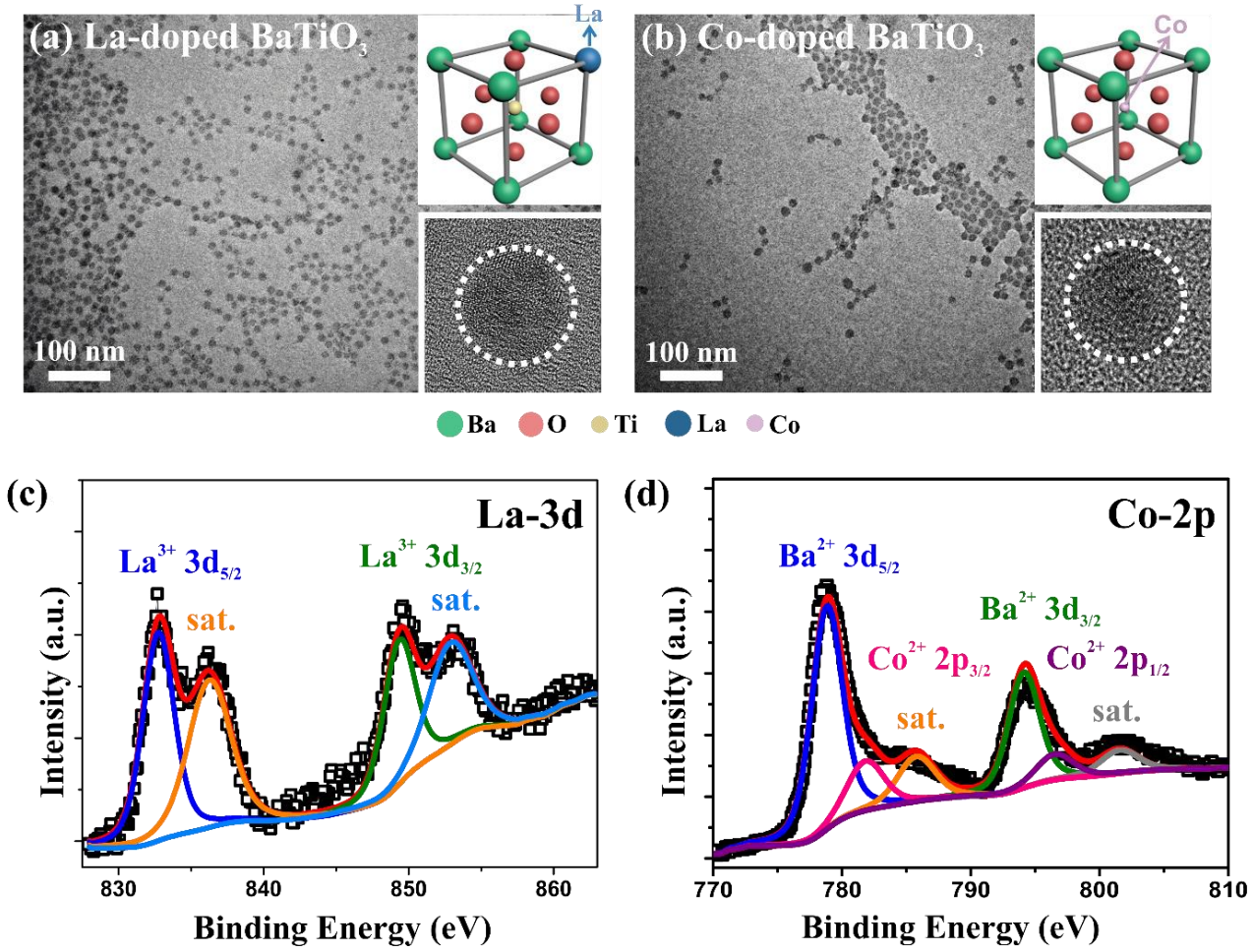

Figure 5.21 (a-b) Representative TEM images of as-synthesized (before annealing) doped $BaTiO_3$ NPs with different dopants: **(a)** 5 mol% La and **(b)** 5 mol% Co. Upper-right insets in **(a)** and **(b)** are the proposed corresponding crystal structure after doping. Green, red, blue, yellow and pink spheres represent Ba, O, La, Ti and Co atoms, respectively. Lower-right insets in **(a)** and **(b)** are the HRTEM images of a single 5 mol% La-doped and 5 mol% Co-doped $BaTiO_3$ NPs, respectively, after mixing with GO and annealing in N_2 at 600 ^oC (i.e., after annealing). **(c-d)** XPS spectra of **(c)** La and **(d)** Co after doping in La-doped and Co-doped $BaTiO_3$ NPs, respectively, after annealing.

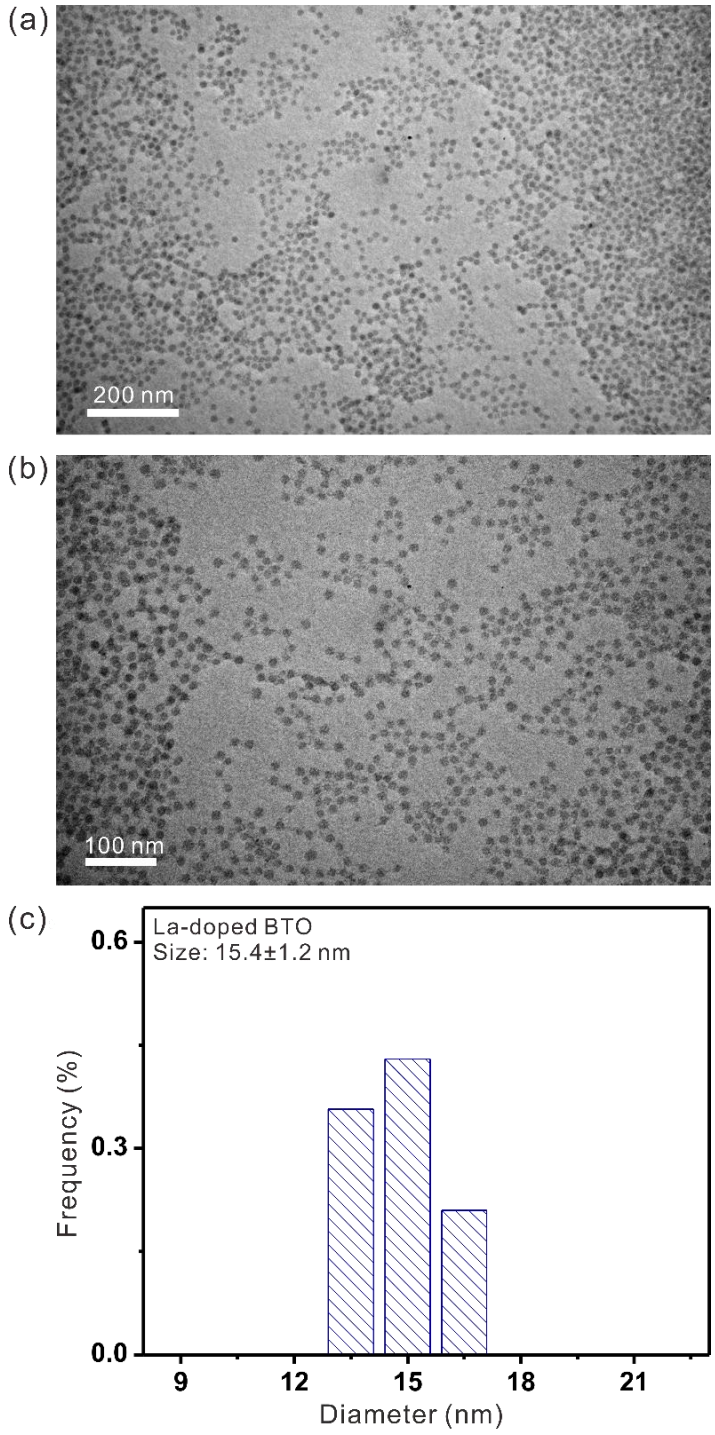

Figure 5.22 (a, b) TEM images of as-synthesized La (5 mol%)-doped $BaTiO_3$ nanoparticles at different magnifications. **(c)** Statistics of size distribution of as-synthesized La-doped $BaTiO_3$ nanoparticles (using Sample 2 in **Table 5.1** as nanoreactor), the average nanoparticle size from calculation is 15.4 $\pm$ 1.2 nm.

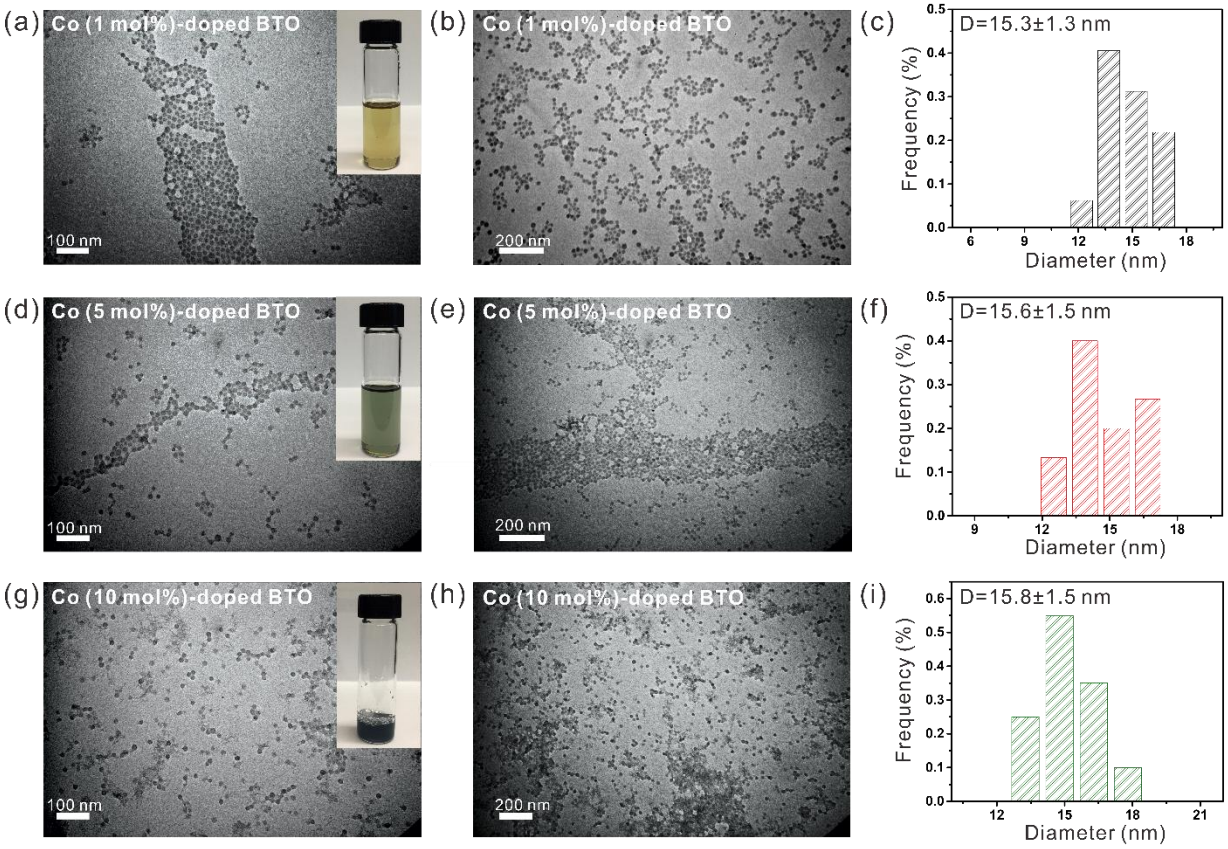

Figure 5.23 TEM images of as-synthesized Co-doped $BaTiO_3$ nanoparticles with different amounts of Co. **(a, b)** 1 mol%, **(d, e)** 5 mol% and **(g, h)** 10 mol%. Insets in **(a, c, e)** are the digital images of the nanoparticle toluene solution containing as-synthesized Co-doped $BaTiO_3$ nanoparticles (using Sample 2 in **Table 5.1** as nanoreactor). The size histograms of the corresponding Co-doped $BaTiO_3$ nanoparticle at different dopant concentrations are shown in **(c, f, i)**.

After the La-doped and Co-doped $BaTiO_3$ NPs were made, the product was again mixed with GO and annealed in N_2 at 600 ^oC for 2 h to increase their crystallinity (see *Experimental Section*). The HRTEM images of La-doped and Co-doped $BaTiO_3$ NPs after annealing with clear crystalline lattice are shown as insets (lower right) in **Figure 5.21 (a-b)**, respectively. The upper right insets in **Figure 5.21 (a-b)** are the proposed unit cell structures after doping. Due to the similarity in ionic radii (Ba^{2+}: 149 pm, La^{3+}: 117.2 pm, Co^{2+}: 79 pm, and Ti^{4+}: 74.5 pm), La^{3+} ions have higher tendency to replace Ba^{2+} ions (A-site), while Co^{2+} ions tend to substitute Ti^{4+} ions (B-site), as supported by literature.[32,36] Thus, electrons and cation vacancies may be generated when

doping $BaTiO_3$ NPs with La^{3+} ion, whereas anion vacancies may be formed when doping $BaTiO_3$ NPs with Co^{2+} ion in order to maintain the charge neutrality. In particular, positive charges generated from the substitution of Ba^{2+} with La^{3+} can be compensated by negatively charge defects, i.e., barium vacancies, titanium vacancies and electrons,[31] while negative charges created from the replacement of Ti^{4+} with Co^{2+} can be balanced by positively charged oxygen vacancies.[32]

The successful doping of La and Co was verified by XPS measurements. The representative XPS spectra of 5 mol% La-doped and Co-doped $BaTiO_3$ NPs, after mixing with GO and annealing in N_2 at 600 ^oC, are shown in **Figure 5.21 (c)** and **Figure 5.21 (d)**, respectively. The binding energies of La^{3+} $3d_{5/2}$ and La^{3+} $3d_{3/2}$ peaks are located at 834 eV and 849.9 eV with the satellite peaks (denoted "sat.") presented at 838 and 853 eV (**Figure 5.21 (c)**). As for Co 2p, the XPS result can be deconvoluted into four peaks (**Figure 5.21 (d)**). The binding energies of 779.7 and 795 are attributed to Ba^{2+} ions, consistent with the peak positions of pure $BaTiO_3$ NPs (**Figure 5.15 (d)**). The intermediate peaks with higher binding energy of 782 eV (Co $2p_{3/2}$) and 796 eV (Co $2p_{1/2}$) are associated with Co^{2+} ions. Finally, the peaks at higher binding energy (786 eV and 802 eV) are identified as satellite peaks.

We note that using the star-like diblock copolymer nanoreactor, the size of doped NPs can be maintained while varying the dopant concentrations at the proper molar ratio of dopant precursors to $BaTiO_3$ precursors (TEM images in **Figure 5.23**). Clearly, the morphologies of the doped $BaTiO_3$ NPs are still uniform even at 10 mol% dopant concentration. The insets in **Figure 5.23 (a, d,** and **g)** show the digital images of doped NPs dispersed in toluene, where the solution color changed from yellow (**Figure 5.23 (a)**), green (**Figure 5.23 (d)**) to blue (**Figure 5.23 (g)**) as the dopant concentration increased. The size histograms of $BaTiO_3$ NPs doped with 1 mol%, 5 mol% and 10 mol% Co, respectively, are shown in **Figure 5.23 (c, f,** and **i)**. It is interesting to note

that the sizes of $BaTiO_3$ NPs with different dopant concentrations are similar to each other, signifying the flexibility of the $BaTiO_3$ NP as the framework for doping with varied elements and doping concentrations. The corresponding XRD profiles for annealed $BaTiO_3$ NPs that doped with different amounts of Co dopants are shown in **Figure 5.24**. As the dopant concentration increased, the peak sharpness of doped $BaTiO_3$ decreased significantly. The characteristic peaks for 1 mol% and 5 mol% Co-doped $BaTiO_3$ can be clearly identified, while disappearing for the 10 mol% Co-doped sample. The decrease of the peak intensity may result from the generation of oxygen vacancies due to charge compensation when replacing Ti^{4+} with Co^{2+}, thus destroying the continuously-ordered crystal structure.[37,38] However, no new or secondary peaks emerged after doping 10 mol% Co, suggesting Co precursors did not segregate into individual Co-based materials. On the basis of the results above, we chose 5 mol% La-doped and Co-doped $BaTiO_3$ NPs, instead of 1 mol% (due to less significant doping effect) and 10 mol% (due to partially-deformed crystal structure; **Figure 5.24**) doped NPs, for investigating their electrocatalytic properties.

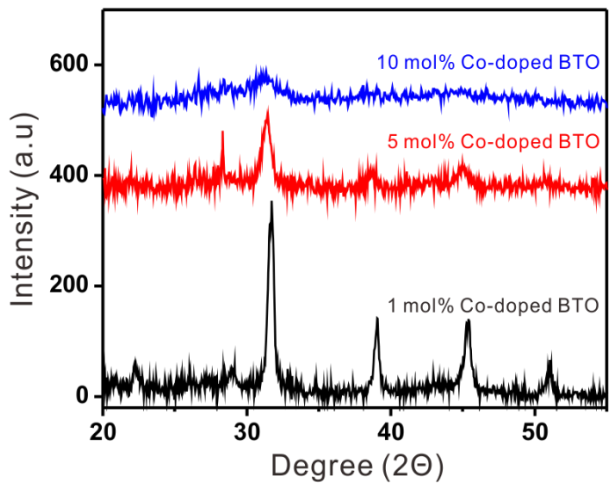

Figure 5.24 XRD profile of Co-doped $BaTiO_3$ nanoparticles with different amounts of Co dopants after mixing with graphene oxide (GO) and then annealed in N_2 at 600 ^oC (i.e., yielding Co-doped $BaTiO_3$ nanoparticle (NP) dispersed on the surface of reduced GO (rGO); a Co-doped $BaTiO_3$ NP/rGO composites).

We now turn our attention to scrutinize size- and composition-dependent ORR activities of as-synthesized $BaTiO_3$ (size-dependent), as well as crystallized $BaTiO_3$, La- and Co-doped $BaTiO_3$ NPs on rGO (composition-dependent), respectively, in N_2 and O_2-saturated alkaline electrolytes (0.1 M KOH) in a three-electrode cell with rotating disk electrodes. All potentials were referenced to a reversible hydrogen electrode (RHE). To assess the ORR activity, the respective materials were first loaded onto glassy carbon (GC) electrodes for cyclic voltammetry (CV) in O_2- versus N_2-saturated 0.1 M KOH (**Figure 5.25 (a)**). Featureless voltammetric curves were observed for all four samples when measured in N_2-saturated solutions (dash curves in **Figure 5.25 (a)**). In contrast, distinct peaks appeared at varied potentials for as-synthesized $BaTiO_3$, crystallized $BaTiO_3$, La-doped $BaTiO_3$ and Co-doped $BaTiO_3$ NPs when tested in O_2-saturated alkaline solutions (solid curves). Remarkably, both La-doped and Co-doped $BaTiO_3$ NPs demonstrated much more positive ORR onset potential (~0.80V and ~0.84V relative to the RHE, defined as the potential at which two tangent lines intersected) and higher limiting current density, suggesting the doped $BaTiO_3$ NPs are promising candidates as ORR catalysts.

To further evaluate the ORR activity, linear sweep voltammetry (LSV) curves of the catalysts were recorded in O_2-saturated electrolytes at a scan rate of 5 mVs^{-1} at 1600 rpm. **Figure 5.25 (b)** reveals the NP size effect of as-synthesized $BaTiO_3$ NPs on the ORR performance, enabled by star-like diblock copolymer nanoreactor strategy that renders precise tailoring of the dimension of perovskite NPs, which has been proven to be difficult to achieve because of high formation energies of perovskites.[39,40] Quite intriguingly, as the size of catalyst decreased (**Figure 5.1 (b-d)**), the ORR activities progressively enhanced, representing more positive onset potential and half-wave potential as well as larger limiting current density. Compared to those of the largest-sized catalyst (D = 20.6 ± 1.4 nm), both onset potential and half-wave potential of the smallest-

sized catalyst (D = 8.1 ± 0.9 nm) were improved (**Figures 5.26**). Similar enhancement in ORR performance with decreased NPs size was observed after annealing the NPs (**Figures 5.27**). In addition to more positive onset potential and half-wave potential, the limiting current density increased by 1.4 times, from 4.1 mA/cm^2 for 20.6 nm $BaTiO_3$ NPs to 5.8 mA/cm^2 for 8.1 nm $BaTiO_3$ NPs of the smallest size (**Figures 5.27**). The promoted ORR performance can possibly be attributed to improved electroconductivity as well as larger surface area as the NP size decreased, thus increasing electrochemical active sites for adsorbing oxygen during ORR reaction.[41-43]

Figure 5.25 (c) compares the effect of varied compositions (pristine as well as doped with different elements at 5 mol% dopant concentration) on the ORR properties. We note that all the $BaTiO_3$ NPs (pristine as well as La- and Co-doped) measured had the average sizes of 15 nm, synthesized by using Sample 2 as nanoreactor (**Table 5.1**). Both the A-site doping (substituting Ba^{2+} with La^{3+}) and B-site doping (replacing Ti^{4+} with Co^{2+}) manifested greatly enhanced performance (i.e., more positive ORR onset potential and higher limiting current density). Notably, despite the contributions of the bare GC electrode and the GC-supported rGO electrode for ORR were not negligible under the same measuring conditions, the enhanced ORR activities were clearly dominated by the doped catalysts (**Figure 5.28**). A significant improvement can be seen even at low dopant concentration (5 mol%). The comparison between Co-doped and La-doped $BaTiO_3$ NPs shows the former significantly outperformed the latter. The detailed results of CV and LSV measurements of La-doped $BaTiO_3$ with different rotation speeds are shown in **Figure 5.29 Figure 5.30** compares the onset potential among pristine and doped $BaTiO_3$ NP catalysts.

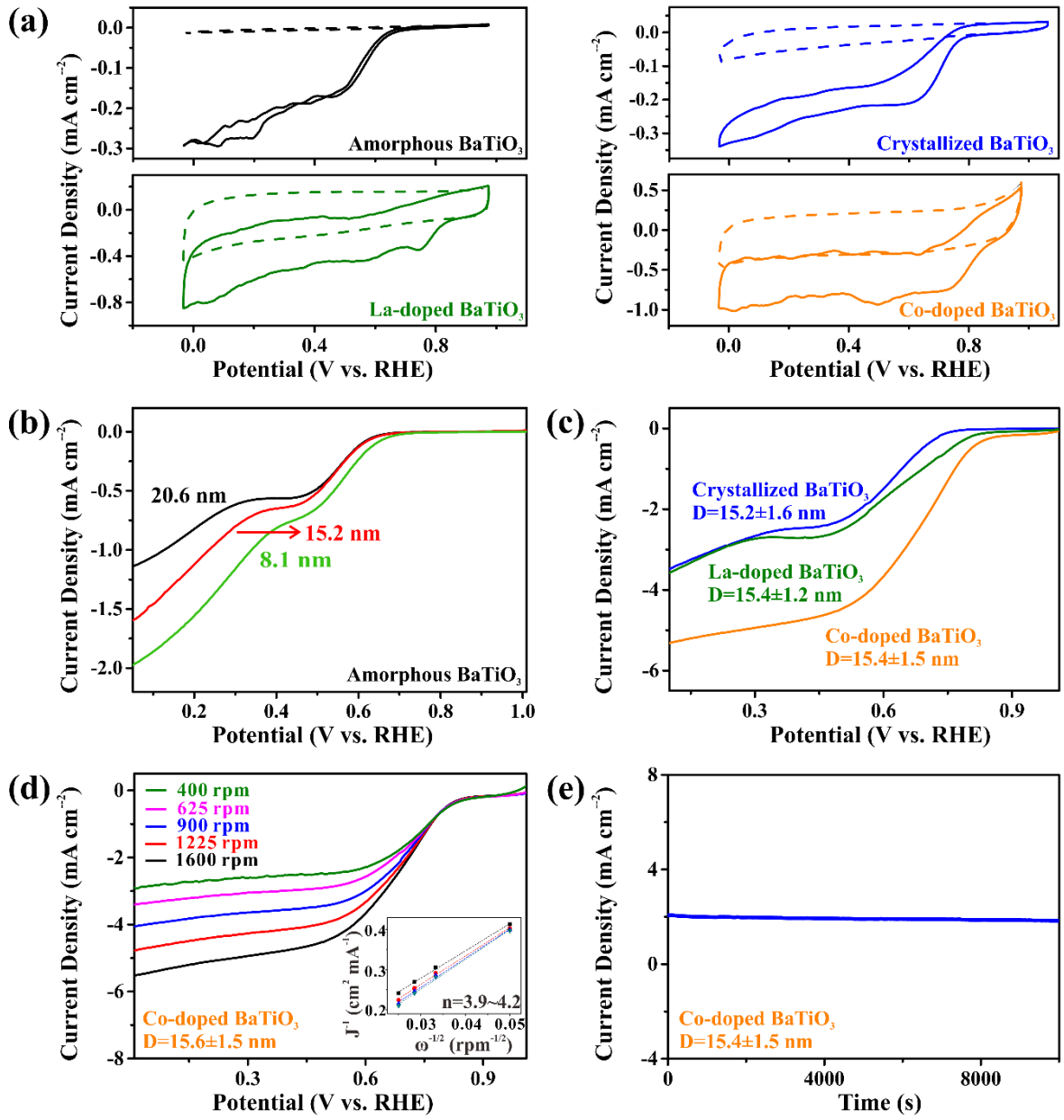

Figure 5.25 (a) CV curves of as-synthesized amorphous $BaTiO_3$, crystallized $BaTiO_3$, 5 mol% La-doped $BaTiO_3$ and 5 mol% Co-doped $BaTiO_3$ NPs on glassy carbon electrodes in O_2-saturated (solid curve) or N_2-saturated (dash curve) 0.1 M KOH. **(b-c)** Rotating-disk voltammograms of **(b)** as-synthesized amorphous $BaTiO_3$ NPs of different sizes and **(c)** crystallized $BaTiO_3$ NPs with (i.e., 5 mol% of La- and Co-doping) and without dopants at a sweep rate of 5 mV/s and a rotation rate of 1600 rpm. **(d)** Rotating-disk voltammograms of 5 mol% Co-doped $BaTiO_3$ NPs at a sweep rate of 5 mV/s and different rotation rates. The inset in **(d)** shows the corresponding Koutechy-Levich plots at different potentials. **(e)** Chronoamperometric responses of 5 mol% Co-doped $BaTiO_3$ NPs at 0.7 V. The NPs with the average size of ~15 nm in **(c-e)** were synthesized by employing star-like PAA-*b*-PS nanoreactor (i.e., Samples 2 in **Table 5.1**).

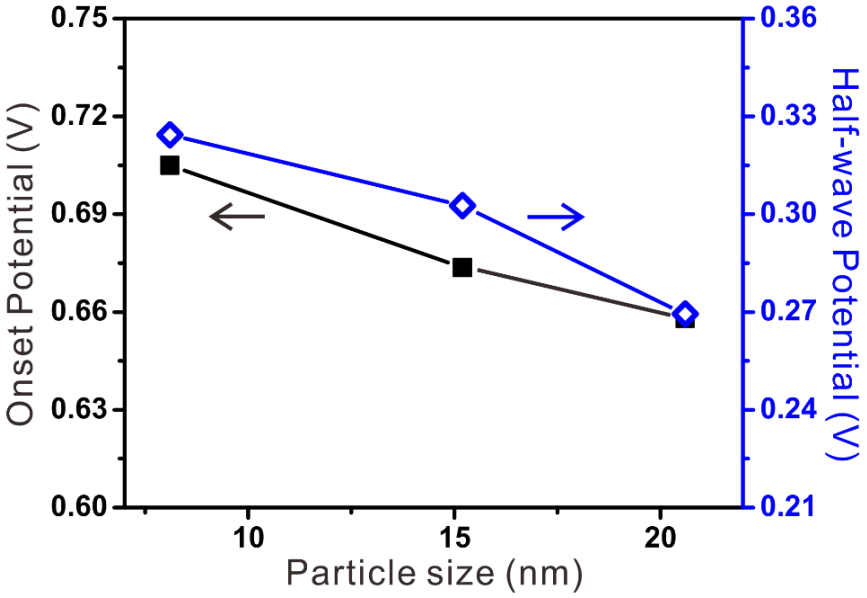

Figure 5.26 Onset potential and half-wave potential of as-synthesized $BaTiO_3$ nanoparticles at different sizes (i.e., 8.1 nm, 15.2 nm and 20.6 nm) measured in 0.1 M KOH solution at a scanning rate of 5 mV s^{-1} and a rotation speed of 1600 rpm.

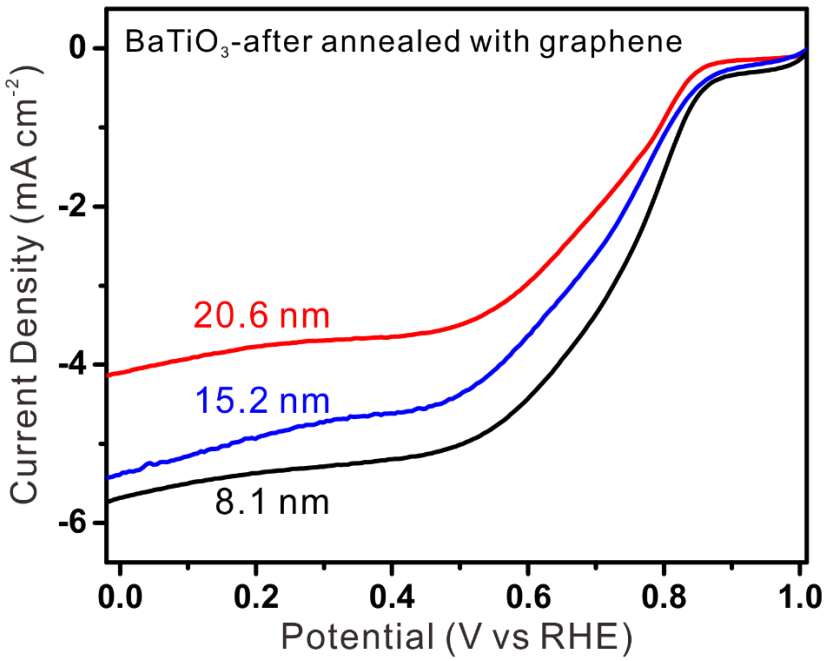

Figure 5.27 Oxygen reduction polarization curves of crystallized $BaTiO_3$ nanoparticles at different sizes.

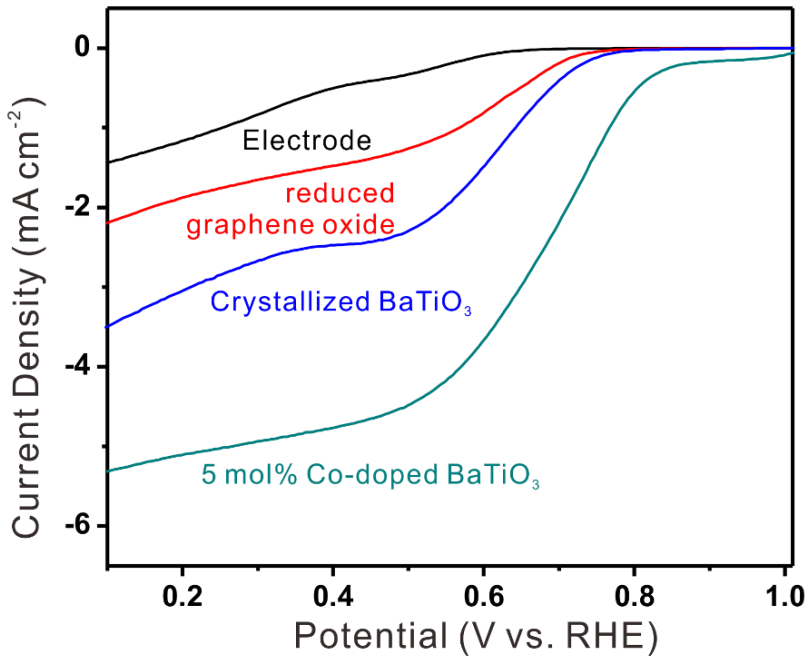

Figure 5.28 Oxygen reduction currents of glassy carbon electrode, reduced graphene oxide, crystallized $BaTiO_3$ nanoparticles (D = 15.2 nm) and 5 mol% Co-doped $BaTiO_3$ nanoparticles (D = 15.6 nm) in O_2-saturated 0.1 M KOH.

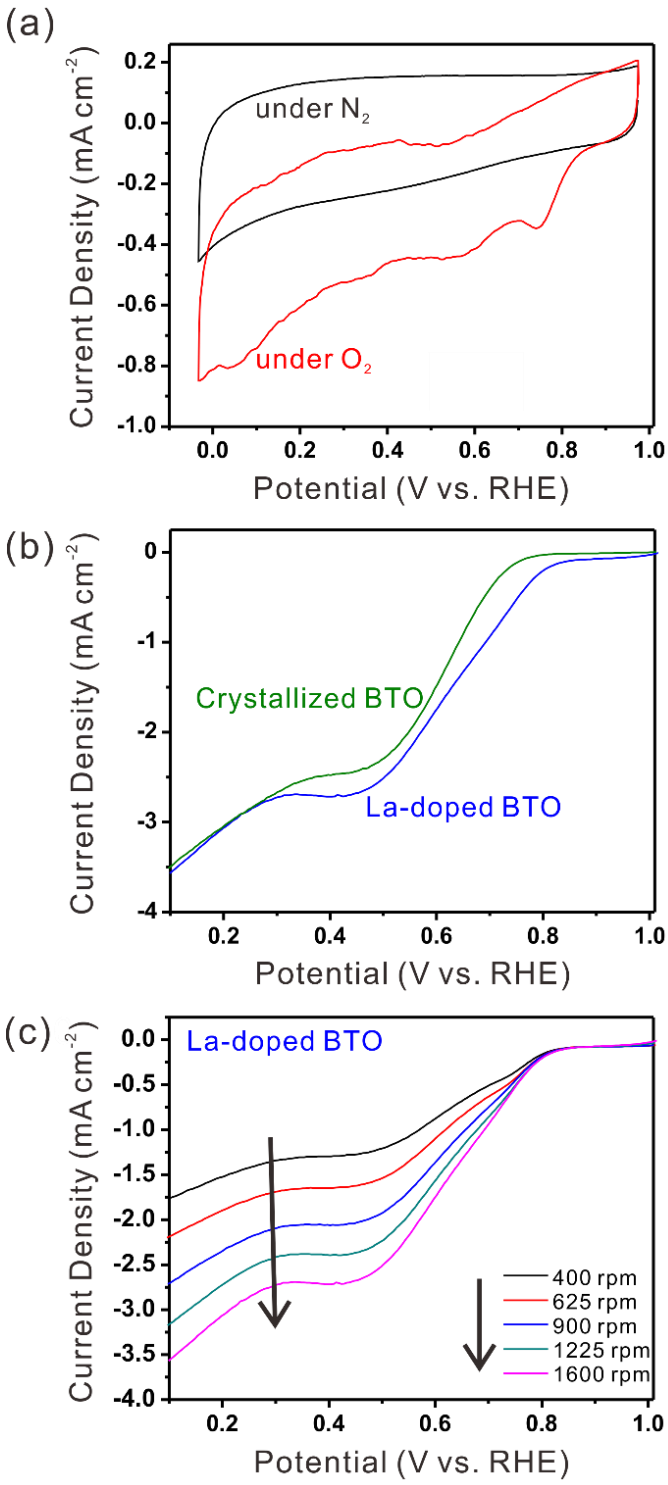

Figure 5.29 (a) CV of 5 mol% La-doped $BaTiO_3$ nanoparticles in oxygen (red) and nitrogen (black) saturated 0.1 M KOH. **(b)** Oxygen reduction currents of crystallized $BaTiO_3$ nanoparticles and 5 mol% La-doped $BaTiO_3$ nanoparticles on glassy carbon electrode in O_2-saturated 0.1 M KOH at a sweep rate of 5 mV/s and rotation rate of 1600 rpm. **(c)** Rotating-disk voltammogram of 5 mol% La-doped $BaTiO_3$ nanoparticles in O_2-saturated 0.1 M KOH at a sweep rate of 5 mV/s and different rotation rates. All the nanoparticles measured here were synthesized by using Sample 2 listed in **Table 5.1** as nanoreactor.

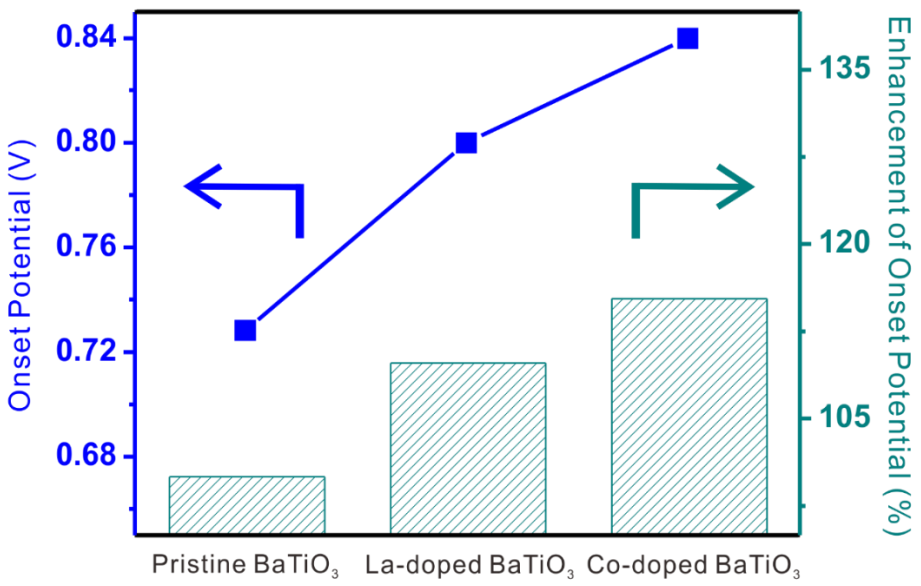

Figure 5.30 Onset potential and enhancement of onset potential of crystalline $BaTiO_3$ nanoparticles with different types of dopants measured in 0.1 M KOH solution at a scanning rate of 5 mV/s and a rotation speed of 1600 rpm.

Figure 5.25 (d) exemplifies the dependence of the disk current (i_D) on the angular rotation (ω) for Co-doped $BaTiO_3$ NPs, following the Koutechy-Levich formalism:[44]

$$\frac{1}{i_D} = \frac{1}{i_k} + \frac{1}{i_L} = \frac{1}{i_k} + \frac{1}{0.62nAFcD^{2/3}\nu^{-1/6}\omega^{1/2}}$$

where i_k and i_L are the kinetically and mass-transport limiting currents, respectively. i_L depends on the number of transferred electrons (n), diffusion coefficient of oxygen in 0.1 M KOH (D), bulk oxygen concentration (c), and kinematic viscosity (ν). Other parameters include the disk geometric area (A) and the Faraday constant (F). The detailed calculations are shown in *Supplementary Information*. The linear Koutechy-Levich plots (inset of **Figure 5.25 (d)** and **Figure 5.31**) and nearly parallel fitting lines suggested first-order reaction kinetics towards the concentration of dissolved oxygen. The electron transfer number (n) was calculated to be 3.9-4.2 between 0.40-

0.55V from the slope of Koutechy-Levich plots, signifying a 4*e* oxygen reduction process for 5 mol% Co-doped $BaTiO_3$ NPs (D= 15.6 ± 1.5 nm) deposited on rGO (i.e., Co-doped $BaTiO_3$ NPs/rGO composites).

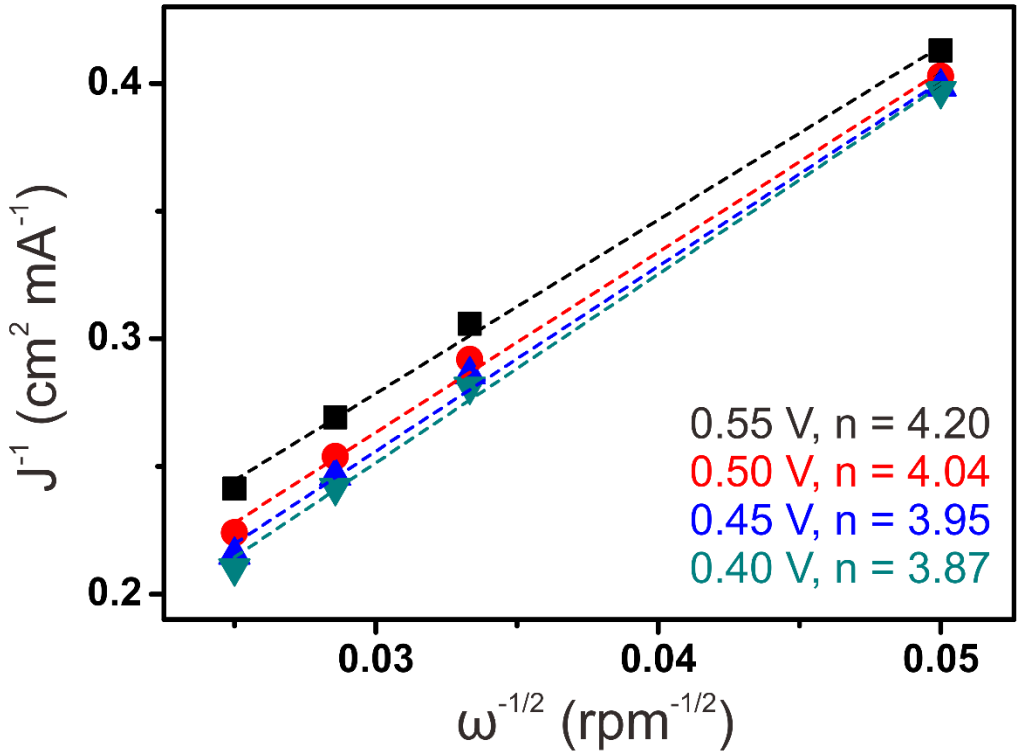

Figure 5.31 Koutechy-Levich plots ($J^{-1} \sim \omega^{-1/2}$) of 5 mol% Co-doped $BaTiO_3$ nanoparticles (D= 15.6 ± 1.5 nm)/rGO hybrid composites at different potentials.

To investigate the effect of Co dopant concentration of Co-doped $BaTiO_3$ NPs on ORR properties, a series of samples with 0, 1, 5 and 10 mol% Co dopants were synthesized and measured (**Figure 5.32**). As the dopant concentration increased, the ORR properties were progressively enhanced, representing a more positive onset potential, half-wave potential and higher limiting current density. Notably, in what follows, the discussion was centered on 5 mol% Co-doped $BaTiO_3$ NPs as the perovskite structure seemed not well retained when the Co dopant concentration increased to 10 mol%, as suggested by the weak XRD signal even after annealing

(**Figure 5.24**). We note that the potential of Co-doped $BaTiO_3$ NPs was extended to 2.0 V versus RHE to the water oxidation regime and evaluated electrocatalytic oxygen evolution reaction (OER) activity (**Figure 5.33**). Interestingly, our results indicated doping perovskite oxides may be a feasible approach for improving the electrocatalytic properties (**Figure 5.33**), which can be further enhanced by judiciously choosing other dopants of interest and their concentrations.

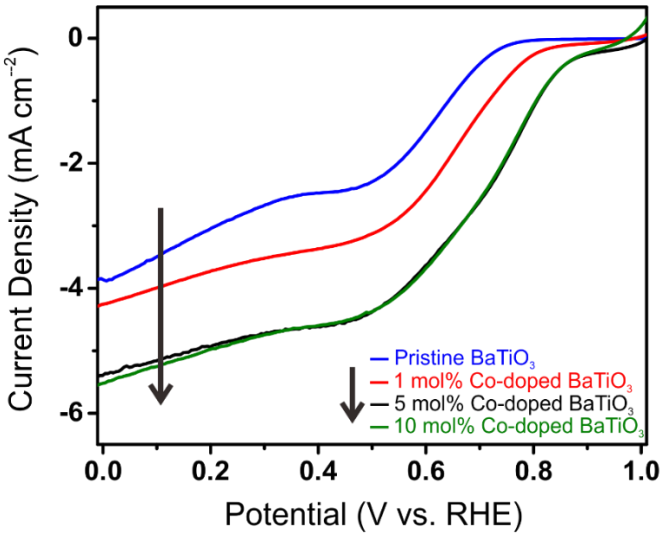

Figure 5.32 Oxygen reduction currents of crystallized $BaTiO_3$ nanoparticles and Co-doped $BaTiO_3$ nanoparticles at different dopant concentrations on glassy carbon electrode in O_2-saturated 0.1 M KOH at a sweep rate of 5 mV/s and a rotation rate of 1600 rpm.

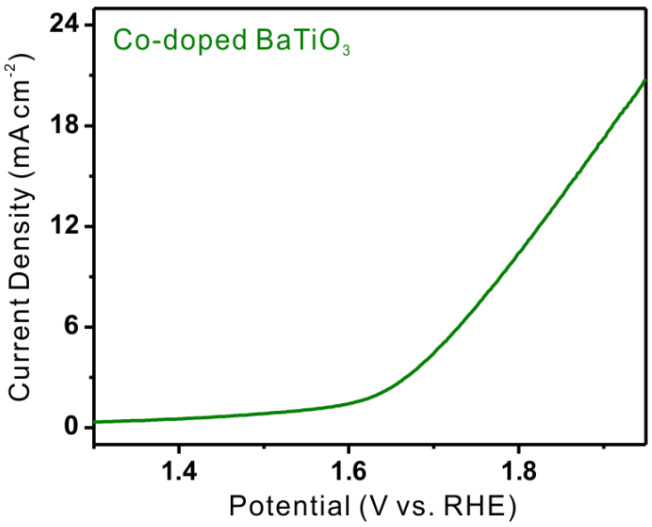

Figure 5.33 Oxygen evolution currents of 5 mol% Co-doped $BaTiO_3$ nanoparticles loaded onto glassy carbon electrode measured in 0.1 M KOH at a sweep rate of 5 mV/s and a rotation rate of 1600 rpm. Clearly, Co-doped $BaTiO_3$ NPs exhibited a superior overpotential of OER as well as higher limiting current density compared to $BaTiO_3$ particles synthesized and annealed at higher temperature (i.e., 1300 ^oC) in vacuum as previously reported in literature. Further enhancement may be achieved by judiciously choosing dopant types and their concentrations.

To further increase the ORR and OER activities of Co-doped $BaTiO_3$ NPs, oxygen vacancies were introduced via a simple reductive annealing process at low temperature[45] (i.e., with a forming gas of 5% H_2 and 95% N_2 at 350 ^oC). According to the previous study in literature,[45] oxygen-deficient perovskite ($A_2B_2O_5$) will be generated by using a forming gas containing 5% H_2. In our system, compared to those before annealing, increased ORR (**Figure 5.34**) and OER (**Figure 5.35**) activities after annealing in forming gas were observed, which can possibly be ascribed to the facile transport of intermediates during the reaction due to the oxygen vacancies generated from reductive annealing process.[45,46] Finally, the stability of Co-doped $BaTiO_3$ NPs towards ORR at constant potential of 0.7 V was tested (**Figure 5.25 (e)**). A stable catalytic activity on the Co-doped $BaTiO_3$ NPs was achieved, displaying a constant current density of 1.84 mA/cm^2, which is consistent with the LSV curve shown in **Figure 5.25 (c)**. After continuous operation for 9000s,

only slight decrease in current density was seen, verifying high stability of as-synthesized catalyst during the ORR process in alkaline medium.

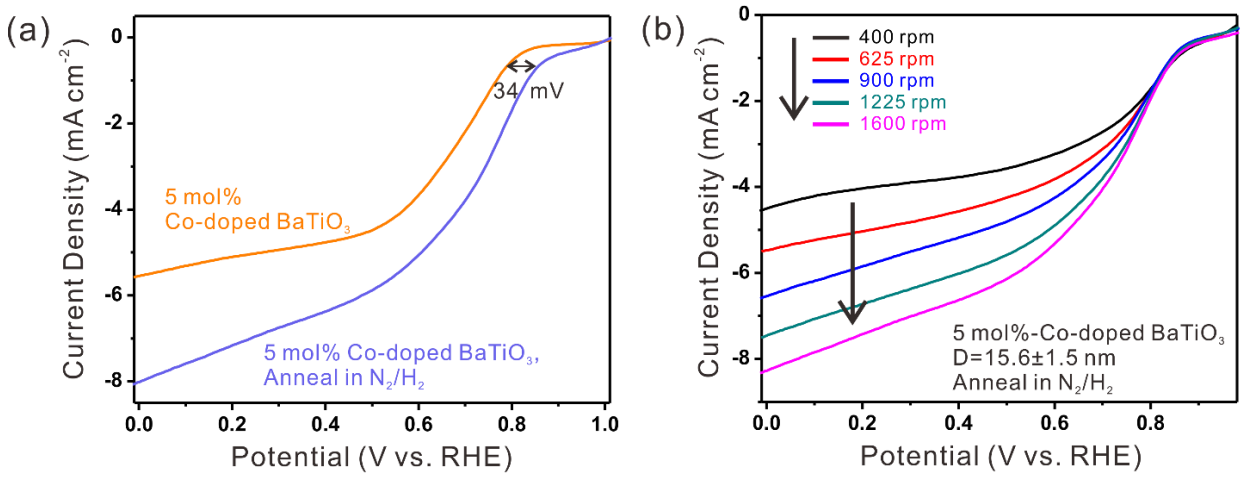

Figure 5.34 (a) Oxygen reduction polarization curves of 5 mol% Co-doped $BaTiO_3$ nanoparticles (D = 15.6 nm, synthesized by using Sample 2 in **Table 5.1** as nanoreactor) before and after further annealed in $95N_2$-$5H_2$. (b) Rotating-disk voltammograms of the corresponding annealed Co-doped $BaTiO_3$ nanoparticles at different rotation rates.

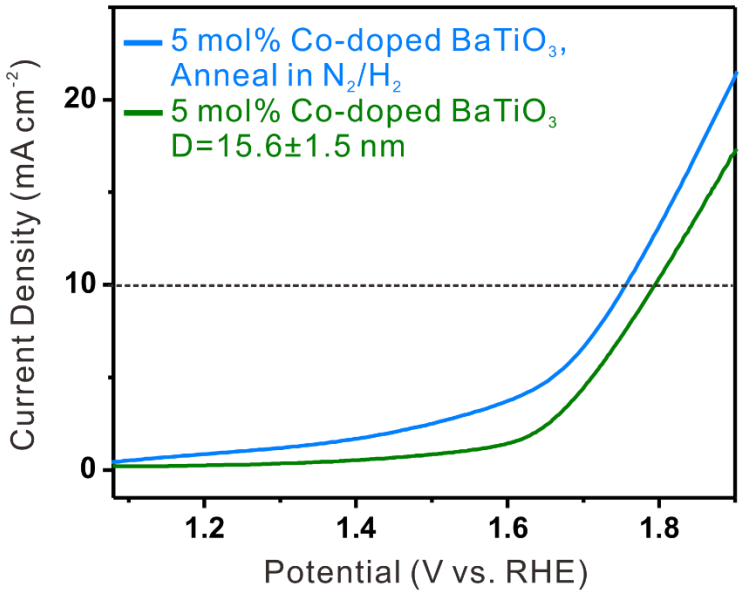

Figure 5.35 Oxygen evolution currents of 5 mol% Co-doped $BaTiO_3$ nanoparticles (D = 15.6 nm, synthesized by using Sample 2 in **Table 5.1** as nanoreactor) before and after further annealed in $95N_2$-$5H_2$, loaded onto glassy carbon electrode and measured in 0.1 M KOH.

To elucidate the underlying mechanism on the enhanced ORR performance of $BaTiO_3$ NPs after doping, we performed first-principles calculations based on density functional theory (DFT),[47,48] as implemented in the Vienna Ab initio Simulation Package (VASP).[49,50] As shown in **Figure 5.35 (a)**, we considered a (100) surface by a 9-atomic layer thick $BaTiO_3$ slab. All atoms were relaxed except for the bottom 4 atomic layers to mimic the bulk environment (lower panel; **Figure 5.35 (a-f)**). A $2\sqrt{2} \times 2\sqrt{2}$ supercell of the $BaTiO_3$ slab was chosen to model the effects of doping and surface processes. Such a supercell contains 40 Ba atoms, 32 Ti atoms, and 104 O atoms. **Figure 5.35 (b-c)** shows the relaxed atomic configurations of Co-doped $BaTiO_3$ and La-doped $BaTiO_3$, respectively, where a single Ti (Ba) atom is replaced by a Co (La) atom as the atomic radius and shell structure between Ti (Ba) and Co (La) atoms are similar. The relaxed atomic configurations of the surfaces with oxygen adsorption are shown in **Figure 5.35 (d-f)**. **Figure 5.35 (g-i)** depicts the projected density of states (PDOS) of the first and second atomic layers of the pristine $BaTiO_3$, Co-doped $BaTiO_3$, and La-doped $BaTiO_3$ surface. A bandgap of 1.523 eV around the Fermi energy can be clearly identified for pristine $BaTiO_3$. After doped with Co, several defect states occur within the bandgap, and these defect states are mainly from the Co dopant (**Figure 5.35 (h)**). In contrast to the case of Co-doping, La-doping did not introduce extra states between the valence band and the conduction band. Instead, La-doping lifts the Fermi energy up into the conduction band (**Figure 5.35 (i)**). Both changes in electronic states after doping with Co and La may in turn lead to an increase in the electrical conductivity. According to our calculations, the energy bands corresponding to the defect states of Co-doped $BaTiO_3$ is quite flat, signifying that these defect states are localized. Therefore, the electron transport in Co-doped $BaTiO_3$ should involve hopping through the localized defect states. Nevertheless, electrons in La-doped $BaTiO_3$ can only flow via the delocalized states of the conduction band.

Next, we examined how ORR reaction is affected by doping via calculating the free energy difference. Setting $\Phi = \Phi_{eq}$, the free energy diagrams can be obtained for comparison between pristine $BaTiO_3$ and Co-doped $BaTiO_3$ (**Figure 5.35 (j)**), as well as pristine $BaTiO_3$ and La-doped $BaTiO_3$ (**Figure 5.35 (k)**), via both PBE exchange correlation energy functional (solid line)[51] and the HSE06 (dash line).[52] Notably, the second reaction step was found to be the rate-limiting step for all the cases (pristine and doped $BaTiO_3$). The free energy barriers within this step are 0.942 (=0.269-(-0.673); for $BaTiO_3$), 0.752 (=0.430-(-0.322); for Co-doped $BaTiO_3$), and 0.547 (=0.622-(-0.075); for La-doped $BaTiO_3$) eV, respectively, based on PBE exchange correlation energy functional. The decrease in the free energy barrier can be understood in terms of adsorption energy. Specifically, it is the adsorption energy difference $\Delta E_2^{ads} = E_{\mathrm{ads}}(\mathrm{OOH}) - E_{\mathrm{ads}}(\mathrm{OO})$ that contributes primarily to the free energy change ΔG_2. From the simulation results shown in **Table 5.3**, the adsorption energies of OH, OO, OOH, and O were all found to be enhanced[53,54] and ΔE_2^{ads} is reduced after doping with both dopants (i.e., Co and La). As such, the free energy barriers of the ORR reaction are reduced, which is consistent with the enhanced ORR performance of $BaTiO_3$ after doping seen in experiments. Particularly, the enhanced adsorption is due to the pronounced substrate-adsorbate charge transfer in the case of La doping, and is because of the strong hybridization between t_{2g} orbitals of Co with the adsorbates for the Co doping case, respectively, as demonstrated in the case of oxygen adsorption (**Figure 5.36**).

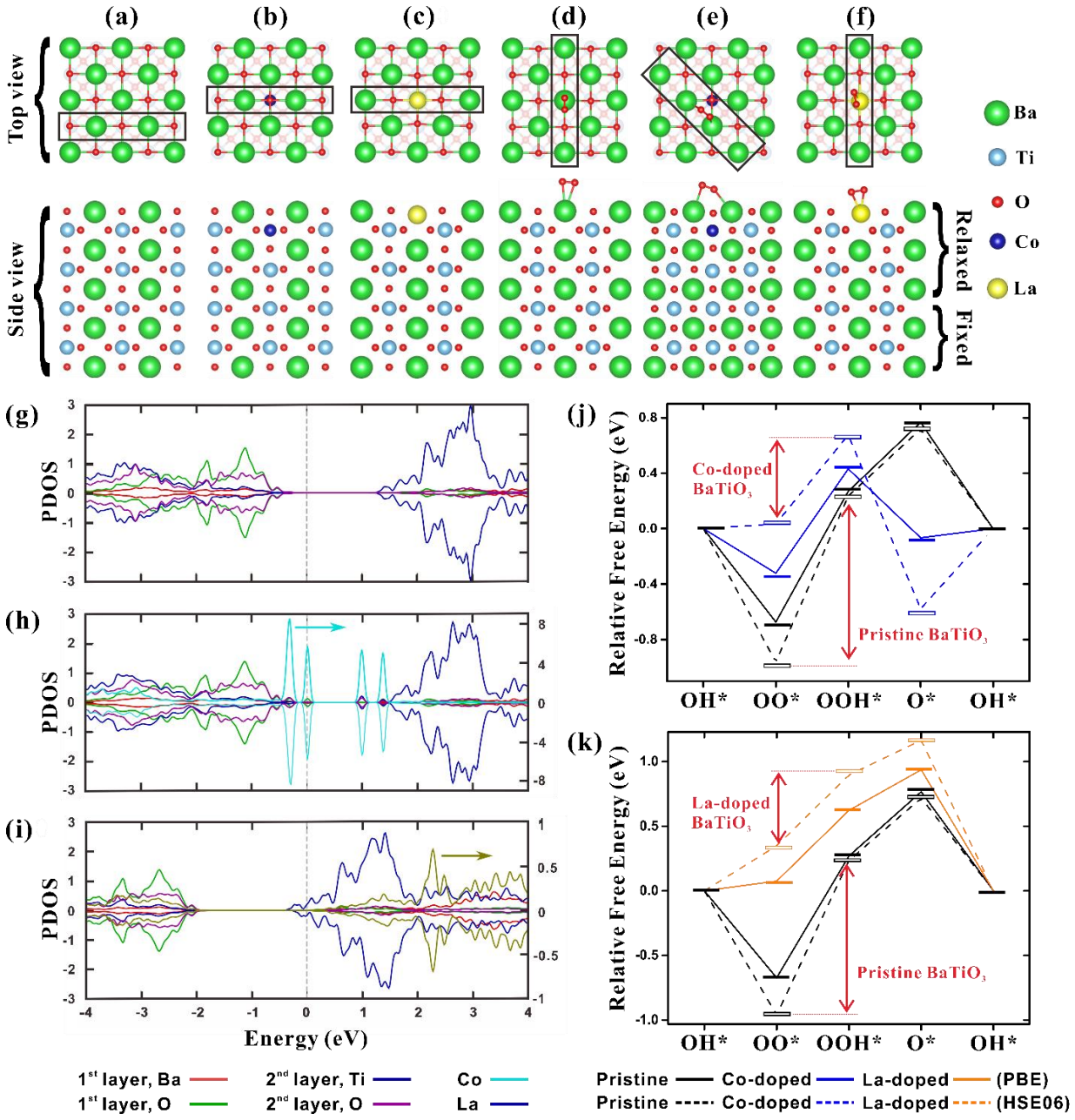

Figure 5.35 (a)-(f) Relaxed atomic configuration of pristine, Co-doped, and La-doped (100) $BaTiO_3$ surfaces **(a)-(c)** in the absence of oxygen adsorption and **(d)-(f)** with oxygen adsorption. In the top view, all atoms, except those in the topmost atomic layer and the dopant atom, are made opaque to highlight the surface layer. The black rectangles in the top view indicate the cross section for generating the side view below. **(g)-(i)** Projected density of states (PDOS) of the first and second atomic layers for the three surfaces shown in **(a)-(c)**, respectively. Fermi energy is set to zero. Unit for PDOS: number of states/eV/atom. **(j)** and **(k)** Free energy diagrams for the ORR reaction of **(j)** pristine $BaTiO_3$ and Co-doped $BaTiO_3$ and **(k)** pristine $BaTiO_3$ and La-doped $BaTiO_3$, respectively based on the Perdew–Burke–Ernzerhof (PBE, solid line) exchange correlation energy functional and the hybrid functional developed by Heyd–Scuseria–Ernzerhof (HSE06, dash line). The highest free energy barriers are marked in **(j)** and **(k)** with red arrows. Equilibrium external potential is adopted such that the net change in the free energy after a circle of ORR reaction equals zero.

Table 5.3 Adsorption energies for OH, OO, OOH, and O on the $BaTiO_3$ (100) surface with and without doping.

E_{ads} (eV)	OH	OO	OOH	O
$BaTiO_3$	-1.894	-0.439	-0.838	-2.186
Co-doped $BaTiO_3$	-2.533	-0.756	-1.369	-3.722
La-doped $BaTiO_3$	-4.020	-2.001	-2.815	-4.238

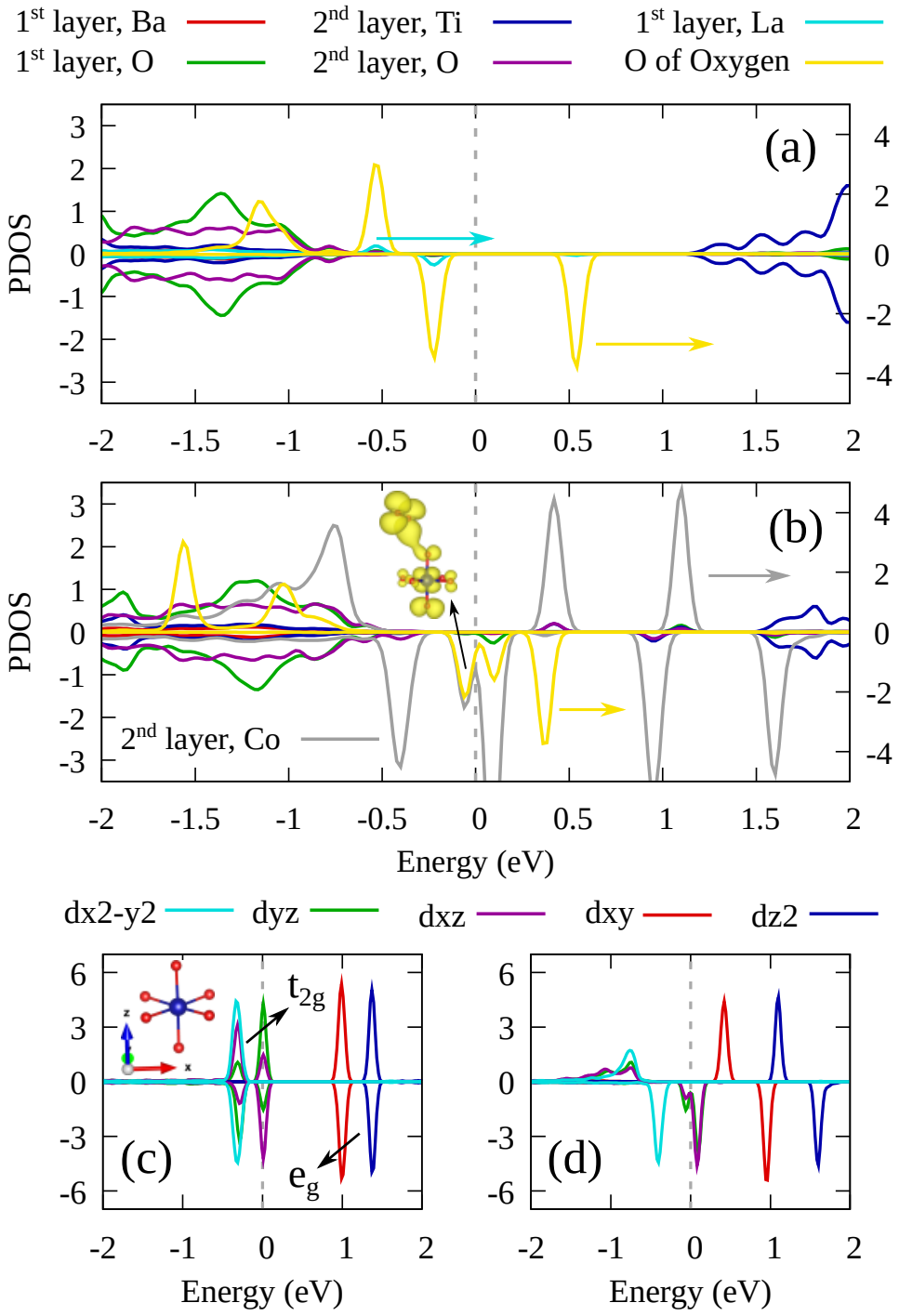

Figure 5.36 Projected density of states (PDOS) to surface atoms of **(a)** La-doped and **(b)** Co-doped (100) $BaTiO_3$ surfaces with the adsorption of an oxygen molecule per unit cell. PDOS to d orbitals of Co which is doped to the (100) $BaTiO_3$ surface **(c)** without and **(d)** with the adsorption of an oxygen molecule per unit cell. Positive PDOS is for spin-up electrons and negative PDOS is for spin-down electrons. The inset of panel **(c)** shows the crystal environment of Co for identifying t_{2g} and e_g orbitals. Unit for PDOS: number of states/eV/atom.

For a clean surface without any adsorbate, La dopants donate electrons to $BaTiO_3$ such that the Fermi level is lifted into the conduction band. After adsorption of an oxygen molecule, the electrons donated by La dopants are transferred to the oxygen molecule, which is evidenced by the conduction band becoming unoccupied again as shown in **Figure 5.36 (a)**. This amount of electron transfer is not present for oxygen adsorption on a pristine $BaTiO_3$ surface, underpinning the enhancement of the adsorption energy by La doping. **Figure 5.36 (b)** shows that the PDOS of Co and the PDOS of oxygen share the same peak positions around Fermi energy, and their magnitudes are both significantly large. This signifies that Co is hybridized with the adsorbed oxygen molecule although they are separated by a surface oxygen atom of $BaTiO_3$. The hybridization is further confirmed by the fact that a single Kohn-Sham orbital spreading over both the Co atom and the oxygen molecule, as shown in the inset of **Figure 5.36 (b)**. Moreover, **Figure 5.36 (c-d)** further display that it is the t_{2g} d orbitals of Co that hybridizes with the oxygen molecule.

Taken together, doping with Co and La dopants dramatically modifies the electronic structure of $BaTiO_3$ surface around Fermi energy, which may increase the electrical conductivity. Moreover, on the basis of free energy diagram before and after doping, free energy barriers were found to decrease after doping with both dopants owing to the change in adsorption energies of the intermediates during ORR reaction. As the calculations from both PDOS and free energy diagram correlate qualitatively well with the experimental results where the onset potentials, half-wave potential, and limiting current density increased when doped by both dopants, the enhanced ORR performance after doping could be ascribed to the reduced free energy barrier imposed by the formation of -OOH species during ORR reaction as well as the increased conductivity of $BaTiO_3$ NPs as a result of change in electronic states.

5.4 Conclusion

In summary, we developed a versatile route to uniform perovskite NPs with precisely controlled sizes and compositions (i.e., $BaTiO_3$, $PbTiO_3$, La-doped $BaTiO_3$ and Co-doped $BaTiO_3$) via capitalizing on amphiphilic star-like PAA-*b*-PS diblock copolymers as nanoreactors, and correlated the ORR activities to their sizes and compositions. Particularly, the capability of

tailoring the NP sizes (i.e., 8, 15 and 20 nm) is rendered by conveniently controlling the ATRP reaction time that yields inner PAA blocks of different molecular weights (i.e., lengths) for templating the precursors coordination and growth into NPs. Moreover, as-synthesized perovskite NPs are intimately ligated with outer PS blocks via original covalent bonding between inner PAA and outer PS blocks, leading to good solubility and long-term stability of NPs in various organic solvents. Notably, the crystallinity of perovskite NPs could be readily enhanced with the morphology retention when annealing as-synthesized NPs dispersed on graphene oxide. Investigation into size-dependent electrocatalysis of perovskite NPs reveals a progressively increased ORR activity as the NP size decreases. Moreover, the doped $BaTiO_3$ NPs (both La- and Co-doped) greatly outperform pristine $BaTiO_3$ NPs even at low dopant concentration, representing more positive onset potential and half-wave potential, large limiting current density, and excellent stability. The first-principles calculations demonstrate that the enhanced ORR performance of $BaTiO_3$ NPs after doping is a synergy of the reduced free energy barrier of the ORR reaction because of increased adsorption energy of intermediates and the improved conductivity as a result of the modification of electronic states. In addition to size and dopant effects, the influences of other possible factors such as the carbon content in catalysts that are generated due to the annealing of the outer PS chains at 600 ^{o}C in N_2 as well as defects (e.g., oxygen vacancies) on the surface of catalysts on ORR performance may also need to be considered, which will be carried out.

In principle, in addition to perovskites, a myriad of other functional nanomaterials (i.e., metal oxides, chalcogenides, carbides, nitrides and phosphates) with exquisitely controlled size, composition, and surface chemistry (i.e., changing the outer block of star-like diblock copolymer to functional polymers other than PS) may also be crafted by our amphiphilic star-like block copolymer nanoreactor strategy. Thus, these nanomaterials could render the scrutiny of the

correlation of size, composite, and surface chemistry to electrocatalytic performance, thereby underpinning future advances in developing a set of highly-active ORR, OER, or bifunctional ORR/OER electrocatalysts for use in rechargeable metal-air batteries, regenerative fuel cells, etc.

5.5 References

1. Liang, Y. *et al.* Co_3O_4 nanocrystals on graphene as a synergistic catalyst for oxygen reduction reaction. *Nat. Mater.* **10**, 780-786 (2011).
2. Zhu, H., Zhang, P. & Dai, S. Recent advances of lanthanum-based perovskite oxides for catalysis. *ACS Catal.* **5**, 6370-6385 (2015).
3. Stephens, I. E., Bondarenko, A. S., Grønbjerg, U., Rossmeisl, J. & Chorkendorff, I. Understanding the electrocatalysis of oxygen reduction on platinum and its alloys. *Energy Environ. Sci.* **5**, 6744-6762 (2012).
4. Tong, Y. *et al.* Spin-state regulation of perovskite cobaltite to realize enhanced oxygen evolution activity. *Chem* **3**, 812-821 (2017).
5. Suntivich, J. *et al.* Design principles for oxygen-reduction activity on perovskite oxide catalysts for fuel cells and metal–air batteries. *Nat. Chem.* **3**, 546-550 (2011).
6. Lefèvre, M., Proietti, E., Jaouen, F. & Dodelet, J.-P. Iron-based catalysts with improved oxygen reduction activity in polymer electrolyte fuel cells. *Science* **324**, 71-74 (2009).
7. Jung, H. M., Kang, J.-H., Yang, S. Y., Won, J. C. & Kim, Y. S. Barium titanate nanoparticles with diblock copolymer shielding layers for high-energy density nanocomposites. *Chem. Mater.* **22**, 450-456 (2010).
8. Kim, P. *et al.* Phosphonic acid-modified barium titanate polymer nanocomposites with high permittivity and dielectric strength. *Adv. Mater.* **19**, 1001-1005 (2007).
9. Yamada, I. *et al.* Bifunctional oxygen reaction catalysis of quadruple manganese perovskites. *Adv. Mater.* **29**, 1603004 (2017).
10. Peng, S. *et al.* Electronic and defective engineering of electrospun $CaMnO_3$ nanotubes for enhanced oxygen electrocatalysis in rechargeable zinc–air batteries. *Adv. Energy Mater.* **8**, 1800612 (2018).
11. Yoo, J. S., Liu, Y., Rong, X. & Kolpak, A. M. Electronic origin and kinetic feasibility of the lattice oxygen participation during the oxygen evolution reaction on perovskites. *J. Phys. Chem. Lett.* **9**, 1473-1479 (2018).
12. Grimaud, A. *et al.* Double perovskites as a family of highly active catalysts for oxygen evolution in alkaline solution. *Nat. Commun.* **4**, 2439 (2013).
13. Mao, Y., Mao, S., Ye, Z.-G., Xie, Z. & Zheng, L. Size-dependences of the dielectric and ferroelectric properties of $BaTiO_3$/polyvinylidene fluoride nanocomposites. *J. Appl. Phys.* **108**, 014102 (2010).
14. Guo, H. *et al.* Structure evolution and dielectric behavior of polystyrene-capped barium titanate nanoparticles. *J. Mater. Chem.* **22**, 23944-23951 (2012).
15. Huang, X., Zhao, G., Wang, G. & Irvine, J. T. Synthesis and applications of nanoporous perovskite metal oxides. *Chem. Sci.* **9**, 3623-3637 (2018).
16. Jiang, B. *et al.* Barium titanate at the nanoscale: controlled synthesis and dielectric and ferroelectric properties. *Chem. Soc. Rev.* **48**, 1194-1228 (2019).
17. Gomes, M. A., Lima, A. S., Eguiluz, K. I. & Salazar-Banda, G. R. Wet chemical synthesis of rare earth-doped barium titanate nanoparticles. *J. Mater. Sci.* **51**, 4709-4727 (2016).
18. Guo, W., Datye, A. K. & Ward, T. L. Synthesis of barium titanate powders by aerosol pyrolysis of a Pechini-type precursor solution. *J. Mater. Chem.* **15**, 470-477 (2005).
19. Chon, J. *et al.* High-κ dielectric sol− gel hybrid materials containing barium titanate nanoparticles. *Chem. Mater.* **22**, 5445-5452 (2010).
20. Sun, Q. *et al.* Crystalline structure, defect chemistry and room temperature colossal permittivity of Nd-doped barium titanate. *Sci. Rep.* **7**, 42274 (2017).
21. O'Brien, S., Brus, L. & Murray, C. B. Synthesis of monodisperse nanoparticles of barium titanate: toward a generalized strategy of oxide nanoparticle synthesis. *J. Am. Chem. Soc.* **123**, 12085-12086 (2001).
22. Urban, J. J., Spanier, J. E., Ouyang, L., Yun, W. S. & Park, H. Single-crystalline barium titanate nanowires. *Adv. Mater.* **15**, 423-426 (2003).

23. Brutchey, R. L. & Morse, D. E. Template-free, low-temperature synthesis of crystalline barium titanate nanoparticles under bio-inspired conditions. *Angew. Chem. Int. Ed.* **45**, 6564-6566 (2006).
24. Braunecker, W. A. & Matyjaszewski, K. Controlled/living radical polymerization: Features, developments, and perspectives. *Prog. Polym. Sci.* **32**, 93-146 (2007).
25. Wang, J.-S. & Matyjaszewski, K. Controlled/" living" radical polymerization. atom transfer radical polymerization in the presence of transition-metal complexes. *J. Am. Chem. Soc.* **117**, 5614-5615 (1995).
26. Ehre, D., Cohen, H., Lyahovitskaya, V. & Lubomirsky, I. X-ray photoelectron spectroscopy of amorphous and quasiamorphous phases of $BaTiO_3$ and $SrTiO_3$. *Phys. Rev. B* **77**, 184106 (2008).
27. Wang, J. *et al.* Ferroelectricity in a quasiamorphous ultrathin $BaTiO_3$ film. *Phys. Rev. B* **84**, 205426 (2011).
28. Lin, C., Posadas, A., Hadamek, T. & Demkov, A. A. Final-state effect on x-ray photoelectron spectrum of nominally d^1 and *n*-doped d^0 transition-metal oxides. *Phys. Rev. B* **92**, 035110 (2015).
29. Zhang, S.-W. *et al.* Copper-nanoparticle-dispersed amorphous $BaTiO_3$ thin films as hole-trapping centers: enhanced photocatalytic activity and stability. *RSC Adv.* **9**, 5045-5052 (2019).
30. Maglione, M., Böhmer, R., Loidl, A. & Höchli, U. Polar relaxation mode in pure and iron-doped barium titanate. *Phys. Rev. B* **40**, 11441 (1989).
31. Freeman, C. L., Dawson, J. A., Harding, J. H., Ben, L. B. & Sinclair, D. C. The Influence of A-Site Rare Earth Ion Size in Controlling the Curie Temperature of $Ba_{1-x}RE_xTi_{1-x/4}O_3$. *Adv. Funct. Mater.* **23**, 491-495 (2013).
32. Verma, K. C. & Kotnala, R. Multiferroic approach for Cr, Mn, Fe, Co, Ni, Cu substituted $BaTiO_3$ nanoparticles. *Mater. Res. Express.* **3**, 055006 (2016).
33. Zhou, S. *et al.* Engineering electrocatalytic activity in nanosized perovskite cobaltite through surface spin-state transition. *Nat. Commun.* **7**, 1-7 (2016).
34. Wang, Y. & Cheng, H.-P. Oxygen reduction activity on perovskite oxide surfaces: a comparative first-principles study of $LaMnO_3$, $LaFeO_3$, and $LaCrO_3$. *J. Phys. Chem. C* **117**, 2106-2112 (2013).
35. Pang, X., Zhao, L., Han, W., Xin, X. & Lin, Z. A general and robust strategy for the synthesis of nearly monodisperse colloidal nanocrystals. *Nat. Nanotechnol.* **8**, 426 (2013).
36. Morrison, F. D., Sinclair, D. C. & West, A. R. Electrical and structural characteristics of lanthanum-doped barium titanate ceramics. *J. Appl. Phys.* **86**, 6355-6366 (1999).
37. Shuai, Y. *et al.* Decisive role of oxygen vacancy in ferroelectric versus ferromagnetic Mn-doped $BaTiO_3$ thin films. *J. Appl. Phys.* **109**, 084105 (2011).
38. Costanzo, T., McCracken, J., Rotaru, A. & Caruntu, G. Quasi-Monodisperse Transition-Metal-Doped $BaTiO_3$ (M= Cr, Mn, Fe, Co) Colloidal Nanocrystals with Multiferroic Properties. *ACS Appl. Nano Mater.* **1**, 4863-4874 (2018).
39. Risch, M. Perovskite electrocatalysts for the oxygen reduction reaction in alkaline media. *Catalysts* **7**, 154 (2017).
40. Zeng, Z., Calle-Vallejo, F., Mogensen, M. B. & Rossmeisl, J. Generalized trends in the formation energies of perovskite oxides. *Phys. Chem. Chem. Phys.* **15**, 7526-7533 (2013).
41. Kim, W. S. *et al.* Facile synthesis of perovskite $LaMnO_{3+\delta}$ nanoparticles for the oxygen reduction reaction. *J. Catal.* **344**, 578-582 (2016).
42. Seo, J., Cha, D., Takanabe, K., Kubota, J. & Domen, K. Particle size dependence on oxygen reduction reaction activity of electrodeposited TaO_x catalysts in acidic media. *Phys. Chem. Chem. Phys.* **16**, 895-898 (2014).
43. Ohnishi, R., Takanabe, K., Katayama, M., Kubota, J. & Domen, K. Nano-nitride cathode catalysts of Ti, Ta, and Nb for polymer electrolyte fuel cells: Temperature-programmed desorption investigation of molecularly adsorbed oxygen at low temperature. *J. Phys. Chem. C* **117**, 496-502 (2013).
44. Celorrio, V. *et al.* Oxygen Reduction at Carbon-Supported Lanthanides: The Role of the B-Site. *ChemElectroChem* **3**, 283-291 (2016).
45. Kim, J., Yin, X., Tsao, K.-C., Fang, S. & Yang, H. $Ca_2Mn_2O_5$ as oxygen-deficient perovskite electrocatalyst for oxygen evolution reaction. *J. Am. Chem. Soc.* **136**, 14646-14649 (2014).

46. Zhang, J. *et al.* In situ formation of oxygen vacancy in perovskite $Sr_{0.95}Ti_{0.8}Nb_{0.1}M_{0.1}O_3$ (M= Mn, Cr) toward efficient carbon dioxide electrolysis. *Sci. Rep.* **4**, 1-14 (2014).
47. Hohenberg, P. & Kohn, W. Inhomogeneous electron gas. *Phys. Rev.* **136**, B864 (1964).
48. Kohn, W. & Sham, L. J. Self-consistent equations including exchange and correlation effects. *Phys. Rev.* **140**, A1133 (1965).
49. Kresse, G. Ab initio molecular dynamics for liquid metals. *J. Non-Cryst. Solids* **192**, 222-229 (1995).
50. Kresse, G. & Joubert, D. From ultrasoft pseudopotentials to the projector augmented-wave method. *Phys. Rev. B* **59**, 1758 (1999).
51. Perdew, J. P., Burke, K. & Ernzerhof, M. Generalized gradient approximation made simple. *Phys. Rev. Lett.* **77**, 3865 (1996).
52. Krukau, A. V., Vydrov, O. A., Izmaylov, A. F. & Scuseria, G. E. Influence of the exchange screening parameter on the performance of screened hybrid functionals. *J. Chem. Phys.* **125**, 224106 (2006).
53. An, L. *et al.* Heterostructure-promoted oxygen electrocatalysis enables rechargeable zinc–air battery with neutral aqueous electrolyte. *J. Am. Chem. Soc.* **140**, 17624-17631 (2018).
54. Rück, M., Bandarenka, A., Calle-Vallejo, F. & Gagliardi, A. Oxygen reduction reaction: rapid prediction of mass activity of nanostructured platinum electrocatalysts. *J. Phys. Chem. Lett.* **9**, 4463-4468 (2018).

CHAPTER 6. MONODISPERSE RUDDLESDEN-POPPER LAYERED PEROVSKITE NANOCATALYSTS WITH CONTROLLABLE SIZE FOR ENHANCED OXYGEN REDUCTION AND EVOLUTION REACTIONS

Yeu-Wei Harn *et al.* in preparation (to be submitted to *Advanced Materials*)

6.1 Introduction

Oxygen electrode reactions, including oxygen evolution reaction (OER) and oxygen reduction reaction (ORR), are ubiquitous in energy conversion and storage devices, while their sluggish kinetics and high overpotentials significantly impact the device performance.[1-2] Perovskites, as noble-metal-free alternatives, have attracted much interest arising from the synergic advantages of high intrinsic activities, flexibility in adopting a myriad of composition and structure, environmental friendliness, and structural stability.[3-4] Among all the identified critical parameters affecting the catalytic activity of perovskites, crystal structure is one of the most important descriptors as it dominates the electronic structure, and thus the resulting physicochemical properties and related performance.[5] For instance, single-crystalline $SrRuO_3$ thin films of both orthorhombic and tetragonal phases were synthesized. 30% decrease in the overpotential for the OER activity of $SrRuO_3$ of tetragonal phase was then discovered, resulting from the phase-transition-induced modification in the electronic structure.[6] Another example lied in $LaNiO_3$. No localization of an e_g electron was permitted in the bulk of rhombohedral structure whereas a localized e_g electron was allowed with the surface of tetragonal structure because of different site symmetries, rendering completely different electrocatalytic activities.[3]

Currently, the research mainly focuses on simple perovskites with the general formula of ABO_3, where A is a rare earth metal and B is a transition metal. In addition to simple perovskites, layered

perovskites (e.g. Ruddlesden-Popper layered perovskites with a general formula of $A_{n+1}B_nO_{3n+1}$, and double perovskites with a general formula of $AA'B_2O_6$ or $A_2BB'O_6$) with intriguing structures have attracted increasing attention.[7-10] They have demonstrated high chemical diffusion and surface-exchange coefficient toward ORR,[11] mixed ionic-electronic conductivity[12] and excellent oxygen-ion diffusion as well as proton conductivity,[13] which can be beneficial to applications in fuel cells,[14] rechargeable metal-air batteries,[7, 15] and oxygen permeation membranes.[16] For example, the superior activities and stability of double perovskites $(Ln_{0.5}Ba_{0.5})CoO_{3-\delta}$ (Ln = Pr, Sm, Gd and Ho) for OER in alkaline solution were demonstrated, which resulted from the optimum location of the O p band center relative to the Fermi level that was identified by the ab initio studies.[17] On the other hand, $La_{1.7}Ca_{0.3}Ni_{0.75}Cu_{0.25}O_4$ (LCNC), with Ruddlesden-Popper layered perovskite structure, revealed a reduced charge overpotential for Li_2O_2 oxidation by more than 0.4 V compared to the catalyst (i.e., LCNO)-free carbon electrode, which can be attributed to the interlayer characteristics of the layered perovskite structure in facilitating the oxygen evolution process.[18] In addition, the catalytic activity toward oxygen exchange/reduction of $La_2NiO_{4+\delta}$ with various surface structures was investigated.[11] Due to the optimal energetics associated with surface oxygen exchange, Ni oxide-terminated $La_2NiO_{4+\delta}$ with (001) surfaces was identified with the highest catalytic activity as well as stability under reaction conditions.[11] Nevertheless, the studies on bifunctionality (both ORR and OER) over Ruddlesden-Popper layered perovskites, especially at low temperature are limited, and most of them focused on nickel oxide-based Ruddlesden-Popper type materials.[11, 19] Particularly, *to the best of our knowledge*, the electrocatalytic activities of cobalt oxides-based materials with Ruddlesden-Popper layered perovskite structure at room temperature has yet to be explored.

Here, we report a versatile synthetic strategy for crafting lanthanum (La)-based nanoparticles, i.e., $LaFeO_3$, $LaMnO_3$ and La_2CoO_4, with various crystal structures by capitalizing amphiphilic star-like diblock copolymers as nanoreactors and introduce the Ruddlesden-Popper layered perovskite, La_2CoO_4, as a highly active and durable bifunctional electrocatalyst for both ORR and OER at low temperature. Intriguingly, the synthetic temperature for obtaining pure La_2CoO_4, generally higher than 1000 ^oC in previous literature,[20] can be greatly reduced (to 600 ^oC when annealed with graphene oxide) with our synthetic method. The discrepancy is possibly originated from reduced particle size (i.e., > couple hundreds of nm in previously literature compared to < 25 nm in this study). In addition, by precisely controlling the molecular weight of the inner poly(acrylic acid) (PAA) block, the size of the as-synthesized nanoparticles, which occupied the compartment of inner PAA block exclusively via strong coordination interaction between precursors and the functional group of PAA block, can be facilely tailored. Therefore, this nanoreactor-assisted strategy enables the investigation into size-dependent electrocatalytic activities of layered perovskite NPs, rendering nanocatalysts with optimized performance. Finally, the detailed characterizations suggest that the excellent electrocatalytic performance of La_2CoO_4 could possibly be ascribed to highly active lattice oxygen and the increased amount of hydroxyl (OH^-) groups. By extension, the strategy of exploiting the star-like polymers as nanoreactors can provide the opportunities to scrutinize structure-dependent electrocatalytic activities of the perovskites and their derivatives with controllable size because of the significantly reduced synthetic temperature, thus resulting in high-performance bifunctional nanocatalysts in the field of energy conversion and storage.

6.2 Experiment Details

The detailed synthetic processes of star-like PAA-*b*-PS diblock copolymer nanoreactor as well as La-based nanoparticles ($LaFeO_3$, $LaMnO_3$ and La_2CoO_4 nanoparticles) have been described in Chapter 3, *3.1* and *3.2*, respectively. Below we just specified the procedure for the characterizations used in this study and electrochemical measurements.

6.2.1 Characterization

Molecular weights of polymers and molecular weight distribution were characterized by gel permeation chromatography (GPC), equipped with an Agilent1100 with a G1310A pump, a G1362A refractive detector, and a G1314A variable wavelength detector. THF was used as the eluent at 1.0 ml/min and 35 ^{o}C. By using PS standard samples, one 5 μm LP gel column (500 Å, molecular range: 500-2 $\times 10^4$ g/ mol) and two 5 μm LP gel mixed bed columns (molecular range: 200-3 $\times$ 10^6 g/mol) were calibrated. Proton nuclear magnetic resonance (^{1}H NMR) characterizations were conducted on Varian VXR-300 spectroscopy using $CDCl_3$ as solvent. The morphology and size distribution histogram of PS-ligated La-based NPs were measured by transmission electron microscope (TEM, JOEL 100; operated at 100 kV). TEM samples were prepared by dropping a dilution toluene solution containing La-based NPs onto a carbon-coated copper TEM grid (300 mesh) and dried naturally in ambient conditions. Dynamic light scattering (DLS) results were obtained using laser light scattering spectrometer (Wyatt DyanoPro) at 25 ^{o}C. The crystalline structures of La-based perovskite NPs were measured by X-ray powder diffraction (XRD, Pananlytic XPert PRO Alpha-1 XRD, Cu Kα radiation (λ = 0.154 nm)). Chemical states for the elements of the La-based perovskite NPs were measured by X-ray photoelectron spectroscopy (XPS, Thermo K-alpha XPS).

6.2.2 Electrochemical Measurements

Electrochemical measurements were conducted in a three-electrode system using an Ag/AgCl electrode as the reference electrode, graphite rode as the counter electrode, and a glassy carbon electrode deposited with the composite of La-based perovskite NPs, rGO and carbon black (CB) as the working electrode. The step for preparing inks containing the as-prepared composite was described as follows. First, 0.75 mg of catalyst (consisted of La-based perovskite NPs and rGO), 0.25 mg of CB, and 20 ul of 5 wt% Nafion solution were dispersed in 0.15 ml of 1:1 v/v water/ethanol mixed solvent. After sonicating for more than 1 h, 25 µl of the catalyst ink was loaded onto glassy carbon electrode by dropping 5 µl at a time 5 times, rendering ~0.156 mg loading of the catalyst. The ink was dried slowly in ambient condition, and a uniform catalyst film deposited on the electrode surface was then obtained. Notably, the addition of CB when preparing the catalyst was due to low conductivity of the annealed composite (consisting of La-based perovskite NPs and rGO), possibly due to some rGO losses during the two-step annealing condition. Cyclic voltammetry (CV) was first performed with 0.1 M KOH as electrolyte that was saturated with oxygen by bubbling O_2 prior to the start of each measurement. The working electrode was cycled 10 times at a scan rate of 10 mV s^{-1} before the data was recorded. In control experiments, CV measurements were also conducted in N_2-saturated environment by switching to N_2 flow through the electrochemical cell.

For measuring both oxygen reduction reaction (ORR) and oxygen evolution reaction (OER) activities at ambient temperature, rotation disc electrode (RDE) measurements were conducted and the same method for preparing the catalyst on working electrode was used. In terms of ORR measurements, linear sweep voltammetry (LSV) was recorded in an applied potential between 100 mV and -1 V vs. Ag/AgCl at a scan rate of 5 mV s^{-1}. During the measurements, a continuous O_2

flow was supplied to ensure the electrolyte was saturated with O_2. The disk rotation rates for the ORR ranged from 400 to 1600 rpm. The ORR stability in O_2-saturated 0.1 M KOH was performed by chronoamperometry (*i* - *t*) at 0.75 V. The kinetic parameters in ORR, including the electron transfer number (*n*) and the kinetic current density (J_k) can be obtained by Koutechy-Levich (K-L, J^{-1} vs. ω^{-1}) plot. The slopes of their best linear fit lines were used to calculate the electrons transferred number (*n*) based on the equation below.

$$\frac{1}{J} = \frac{1}{J_L} + \frac{1}{J_K} = \frac{1}{B\omega^{\frac{1}{2}}} + \frac{1}{J_K}$$

$$B = 0.62nFC_0(D_0)^{\frac{2}{3}}\nu^{\frac{-1}{6}}$$

$$J_K = nFkC_0$$

where J is the current density of experimental measurement, J_K and J_L are the kinetic- and diffusion-limiting current densities, separately, ω is the angular velocity, *n* is the electron transfer number, *F* is the Faraday constant ($96485\ \mathrm{C\ mol^{-1}}$), C_o is the bulk concentration of O_2 in 0.1 M KOH electrolyte ($1.21 \times 10^{-6}\ \mathrm{mol\ cm^{-3}}$) D_0 is the diffusion coefficient of oxygen ($1.9 \times 10^{-5}\ cm^2\ \mathrm{s^{-1}}$), *v* is the kinematic viscosity of the electrolyte ($0.01\ cm^2\ \mathrm{s^{-1}}$) and *k* is the electron-transfer rate constant.

For OER measurements, which were conducted in 1 M KOH electrolyte, the experimental conditions were the same as the ORR measurement except the applied potential range changed between 100 mV and 1 V vs. Ag/AgCl. The polarization curves were replotted as applied potential (V) vs. log current (log *j*) to get Tafel plots for quantification of the OER activities of all the La-based perovskite NPs. The OER stability tests were carried out by recording the corresponding LSV before and after 1500 cycles of CV measurements ranging from 0.1 V to 0.9 V vs. Ag/AgCl at the scan rate of 200 mV s^{-1}. In this work, all the potentials vs. Ag/AgCl were converted to the

reversible hydrogen electrode (RHE) by the equation: $E(RHE) = E(Ag/AgCl) + 0.059 \times pH + E^0(Ag/AgCl)\ (0.1976\ V)\ V$.

6.3 Results and Discussion

The synthetic strategy for monodisperse La-based perovskite and layered perovskite nanoparticles (NPs), i.e., $LaFeO_3$, $LaMnO_3$ and $LaCo_2O_4$ NPs, ligated with outer polystyrene (PS) block on the surface via employing amphiphilic star-like poly(acrylic acrylate)-*block*-PS (denoted PAA-*b*-PS) diblock copolymer as nanoreactor are depicted in **Figure 6.1**. Amphiphilic star-like PAA-*b*-PS diblock copolymers with varied molecular weights of the inner PAA block can be synthesized by atom transfer radical polymerization (ATRP) of *tert*-butyl acrylate (*t*BA) and styrene, sequentially, capitalizing on brominated β-CD (denoted 21Br- β-CD) as the initiator (upper second panel in **Figure 6.1**), then hydrolysis of the inner P*t*BA block into PAA. The nearly 100% esterification efficiency of converting 21 hydroxyl groups of β-CD into Br-containing sites was verified by proton nuclear magnetic resonance (^{1}H NMR, **Figure 6.2 (a)**). Successful ATRP of both *t*BA and styrene with tailorable molecular weight and narrow molecular weight distribution was confirmed by both ^{1}H NMR (**Figure 6.2 (b, c)**) and monomodal gel permeation chromatography (GPC, **Figure 6.3**) traces. The *tert*-butyl substituents of the inner P*t*BA block can be easily hydrolyzed by using trifluoroacetic acid, yielding star-like PAA-*b*-PS diblock copolymer. DLS results exhibited uniform sizes of the amphiphilic star-like PAA-*b*-PS diblock copolymers, and the size gradually increased as the molecular weight of the star-like polymer increased (**Figure 6.4**), rendering star-like PAA-*b*-PS diblock copolymers excellent nanoreactors for forming uniform NPs with controllable size, as demonstrated below.

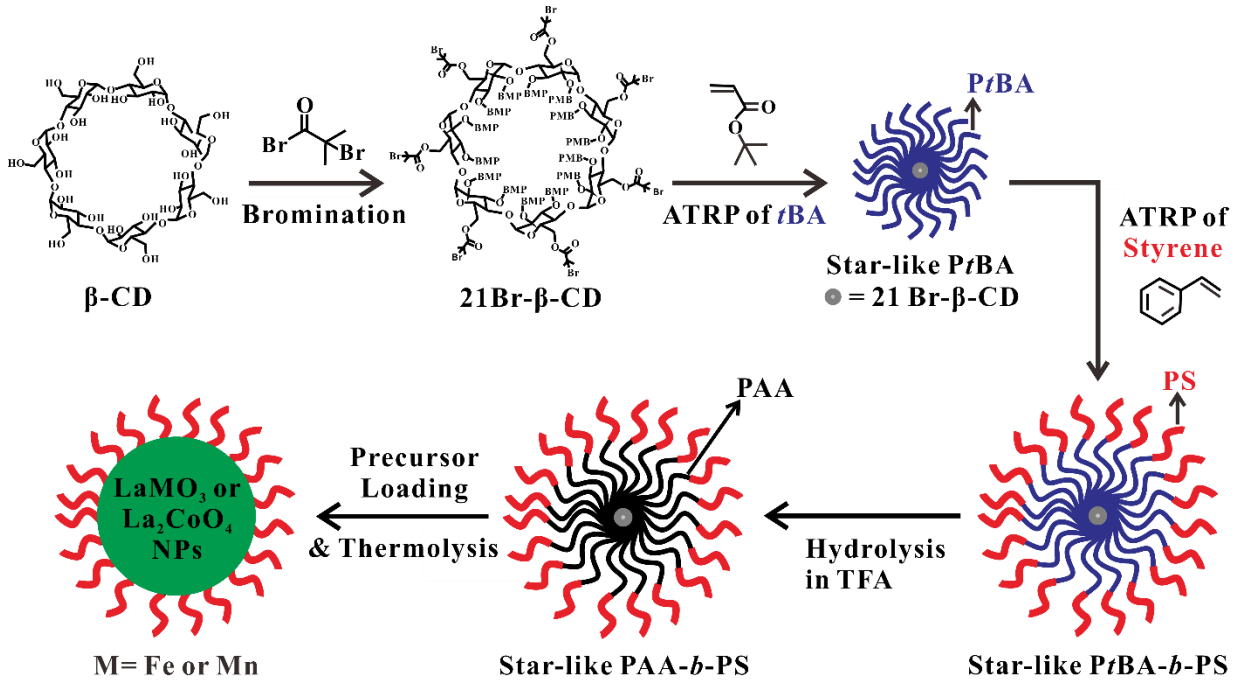

Figure 6.1 Stepwise representation of synthetic route to PS-ligated La-based perovskite and layered perovskite nanoparticles by employing star-like PAA-*b*-PS diblock copolymer as nanoreactors.

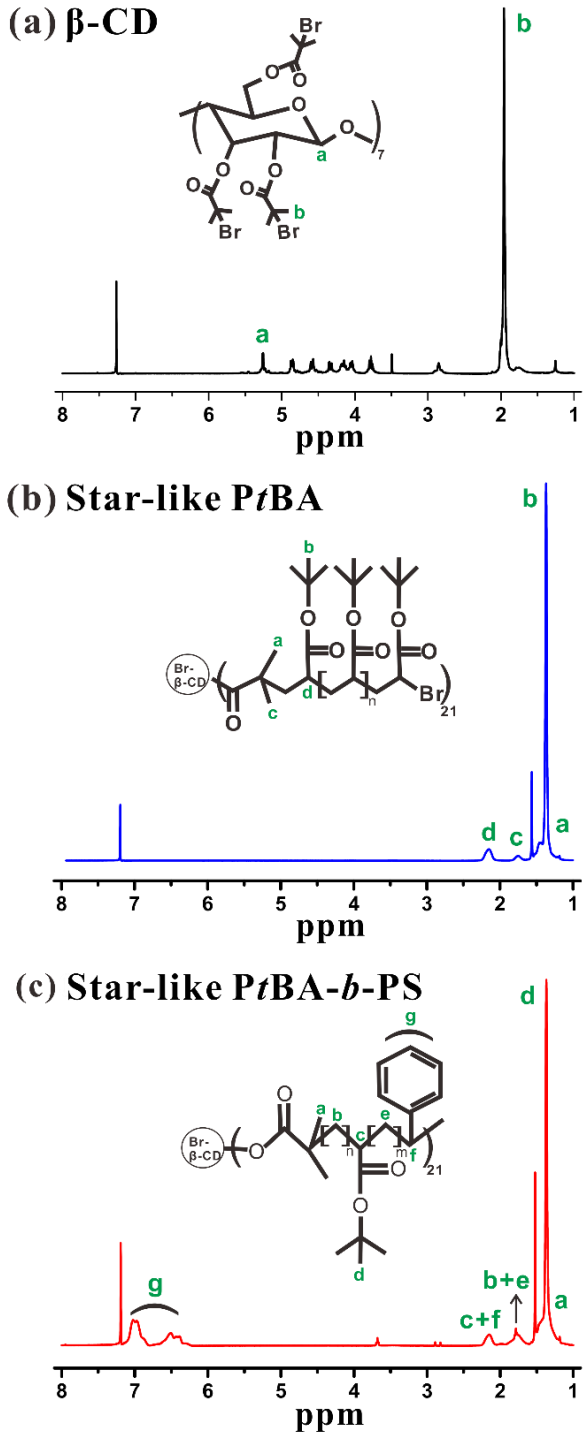

Figure 6.2 ^{1}H NMR spectra of **(a)** brominated β-CD (denoted 21Br-β-CD). **(b)** Star-like poly(*tert*-butyl acrylate) (P*t*BA) homopolymer and **(c)** star-like poly(*tert*-butyl acrylate)-*block*-polystyrene (denoted P*t*BA-*b*-PS). All samples were measured by using $CDCl_3$ as solvent.

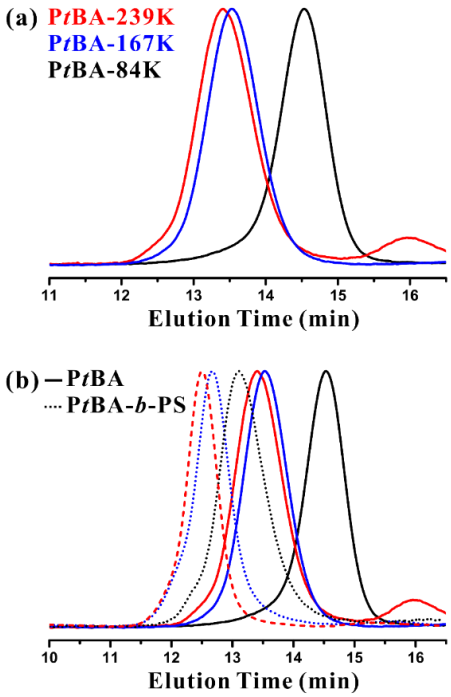

Figure 6.3 (a) GPC results of three star-like P*t*BA homopolymers, corresponding to the inner P*t*BA block of Sample 1-3 in **Table 6.1**, respectively. **(b)** GPC results of three star-like P*t*BA homopolymer (solid line) and three star-like P*t*BA-*b*-PS diblock copolymer (dash line), corresponding to Sample 1-3 in **Table 6.1**, respectively. Curve with the same color in **(b)** (between solid line and dash line) indicates the second PS block was grown from the corresponding inner P*t*BA block.

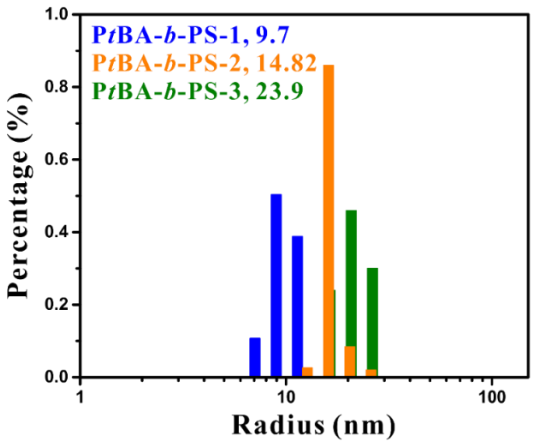

Figure 6.4 Dynamic light scattering (DLS) characterization on a series of star-like P*t*BA-*b*-PS diblock copolymers in diphenyl ether (DPE). The histogram in blue, orange, and green color represents the radius distribution of Sample 1-3 listed in **Table 6.1**, respectively.

The resulting star-like PAA-*b*-PS diblock copolymers can be employed as nanoreactors for crafting of monodisperse, PS-ligated perovskite and layered perovskite NPs, including $LaFeO_3$ and $LaMnO_3$ with perovskite structure and La_2CoO_4 with Ruddlesden-Popper layered perovskite structure (see *Experimental Section* for more synthetic details). In brief, star-like diblock copolymer and precursors (for both La and corresponding transition metal) were first dissolved in reaction solvent (i.e., diphenyl ether). Sufficient stirring time of this solution was required to ensure metal moieties of precursors coordinated with the carboxylic acid groups (-COOH) of inner PAA block selectively and the hydrophilic PAA regime was fully occupied by the precursors. The high concentration of precursors within PAA compartment can thus facilitate the nucleation and growth of the NPs during NPs formation via thermolysis (lower left panel in **Figure 6.1**). Notably, this nanoreactor-assisted synthetic strategy is advantageous in two aspects. First, since the precursors and thus the as-synthesized NPs were confined within the inner PAA block, the diameter of the perovskite and layered perovskite NPs can be easily tuned by changing the molecular weight of the inner PAA block of the star-like PAA-*b*-PS diblock copolymer (the detailed information of star-like P*t*BA homopolymer, star-like P*t*BA-*b*-PS diblock copolymer and the average diameter of the resulting NPs grown using the respective nanoreactors were shown in **Table 6.1**). Second, the as-synthesized NPs had less tendency to aggregate and good solubility in various common organic solvents because the surface of the NPs was intimately and permanently capped with outer PS block.

Table 6.1 Summary of star-like P*t*BA homopolymers, star-like P*t*BA-*b*-PS diblock copolymers, hydrodynamic radii of the star-like PAA-*b*-PS diblock copolymers and the sizes of La-based perovskite and layer perovskite nanoparticle by employing the corresponding star-like PAA-*b*-PS diblock copolymers as nanoreactors

Samples	$M_{n,\ GPC}$ of star-like P*t*BA block[a]	$M_{n,\ NMR}$ of star-like P*t*BA block[b]	$M_{n,\ GPC}$ of star-like P*t*BA-*b*-PS block[c]	$M_{n,\ NMR}$ of PS block[d]	PDI[e]	Hydrodynamic radii of star-like PAA-*b*-PS diblock copolymers[f]	Sizes of NPs[g]
1	84K	5,000	219K	4,000	1.16	9.7 nm	8.5 ± 0.8 nm (La_2CoO_4)
2	167K	5,900	342K	4,400	1.15	14.8 nm	16.2 ± 1.4 nm ($LaFeO_3$) 16.7 ± 1.3 nm ($LaMnO_3$) 17.1 ± 1.5 nm (La_2CoO_4)
3	239K	6,500	413K	4,500	1.13	23.9 nm	22.1 ± 2.2 nm (La_2CoO_4)

Notes: [a] Number-average molecular weight, $M_{n,\ GPC}$ of star-like P*t*BA homopolymer determined by GPC, calibrated by PS standards. [b] M_n of each P*t*BA arm calculated from ^{1}H NMR data (**Figure S1b**) based on the following equation:

$$M_{n,\ PtBA} = \frac{A_b/9}{A_a/6} \times 128.17$$

where A_b and A_a are the integral area of the methyl protons in the *tert*-butyl group of P*t*BA chains and the integral area of methyl protons at the α-end of P*t*BA chains, separately, and 128.17 is the molecular weight of the *t*BA monomer. [c] Number-average molecular weight, $M_{n,\ GPC}$ of star-like P*t*BA-*b*-PS diblock copolymer determined by GPC. [d] M_n of each PS arm calculated from ^{1}H NMR data (**Figure 6.2 (c)**) based on the following equation:

$$M_{n,\ PS} = \frac{A_g/5}{A_a/6} \times 104.15$$

where A_g and A_a are the integral area of phenyl protons on the PS block and the integral area of methyl protons at the α-end of the diblock arm, respectively, and 104.15 is the molecular weight of St monomer. [e] Polydispersity (PDI) was recorded by GPC. [f] The hydrodynamic radii were obtained by dynamic light scattering (DLS) measurement (**Figure 6.4**). [g] The size of NPs is statistically averaged over 100 NPs in TEM images by using *ImageJ* software.

Representative transmission electron microscopy (TEM) images of three La-based NPs, namely $LaFeO_3$, $LaMnO_3$ and La_2CoO_4 NPs with an average diameter of 16.2 ± 1.4 nm, 16.7 ± 1.3 nm and 17.1 ± 1.5 nm, are shown in **Figure 6.5 (a)**, **(c)**, and **(e)**, respectively. The size distribution histograms of each kind of NP are demonstrated in **Figure 6.5 (b, d, f)**, for $LaFeO_3$, $LaMnO_3$ and La_2CoO_4 NPs, separately, indicating the as-synthesized NPs are remarkably uniform. All three kinds of La-based NPs were crafted by exploiting the same star-like PAA-*b*-PS diblock copolymer as nanoreactor (Sample 2 in **Table 6.1**). The similarity in the average sizes of three La-based NPs further verified the effectiveness of this synthetic strategy to yield a rich diversity of uniform NPs with dimensions that can be precisely tailored. Moreover, owing to the ligated PS block on the surface, the raw solution can be purified via a simple precipitation-dissolution process, confirmed by monodisperse NPs without aggregation or impurities in the TEM images. To further substantiate the function of star-like diblock copolymer nanoreactors during the formation of NPs, control experiments were conducted by the same synthetic conditions except no nanoreactor was introduced. Only big aggregations and matrix-like products, both with irregular morphology, were found in the TEM images (**Figure 6.6**) because ligands for preventing aggregation were lacking. Therefore, we can conclude that the growth of NPs was indeed structure-directed by the inner PAA blocks.

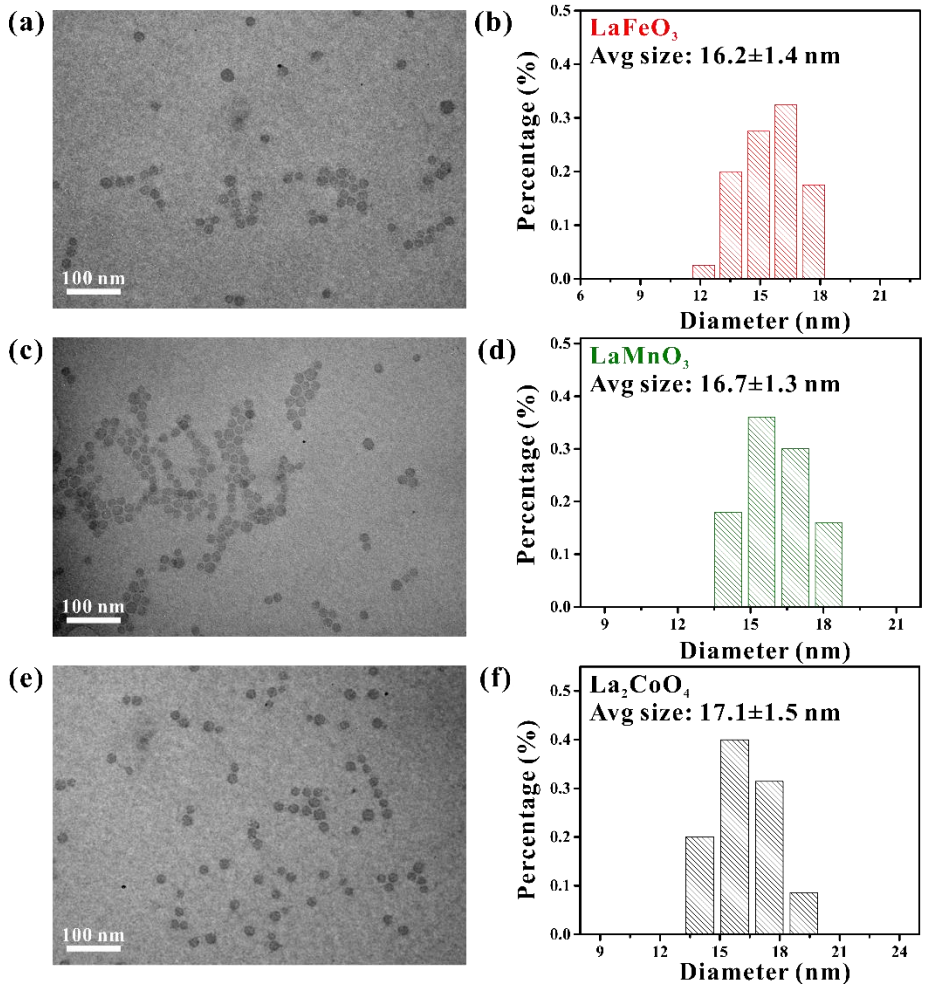

Figure 6.5 TEM images of as-synthesized, PS-ligated La-based perovskite and layered perovskite nanoparticles of **(a)** $LaFeO_3$, **(c)** $LaMnO_3$ and **(e)** La_2CoO_4, crafted by employing star-like PAA-*b*-PS diblock copolymer (Sample 2 listed in **Table S1**) as nanoreactor. **(b, d, f)** Size distribution histogram of the corresponding nanoparticles, measured by calculating the diameter of 100 NPs with *ImageJ* from the TEM images.

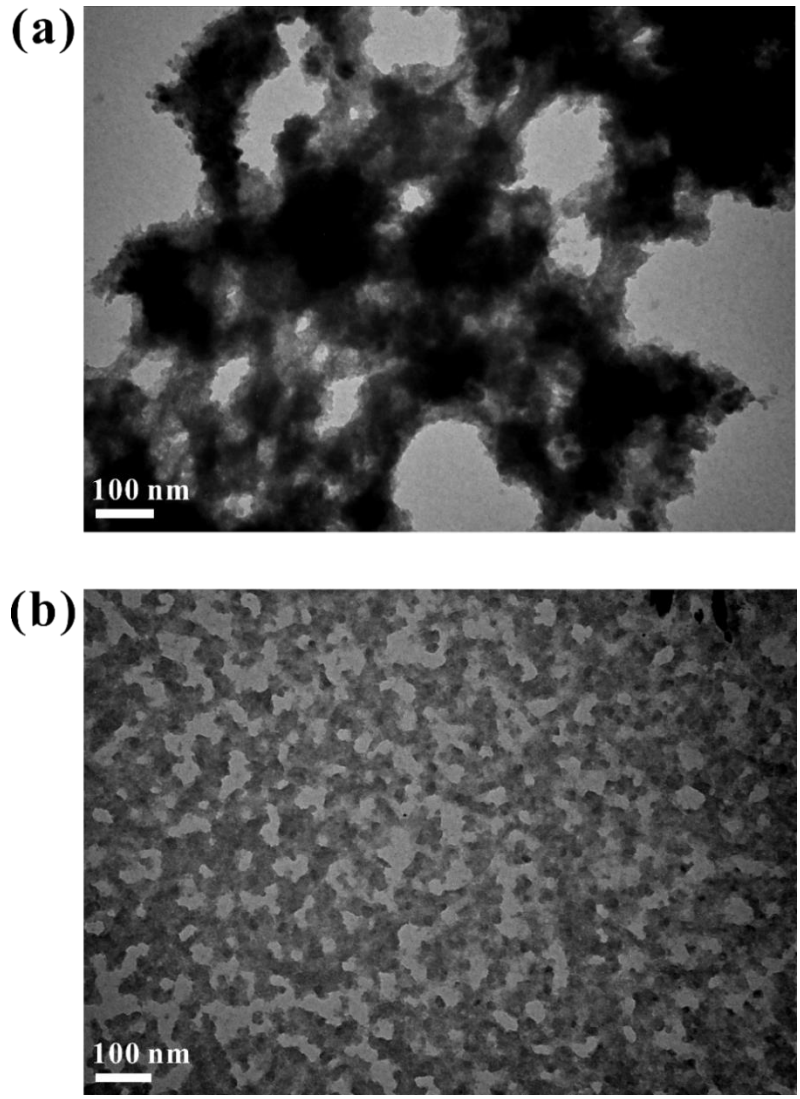

Figure 6.6 Representative TEM images of the control sample, i.e., La-based perovskite and layered perovskite synthesized under the same experimental condition yet without the addition of star-like PAA-*b*-PS diblock copolymer nanoreactor.

Figure 6.7 depicts the representative X-ray diffraction (XRD) spectrum of all three kinds of La-based perovskite and layered perovskite NPs, i.e., $LaFeO_3$ (**Figure 6.7 (a)**), $LaMnO_3$ (**Figure 6.7 (b)**) and La_2CoO_4 (**Figure 6.7 (c)**), respectively. All three XRD profiles of the as-synthesized NPs were found with low crystallinity, suggesting the reaction temperature for NPs synthesis (i.e., ~250 ^oC) was not high enough for complete thermolysis of the precursors. Therefore, further

annealing process was required to obtain the product with high purity and enhanced crystallinity. To maintain the uniformity and high-dispersity characteristics of the as-synthetized NPs, the PS-ligated La-based NPs were mixed with graphene oxide (GO, **Figure 6.8 (a-b)**) with the predetermined weight ratio between the two before annealing. Thorough stirring before subjected to annealing condition was necessary to ensure those as-synthesized NPs dispersed well, with certain NP-NP distance, on GO. Before annealing, two weight ratios between as-synthesized NPs and GO (i.e., 1 to 1 (**Figure 6.8 (c-d)**) and 2 to 1 (**Figure 6.8 (e-f)**)) were performed to decide the optimal condition for the following characterization and properties investigation. Particularly, despite a closer distance between NPs after annealing with the 2 to 1 weight ratio, disperse NPs with similar size compared to that before annealing can be observed in both ratios after annealing (**Figure 6.8 (g-h)**). We thus chose the weight ratio of 2 to 1 for the annealing and properties measurements afterward. The crystallinities were significantly improved for all the La-based NPs and GO was converted into reduced graphene oxide (rGO) after the two-step annealing process, (i.e., 350 ^{o}C in air, followed by 600 ^{o}C in N_2, see *Experimental Section* for more details.), substantiated by the appearance of the obvious characteristic diffraction peaks from XRD spectra (black curve in **Figure 6.7 (a-c)**). The XRD diffraction patterns can be identified as $LaFeO_3$ with orthorhombic structure, $LaMnO_3$ with rhombohedral structure and La_2CoO_4 with orthorhombic structure, respectively, all consistent with the corresponding standard XRD profiles and/or previous literatures.[21]

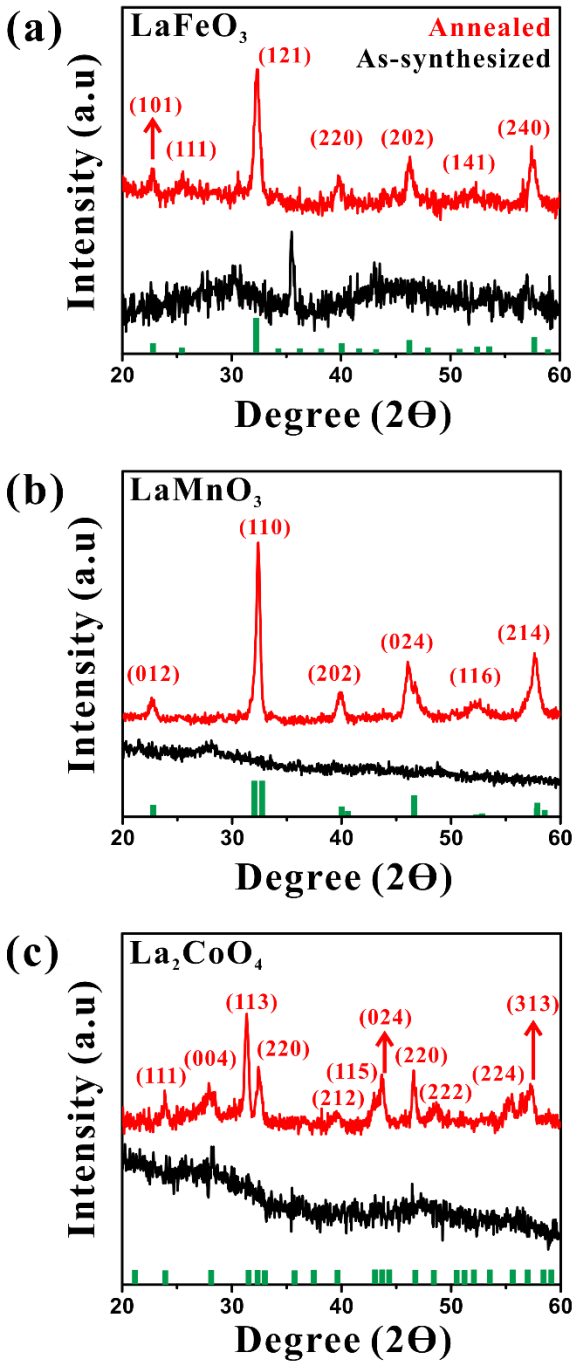

Figure 6.7 XRD patterns of PS-ligated **(a)** $LaFeO_3$ and **(b)** $LaMnO_3$ perovskite nanoparticles as well as **(c)** La_2CoO_4 layered perovskite nanoparticles. All the nanoparticles are synthesized by employing Sample 2 listed in **Table 6.1** as nanoreactor. Two curves in each figure represent the XRD results of as-synthesized nanoparticles (black curve), and nanoparticles after annealing (red curve). Each XRD spectrum is consistent with the corresponding reference pattern (green line) of $LaFeO_3$ (JCPDS no. 37-1459), $LaMnO_3$ (JCPDS no. 50-0928) and La_2CoO_4 (previous literature).[21]

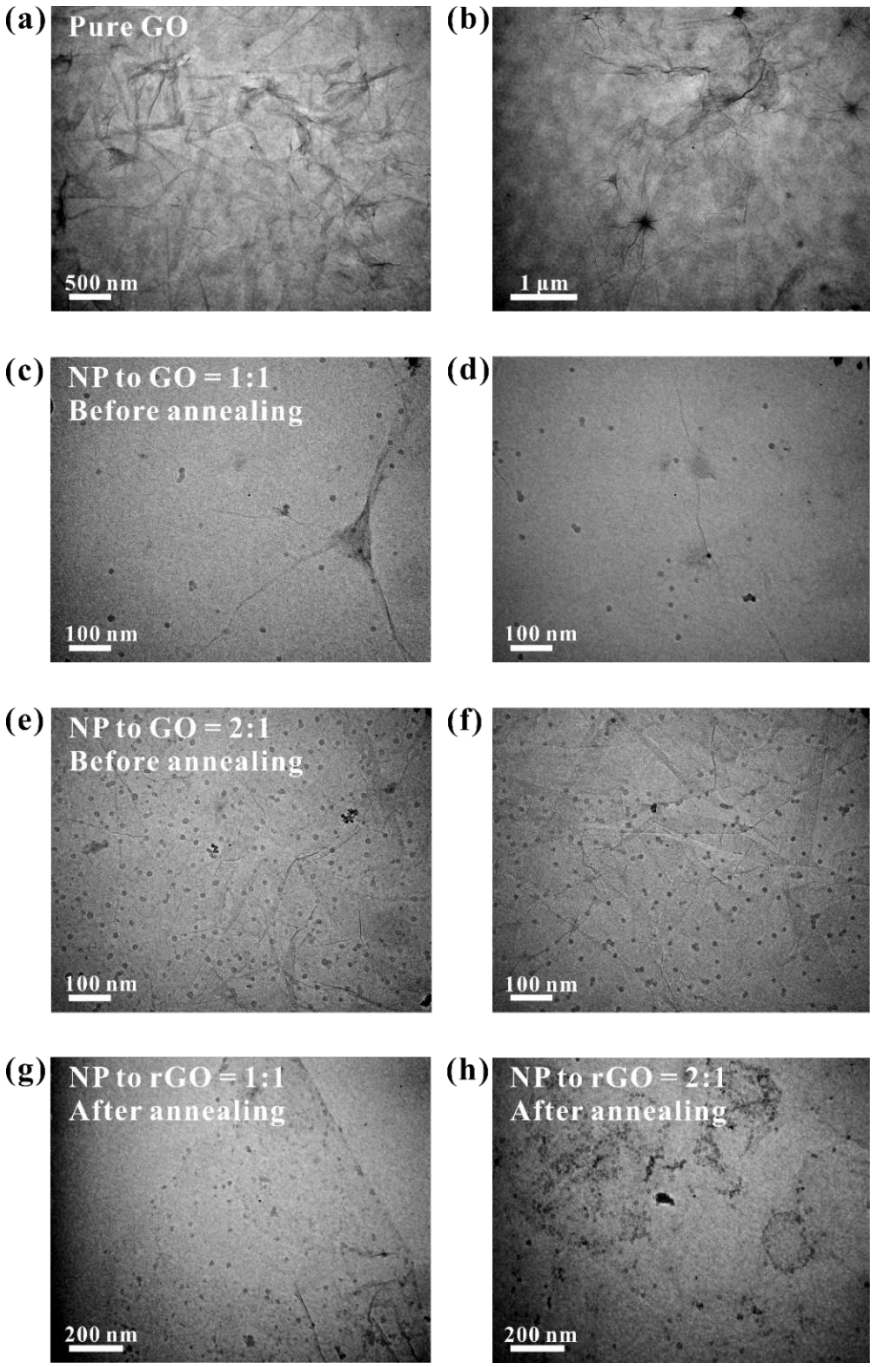

Figure 6.8 TEM images of **(a, b)** pure graphene oxide (GO), GO mixed with as-synthesized La-based nanoparticle with **(c, d)** less nanoparticle concentration (1:1 weight ratio between La-based nanoparticle and GO) and **(e, f)** more nanoparticle concentration (2:1 weight ratio between La-based nanoparticle and GO) before annealing. Composite of reduced graphene oxide (rGO) with corresponding **(g)** 1:1 weight ratio and **(h)** 2:1 weight ratio after two-step annealing. Note that here we used as-synthesized $LaMnO_3$ perovskite nanoparticles, prepared by employing Sample 2 in **Table 6.1**, as an example. The black spots in **(a)** and **(b)** were the folds of GO. Similar images were observed in all three kinds of La-based perovskite and layered perovskite nanoparticles.

We noted that because of varied hydrolysis or thermolysis rate for the system with two or more precursors, impurities were frequently observed by the appearance of additional peaks in the XRD profiles and may eventually lead to low mass activities.[22] Here, impurities from single oxide (i.e., MnO_2 and La_2O_3, pointed out by arrows in **Figure 6.9**) appeared when the molar ratio between La precursor and Mn precursor was 0.5:1 and 0.75:1, respectively, possibly due to different coordination interaction ability between two metal moieties and the functional group of inner PAA block. Nevertheless, PS-ligated $LaMnO_3$ perovskite NPs without impurities can be obtained when the molar ratio between the two precursors was chosen properly (i.e., 0.63:1, the orange curve in **Figure 6.9**) because different coordination interactions can thus be compensated, rendering opportunities for achieving phase-pure materials with two or more precursors. On the other hand, PS-ligated layered La_2CoO_4 perovskite NPs, instead of $LaCoO_3$ NPs with perovskite structure, were obtained despite same experimental conditions for synthesizing $LaFeO_3$ and $LaMnO_3$ was used. Further changing the molar ratio between the two precursors (**Figure 6.10 (a)**) and annealing conditions (i.e., various annealing times in air as well as various annealing temperatures in N_2, **Figure 6.10 (b)**) cannot convert layered perovskite structure into perovskite structure. The reason for the presence of layered perovskite structure is unclear, while we can conclude that under the synthetic parameters we tried, $LaCoO_3$ NPs with perovskite structure cannot be attained. Intriguingly, the La-Co-O phase diagram showed that layered La_2CoO_4 perovskite structure did not appear at the synthetic temperature lower than 1700 ^oC.[23] In addition, the synthesis of Ruddlesden-Popper layered perovskites was typically performed or in combination with high-temperature treatments above 1000 ^oC, according to other reports.[24] Therefore, the reaction temperature for acquiring layered La_2CoO_4 perovskite NPs can be remarkably reduced via this nanoreactor-assisted synthetic strategy, potentially due to the nanometer-scaled product.

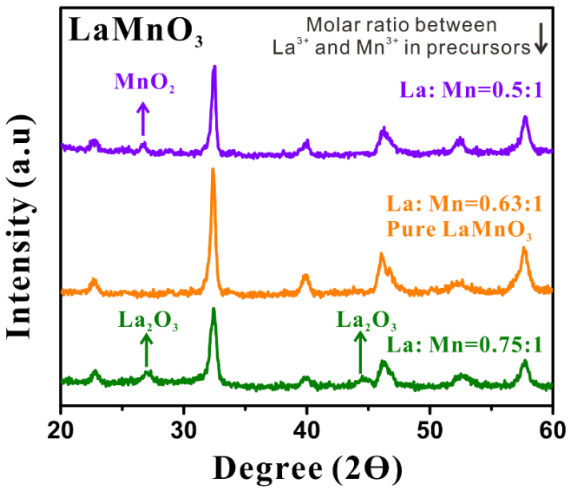

Figure 6.9 XRD results of $LaMnO_3$ perovskite nanoparticles with varied molar ratio between La and Mn in precursors after two-step annealing.

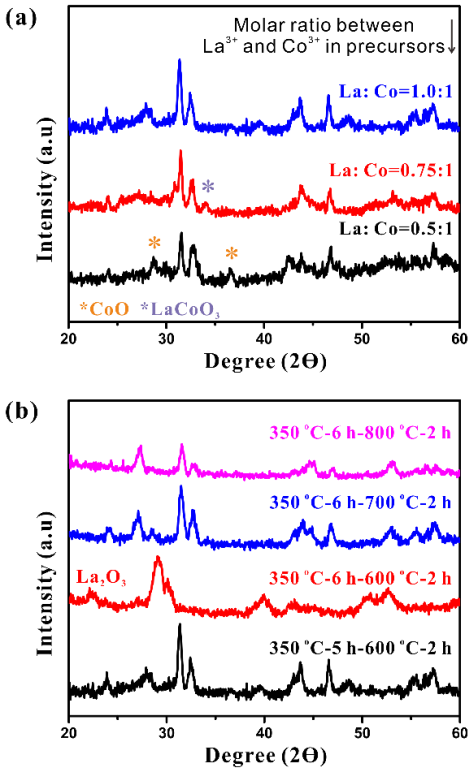

Figure 6.10 XRD results of La_2CoO_4 perovskite nanoparticles after two-step annealing with **(a)** varied molar ratio between La and Co precursors, and **(b)** different annealing procedures. The number in **(b)** represented the complete annealing process. For example, 350C-5 h-600C-2 h (black curve) indicated that sample was annealed in air at 350 °C for 6 h, followed by annealed in N_2 at 600 °C for 2 h.

Figure 6.11 (a-c) displays the X-ray photoelectron spectroscopy (XPS) survey spectra of $LaFeO_3$, $LaMnO_3$ and La_2CoO_4 after annealing, respectively. Specifically, the high-resolution spectra of individual elements of layered La_2CoO_4 perovskite NPs after annealing, including La 3d, Co 2p and O 1s are presented in **Figure 6.12**. The binding energies of 835 eV and 851 eV are attributed to La^{3+} $3d_{5/2}$ and La^{3+} $3d_{3/2}$, separately, while those of 839 eV and 856 eV are identified as satellite peaks (**Figure 6.12 (a)**).[25] In terms of Co 2p, the XPS result can be deconvoluted into four peaks, with binding energies of Co^{2+} $2p_{3/2}$ and Co^{2+} $2p_{1/2}$ peaks located at 781 eV and 797 eV as well as satellite peaks located at 787 eV and 803 eV (**Figure 6.12 (b)**).[26] Finally, **Figure 6.12 (c)** depicts the O 1s XPS spectrum, which can be deconvoluted into three characteristic peaks, including lattice oxygen species (~529.5 eV for O^{2-}), hydroxyl groups (~531.5 eV for OH^-), as well as adsorbed molecular water (~533 eV for H_2O), consistent with previously reported values.[1, 4] The relative content of these species is known to influence the electrocatalytic activity, which will be discussed in the following paragraphs. Similar XPS results of La and O elements were found in $LaFeO_3$ (**Figure 6.13 (9a, c)**) and $LaMnO_3$ (**Figure 6.14 (a, c)**) after annealing. Additionally, the XPS profiles for Fe (**Figure 6.13 (b)**) and Mn (**Figure 6.14 (b)**) verified both transition metals were in the expected oxidation states of +3.[27-28]

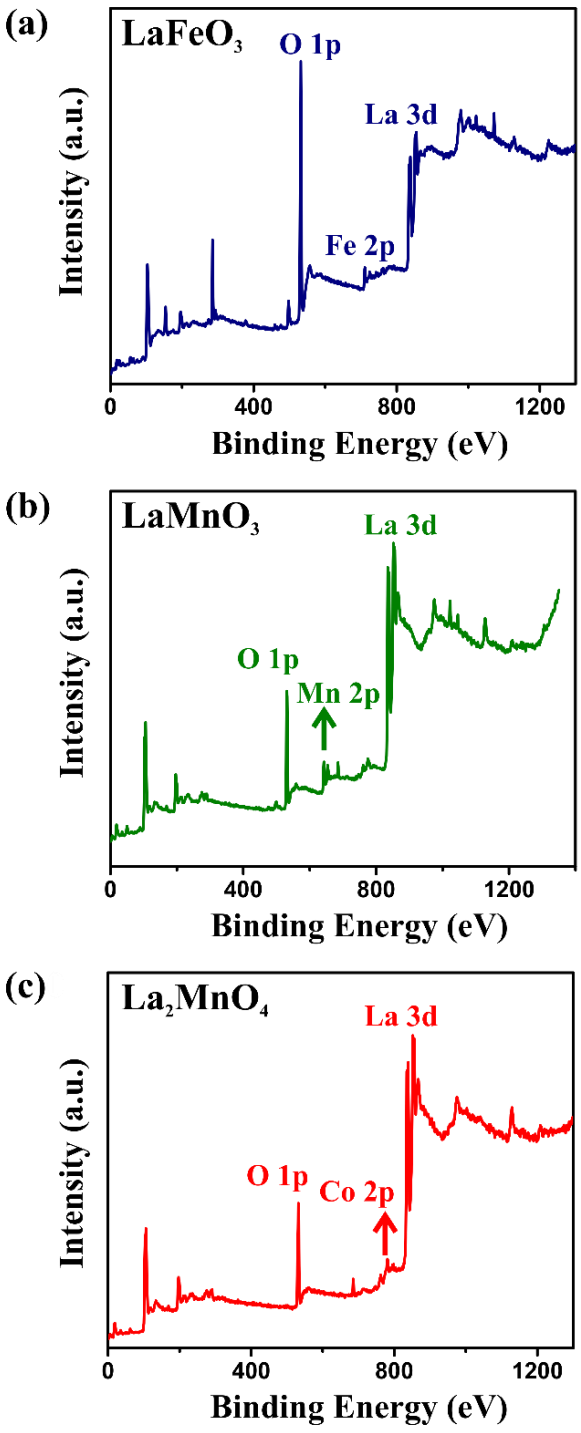

Figure 6.11 XPS full spectra of **(a)** $LaFeO_3$, **(b)** $LaMnO_3$ and **(c)** La_2CoO_4 nanoparticles after two-step annealing, respectively. All the nanoparticles measured are crafted via employing Sample 2 in **Table 6.1** as nanoreactor.

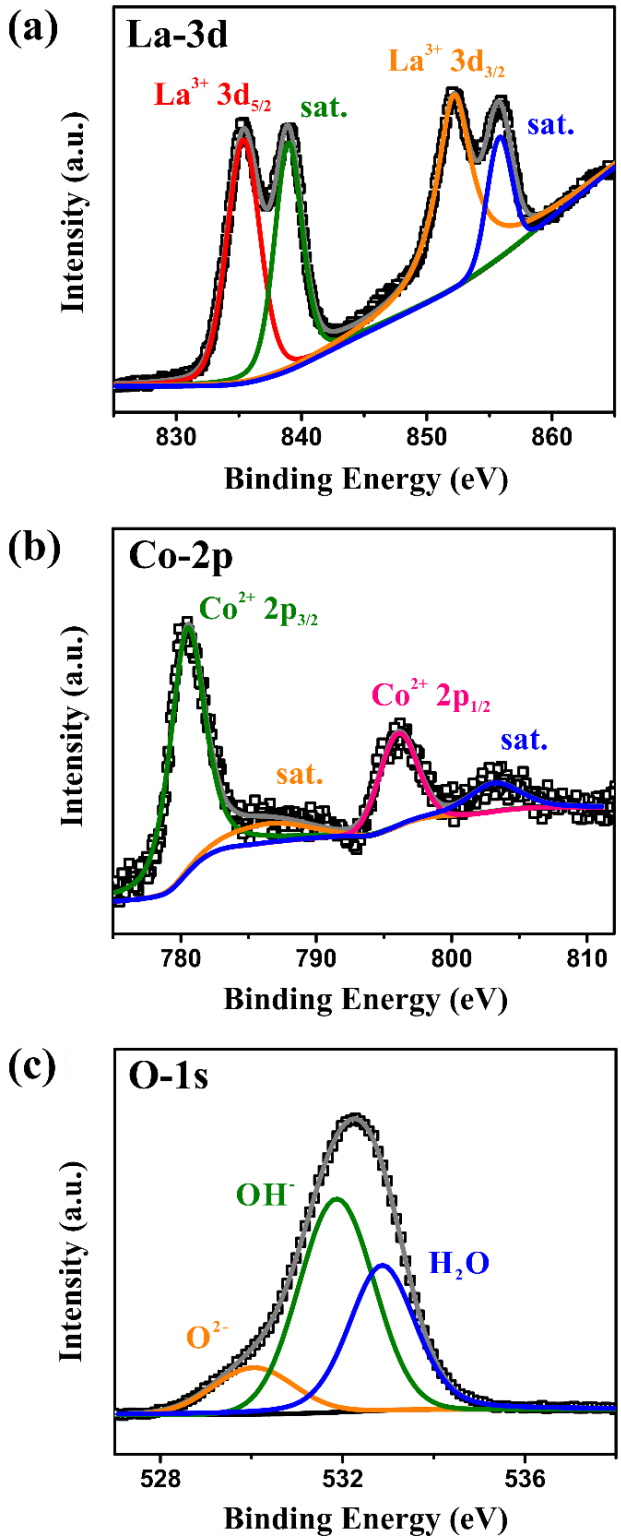

Figure 6.12 (a) La 3d, **(b)** Co 2p and **(c)** O 1s XPS spectra of La_2CoO_4 nanoparticles after annealing, crafted via employing Sample 2 listed in **Table 6.1** as nanoreactor.

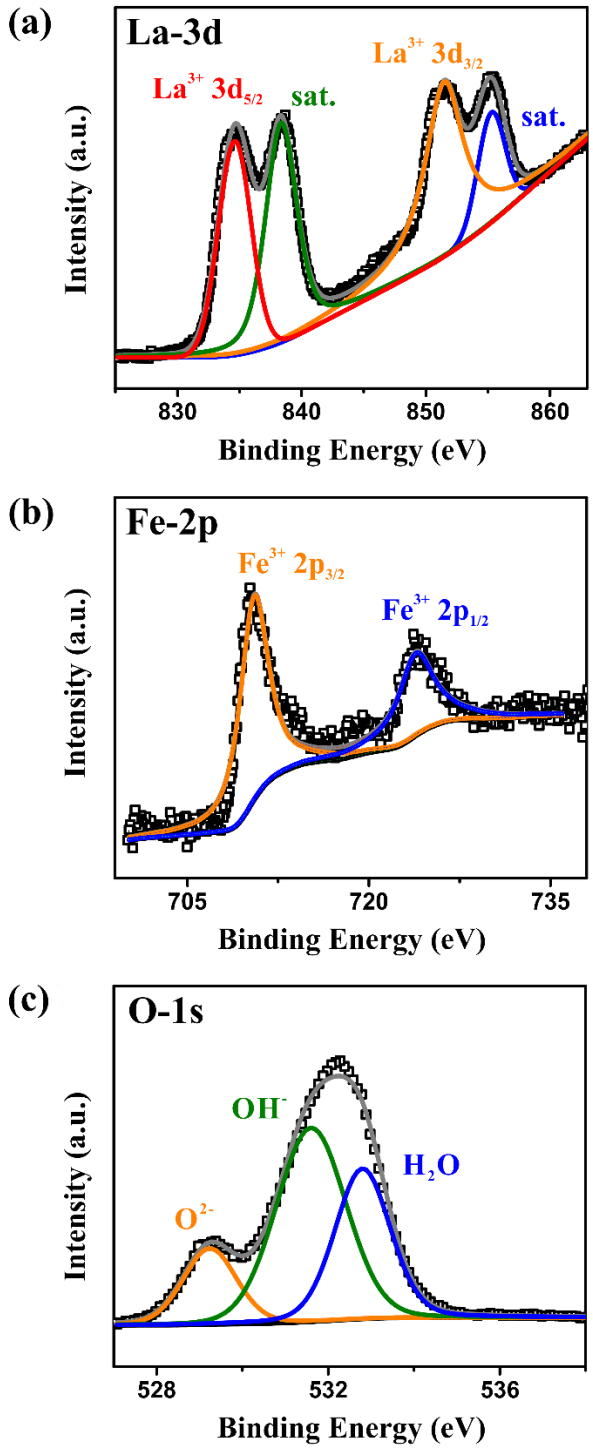

Figure 6.13 (a) La 3d, **(b)** Fe 2p, and **(c)** O 1s XPS spectra of $LaFeO_3$ nanoparticles after two-step annealing, crafted via employing Sample 2 in **Table 6.1** as nanoreactor.

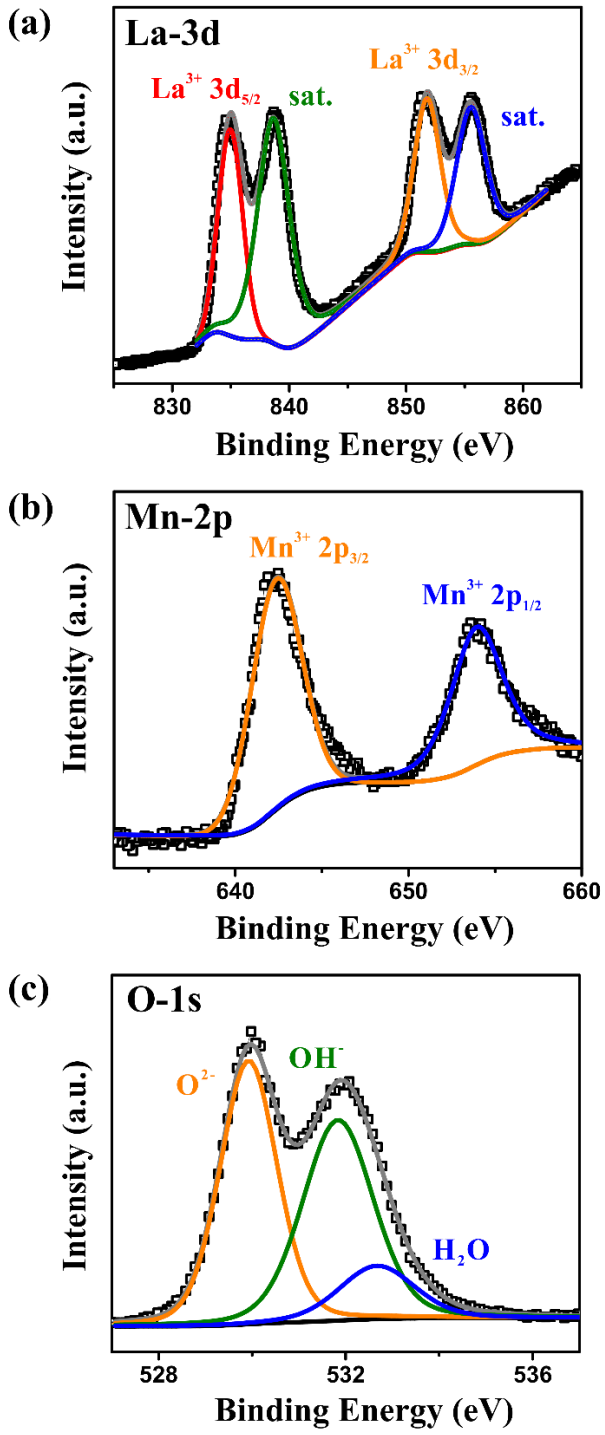

Figure 6.14 (a) La 3d, **(b)** Mn 2p, and **(c)** O 1s XPS spectra of $LaMnO_3$ nanoparticles after two-step annealing, crafted via employing Sample 2 in **Table 6.1** as nanoreactor.

The ORR and OER performance of La-based perovskite and layered perovskite NPs dispersed on rGO with the addition of carbon black (CB) were investigated by using rotating disk electrode (RDE) measurements in 0.1 M KOH and 1 M KOH solution, respectively (see *Experimental Section* for more details). **Figure 6.15** shows the ORR polarization curves of $LaFeO_3$, $LaMnO_3$ and La_2CoO_4 NPs. Among the three, La_2CoO_4 NPs exhibit the best activity (**Figure 6.15 (a-b), Figure 6.16 (a),** and **Figure 6.17 (a)**), with more positive onset potential, half-wave potential and larger limiting current density. For instance, La_2CoO_4 NPs show the highest half-wave potential for the ORR at 0.716 V, followed by $LaMnO_3$ (0.665 V) and $LaFeO_3$ (0.616 V). In addition, the largest limiting current density of La_2CoO_4 (-6.21 mA cm^{-2}), compared to those of $LaMnO_3$ (-5.75 mA cm^{-2}) and $LaFeO_3$ (-4.1 mA cm^{-2}), can further confirm its excellent ORR performance. Notably, the small contributions of bare glassy carbon (GC) electrode, rGO and CB to both ORR and OER activities (**Figure 6.18**) indicates the observed electrocatalytic performance was dominated by La-based perovskite and layered perovskite NPs. To explore the kinetic of $LaFeO_3$, $LaMnO_3$ and La_2CoO_4 NPs, the rotating-disk measurements with various rotation rates were carried out (**Figure 6.16 (b)**, **Figure 6.17 (b)**, and **Figure 6.15 (c)**, respectively), and the corresponding electron transfer number (*n*) was analyzed from the slopes of Koutechy-Levich plots at different potentials (**Figure 6.15 (d)**). As a result, the electron transfer numbers of $LaFeO_3$ and $LaMnO_3$ NPs are 2.69 and 3.77, respectively, while La_2CoO_4 NPs still exhibit the highest electron transfer number, i.e., 4.16, favoring a 4*e* ORR pathway process. The 4*e* pathway is generally preferred since it can achieve ORR catalytic activity with high efficiency in electrochemical energy conversion systems, and most of the reacted oxygen is reduced to H_2O.[8] Finally, the comparisons of ORR performance, including limiting current density, the potential

applied at -1 mA cm^{-2}, as well as electron transfer number (*n*), between three La-based perovskite and layered perovskite NPs are summarized in **Figure 6.19**.

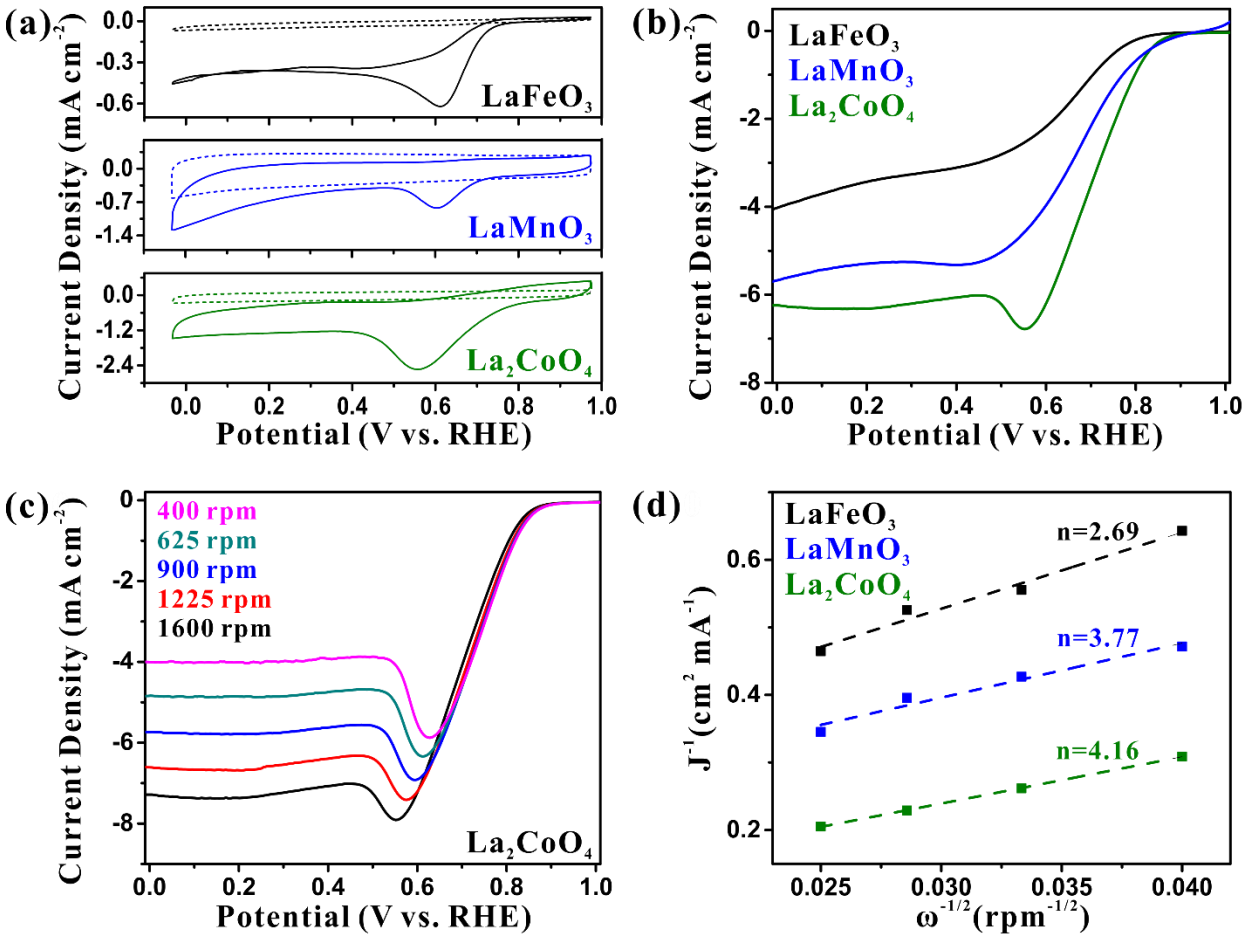

Figure 6.15 (a) Cyclic voltammetry (CV) scans of $LaFeO_3$, $LaMnO_3$ and La_2CoO_4 nanoparticles on glassy carbon electrodes in 0.1 M KOH solution saturated with N_2 (dash line) and O_2 (solid line) at a scan rate of 5 mV/s. **(b)** The oxygen reduction reaction (ORR) polarization curves on rotating disk electrode with $LaFeO_3$, $LaMnO_3$ and La_2CoO_4 nanoparticles in O_2-saturated 0.1 M KOH solution at a scan rate of 5 mV/s and a rotation rate of 1600 rpm. **(c)** Polarization curves of ORR with La_2CoO_4 nanoparticles at a scan rate of 5 mV/s and various rotation rates, ranged from 400-1600 rpm. **(d)** Koutechy-Levich plots of $LaFeO_3$, $LaMnO_3$ and La_2CoO_4 nanoparticles at different potentials. All the nanoparticles measured were synthesized by employing Sample 2 listed in **Table 6.1** as nanoreactor.

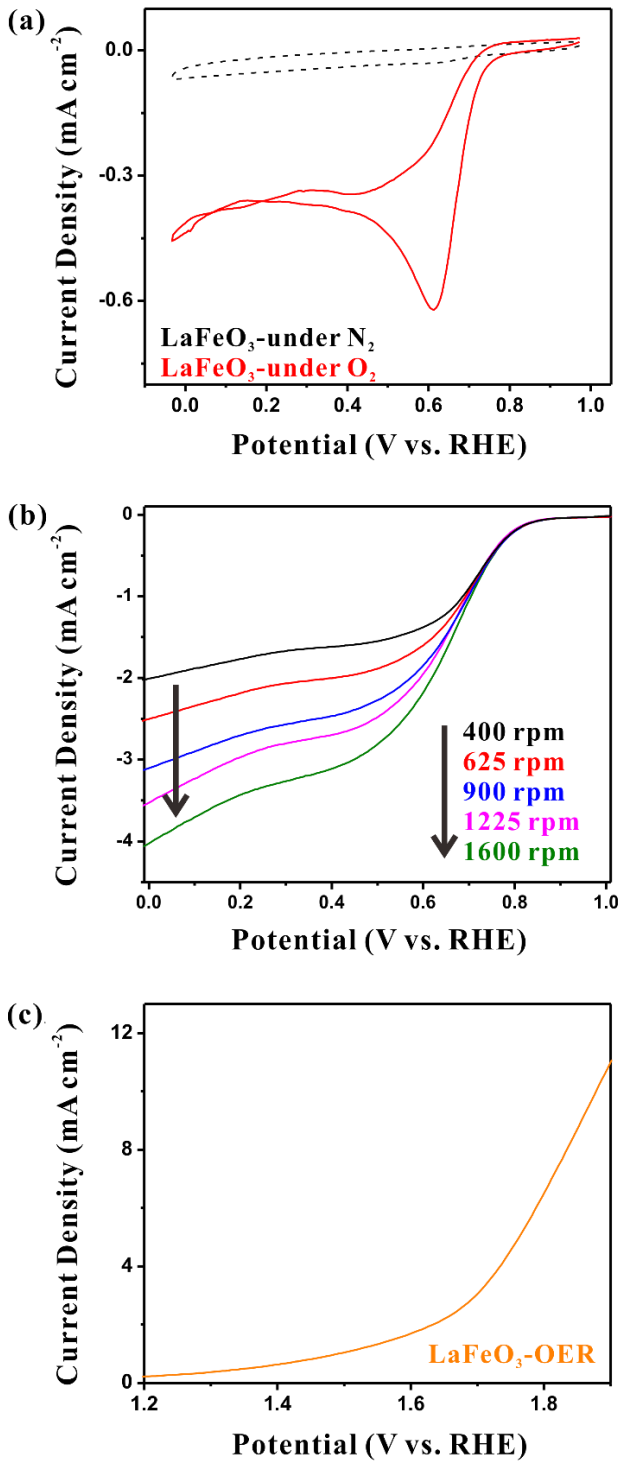

Figure 6.16 (a) CV of $LaFeO_3$ nanoparticles in oxygen- (red) and nitrogen- (black) saturated 0.1 M KOH solution. **(b)** Polarization curves of ORR with $LaFeO_3$ nanoparticles in O_2-saturated 0.l M KOH at a scan rate of 5 mV/s and various rotation rates, ranged from 400-1600 rpm. **(c)** Oxygen evolution current of $LaFeO_3$ nanoparticles in O_2-saturated 1 M KOH at a scan rate of 5 mV s^{-1} and a rotation rate of 1600 rpm. All the $LaFeO_3$ nanoparticles (D = 16.2 nm) measured were synthesized with Sample 2 in **Table 6.1**.

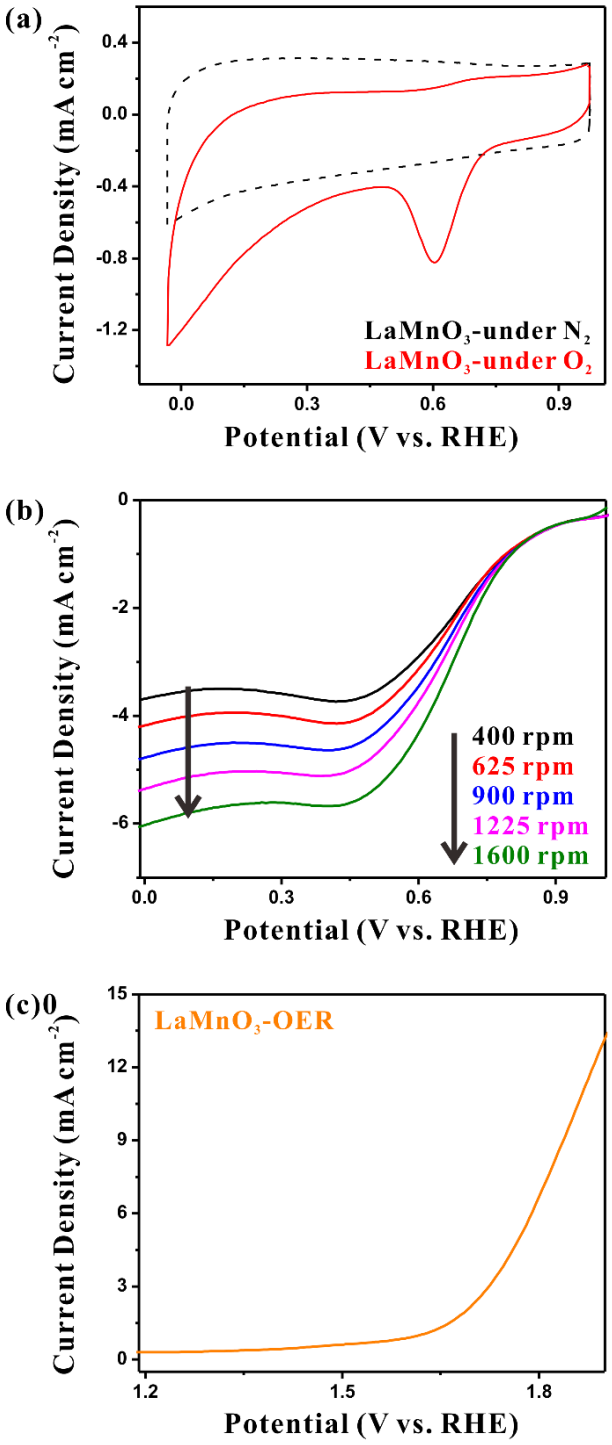

Figure 6.17 (a) CV of $LaMnO_3$ nanoparticles in oxygen- (red) and nitrogen- (black) saturated 0.1 M KOH solution. **(b)** Polarization curves of ORR with $LaMnO_3$ nanoparticles in O_2-saturated 0.l M KOH at a scan rate of 5 mV/s and various rotation rates, ranged from 400-1600 rpm. **(c)** Oxygen evolution current of $LaMnO_3$ nanoparticles in O_2-saturated 1 M KOH at a scan rate of 5 mV s^{-1} and a rotation rate of 1600 rpm. All the $LaMnO_3$ nanoparticles (D = 16.7 nm) measured were synthesized with Sample 2 in **Table 6.1**.

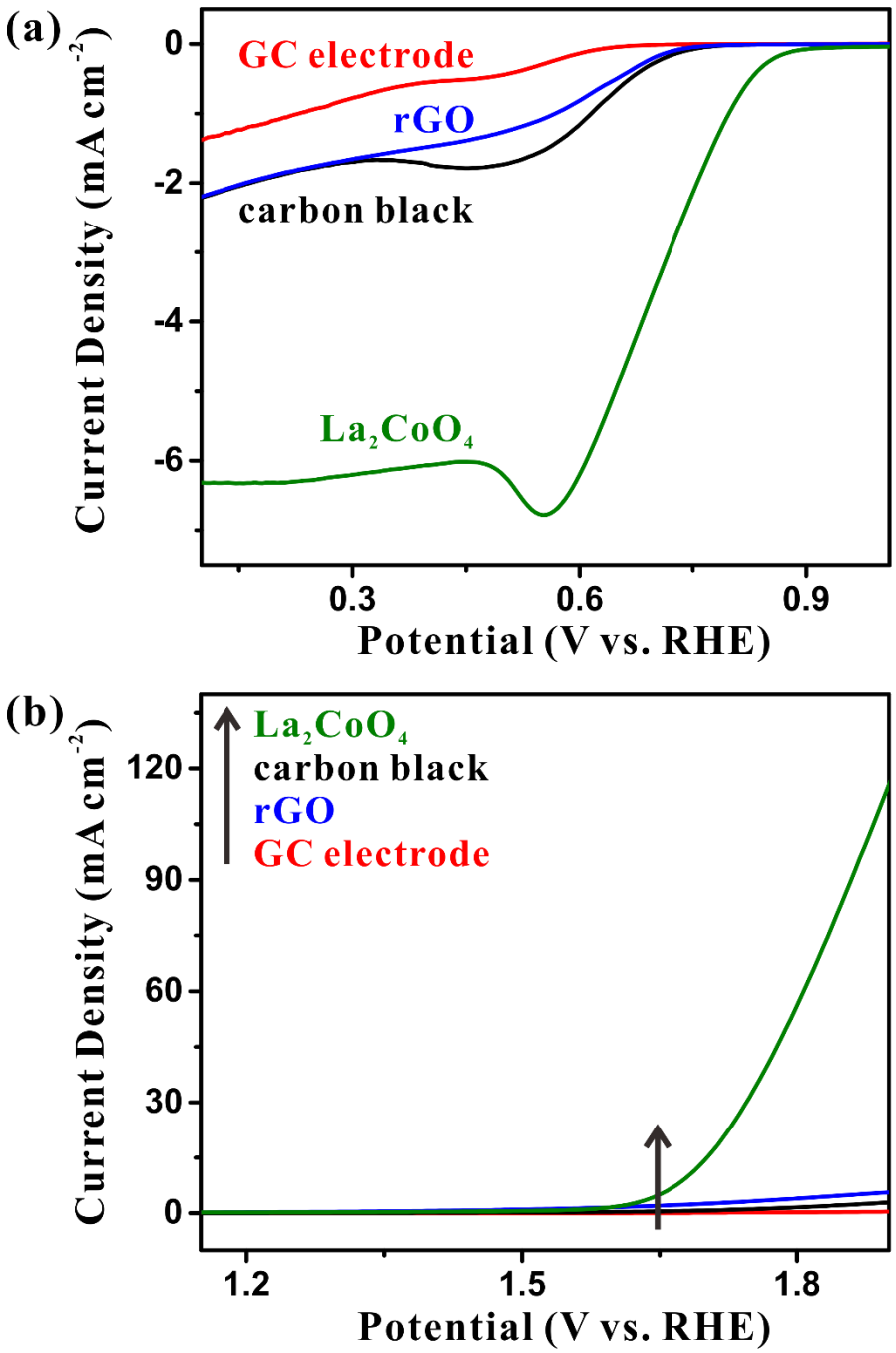

Figure 6.18 (a) Oxygen reduction current and **(b)** oxygen evolution current of glassy carbon (GC) electrode, rGO, carbon black, and La_2CoO_4 nanoparticles (D = 17.1 nm) in O_2-saturated KOH.

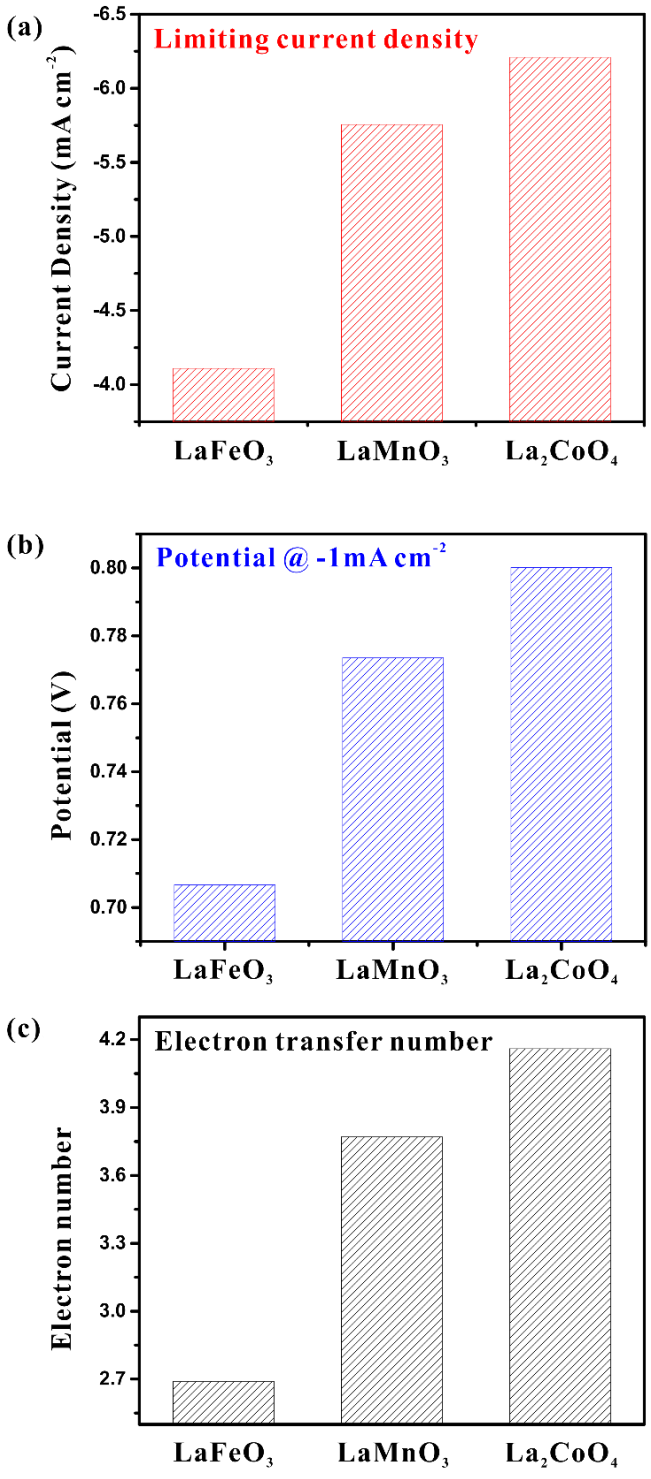

Figure 6.19 Comparison of oxygen reduction reaction activities of three La-based perovskite and layered perovskite nanoparticles of **(a)** limiting current density, **(b)** the potential at which current density = -1 mA cm^{-2} and **(c)** electron transfer number.

For OER, the layered La_2CoO_4 perovskite NPs demonstrates superior OER activity compared to other La-based perovskite NPs, revealed by significantly higher limiting current density and lower overpotential (**Figure 6.20 (a), Figure 6.16 (c),** and **Figure 6.17 (c)**). Typically, the potential required for obtaining the current density of 10 mA cm^{-2} is 1.68 V for La_2CoO_4, which is lower than that of $LaFeO_3$ (1.93 V) and $LaMnO_3$ (1.85 V). In the OER Tafel plot (**Figure 6.20 (b)**), the Tafel slope of La_2CoO_4 NPs (90 mV $decade^{-1}$) is substantially lower than that of the other two (278 mV $decade^{-1}$ for $LaFeO_3$ and 208 mV $decade^{-1}$ for $LaMnO_3$, respectively), indicating the excellent catalytic activity of layered La_2CoO_4 perovskite NPs to drive the OER kinetics at a lower overpotential. The increasing current density at specific applied potential (i.e., 1.8 V) and decreasing Tafel slope, following the order of $LaFeO_3$, $LaMnO_3$ and La_2CoO_4 NPs are summarized in **Figure 6.20 (c)**. Moreover, the bifunctional electrocatalytic activity of all three La-based NPs was measured and evaluated by subtracting the potential at -3 mA cm^{-2} for the ORR (E_{ORR}) from the potential at 10 mA cm^{-2} for the OER (E_{OER}).[1, 5] The smaller difference (ΔE) between the two values suggests a more enhanced electrocatalytic activity for the reversible oxygen electrodes. The ΔE values of the perovskite and layered perovskite NPs are 1.48, 1.2, and 0.96 V for $LaFeO_3$, $LaMnO_3$ and La_2CoO_4 NPs, respectively (**Figure 6.20 (d)**), suggesting that not only layered La_2CoO_4 perovskite NPs is the electrocatalyst with the best performance among the three La-based NPs, but this excellent bifunctionality is also comparable with those well-recognized and extensively-studied perovskite-based catalysts, such as (un)doped La-based perovskites, $Ba_{0.5}Sr_{0.5}Co_{0.8}Fe_{0.2}O_{3-\delta}$, $NdBa_{0.5}Sr_{0.5}Co_{1.5}Fe_{0.5}O_{5+\delta}$, $GdBa_{0.5}Sr_{0.5}Co_{1.5}Fe_{0.5}O_{5+\delta}$, etc. as reported elsewhere previously (**Table 6.2**).[8, 29-32]

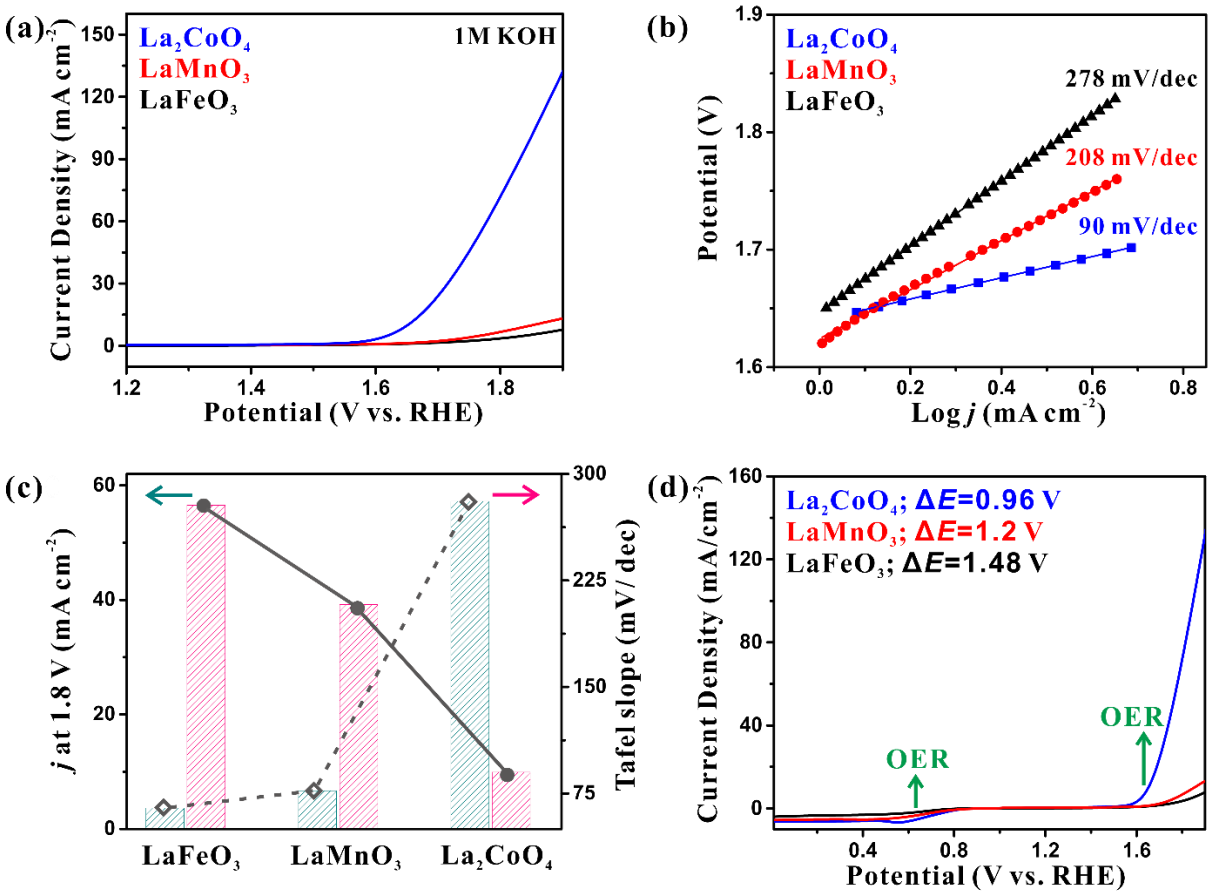

Figure 6.20 (a) The oxygen evolution reaction (OER) polarization curves of $LaFeO_3$, $LaMnO_3$ and La_2CoO_4 nanoparticles in 1 M KOH solution at a scan rate of 5 mV/s and a rotation rate of 1600 rpm, and **(b)** the corresponding Tafel plots. **(c)** The relationship between OER activity (solid line); Tafel slope (dashed line) and the type of electrocatalyst (i.e., $LaFeO_3$, $LaMnO_3$ and La_2CoO_4 nanoparticles). **(d)** OER/ORR polarization curves for $LaFeO_3$, $LaMnO_3$ and La_2CoO_4 nanoparticles. All the nanoparticles measured were synthesized by employing Sample 2 listed in **Table 6.1** as nanoreactor.

Table 6.2 The bifunctionality comparison among the layered La_2CoO_4 perovskite catalysts and the previously reported bifunctional electrocatalysts.

Oxygen Catalysts	E_{ORR} at 3 mA cm^{-2} (V vs. RHE)	E_{OER} at 10 mA cm^{-2} (V vs. RHE)	ΔE ($E_{OER} - E_{ORR}$) (V)	References
La_2CoO_4 (D = 8.5 nm)	0.77 vs. RHE	1.65 vs. RHE	0.88	This work
La_2CoO_4 (D = 17.1 nm)	0.72 vs. RHE	1.68 vs. RHE	0.96	This work
La_2CoO_4 (D = 22.1 nm)	0.63 vs. RHE	1.69 vs. RHE	1.06	This work
$LaNiO_{3-\delta}$	-0.40 vs. Ag/AgCl	-0.76 vs. Ag/AgCl	1.16	5
$LaNiO_3$	0.64 vs. RHE	1.66 vs. RHE	1.02	6
$LaNiO_3$	0.77 vs. RHE	1.74 vs. RHE	0.97	7
$LaNiO_3$	0.64 vs. RHE	1.67 vs. RHE	1.03	8
$LaNi_{0.8}Fe_{0.2}O_3$	0.40 vs. SCE	0.67 vs. SCE	1.07	9
$La_{0.95}FeO_3$	0.58 vs. RHE @ 1 mA cm^{-2}	1.64 vs. RHE	1.06	10
$LaTi_{0.65}Fe_{0.35}O_{3-\delta}$	0.72 vs. RHE	1.77 vs. RHE	1.05	11
$LaCoO_3$	0.64 vs. RHE	1.64 vs. RHE	1.00	12
$LaCoO_3$	0.594 vs. RHE @ 1 mA cm^{-2}	1.657 vs. RHE	1.063	13
$La_{0.95}CoO_{3-\delta}$	0.635 vs. RHE @ 1 mA cm^{-2}	1.639 vs. RHE	1.004	13
$La_{0.9}CoO_{3-\delta}$	0.662vs. RHE @ 1 mA cm^{-2}	1.610 vs. RHE	0.948	13
$La_{0.5}Sr_{0.5}CoO_{3-\delta}$	0.76 vs. RHE	1.83 vs. RHE	1.07	14
$La_{0.5}Sr_{0.5}Co_{0.8}Fe_{0.8}O_3$	0.41 vs. SCE	0.78 vs. SCE	1.19	15
$La_{0.8}Sr_{0.2}MnO_3$	-0.13 vs. Ag/AgCl @ 1 mA cm^{-2}	0.95 vs. Ag/AgCl	1.08	16
$La_{0.58}Sr_{0.5}Co_{0.8}Fe_{0.8}O_{3-\delta}$	0.77 vs. RHE	1.68 vs. RHE	0.91	17
$CaMnO_3$	0.72 vs. RHE	1.89 vs. RHE	1.17	18
$Ba_{0.5}Sr_{0.5}Co_{0.8}Fe_{0.2}O_{3-\delta}$ (BSCF)	0.641 vs. RHE	1.625 vs. RHE	0.984	19
$Ba_{0.5}Sr_{0.5}Co_{0.8}Fe_{0.2}O_{3-\delta}$ (BSCF)	0.619 vs. RHE	1.681 vs. RHE	1.062	20
$NdBa_{0.5}Sr_{0.5}Co_{1.5}Fe_{0.5}O_{5+\delta}$ (NBSCF)	0.651 vs. RHE	1.624 vs. RHE	0.973	20
$NdBa_{0.5}Sr_{0.5}Co_{1.5}Fe_{0.5}O_{5+\delta}$ (NBSCF)	0.653 vs. RHE	1.604 vs. RHE	0.951	19
$Nd_{1.5}Ba_{1.5}CoFeMnO_{9-\delta}$ (NBCFM)	0.698 vs. RHE	1.589 vs. RHE	0.891	19

$SmBa_{0.5}Sr_{0.5}Co_{1.5}Fe_{0.5}O_{5+\delta}$ (SBSCF)	0.649 vs. RHE	1.637 vs. RHE	0.988	20
$GdBa_{0.5}Sr_{0.5}Co_{1.5}Fe_{0.5}O_{5+\delta}$ (GBSCF)	0.648 vs. RHE	1.655 vs. RHE	1.007	20
$MnCoFeO_4$	0.78 vs. RHE	1.78 vs. RHE	0.93	21
Pt/C	0.97 vs. RHE	2.19 vs. RHE	1.22	17
20 wt% Pt/C	0.86 vs. RHE	2.02 vs. RHE	1.16	22
IrO_2	0.38 vs. RHE	1.70 vs. RHE	1.32	17
20 wt% Ir/C	0.69 vs. RHE	1.61 vs. RHE	0.92	22
20 wt% RuO_2/C	0.68 vs. RHE	1.62 vs. RHE	0.94	21
20 wt% Ru/C	0.61 vs. RHE	1.62 vs. RHE	1.01	22

The long-term stability of catalysts is essential for potential applications as electrochemical devices. Here, layered La_2CoO_4 perovskite NPs, exhibiting the best ORR and OER performance, was chosen for further stability study. First, the stability of the layered La_2CoO_4 perovskite NPs was explored by continuous chronopotentiometric response as a function of time, which was measured at 1.75 mA cm^{-2} for ORR at a rotation rate of 1600 rpm for ~42000 s (11.7 h). As shown in **Figure 6.21 (a)**, layered La_2CoO_4 perovskite NPs exhibits a relatively stable ORR activity, although a slight increase of the overpotential can be observed during the testing. In terms of OER, the stability of layered La_2CoO_4 perovskite NPs was measured by cyclic voltammetry under accelerated degradation conditions in the potential regime of 0.1 V to 0.9 V (vs. Ag/AgCl) at a scan rate of 200 mV s^{-1} under oxygen atmosphere. The OER stability can be evaluated by the increment of potential at 10 mA cm^{-2} from OER linear sweep voltammetry (LSV) curves after cycling 1500 times (**Figure 6.21 (b)**). From the inset of **Figure 6.21 (b)**, we can observe that layered La_2CoO_4 perovskite NPs only demonstrate 2.1 mV difference in potential, which is significantly smaller than the commonly-seen difference (i.e., tens of mV) with similar cycling times of perovskite-based catalysts.[33-34] All the ORR and OER activities in conjunction with the

long-term stability analyses substantiated the great promising of layered La_2CoO_4 perovskite NPs as a high-performance and stable bifunctional catalyst for both ORR and OER.

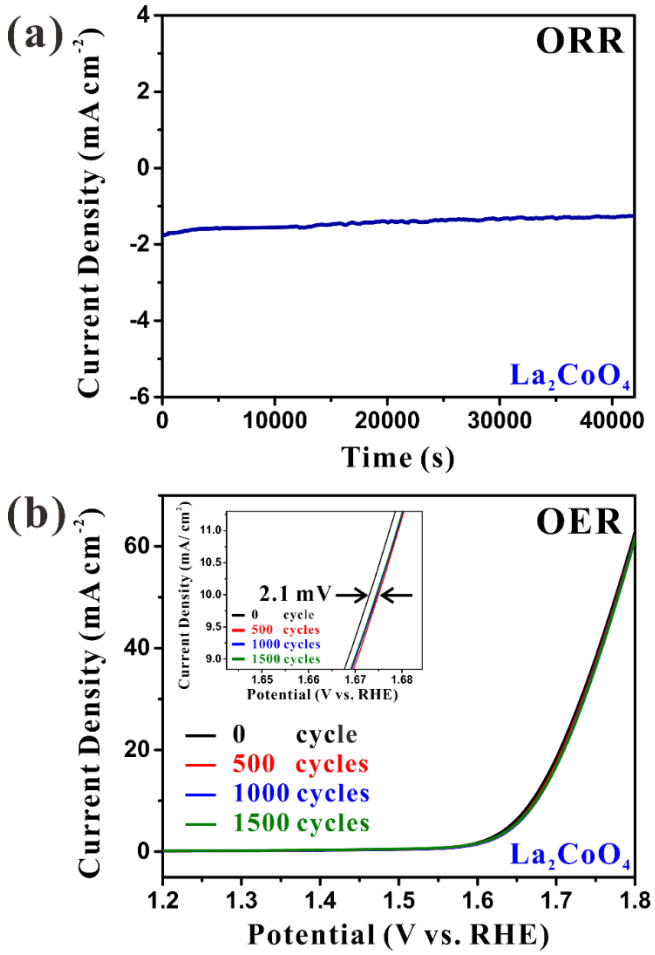

Figure 6.21 (a) ORR chronopotentiometric response of La_2CoO_4 nanoparticles at the applied potential of 0.75 V (vs. RHE) in O_2-saturated 0.1 M KOH. **(b)** OER linear sweep voltammetry (LSV) curves of La_2CoO_4 nanoparticles before and after CV cycling of 1500 cycles within the potential range of 0.1 V to 0.9 V (vs. Ag/AgCl) in O_2-saturated 1 M KOH. Both tests were performed at a rotation speed of 1600 rpm. All the nanoparticles measured were synthesized by employing Sample 2 listed in **Table 6.1** as nanoreactor.

Elucidating the mechanisms attributed to the superior bifunctional electrocatalytic performance (especially the OER activity) of layered La_2CoO_4 perovskite catalysts is crucial for

designing the optimized materials. The excellent electrocatalytic performances may be originated from two principal reasons: highly active lattice oxygen and the increased number of the hydroxyl species (OH^-).[1, 8, 20, 35] First, it was reported that when shifting the oxygen p band closer to the Fermi level, which was accompanied by a reduced energy gap between the metal 3d and O 2p band centers and thus a stronger covalency of the metal-oxygen bond, the redox activity of the lattice oxygen can be triggered to increase the ORR and OER activities of perovskites.[35-36] Moreover, since the OER mechanism may change from concerted proton-electron transfer steps to non-concerted proton-electron transfer steps when lattice oxygen participated in the reaction, the transition from pH-independent to pH-dependent OER kinetics can be observed experimentally.[37-40] For instance, less-covalent $LaCoO_3$ exhibited pH-independent OER behavior (i.e., approximately unchanged OER currents when pH increased from 12.5 to 14), while highly-covalent $SrCoO_{3-\delta}$ exhibited pH-dependent OER behavior, (i.e., increased OER currents by one order when pH increased from 12.5 to 14).[36] Based on this mechanism, one of the reasons for the enhanced catalytic activities of a series of Ruddlesden-Popper catalysts was attributed to the involvement of lattice oxygen to prompt the redox activity. In addition, layered La_2CoO_4 perovskite, among all the doped and undoped Ruddlesden-Popper layered perovskites measured, rendered the lattice oxygen with the highest activity because of the enlarged critical radius (r_c) of the opening space within lattice for oxygen, which can be beneficial to ORR/OER activities.[20] In our study, we thus propose the lattice oxygen of layered La_2CoO_4 perovskite NPs is activated for boosting both ORR and OER activity, substantiated by pH-dependent OER performance (**Figure 6.22**). OER current density from LSV measurement was observed to increase with increased pH significantly only for layered La_2CoO_4 perovskite NPs, while remaining unchanged (or slightly increase) for both $LaFeO_3$ and $LaMnO_3$ perovskite NPs (**Figure 6.22 (a)**). **Figure 6.22 (b)** further

depicts the current density at 1.8 V (vs. RHE) as a function of pH (between pH = 13 and 14), exhibiting obviously different dependence of OER activity on pH of the electrolyte. These results verified the occurrence of transition between different reaction mechanisms due to the participation of lattice oxygen. Second, since the rate-limiting step of the OER and ORR is often identified as the OH^- adsorption and desorption on the surface of the catalysts, the increased OH^- species at the surface of the catalyst can enhance both electrocatalytic activities in alkaline solution.[1, 7-8, 27] Furthermore, the concentration of OH^- species is heavily affected by the chemical properties of the catalysts' surface.[8] Here, the abundance of surface OH^- species of three La-based perovskite and layered perovskite NPs was assessed by XPS. **Figure 6.23 (a-c)** shows the O 1s XPS spectrum of $LaFeO_3$, $LaMnO_3$ and La_2CoO_4 NPs synthesized via employing Sample 2 in **Table 6.1** after annealing, respectively. All the O 1s spectra are deconvoluted into three components as mentioned earlier, with the peak located at 531.5 eV for OH^-, specifically. Obviously, layered La_2CoO_4 perovskite NPs demonstrates the highest value of 4.23 for the ratio of OH^-/O^{2-} as compared to the other two La-based perovskite NPs ($LaFeO_3$, 3.2 and $LaMnO_3$, 0.95, **Figure 6.23**), which may be responsible for the higher reaction rate of layered La_2CoO_4 perovskite NPs for oxygen electrode reactions.

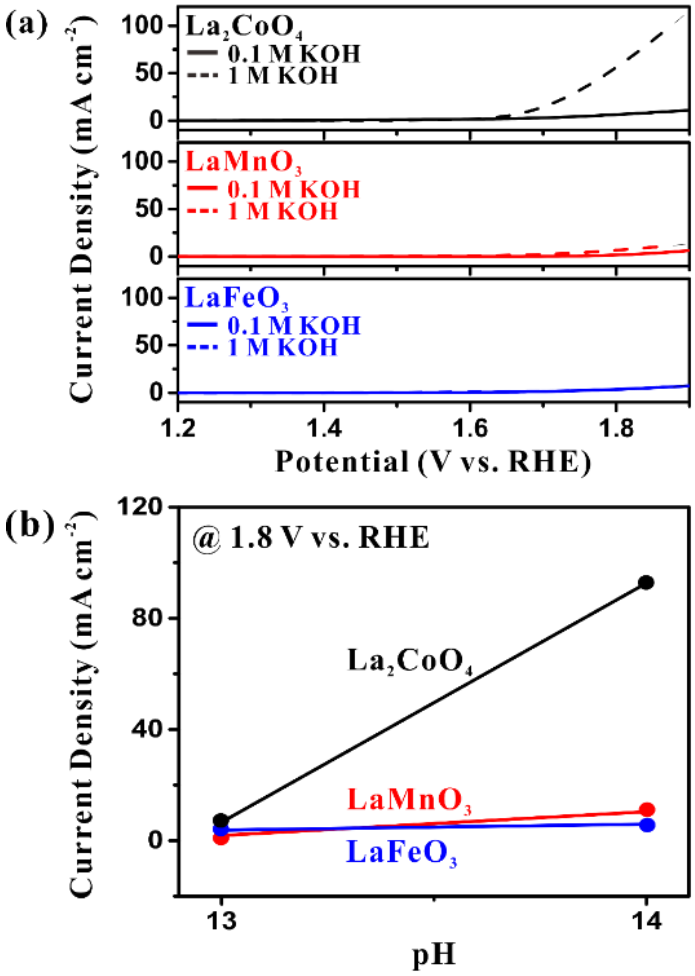

Figure 6.22 pH-dependent OER activity of La-based perovskite and layered perovskite nanoparticles **(a)** OER linear sweep voltammetry (LSV) from O_2-saturated 0.1 M KOH (pH = 13) to 1 M KOH (pH = 14) recorded at a scan rate of 5 mV s^{-1} and a rotation rate of 1600 rpm. **(b)** OER activity at 1.8 V vs. RHE as a function of pH of the electrolyte.

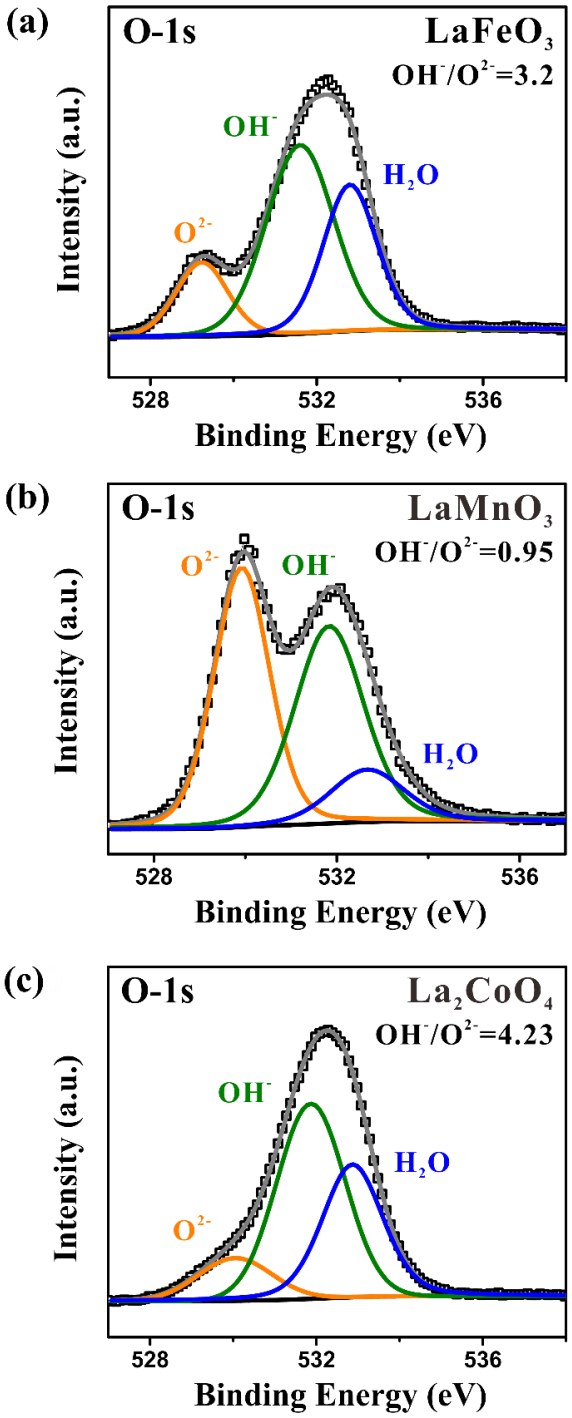

Figure 6.23 O 1s XPS spectra of **(a)** $LaFeO_3$, **(b)** $LaMnO_3$, and **(c)** La_2CoO_4 nanoparticles after two-step annealing.

In addition to different compositions, the dependence of electrocatalytic activity on the size of the catalysts was investigated, enabled by the capability of this star-like nanoreactor synthetic strategy to precisely tailor the size of the as-synthesized NPs. **Figure 6.24 (a, c, e)** exhibits the representative TEM images of PS-ligated La_2CoO_4 NPs of different sizes synthesized by capitalizing different star-like PAA-*b*-PS diblock copolymers as nanoreactors (i.e., Sample 1-3 in **Table 6.1**). Their corresponding average diameters are 8.5 ± 0.8 nm (using Sample 1 as nanoreactor), 17.1 ± 1.5 nm (using Sample 2 as nanoreactor) and 22.1 ± 2.2 nm (using Sample 3 as nanoreactor), which can be found from the respective NP size distribution histogram in **Figure 6.24 (b, d, f)**. The narrow average size distribution can verify the robustness of this synthetic strategy for tuning the size of the resulting NPs. In particular, we synthesized the catalysts of the best ORR and OER performance (i.e., La_2CoO_4), among the three La-based catalysts, with varied sizes to explore if we can further improve the activity by changing the size of the catalysts. **Figure 6.25** demonstrates the size effect of the layered La_2CoO_4 perovskite NPs on both ORR (**Figure 6.25 (a)**) and OER (**Figure 6.25 (b)**) activities, which have been limitedly-studied due to the difficulty for obtaining layered perovskites with well-controlled dimension. Enhanced ORR activities (i.e., more positive half-wave potential and larger limiting current density) and OER activities (smaller overpotential and larger limiting current density) were discovered when the size of the catalyst decreased. Layered La_2CoO_4 perovskite NPs with the smallest size (D = 8.5 nm) therefore shows the best bifunctional electrocatalytic activities among all three sizes, represented by continuously-decreasing ΔE values from 1.06 (with La_2CoO_4 of D = 22.1 nm ± 2.2 nm), 0.96 (with La_2CoO_4 of D = 17.1 nm ± 1.5 nm) to 0.88 (with La_2CoO_4 of D = 8.5 nm ± 0.8 nm) (**Figure 6.26**). The improved ORR and OER performance as the size decreased can be originated from larger surface area, thus more active sites for electrocatalytic reactions,[41-42] as well as possibly

improved electroconductivity of the catalysts.[43] Finally, summaries of bifunctional oxygen electrode activity of varied compositions (i.e., $LaFeO_3$, $LaMnO_3$ and La_2CoO_4 NPs with similar size, D = 16-17 nm) and varied sizes (i.e., La_2CoO_4 NPs of 8.5, 17.1 and 22.1 nm) are provided in **Figure 6.27**, suggesting layered La_2CoO_4 NPs can be an outstanding electrocatalyst for both ORR and OER.

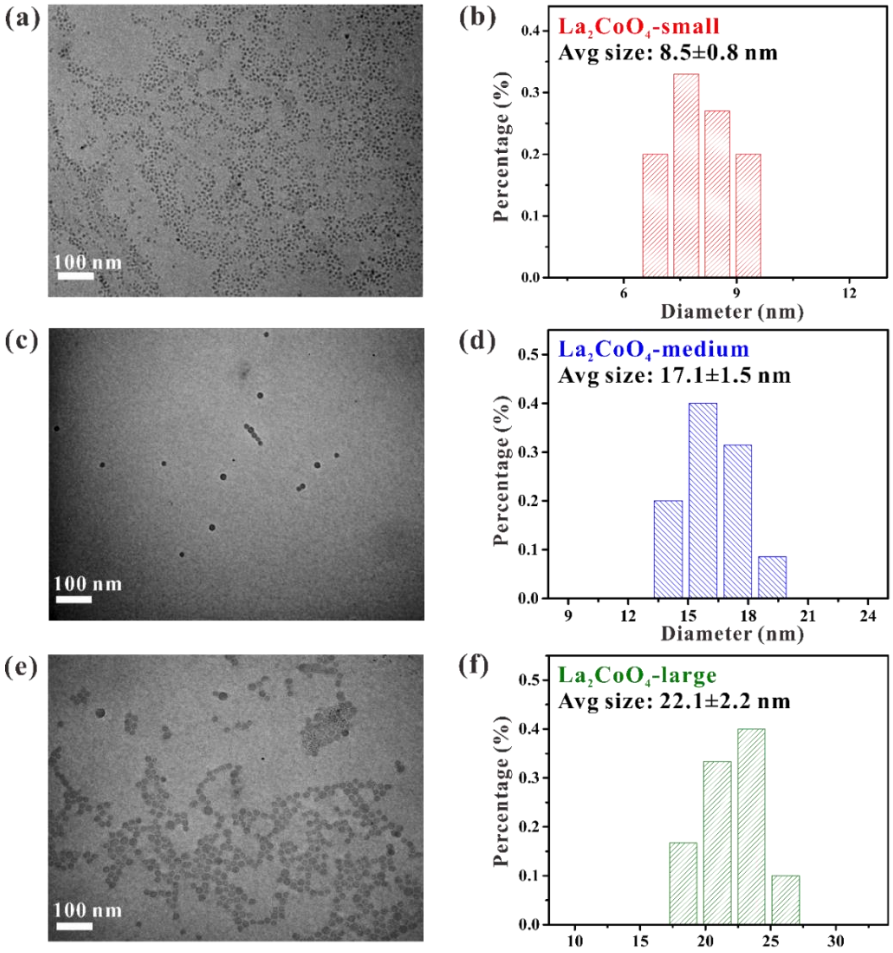

Figure 6.24 TEM images of as-synthesized PS-ligated layered perovskite La_2CoO_4 nanoparticles with the average diameter of **(a)** 8.5 nm, **(c)** 17.1 nm and **(e)** 22.1 nm, which were synthesized by employing respective star-like PAA-*b*-PS diblock copolymers as nanoreactors (i.e., Sample 1-3 in **Table 6.1**). **(b, d, f)** Size distribution histogram of corresponding PS-ligated La_2CoO_4 nanoparticles, measured by calculating the diameter of 100 NPs with *ImageJ* from the TEM images. The crystallinity of all the particles was improved by two-step annealing before electrocatalytic measurement.

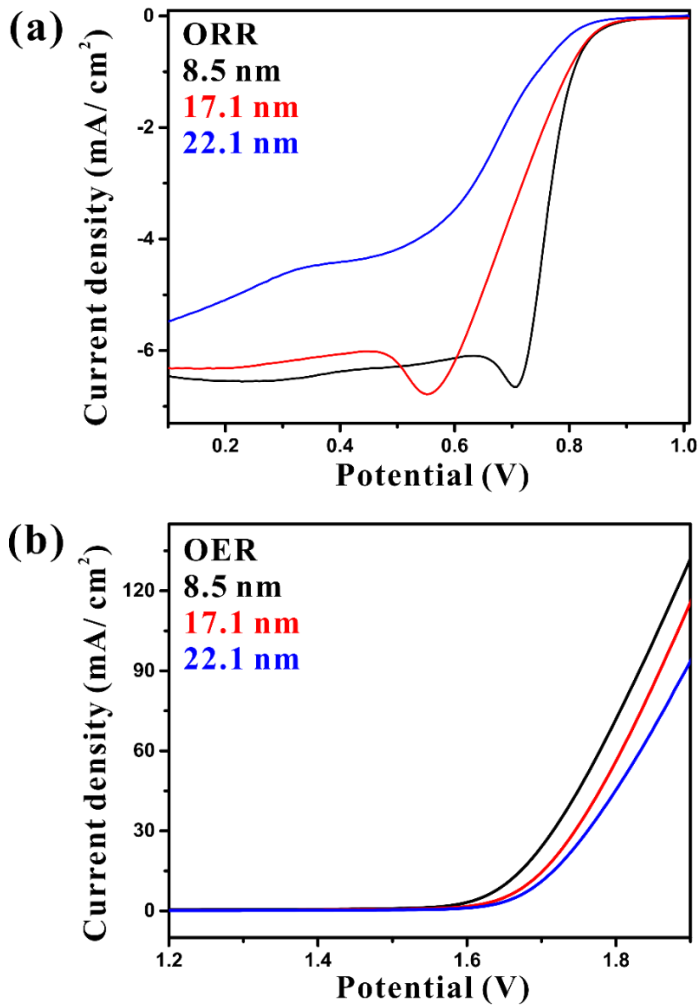

Figure 6.25 (a) The ORR polarization curves of La_2CoO_4 nanoparticles with varied sizes in O_2-saturated 0.1 M KOH solution. **(b)** The OER polarization curves of La_2CoO_4 nanoparticles with varied sizes in 1 M KOH solution. Both tests were conducted at a scan rate of 5 mV/s and a rotation rate of 1600 rpm. The measured La_2CoO_4 nanoparticles of 8.5 nm, 17.1 nm and 22.1 nm were synthesized by employing respective star-like PAA-*b*-PS diblock copolymers as nanoreactors (i.e., Sample 1-3 in **Table 6.1**).

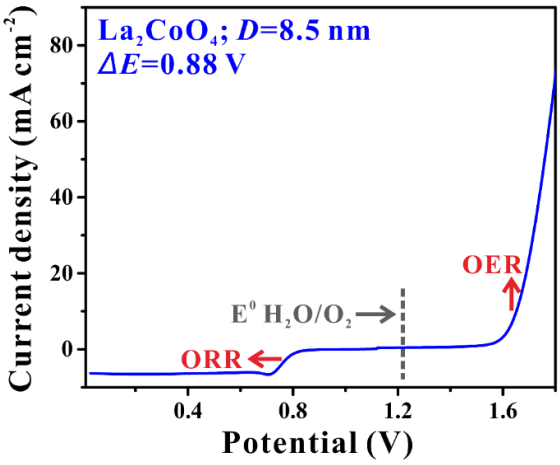

Figure 6.26 OER/ORR polarization curves for smallest-sized $LaCo_2O_4$ nanoparticles (D = 8.5 nm) catalyst. The nanoparticles measured were crafted via employing Sample 1 in **Table 6.1** as nanoreactor.

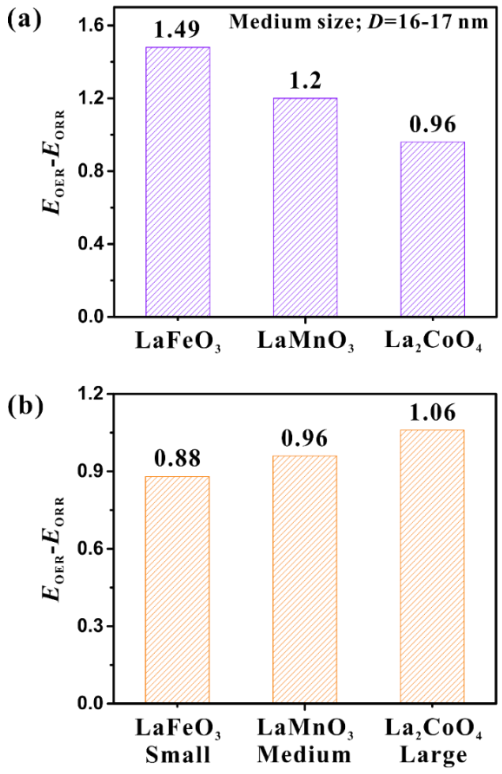

Figure 6.27 Oxygen electrode activities (E_{OER}-E_{ORR}) of catalysts with **(a)** varied compositions, i.e., $LaFeO_3$, $LaMnO_3$, and La_2CoO_4 nanoparticles, all crafted by employing Sample 2 in **Table 6.1** as nanoreactor, and **(b)** varied sizes of La_2CoO_4 nanoparticles, i.e., 8.5 nm, 17.1 nm, and 22.1 nm, crafted by employing Sample 1-3 in **Table 6.1** as nanoreactors, respectively.

6.4 Conclusion

In summary, we proposed a versatile synthetic strategy to achieve La-based NPs with perovskite and layered perovskite structure by employing star-like PAA-*b*-PS diblock copolymers as nanoreactors, and demonstrated that layered La_2CoO_4 perovskite NPs exhibits remarkable electrocatalytic activities and stability for oxygen electrode reactions over previously-reported perovskite and perovskite derivative electrocatalysts. Intriguingly, the synthesis temperature was significantly reduced by this nanoreactor-assisted approach for achieving all three La-based NPs (i.e., $LaFeO_3$, $LaMnO_3$ and La_2CoO_4), especially for layered La_2CoO_4 perovskite NPs, possibly due to the nanometer-scaled product. In addition, the capability of tailoring the as-synthesized NPs by changing the molecular weight of inner PAA block, thus the compartment for precursors to coordinate and NPs to grow, allows the investigation into the correlation between the size of the catalysts and electrocatalytic performance. The excellent catalytic activities of layered La_2CoO_4 perovskite NPs for both ORR and OER, which are superior to those of $LaFeO_3$ and $LaMnO_3$ perovskite NPs, could be attributed to highly active lattice oxygen as well as the increased amount of hydroxyl groups. Furthermore, size-dependent electrocatalysis of layered La_2CoO_4 perovskite NPs exhibits an enhanced ORR and OER activities as the NPs size decreases, resulting in the optimized performance of this catalyst. In particular, the oxygen activity (i.e., ΔE value) of layered La_2CoO_4 perovskite NPs of the smallest size (D = 8.5 nm) is 0.88 V, which is comparable or even greater than that of the previously reported transition metal-based perovskites and perovskite derivatives. Therefore, the newly-explored layered La_2CoO_4 perovskite NPs shows great potential in a wide range of energy devices, including intermediate temperature-reversible solid oxide fuel cells, metal-air batteries, etc. In general, structure engineering to yield layered perovskites can be regarded as an effective approach for fundamentally understanding the correlation between crystal

structure, electronic configuration and electrocatalytic activities and thus promoting the performance of the catalysts.

6.5 References

1. Kim, N.-I.; Sa, Y. J.; Yoo, T. S.; Choi, S. R.; Afzal, R. A.; Choi, T.; Seo, Y.-S.; Lee, K.-S.; Hwang, J. Y.; Choi, W. S., Oxygen-deficient triple perovskites as highly active and durable bifunctional electrocatalysts for oxygen electrode reactions. *Science advances* **2018,** *4* (6), eaap9360.
2. Suntivich, J.; May, K. J.; Gasteiger, H. A.; Goodenough, J. B.; Shao-Horn, Y., A perovskite oxide optimized for oxygen evolution catalysis from molecular orbital principles. *Science* **2011,** *334* (6061), 1383-1385.
3. Suntivich, J.; Gasteiger, H. A.; Yabuuchi, N.; Nakanishi, H.; Goodenough, J. B.; Shao-Horn, Y., Design principles for oxygen-reduction activity on perovskite oxide catalysts for fuel cells and metal–air batteries. *Nature chemistry* **2011,** *3* (7), 546-550.
4. Zhou, S.; Miao, X.; Zhao, X.; Ma, C.; Qiu, Y.; Hu, Z.; Zhao, J.; Shi, L.; Zeng, J., Engineering electrocatalytic activity in nanosized perovskite cobaltite through surface spin-state transition. *Nature communications* **2016,** *7* (1), 1-7.
5. Chen, D.; Chen, C.; Baiyee, Z. M.; Shao, Z.; Ciucci, F., Nonstoichiometric oxides as low-cost and highly-efficient oxygen reduction/evolution catalysts for low-temperature electrochemical devices. *Chemical reviews* **2015,** *115* (18), 9869-9921.
6. Lee, S. A.; Oh, S.; Hwang, J.-Y.; Choi, M.; Youn, C.; Kim, J. W.; Chang, S. H.; Woo, S.; Bae, J.-S.; Park, S., Enhanced electrocatalytic activity via phase transitions in strongly correlated SrRuO 3 thin films. *Energy & Environmental Science* **2017,** *10* (4), 924-930.
7. Jung, K.-N.; Jung, J.-H.; Im, W. B.; Yoon, S.; Shin, K.-H.; Lee, J.-W., Doped lanthanum nickelates with a layered perovskite structure as bifunctional cathode catalysts for rechargeable metal–air batteries. *ACS applied materials & interfaces* **2013,** *5* (20), 9902-9907.
8. Kim, N.-I.; Afzal, R. A.; Choi, S. R.; Lee, S. W.; Ahn, D.; Bhattacharjee, S.; Lee, S.-C.; Kim, J. H.; Park, J.-Y., Highly active and durable nitrogen doped-reduced graphene oxide/double perovskite bifunctional hybrid catalysts. *Journal of Materials Chemistry A* **2017,** *5* (25), 13019-13031.
9. Huang, Y.-H.; Dass, R. I.; Xing, Z.-L.; Goodenough, J. B., Double perovskites as anode materials for solid-oxide fuel cells. *Science* **2006,** *312* (5771), 254-257.
10. Carneiro, J. S. A.; Williams, J.; Gryko, A.; Herrera, L. P.; Nikolla, E., Embracing the Complexity of Catalytic Structures: A Viewpoint on the Synthesis of Nonstoichiometric Mixed Metal Oxides for Catalysis. *ACS Catalysis* **2020,** *10* (1), 516-527.
11. Ma, X.; Carneiro, J. S.; Gu, X.-K.; Qin, H.; Xin, H.; Sun, K.; Nikolla, E., Engineering complex, layered metal oxides: High-performance nickelate oxide nanostructures for oxygen exchange and reduction. *ACS Catalysis* **2015,** *5* (7), 4013-4019.
12. Tarancón, A.; Burriel, M.; Santiso, J.; Skinner, S. J.; Kilner, J. A., Advances in layered oxide cathodes for intermediate temperature solid oxide fuel cells. *Journal of Materials chemistry* **2010,** *20* (19), 3799-3813.
13. Xie, W.; Lee, Y.-L.; Shao-Horn, Y.; Morgan, D., Oxygen Point Defect Chemistry in Ruddlesden–Popper Oxides (La1–x Sr x) 2MO4±δ (M= Co, Ni, Cu). *The journal of physical chemistry letters* **2016,** *7* (10), 1939-1944.
14. Sengodan, S.; Choi, S.; Jun, A.; Shin, T. H.; Ju, Y.-W.; Jeong, H. Y.; Shin, J.; Irvine, J. T.; Kim, G., Layered oxygen-deficient double perovskite as an efficient and stable anode for direct hydrocarbon solid oxide fuel cells. *Nature materials* **2015,** *14* (2), 205-209.
15. Takeguchi, T.; Yamanaka, T.; Takahashi, H.; Watanabe, H.; Kuroki, T.; Nakanishi, H.; Orikasa, Y.; Uchimoto, Y.; Takano, H.; Ohguri, N., Layered perovskite oxide: a reversible air electrode for oxygen evolution/reduction in rechargeable metal-air batteries. *Journal of the American Chemical Society* **2013,** *135* (30), 11125-11130.
16. Zhang, K.; Ge, L.; Ran, R.; Shao, Z.; Liu, S., Synthesis, characterization and evaluation of cation-ordered LnBaCo2O5+ δ as materials of oxygen permeation membranes and cathodes of SOFCs. *Acta Materialia* **2008,** *56* (17), 4876-4889.

17. Grimaud, A.; May, K. J.; Carlton, C. E.; Lee, Y.-L.; Risch, M.; Hong, W. T.; Zhou, J.; Shao-Horn, Y., Double perovskites as a family of highly active catalysts for oxygen evolution in alkaline solution. *Nature communications* **2013,** *4*, 2439.
18. Jung, K.-N.; Lee, J.-I.; Im, W. B.; Yoon, S.; Shin, K.-H.; Lee, J.-W., Promoting Li 2 O 2 oxidation by an La 1.7 Ca 0.3 Ni 0.75 Cu 0.25 O 4 layered perovskite in lithium–oxygen batteries. *Chemical Communications* **2012,** *48* (75), 9406-9408.
19. Liu, R.; Liang, F.; Zhou, W.; Yang, Y.; Zhu, Z., Calcium-doped lanthanum nickelate layered perovskite and nickel oxide nano-hybrid for highly efficient water oxidation. *Nano Energy* **2015,** *12*, 115-122.
20. Huan, Y.; Chen, S.; Zeng, R.; Wei, T.; Dong, D.; Hu, X.; Huang, Y., Intrinsic Effects of Ruddlesden-Popper-Based Bifunctional Catalysts for High-Temperature Oxygen Reduction and Evolution. *Advanced Energy Materials* **2019,** *9* (29), 1901573.
21. Aguadero, A.; Alonso, J. A.; Daza, L., Oxygen excess in La2CoO4+ δ: a neutron diffraction study. *Zeitschrift für Naturforschung B* **2008,** *63* (6), 615-622.
22. Hardin, W. G.; Slanac, D. A.; Wang, X.; Dai, S.; Johnston, K. P.; Stevenson, K. J., Highly active, nonprecious metal perovskite electrocatalysts for bifunctional metal–air battery electrodes. *The journal of physical chemistry letters* **2013,** *4* (8), 1254-1259.
23. Zhang, W.-W.; Povoden-Karadeniz, E.; Xu, H.; Chen, M., Thermodynamic Modeling of the La-Co-O System. *Journal of Phase Equilibria and Diffusion* **2019,** *40* (2), 219-234.
24. Ortatatlı, Ş.; Ternieden, J.; Weidenthaler, C., Low Temperature Formation of Ruddlesden–Popper-Type Layered La2CoO4±δ Perovskite Monitored via In Situ X-ray Powder Diffraction. *European Journal of Inorganic Chemistry* **2018,** *2018* (48), 5238-5245.
25. Yousaf, A. B.; Imran, M.; Farooq, M.; Kasak, P., Interfacial phenomenon and nanostructural enhancements in palladium loaded lanthanum hydroxide nanorods for heterogeneous catalytic applications. *Scientific reports* **2018,** *8* (1), 1-9.
26. Wen, Y.; Peng, S.; Wang, Z.; Hao, J.; Qin, T.; Lu, S.; Zhang, J.; He, D.; Fan, X.; Cao, G., Facile synthesis of ultrathin NiCo 2 S 4 nano-petals inspired by blooming buds for high-performance supercapacitors. *Journal of Materials Chemistry A* **2017,** *5* (15), 7144-7152.
27. Zhu, Y.; Zhou, W.; Yu, J.; Chen, Y.; Liu, M.; Shao, Z., Enhancing electrocatalytic activity of perovskite oxides by tuning cation deficiency for oxygen reduction and evolution reactions. *Chemistry of Materials* **2016,** *28* (6), 1691-1697.
28. Huang, Z.; Zhou, W.; Ouyang, C.; Wu, J.; Zhang, F.; Huang, J.; Gao, Y.; Chu, J., High performance of Mn-Co-Ni-O spinel nanofilms sputtered from acetate precursors. *Scientific reports* **2015,** *5*, 10899.
29. Zhang, D.; Song, Y.; Du, Z.; Wang, L.; Li, Y.; Goodenough, J. B., Active LaNi 1− x Fe x O 3 bifunctional catalysts for air cathodes in alkaline media. *Journal of Materials Chemistry A* **2015,** *3* (18), 9421-9426.
30. Jung, J.-I.; Risch, M.; Park, S.; Kim, M. G.; Nam, G.; Jeong, H.-Y.; Shao-Horn, Y.; Cho, J., Optimizing nanoparticle perovskite for bifunctional oxygen electrocatalysis. *Energy & Environmental Science* **2016,** *9* (1), 176-183.
31. Prabu, M.; Ramakrishnan, P.; Ganesan, P.; Manthiram, A.; Shanmugam, S., LaTi0. 65Fe0. 35O3− δ nanoparticle-decorated nitrogen-doped carbon nanorods as an advanced hierarchical air electrode for rechargeable metal-air batteries. *Nano Energy* **2015,** *15*, 92-103.
32. Jung, J. I.; Jeong, H. Y.; Lee, J. S.; Kim, M. G.; Cho, J., A bifunctional perovskite catalyst for oxygen reduction and evolution. *Angewandte Chemie International Edition* **2014,** *53* (18), 4582-4586.
33. Miao, H.; Wu, X.; Chen, B.; Wang, Q.; Wang, F.; Wang, J.; Zhang, C.; Zhang, H.; Yuan, J.; Zhang, Q., A-site deficient/excessive effects of LaMnO3 perovskite as bifunctional oxygen catalyst for zinc-air batteries. *Electrochimica Acta* **2020,** *333*, 135566.
34. Ashok, A.; Kumar, A.; Bhosale, R. R.; Almomani, F.; Malik, S. S.; Suslov, S.; Tarlochan, F., Combustion synthesis of bifunctional LaMO3 (M= Cr, Mn, Fe, Co, Ni) perovskites for oxygen reduction and oxygen evolution reaction in alkaline media. *Journal of Electroanalytical Chemistry* **2018,** *809*, 22-30.

35. Grimaud, A.; Hong, W. T.; Shao-Horn, Y.; Tarascon, J.-M., Anionic redox processes for electrochemical devices. *Nature materials* **2016,** *15* (2), 121.
36. Grimaud, A.; Diaz-Morales, O.; Han, B.; Hong, W. T.; Lee, Y.-L.; Giordano, L.; Stoerzinger, K. A.; Koper, M. T.; Shao-Horn, Y., Activating lattice oxygen redox reactions in metal oxides to catalyse oxygen evolution. *Nature chemistry* **2017,** *9* (5), 457.
37. Giordano, L.; Han, B.; Risch, M.; Hong, W. T.; Rao, R. R.; Stoerzinger, K. A.; Shao-Horn, Y., pH dependence of OER activity of oxides: current and future perspectives. *Catalysis Today* **2016,** *262*, 2-10.
38. Koper, M. T. M., Theory of multiple proton–electron transfer reactions and its implications for electrocatalysis. *Chemical Science* **2013,** *4* (7), 2710-2723.
39. Trześniewski, B. J.; Diaz-Morales, O.; Vermaas, D. A.; Longo, A.; Bras, W.; Koper, M. T.; Smith, W. A., In situ observation of active oxygen species in Fe-containing Ni-based oxygen evolution catalysts: the effect of pH on electrochemical activity. *Journal of the American Chemical Society* **2015,** *137* (48), 15112-15121.
40. Gu, X.-K.; Samira, S.; Nikolla, E., Oxygen sponges for electrocatalysis: oxygen reduction/evolution on nonstoichiometric, mixed metal oxides. *Chemistry of Materials* **2018,** *30* (9), 2860-2872.
41. Matter, P. H.; Zhang, L.; Ozkan, U. S., The role of nanostructure in nitrogen-containing carbon catalysts for the oxygen reduction reaction. *Journal of Catalysis* **2006,** *239* (1), 83-96.
42. Kim, W. S.; Anoop, G.; Lee, H. J.; Lee, S. S.; Kwak, J. H.; Lee, H. J.; Jo, J. Y., Facile synthesis of perovskite LaMnO3+ δ nanoparticles for the oxygen reduction reaction. *Journal of Catalysis* **2016,** *344*, 578-582.
43. Seo, J.; Cha, D.; Takanabe, K.; Kubota, J.; Domen, K., Particle size dependence on oxygen reduction reaction activity of electrodeposited TaO x catalysts in acidic media. *Physical Chemistry Chemical Physics* **2014,** *16* (3), 895-898.

CHAPTER 7. FACILE MANIPULATION OF MAGNETIC PROPERTIES OF SPINEL MFE2O4 (M = CO, NI, MN) NANOPARTICLES VIA ROBUST SIZE AND COMPOSITION ENGINEERING

Yeu-Wei Harn *et al.* in preparation (to be submitted to *Angewandte Chemie International Edition*)

7.1 Introduction

Monodisperse magnetic nanocrystals have been widely studied during the past decade because the fascinating physical and chemical properties they possess as compared to their counterpart bulk, giving interests in both fundamental scientific understanding and technological applications.[1-4] Specifically, spinel ferrites MFe_2O_4 (M = Co, Ni, Mn, Zn, Cu, Mg, etc.) with oxygen forming an fcc close packing whereas M^{2+} and Fe^{3+} occupying either octahedral interstitial sites or tetrahedral sites, demonstrate intriguing magnetic,[5] magnetoresistive,[6] and magneto-optical properties.[7] All these attractive features lead to a broad range of applications in many state-of-the-art technological fields, e.g., magnetic resonance image,[8] biomedical,[9] catalysis,[10] permanent magnets,[11] ferrofluids,[12] and recording media.[13] Moreover, the magnetic and electrical properties of the MFe_2O_4 can be systematically tailored via changing and/or partial substitution of the divalent M^{2+} cation, as well as tuning the size, shape, and crystallinity.[14-16] For instance, magnetic nanoparticle (NPs) with size around 5-10 nm are preferred for magnetic carriers in bioscience because of high enough magnetic moment and absence of magnetic memory.[17] In contrast, those with size around a couple of tens of nanometers are suitable for magnetic memory because the transition from superparamagnetic to ferro/ferrimagnetic behavior occurs and larger remnant magnetization as well as coercive field can be achieved within this size range.[18]

Due to the relative complexity of spinel magnetic materials, a better understanding of the relationship between the crystal structure, morphologies, synthetic conditions, and the magnetic and/or other desired properties is required. Therefore, finding suitable strategies for synthesizing spinel ferrite nanocrystals with controllable composition, size and shape becomes a critical research focus of magnetic nanomaterials. A large variety of different synthetic methods for obtaining spinel ferrite nanocrystals have been proposed, including sol-gel combustion,[19] microemulsion techniques,[20] coprecipitation,[21] thermal decomposition,[22] etc. Among all the pathways, coprecipitation and thermal decomposition are the most common methods utilized for synthesizing MFe_2O_4 nanomaterials. The coprecipitation method, though advantageous in low cost and high yield, generally suffers from the necessity of careful adjustment of reaction condition and poor control over the size and shape of the product.[21] On the other hand, thermal decomposition of mixed organic M^{2+} and Fe^{3+} compounds (*e.g.*, metal acetylacetonates, metal carbonyls, etc.) with the introduction of surfactants under higher reaction temperature can provide spinel ferrite nanocrystals with good crystallinity as well as uniform size and shape. However, a general and robust synthetic process for directly obtaining spinel ferrite NPs with tunable size, composition, and narrow size distribution without the need to precisely tune the reaction parameters, i.e., reaction temperature, heating rate or even two-step seed-mediated synthesis, remains difficult, resulting in deficient studies of the dependence of magnetic properties on composition and morphology.[14, 22]

In this paper, we proposed a general and versatile strategy for synthesizing polymer-ligated spinel magnetic NPs with judicious control over the size and composition, leading to tailorable magnetic properties, in particular saturation magnetization (M_s) and blocking temperature (T_B). In brief, by capitalizing amphiphilic star-like poly(acrylic acid)-*block*-poly(styrene-*co*-acrylonitrile)

(PAA-*b*-PSAN) as nanoreactors, spinel magnetic NPs can be readily formed. Due to the strong interaction between carboxylic acid groups of the inner PAA blocks with the metal moieties of the precursors, the precursors and thus the spinel magnetic NPs after thermolysis can be loaded and confined within PAA compartment. Therefore, facilely by changing the molecular weight of the inner PAA block, the size of the as-synthesized spinel magnetic NPs can be precisely tuned, and narrow size distribution can be maintained. In addition, a rich diversity of spinel magnetic NPs can be acquired simply by changing the precursors used. Notably, compared to the magnetic NPs that are commonly stabilized by small-molecule ligands, the outer PSAN blocks are permanently and covalently ligated on the surface of the spinel magnetic NPs, preventing NPs from aggregation and providing great solubility in various kinds of organic solvents even after multiple times of purification. The surface chemistry of the NPs can be facilely modified by star-like diblock copolymer with different outer blocks. For example, by employing star-like PAA-*b*-poly(ethylene oxide) (PEO) as nanoreactors, the as-synthesized NPs can then be well-dispersed in polar solvents, facilitating the applications in the biomedical fields. This robust synthetic strategy in turn renders the possibility of revealing the size effect (by NPs with same composition yet tunable sizes) and composition effect (by NPs with similar size yet varied composition), individually on their magnetic properties. With the controlled morphology; composition; good dispersion in various kinds of solvents; superparamagnetic behavior and relatively high saturation magnetization, these as-synthesized spinel magnetic NPs prepared by star-like amphiphilic and hydrophilic diblock copolymer nanoreactors have great potential in various kinds of applications, such as magnetic nanodevice, magnetically recoverable nanocatalysts, hyperthermia cancer treatment, and MRI contrast agents, etc.

7.2 Experiment Details

The synthetic process of star-like PtBA homopolymer has been described in Chapter 3, *3.1*. Below we will specify the procedure for synthesizing second PSAN block from the first P*t*BA block, yielding star-like PAA-*b*-PSAN diblock copolymer nanoreactor. Furthermore, synthesis of star-like PAA-*b*-PEO diblock copolymer as well as using both star-like PAA-*b*-PSAN and PAA-*b*-PEO as nanoreactors for obtaining spinel magnetic nanoparticles and the characterizations used in this study will be described.

7.2.1 Synthesis of 21-arm star-like poly(tert-butyl acrylate)-block-poly(styrene-co-acrylonitrile) (PtBA-b-PSAN) by second ATRP

Star-like P*t*BA-Br was used as the macroinitiator for the synthesis of star-like P*t*BA-*b*-PSAN through ATRP of styrene and acrylonitrile as the comonomers. In a typical procedure, A reaction mixture at star-like P*t*BA-Br: CuBr: PMDETA: styrene: acrylonitrile = 1:1:2:800:200 was mixed in a pressure vessel, degassed by three freeze-pump-thaw cycles and re-charged with argon. The vessel was sealed and immerged in a 90 ºC oil bath under stirring for a desired period. The reaction was subsequently quenched by dipping the vessel into liquid N_2, diluted with THF, and passed through a column of neutral alumina to remove the Cu catalyst. After removing the solvent, the product was precipitated with methanol as the precipitator to yield a white solid.

7.2.2 Synthesis of star-like PtBA-b-PEO diblock copolymers

(a) The star-like P*t*BA obtained in the previous step (0.2 g) was first dissolved in DMF (5 ml). After fully sonicating and stirring to ensure the complete dissolving of the star-like P*t*BA homopolymer, pre-determined sodium azide was added (with the molar ratio of Br in star-like

P*t*BA homopolymer to sodium azide = 1:10), followed by continuous stirring for a day under room temperature and N_2 protection. The reaction solution was then concentrated by a rotary evaporator and then precipitated in a mixed solution of methanol and water (1/5, v/v). The precipitant, i.e., the final product was collected and dried in the vacuum oven at room temperature overnight.

(b) The typical procedure was described below. mPEO-OH was first dissolved in THF under Ar protection, followed by the addition of the DPMK solution until the color of the solution turned into reddish-brown. Propargyl bromide was added drop-by-drop into the reacting solution during 2 h at 0 ^{o}C. Stirring at room temperature was continued for another day. Finally, by precipitating the solution in diethyl ether twice and dried the precipitant in the vacuum at 40 ^{o}C, the product was obtained.

(c) Both star-like P*t*BA-*b*-PEO and alkyne-terminated mPEO were dissolved in DMF and transferred into ampule, followed by the addition of CuBr and PMDETA into the solution. After purging the reaction solution with N_2 for 2 h, the reaction started by placing the ampule in the oil bath (at 90 ^{o}C) for more than a day. By immersing the ampule in liquid N_2, the reaction was terminated. Finally, the solution was first passing through the alumina column to remove the Cu catalyst, then precipitated in cold hexane, and dried in the vacuum oven at room temperature for a day.

7.2.3 Synthesis of 21-arm star-like poly(acrylic acid)-block-poly(styrene-co-acrylonitrile) (PAA-b-PSAN) and star-like poly(acrylic acid)-block-poly(ethylene oxide) (PAA-b-PEO) by hydrolysis

P*t*BA block in the star-like P*t*BA-*b*-PSAN was hydrolyzed into PAA block to yield amphiphilic star-like PAA-*b*-PSAN diblock copolymers. Typically, star-like P*t*BA-*b*-PSAN (0.4 g) was dissolved in $CHCl_3$ (40 ml), followed by the slow addition of TFA (3 ml). After stirring at room temperature for 24 h, the reaction mixture was dried, re-dissolved in DMF, and gradually precipitated in methanol. The dissolution-precipitation process was repeated more than 5 times. The final product was washed with hexane and dried under vacuum to yield a white solid. In terms of star-like PAA-*b*-PEO, the hydrolysis followed similar steps except after hydrolysis, the product was directly obtained by exploiting a rotary evaporator to remove the solvent.

7.2.4 Synthesis of PSAN-ligated and PEO- ligated MFe_2O_4 (M=Mn, Co, Ni) nanoparticles

MFe_2O_4 (M=Mn, Co, Ni) nanoparticles were synthesized by capitalizing on star-like PAA-b-PSAN diblock copolymers as nanoreactors. The strong coordination between the carboxyl groups and metal moieties leads to selective absorption of metal precursors (e.g. $Co(acac)_2$, $Fe(acac)_3$) onto the PAA core. Moreover, the organometallic precursors were pushed into the more polar PAA domain due to poor solubility of precursor in DPE as a result of its low polarity. After thermolysis, PSAN ligated MFe_2O_4 nanoparticles of different sizes were formed effectively with star-like PAA-*b*-PSAN of different molecular weights. In a typical procedure (taken $CoFe_2O_4$ as an example), star-like PAA-*b*-PSAN (10 mg) was dissolved in mixed solvents of DPE (9 ml) and BA (1 ml) under 50 ºC, followed by the addition of $Co(acac)_2$ (76 mg) and $Fe(acac)_3$ (216 mg) and stirred overnight under Ar. PAA core collapsed in DPE due to poor solubility. BA, a polar solvent, was added to create a more stable micelle with the outer PSAN dissolved in DPE and inner PAA stretched in BA. As mentioned above, the metal precursors tended to dominate the swelled PAA core because of polarity preference. The addition of BA led to the nucleation and growth of more

spherical nanoparticles. The reaction was heated to refluxing temperature (about 258 ºC) of the solvent for 12 h under stirring with Ar protection, yielding a dark black solution. The nanoparticles were precipitated and washed with ethanol 4 times and dried under vacuum overnight. On the other hand, for obtaining PEO-capped spinel ferrite nanoparticles, simply by substituting the nanoreactors with star-like PAA-*b*-PEO diblock copolymer, followed by the same reaction procedure, the nanoparticles can be obtained. After successfully attaining PEO-capped nanoparticles, purification steps were conducted by centrifugation at varied speeds to separate polymer-ligated products from residual precursors, and those grown outside of the nanoreactors.

7.2.5 Characterization

Gel permeation chromatography (GPC) equipped with an LC20AD HPLC pump and a refractive index detector (RID-10A, 120 V) was used to measure the number-average molecular weight (M_n) and the dispersity (PDI) of star-like polymers. Calibration was built from monodisperse polystyrenes as standards. THF was used as the eluent with a flow rate of 1.0 ml/min and an operating temperature of 35 °C. Proton nuclear magnetic resonance (^{1}H NMR) spectra of organic samples were recorded on Varian VXR-300 spectroscope. The morphology of all samples was measured by transmission electron microscope (TEM, JEOL 100 CX-II; operated at 100 kV) and high-resolution transmission electron microscope (HRTEM, FEI Tecnai F30; operated at 300 kV). TEM and HRTEM samples were prepared by dropping product solution in ethanol or DMF onto a carbon-coated copper TEM grid (300 mesh) and dried at room temperature. Powder X-ray diffraction (XRD, Rigaku D/max-2400) measurements were conducted using Cu-Kα radiation (40 kV, 120 mA) with a step of 0.08° per 25s and a 2θ range of 20-60°. Raman spectroscopy characterizations were performed on a Renishaw InVia Raman spectrometer equipped with a 532

nm laser. X-ray photoelectron spectroscopy (XPS) measurements were carried out on a Thermo K-alpha electron spectrometer with Al Kα radiation. Thermogravimetric analysis (TGA) was done using a Perkin Elmer DIAMOND TG/DTA instrument in air atmosphere at a heating rate of 10 ^{o}C min^{-1} from room temperature to 800 ^{o}C. Magnetic measurements were conducted with SQUID magnetometer. Hysteresis measurements were done at 300 K with applied fields ranged from -15 kOe to 15 kOe.

7.3 Results and Discussion

Figure 1 shows the synthetic route for monodisperse, PSAN-ligated spinel magnetic NPs via employing star-like PAA-*b*-PSAN diblock copolymers as nanoreactors. First, β-CD had been brominated (denoted as Br-21-β-CD) by esterification, substituting original 21 hydroxyl groups into bromine groups (step 1 in **Figure 7.1**). The conversion of the hydroxyl groups into bromide groups was nearly 100%, as calculated from proton nuclear magnetic resonance (^{1}H NMR) results (**Figure 7.2 (a)**). Using those Br-21-β-CD as initiator, atom transfer radical polymerization (ATRP) had been done twice sequentially with two different monomers, i.e., *tert*-butyl acrylate (*t*BA) and styrene-co-acrylonitrile (SAN), respectively for obtaining star-like P*t*BA homopolymer and star-like P*t*BA-*b*-PSAN diblock copolymers (**Figure 7.1**, step 2 and 3). The molecular weights of each block can be tailored facilely by changing the polymerization time. The successful growth of the inner P*t*BA block and outer PSAN block can be corroborated by both GPC traces as well as ^{1}H NMR spectra. From GPC traces (**Figure 7.3**), we can clearly observe the shift of the peak to the larger-molecular-weight region, proving the second block was indeed grafted onto the first P*t*BA block. Furthermore, the low polydispersity (PDI < 1.15) of both star-like P*t*BA homopolymer and star-like P*t*BA-*b*-PSAN diblock copolymers was achieved, signifying the effectiveness for

controlling the size distribution of the as-synthesized NPs since the size of the NPs were determined by molecular weight and PDI of the inner block. The ^{1}H NMR (**Figure 7.2 (b, c)**) can further substantiate the successful synthesis of star-like P*t*BA and star-like P*t*BA-*b*-PSAN by the obvious characterization shift. The star-like P*t*BA-*b*-PSAN diblock copolymers were then hydrolyzed and converted P*t*BA into poly(acrylic acid) (PAA) (**Figure 7.1**, step 4), yielding the final star-like PAA-*b*-PSAN diblock copolymer that can serve as nanoreactors for spinel magnetic NPs synthesis.

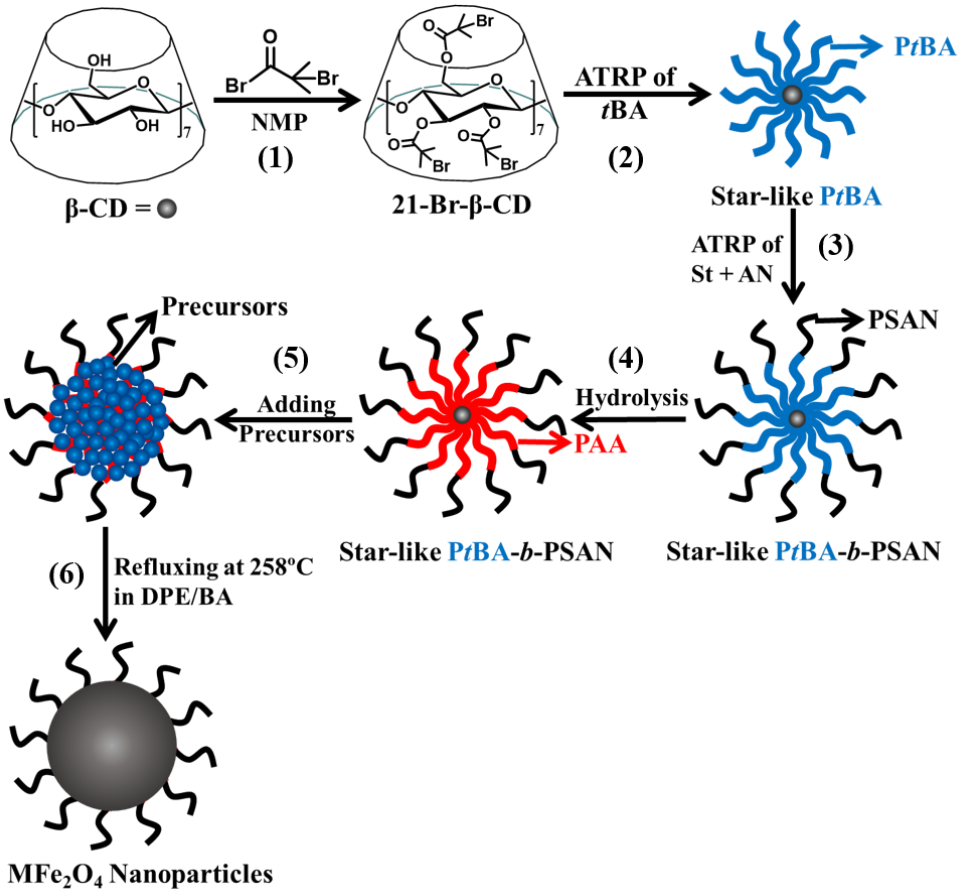

Figure 7.1 Synthetic route to spinel magnetic NPs, i.e., PSAN-ligated $CoFe_2O_4$, $NiFe_2O_4$, and $MnFe_2O_4$, crafted by utilizing star-like PAA-*b*-PSAN diblock copolymers as nanoreactors.

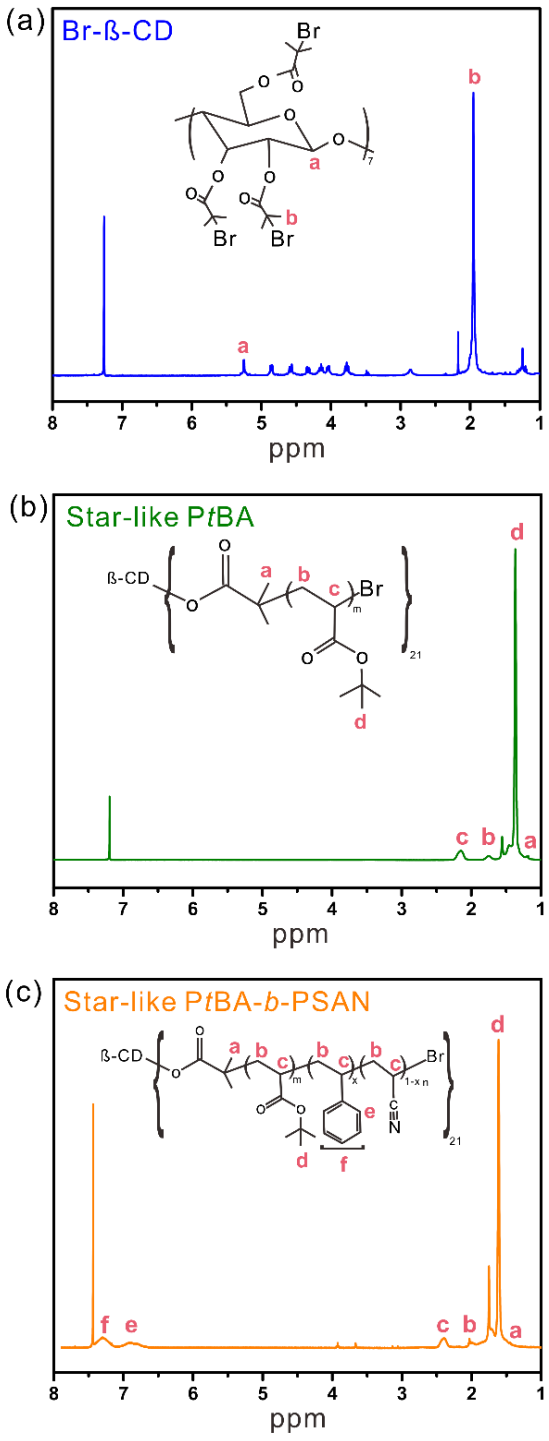

Figure 7.2 ^{1}H-NMR spectra of **(a)** brominated β-CD, i.e., initiator of ATRP, **(b)** star-like P*t*BA homopolymer, and **(c)** star-like P*t*BA-*b*-PSAN diblock copolymer, all measured in deuterated chloroform.

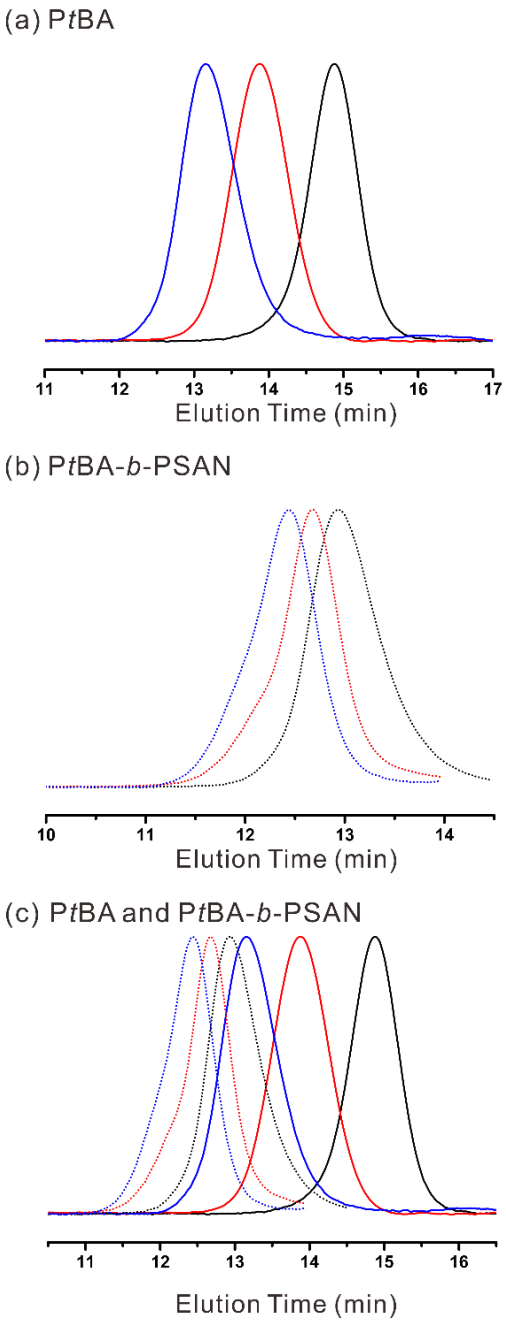

Figure 7.3 GPC results of **(a)** three star-like P*t*BA homopolymer, **(b)** three star-like P*t*BA-*b*-PSAN diblock copolymers and **(c)** superimposition of **(a)** and **(b)**. The same color in **(c)** indicated the second PSAN block polymer (dashed line) was grown onto the corresponding first P*t*BA block (solid line). The molecular weights of the samples are summarized in **Table 7.1**.

To craft uniform and monodisperse spinel magnetic NPs by using star-like diblock copolymers as nanoreactors, first we dissolved the star-like diblock copolymers in a mixed solvent composed of diphenyl ether (DPE) and benzyl alcohol (BA) (9:1 DPE/BA, v/v). The reasons for choosing DPE as the major reaction solvent are high boiling temperature, i.e., high reaction temperature for NPs synthesis that can ensure complete thermolysis and better crystallinity of NPs, as well as good solubility for outer PSAN block. Moreover, the metal precursors tended to occupy the inner PAA compartment due to polarity preference, further leading to effective coordination between metal precursors and carboxylic acid group of PAA block, and enhanced yield of the final spinel magnetic NPs product. The addition of a small amount of BA (a poor solvent for PSAN yet a good solvent for PAA) can partially collapse the outer PSAN block, forming stable unimolecular micelle. Therefore, the successively-added precursor and the formed NPs can be confined within the inner PAA block, allowing the synthesis of uniform spinel ferrite NPs with a well-defined spherical shape. After dissolving the star-like diblock copolymers in the mixed solvent, the solution was being stirred continuously at 50 ^{o}C overnight to guarantee the formation of the stable micellar structure. The precursor of spinel magnetic NPs, i.e., cobalt(II) acetylacetonate ($Co(acac)_2$), manganese(II) acetylacetonate ($Mn(acac)_2$) and nickel(II) acetylacetonate ($Ni(acac)_2$) for the M^{2+} ions of MFe_2O_4 and iron(III) acetylacetonate ($Fe(acac)_3$) for the Fe^{3+} ions, were then added to the reaction solution under stirring for another day (**Figure 7.1**, step 5). Long-enough mixing/loading time is essential for the metal moieties of precursors to coordinate with carboxyl groups of the inner PAA block. Because of this strong interaction, the concentration of the precursors would be higher within the PAA block, compared to the outer PSAN block (without functional group) and that in the solution, resulting in the preferred formation of the spinel magnetic NPs within the PAA compartment. The subsequent thermolysis by raising reaction

temperature to the refluxing temperature of the solvent (~250 ^{o}C) for 12 h led to the nucleation and growth of the monodisperse spinel ferrite NPs (**Figure 7.1**, step 6), which can be dissolved in various kinds of organic solvents facilely due to the permanently ligated outer PSAN block on the surface. To purify the as-synthesized NPs, dissolution-precipitation approach with toluene/DMF and ethanol as the good and the poor solvent, respectively was conducted multiple times, ensuring the impurities and residual solvent were all removed. Compared to other spinel magnetic NPs that are stabilized with small ligands capped on the surface, the spinel magnetic NPs synthesized via employing nanoreactors are very stable and can be well-dispersed in good solvents for PSAN even after multiple purification steps because the outer PSAN polymeric chains covalently ligated on the surface. We also discovered that a slower heating rate for thermolysis can be beneficial to the formation of more uniform NPs, possibly due to slower growth rate and lower concentration of available metal cations from the decomposition of the precursors at a time, suppressing the possibility for product to grow outside of the nanoreactors. Furthermore, the star-like diblock copolymer nanoreactors synthesized by ATRP possessed both controllable molecular weight of the inner and outer block, separately and narrow molecular weight distribution, leading to spinel magnetic NPs with tailorable size and narrow size distribution. **Table 7.1** depicts the molecular weight, both per arm and per star-like polymer of star-like P*t*BA homopolymer and star-like P*t*BA-*b*-PSAN diblock copolymers and their corresponding PDI.

Table 7.1 Summary of star-like PAA homopolymer, star-like PAA-*b*-PSAN diblock copolymer, inner PAA size from the theoretic calculation, and as-synthesized nanoparticle size

Nanoreactor	**$M_{n,\ PtBA}$[a]**	**$M_{n,\ PAA}$[b]**	**PDI**	**$M_{n,\ PSAN}$[c]**	**$M_{n,\ PtBA\text{-}b\text{-}PSAN}$[d]**	**PDI**	**Inner PAA size[e]**	**NPs size (ave.)[f]**
Sample 1	70 K	4K	1.04	5K	239 K	1.15	3 nm	4.3 nm
Sample 2	110 K	8K	1.07	9K	326 K	1.19	7 nm	7.4 nm
Sample 3	207 K	15K	1.12	14K	475 K	1.18	13 nm	11.3nm

Notes: [a] Molecular weight of P*t*BA was obtained from the GPC results. [b] Molecular weight of PAA was calculated from the molecular weight of P*t*BA acquired from GPC results. The single-arm Mn was derived from the standard curve built with 21-arm star-like PS and single-arm PS after cleavage. All GPC results were calibrated with linear PS standards. [c] Molecular weight of PSAN was calculated from the ^{1}H NMR spectra of star-like P*t*BA-*b*-PSAN with known Mn of P*t*BA. [d] Whole molecular weight of P*t*BA-*b*-PSAN was obtained from the GPC results. [e] The core PAA diameter is estimated from full stretched chains. [f] Calculated from TEM image with *ImageJ* software of 100 nanoparticles

Uniform and disperse spinel magnetic NPs can be found in **Figure 7.4**. **Figure 7.4 (a-c)**, (**d-f),** and (**g-i)** showed the transmission electron microscopy (TEM) images of $NiFe_2O_4$, $MnFe_2O_4$, and $CoFe_2O_4$ NPs, respectively with average size from 4 nm, 7 nm to 11 nm via using the star-like PAA-*b*-PSAN diblock copolymers (Sample 1-3 in **Table 7.1)** as nanoreactors. Specifically, by employing the coordination interaction between the carboxylic acid (-COOH) groups within the inner PAA block and the metal moieties of the precursors, NPs can be formed via this polymer-directed synthesis. To prevent the insufficient amount of precursor which might lead to irregular and un-uniform NPs, 10 times the molar ratio of precursor over AA units was added, and PAA compartment was expected to be fully occupied. Those formed outside of the nanoreactors (i.e.,

big chunks of the product without the protection of ligand) due to the excess amount of precursor can be easily removed by centrifugation at different speeds. The uniformity of the as-synthesized NPs was confirmed by statistically calculating the average size and variance among 100 NPs from the TEM images, and the resulting dimension distribution histograms of three different kinds of spinel magnetic NPs were demonstrated in **Figure 7.5**. Remarkably, the sizes of the spinel magnetic NPs synthesized with the same star-like diblock copolymer nanoreactor were all well-comparable, proving the effectiveness and versatility of this approach to obtain NPs with tailorable size and composition. The capability of fabricating the monodisperse magnetic NPs, especially with consistent morphology, i.e., spherical shape and similar dimension, can thus afford a unique platform for exploring the size effect and composition effect, individually on magnetic properties within the nanometer-scale regime. To confirm the role of the star-like diblock copolymer nanoreactors in the magnetic NPs synthesis, control experiments without the addition of the nanoreactors had been conducted (**Figure 7.6**). Irregular-shaped product with large size and large variation in size was observed due to the lack of ligands/surfactants in the system.

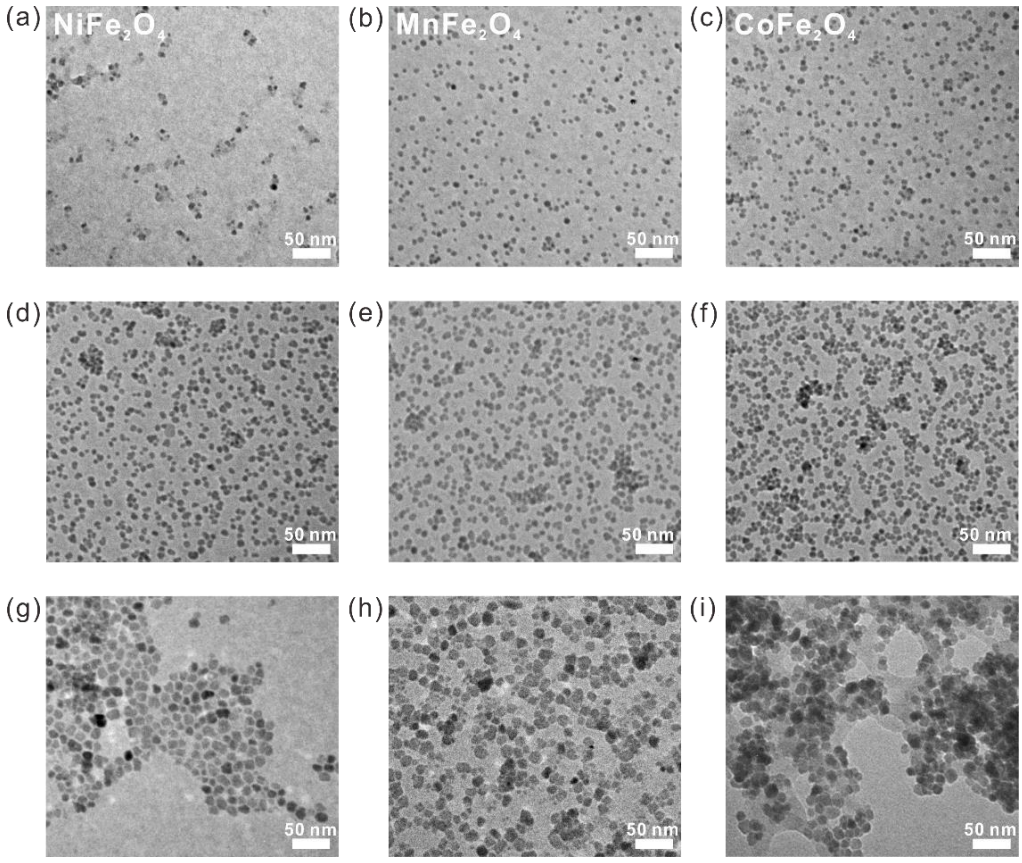

Figure 7.4 TEM images of PSAN-ligated magnetic NPs synthesized by capitalizing respective star-like PAA-*b*-PSAN diblock copolymers as nanoreactors with controllable compositions and dimensions: (a, d, g) PSAN-ligated $NiFe_2O_4$ NPs with an average diameter of 4 nm, 7 nm, and 11 nm, respectively, (b, e, h) PSAN-ligated $MnFe_2O_4$ NPs with an average diameter of 4 nm, 7 nm, and 11 nm, respectively, and (c, f, i) PSAN-ligated $CoFe_2O_4$ NPs with an average diameter of 4 nm, 7 nm, and 11 nm, respectively. All three kinds of spinel magnetic NPs with size from 4 nm, 7 nm to 11 nm were crafted by employing Sample 1 to 3 in **Table 7.1**, respectively.

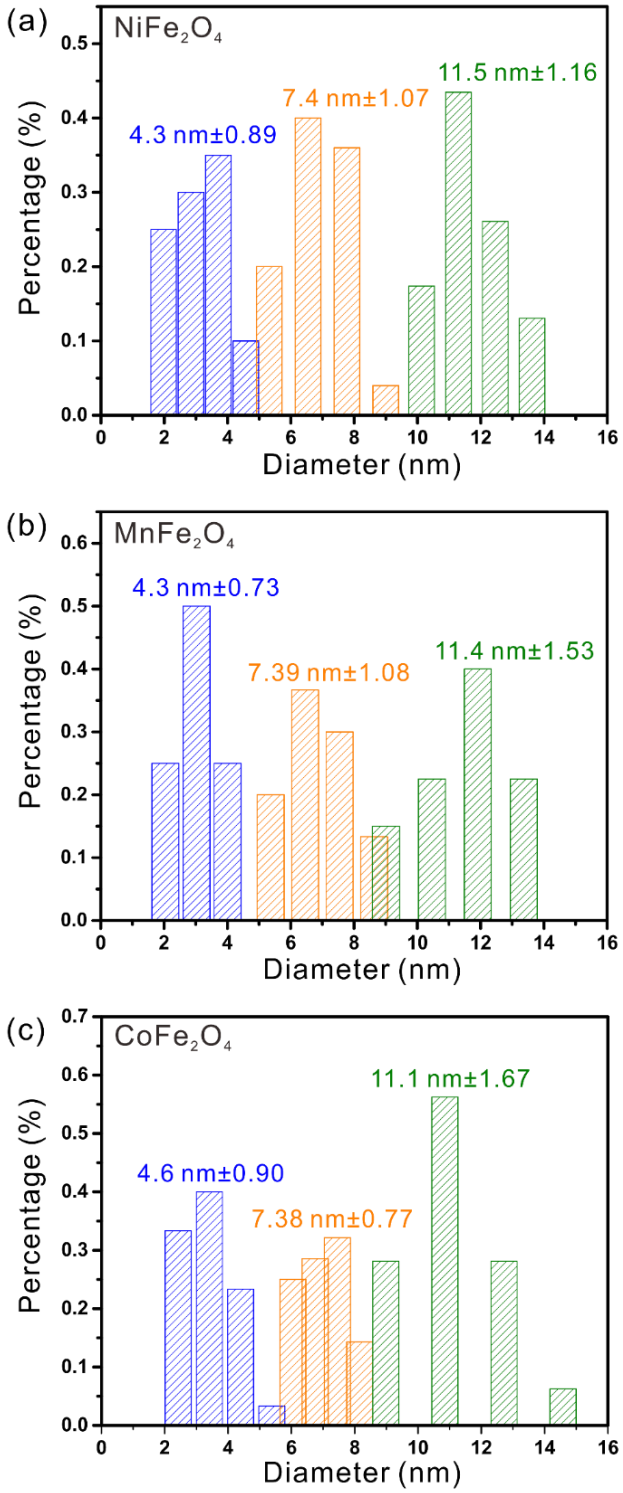

Figure 7.5 Statistic of the size distribution of **(a)** $NiFe_2O_4$, **(b)** $MnFe_2O_4$, and **(c)** $CoFe_2O_4$ with three different sizes. All three kinds of spinel magnetic nanoparticles with size from 4 nm, 7 nm to 11 nm were crafted by employing Sample 1 to 3 in **Table S1**, respectively.

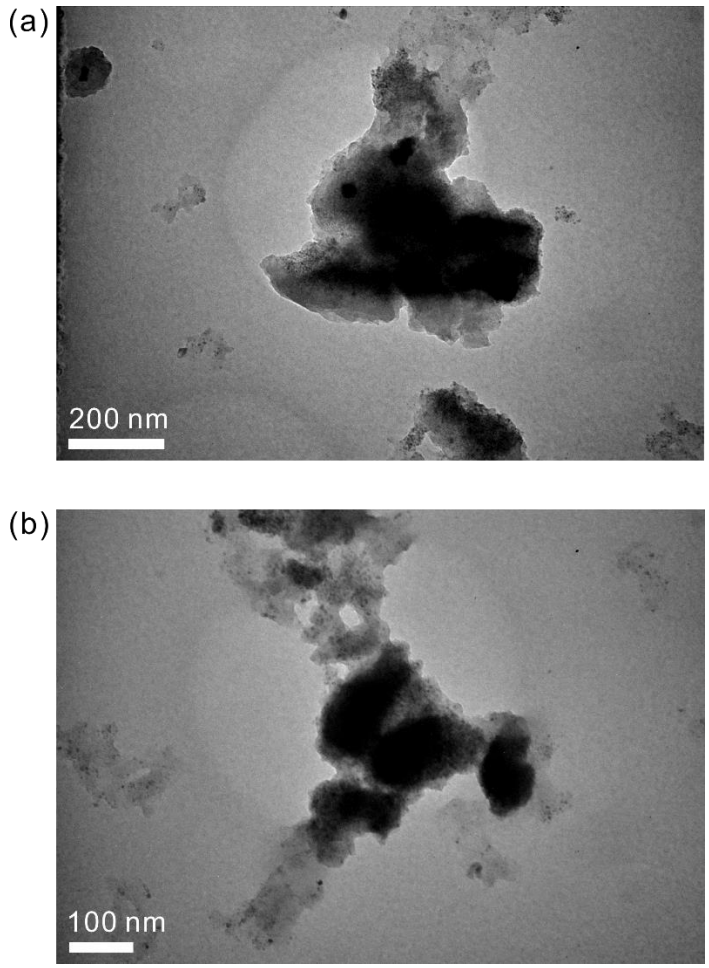

Figure 7.6 TEM images of the control experiment, i.e., synthesis of spinel magnetic nanoparticles with the same experimental conditions without the addition of star-like diblock copolymer nanoreactor.

The capability of changing the surface chemistry, i.e., changing the outer block polymer, of the as-synthesized spinel ferrite nanoparticles was also attained by capitalizing hydrophilic star-like PAA-*b*-PEO diblock copolymer instead of amphiphilic star-like PAA-*b*-PSAN diblock copolymer. In brief, we first synthesized the star-like P*t*BA with pre-determined molecular weight, followed by azidation (denoted as star-like P*t*BA-N_3) to transform the bromine end groups on the PAA chain end into azide groups via nucleophilic substitution reaction. Linear PEO terminated with an alkyne group was prepared at the same time. After successfully obtaining these two reactants, i.e., star-like P*t*BA-N_3 and alkyne-terminated PEO, click reaction between the two was

performed. Finally, after similar hydrolysis procedure, star-like PAA-*b*-PEO diblock copolymer, which again serves as nanoreactors for the subsequent spinel ferrite nanoparticle synthesis, can be rendered. The successful conversion of -Br to -N_3 as well as click reaction can first be corroborated by FTIR characterization, in which the characteristic stretching of -N_3 (~2112 cm-^{1}) appeared (**Figure 7.7 (b)**, indicated by black arrow) after azidation and disappeared after click reaction (**Figure 7.7 (c)**).[23] Moreover, a significant peak shift to the higher molecular weight regime in GPC results can be observed before and after click reaction (**Figure 7.7 (d)**), indicating the increase of molecular weight as well as the whole hydrodynamic volume of the star-like polymer. Consequently, the successful grafting of the second PEO block onto star-like P*t*BA homopolymer had been substantiated. By employing star-like PAA-*b*-PEO diblock copolymer as nanoreactor, representative monodisperse spinel $CoFe_2O_4$ NPs can be obtained, signifying the flexibility of tailoring/designing surface chemistry of the as-synthesized nanoparticles as promising materials for desired applications. **Figure 7.7 (e)** showed the TEM image of the PEO-ligated $CoFe_2O_4$ nanoparticles with excellent dispersity in polar solvents (here we use ethanol to disperse the PEO-ligated nanoparticles) and uniformity in size. The statistic calculation of the average size and size distribution of the corresponding $CoFe_2O_4$ NPs can be found in **Figure 7.7 (f)**. Markedly, since the molecular weight of the inner PAA block was not the same as those three samples listed in **Table 7.1** but particularly similar (slightly smaller) with that of Sample 2, the average size of the nanoparticles synthesized from this star-like PAA-*b*-PEO diblock copolymer nanoreactor was also slightly smaller (~6.5 nm) but consistent with those synthesized via Sample 2 nanoreactors (average size ~7.3-7.4 nm).

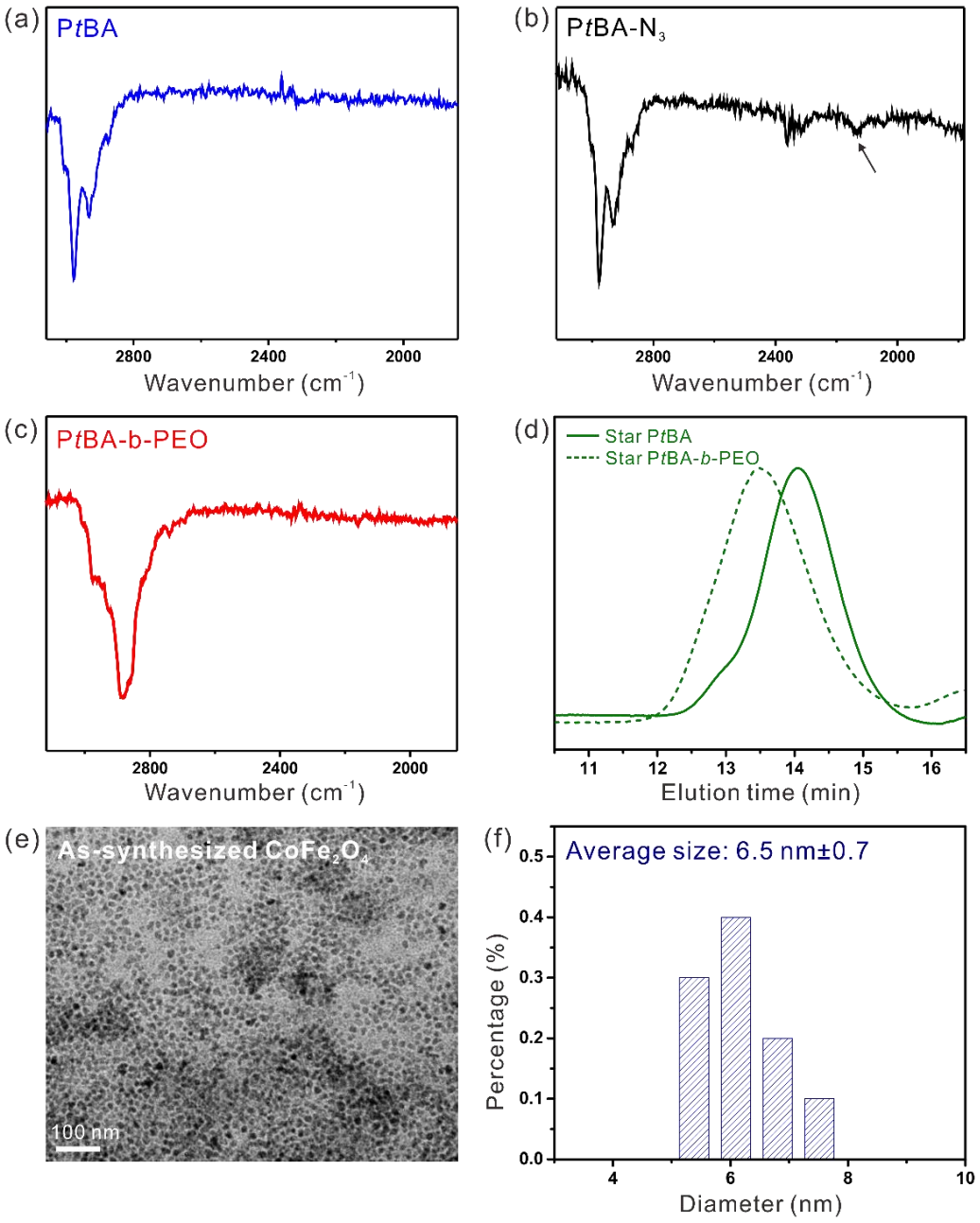

Figure 7.7 FTIR spectra of **(a)** star-like P*t*BA, **(b)** star-like P*t*BA-N_3 and **(c)** star-like P*t*BA-*b*-PEO diblock copolymer. **(d)** GPC traces of star-like P*t*BA homopolymer and star-like P*t*BA-*b*-PEO diblock copolymer. **(e)** TEM image of PEO-ligated spinel $CoFe_2O_4$ nanoparticle and **(f)** the corresponding size distribution histogram by measuring 100 nanoparticles from TEM images with *ImageJ* software.

High-resolution TEM (HRTEM) images can be found in **Figure 7.8 (a-c)** for $NiFe_2O_4$, $MnFe_2O_4$, and $CoFe_2O_4$ NPs, separately. The spherical and disperse NPs can be clearly seen from

all kinds of NPs and the characteristic lattice-fringe distances of 0.48 nm and 0.29 nm for $NiFe_2O_4$, 0.296 nm for $MnFe_2O_4$ and 0.297 nm for $CoFe_2O_4$ NPs can be observed, matching well with the (111) and (220) planes for the corresponding spinel magnetic nanocrystals.[24-25] Structural information of the as-synthesized NPs was obtained from X-ray diffraction (XRD) measurements. In the representative XRD patterns of three kinds of spinel magnetic NPs (**Figure 7.8 (d)**), the position of all the diffraction peaks were consistent with the characteristic peaks of three kinds of spinel phases (without any additional impurity peaks),[26-27] which was beneficial to the precise comparison and discussion on the magnetic properties afterward. Another intriguing feature with the XRD patterns was the line broadening (**Figure 7.9**) observed in all the samples, suggesting the fine nature, i.e., small dimension, of the NPs. By utilizing Scherrer analysis (equation shown below) of the strongest (311) peak, the average crystal size can be estimated:[28]

$$D = \frac{0.9 \times \lambda}{\beta \times cos\theta}$$

, where D is the crystallite size (nm), λ is the wavelength of incident X-ray, β is the full width of the diffraction peak at half of the maximum intensity, and θ is the Bragg angle. All the estimated average particle sizes agreed well with that determined by statistical analysis from the TEM images, implying each particle was a single crystal.[29] The diameters of all the NPs synthesized, both calculated from TEM images and XRD patterns were listed in **Table 7.1**.

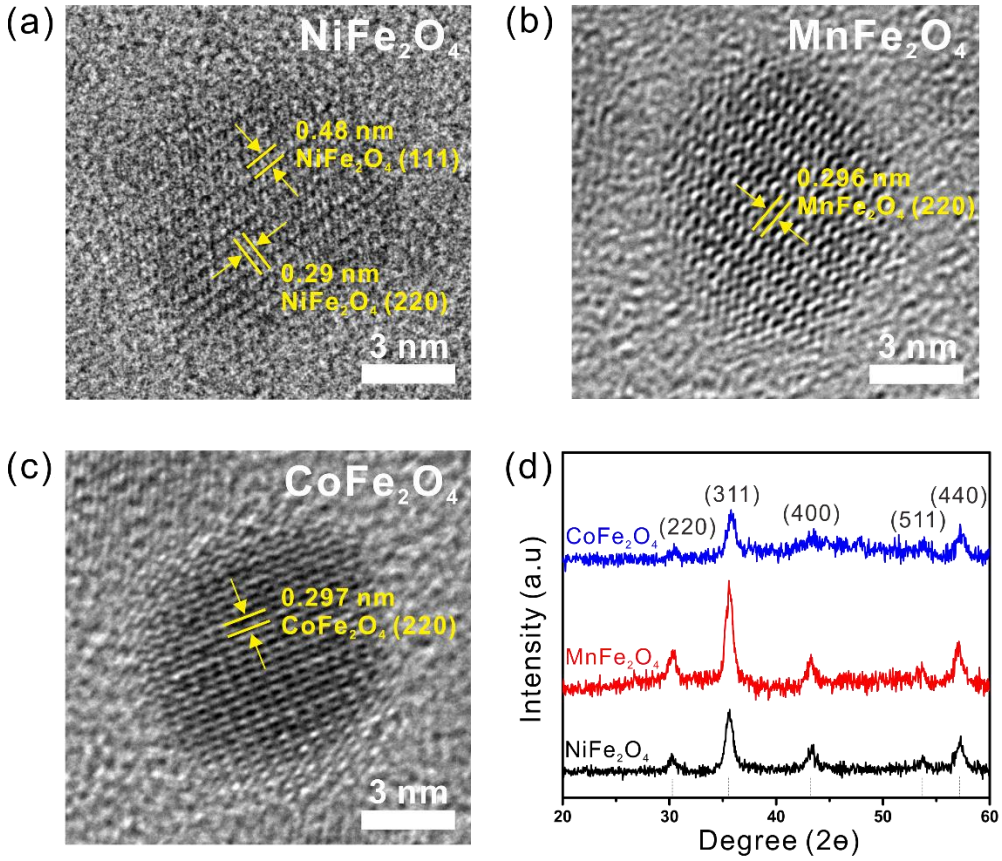

Figure 7.8 Representative HRTEM images of the as-synthesized PSAN-ligated magnetic NPs with different compositions: (a) $NiFe_2O_4$, (b) $MnFe_2O_4$, and (c) $CoFe_2O_4$ and the representative XRD patterns of the corresponding spinel magnetic NPs. All the spinel magnetic NPs measured were crafted by employing Sample 2 in **Table 7.1**.

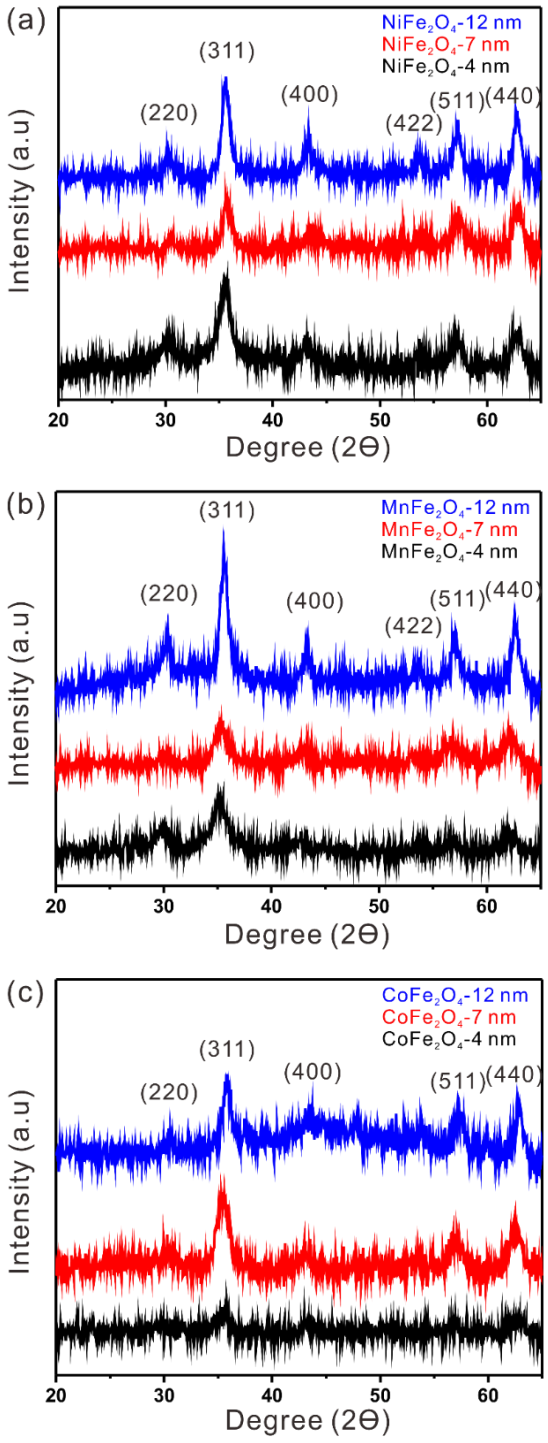

Figure 7.9 XRD patterns of PSAN-ligated spinel magnetic nanoparticles of different compositions and sizes: **(a)** $NiFe_2O_4$, **(b)** $MnFe_2O_4$, and **(c)** $CoFe_2O_4$ nanoparticles. The as-synthesized spinel magnetic nanoparticles with size from 4 nm, 7 nm to 11 nm were crafted by employing Sample 1 to 3 in **Table S1**, respectively.

Due to the similarity in the peak position of XRD patterns for all three kinds of magnetic NPs, X-ray photoelectron spectroscopy (XPS) measurement is essential to verify the presence of chemical elements and to investigate the oxidation states of the elements of the as-synthesized product. The survey XPS spectra were shown in **Figure 7.10** and the high-resolution spectra for $MnFe_2O_4$, $CoFe_2O_4$, and $NiFe_2O_4$ were exhibited in **Figure 7.11**. From all the spectra of M^{2+} element, i.e., Mn, Co, and Ni in **Figure 7.11 (a**, **c,** and **e)**, two major peaks with two satellite peaks can be observed. For instance, it was found that the XPS spectrum of Mn 2p demonstrated two main peaks of Mn $2p_{3/2}$ (641.2 eV) and Mn $2p_{1/2}$ (652.8 eV), consistent with previously reported values for Mn^{2+} chemical state.[30] Moreover, further deconvolution of these two major peaks due to the asymmetric peak shape was conducted and the existence of Mn^{2+} ions at two crystallographic environments, i.e., octahedral (pink curve) and tetrahedra sites (green curve),[31] within the as-synthesized $MnFe_2O_4$ spinel magnetic NPs was discovered. Similarly, in addition to the satellite peaks, the major two peaks for Co (with the binding energy of 780.9 eV and 796.2 eV, corresponding to the valence state of Co^{2+}) and Ni (with the binding energy of 855.5 eV and 873 eV, corresponding to the valence state of Ni^{2+}) had been deconvoluted into two peaks, respectively, again verifying that both Co^{2+} and Ni^{2+} ions were situated in two different environments.[32-33] The high-resolution Fe 2p spectra for three different kinds of spinel ferrites can be found in **Figure 7.11 (b**, **d,** and **f)**. Two peaks situated at 711.7 eV and 724.4 eV, matching with that of Fe $2p_{3/2}$ and Fe $2p_{1/2}$ for Fe^{3+} states, had also been deconvoluted into Fe^{3+} ions at octahedral sites and tetrahedral sites.[34] Two satellite peaks situated at 719.4 eV and 733 eV were associated with the transition of an electron from 3d orbital to the vacant 4s orbital when the ejection of the core 2p photoelectron occurred.[35] In particular, the normal spinel structure indicates the structure with tetrahedral sites occupied by bivalent cations (M^{2+}) and octahedral sites occupied by trivalent

cations (Fe^{3+} in the case of spinel ferrite) (**Figure 7.12 (a)**).[36] Conversely, the inverse spinel structure represents the structure with tetrahedral sites occupied by trivalent cations and octahedral sites occupied by a mixture of bivalent and trivalent cations (**Figure 7.12 (b)**).[37] In terms of structure in our study, we can conclude that all the spinel magnetic NPs synthesized by nanoreactors have a partial/mixed inverse structure, i.e., both octahedral sites and tetrahedral sites were occupied by a mixture of M^{2+} and Fe^{3+} ions, which will further influence their magnetic properties.[38] Here we assume the cation distributions (i.e., ratio of different ions on different sites) were similar for the same kind of spinel NPs regardless of the sizes because of the same synthetic procedure for synthesizing those PSAN-ligated spinel magnetic NPs.

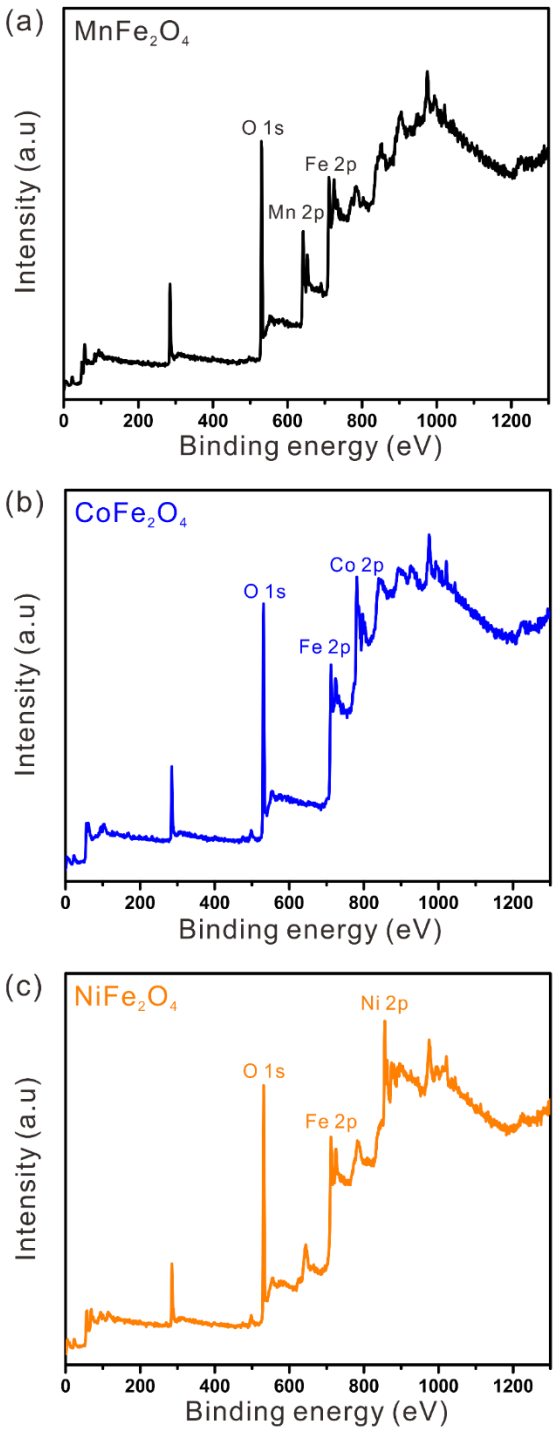

Figure 7.10 XPS whole spectra of PSAN-ligated **(a)** $MnFe_2O_4$ **(b)** $CoFe_2O_4$ and **(c)** $NiFe_2O_4$ nanoparticles. All the spinel magnetic NPs measured were crafted by employing Sample 2 in **Table 7.1**.

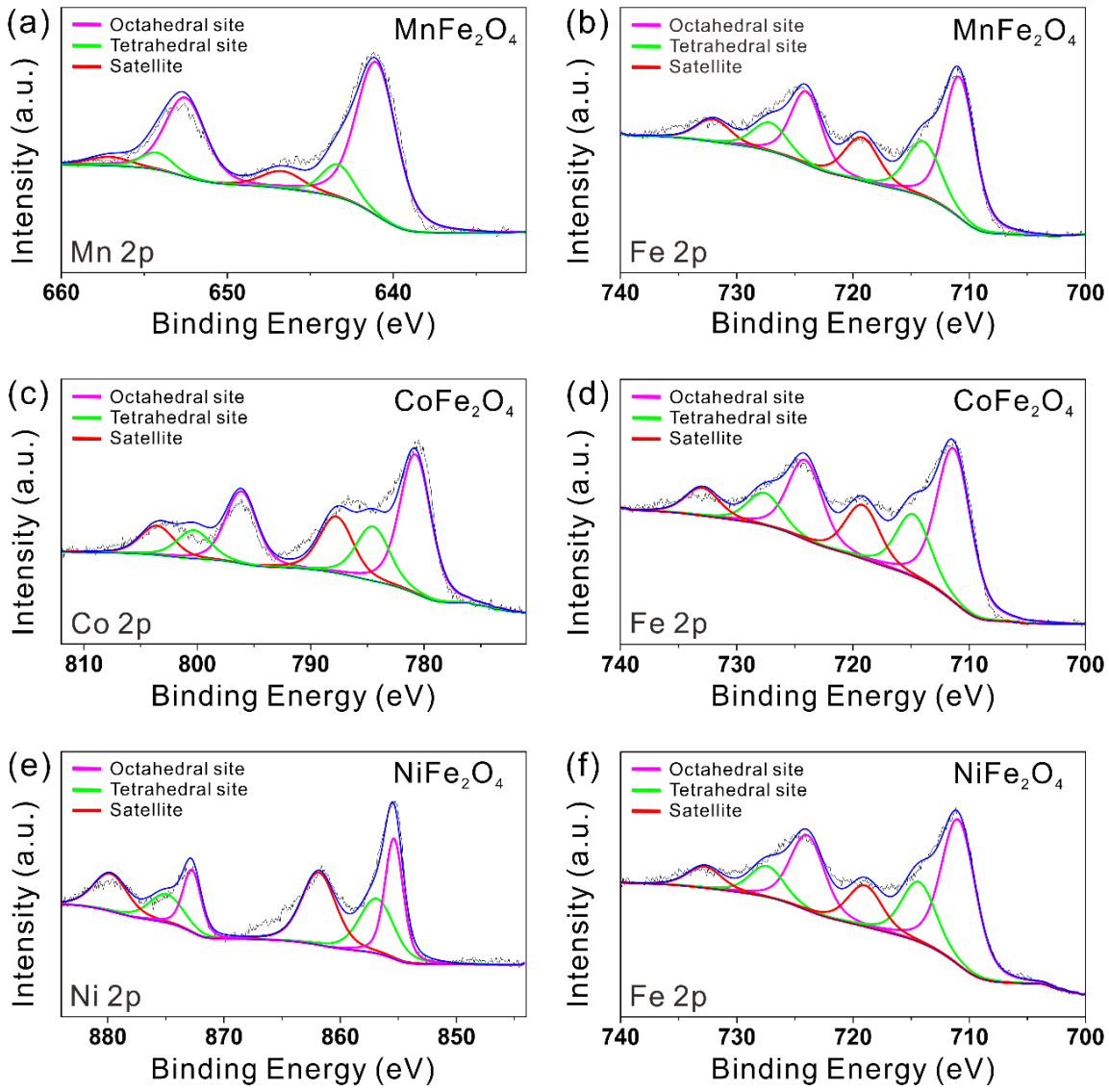

Figure 7.11 XPS of PSAN-ligated spinel magnetic NPs of (a) Mn and (b) Fe of $MnFe_2O_4$, (c) Co and (d) Fe of $CoFe_2O_4$ and (e) Ni and (f) Fe of $NiFe_2O_4$. All the spinel magnetic NPs measured were crafted by employing Sample 2 in **Table 7.1**.

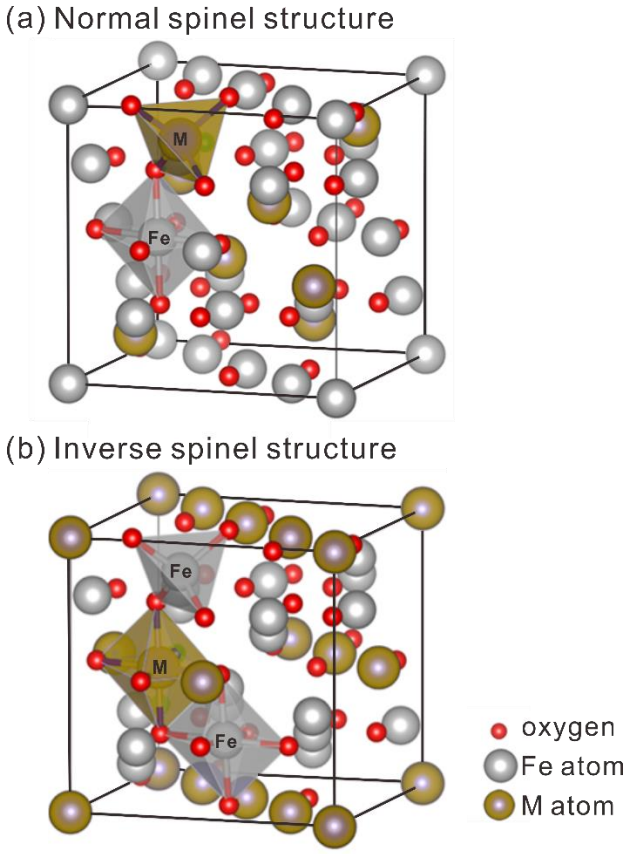

Figure 7.12 Crystal structures of **(a)** normal spinel structure and **(b)** inverse spinel structure.

Raman spectroscopy is very sensitive to purity and many structural disorders, such as lattice distortion, local cation distribution, magnetic ordering, etc. **Figure 7.13** shows the Raman spectra in the range of 100-800 cm^{-1} of as-synthesized $CoFe_2O_4$, $MnFe_2O_4$, and $NiFe_2O_4$ NPs, respectively. Among all the vibrational modes for Raman, only A_{1g} mode, coming from symmetric stretching of oxygen atoms along M-O (and Fe-O), was observed for all three samples around 600-690 cm^{-1}.[39] Specifically, in the spectrum of $CoFe_2O_4$ NPs (**Figure 7.13 (a)**), three first-order Raman modes located at 290 (E_g), 456 (T_{2g}), and 667 cm^{-1} (A_{1g}) can be clearly seen, consistent with those reported previously.[39] It is notable that the splitting of the A_{1g} band indicated the replacement of some Fe^{3+} ions by Co^{2+} ions in the tetrahedral site,[39] verifying the conclusion from XPS results that $CoFe_2O_4$ possessed mixed inverse structure. $T_{2g}(1)$ mode and E_g mode were found

for $MnFe_2O_4$ NPs at 211 and 361 cm^{-1} (**Figure 7.13 (b)**), whereas an unexpected mode at around 266 cm^{-1} had been observed, possibly due to a breakdown of the translation symmetry induced by cationic disorder.[40-41] Finally, the four major Raman active modes, i.e., peak at 328, 471, 561, 681 cm^{-1}, of $NiFe_2O_4$ in **Figure 7.13 (c)** can all be well-assigned to E_g, $T_{2g}(3)$, $T_{2g}(2)$ and A_{1g} as presented in earlier reports.[42] Similarly, the slightly asymmetric peak at 681 cm^{-1} with a small shoulder on the low energy side may result from the distribution in bond distances of Fe-O and Ni-O bond.[43] Therefore, one peak represented the unit cell with all Fe ions and the other one represented the unit cell with mixed Fe and Ni ions, again suggesting that the as-synthesized $NiFe_2O_4$ NPs exhibited mixed spinel structure.

Before investigating the magnetic properties based on varied composition and dimensions, thermogravimetric analysis (TGA) need to be conducted first to precisely calculate the amount of spinel magnetic NPs subjecting to VSM measurement. **Figure 7.14** and **Table 7.2** showed the TGA results for $CoFe_2O_4$, $NiFe_2O_4$, and $MnFe_2O_4$ with varied sizes, respectively. The amount of spinel magnetic NPs had been determined by the residual weight ratio at 800 ^oC. **Figure 7.15** showed the magnetic hysteresis loops, i.e., magnetization versus applied magnetic field plot, measured via vibrating sample magnetometer (VSM) at room temperature (300 K) with applied magnetic field ranged from -15 kOe to 15 kOe for the as-synthesized PSAN-ligated spinel magnetic NPs. The value of saturation magnetization (M_s), coercivity (H_c), and remnant magnetization (M_r) of the corresponding spinel ferrite NPs were summarized in **Table 7.1**. All the spinel ferrite NPs within the size range we have synthesized demonstrated superparamagnetic behaviors with reversible magnetization and narrow hysteresis loop at room temperature except $CoFe_2O_4$ NPs with the largest size that displayed a slightly larger and observable coercivity.

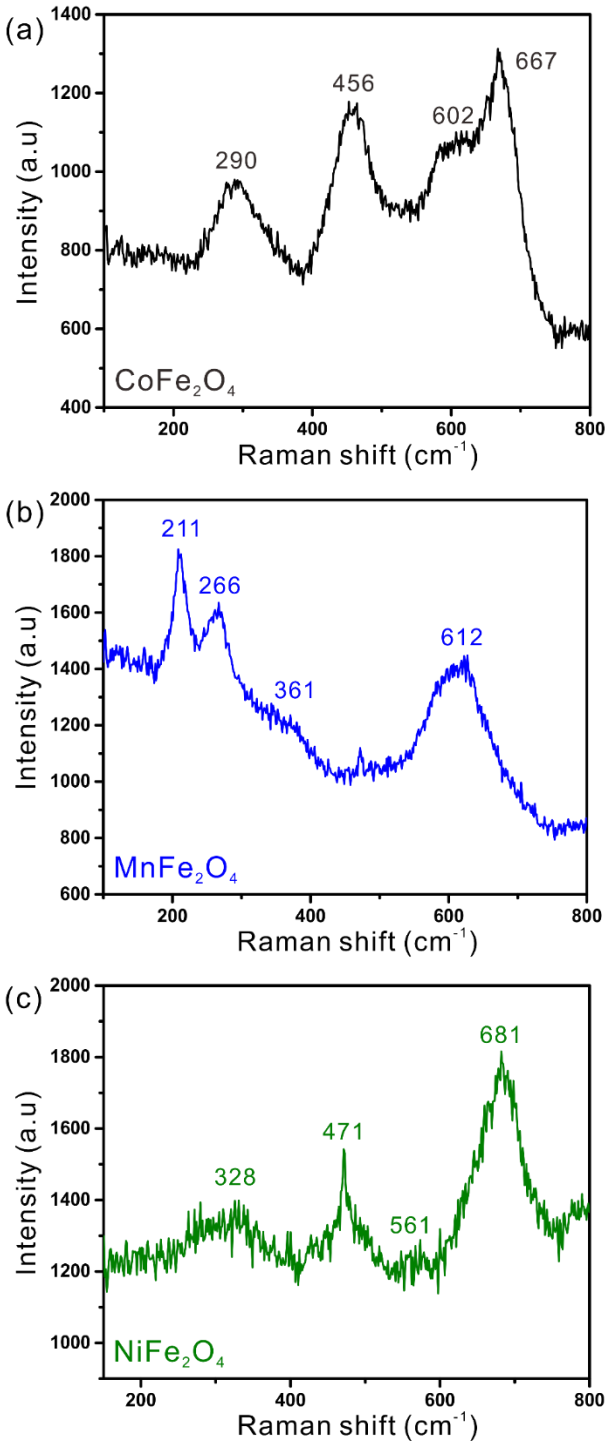

Figure 7.13 Raman spectra of as-synthesized **(a)** $CoFe_2O_4$ **(b)** $MnFe_2O_4$ and **(c)** $NiFe_2O_4$ nanoparticles. All the spinel magnetic NPs measured were crafted by employing Sample 2 in **Table 7.1**.

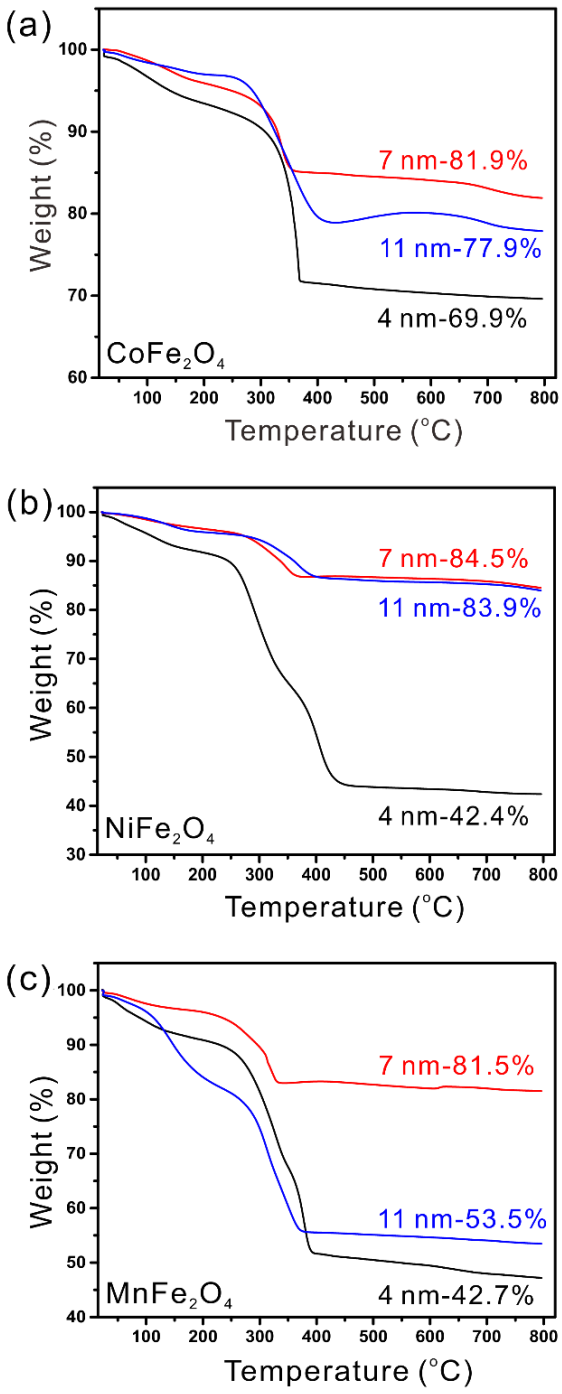

Figure 7.14 Thermogravimetric analysis (TGA) of PSAN-ligated spinel magnetic NPs with different compositions: (a) $CoFe_2O_4$ (b) $NiFe_2O_4$ and (c) $MnFe_2O_4$ of varied sizes. The numbers listed in the figures indicate the residual weight ratio at 800 °C.

Table 7.2 Summary of the weight ratio of spinel magnetic nanoparticles with varied sizes from TGA

Composition	**Sample #**	**Size of the nanoparticles**	**The weight ratio of inorganic material (weight left at 800 ºC)**
$CoFe_2O_4$	1	3 nm	69.6%
	2	7 nm	81.9%
	3	12 nm	77.9%
$NiFe_2O_4$	1	3 nm	42.4%
	2	7 nm	84.5%
	3	12 nm	83.9%
$MnFe_2O_4$	1	3 nm	47.2%
	2	7 nm	81.5%
	3	12 nm	53.5%

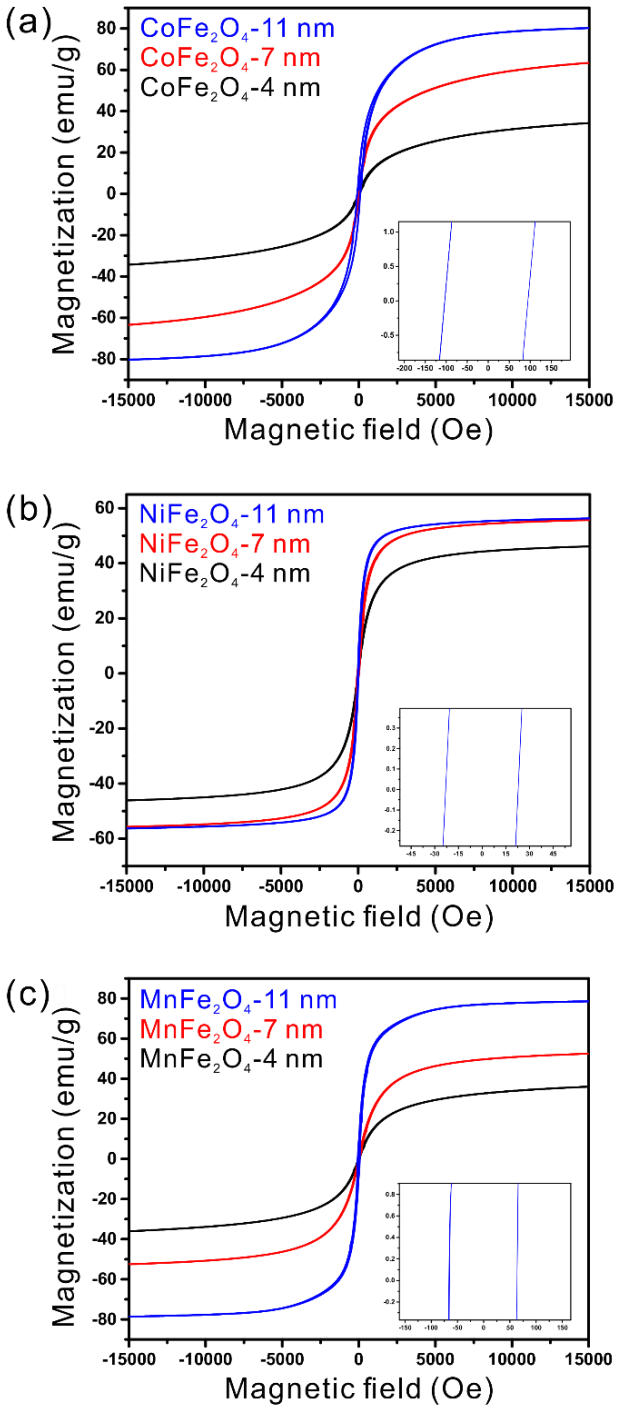

Figure 7.15 Hysteresis loops of PSAN-ligated (a) $CoFe_2O_4$, (b) $NiFe_2O_4$, and (c) $MnFe_2O_4$ NPs with varied sizes.

To discuss the magnetic properties between different compositions of the spinel magnetic NPs with similar size, comparison of M_s between three kinds of spinel magnetic NPs with varied sizes had been rendered. Due to varied number of unpaired 3d electrons, different 3d transition metals (M^{2+}) carry different atomic moment, and these 3d transition metals are expected to have the relative magnitudes of the spin moments with the following order: Mn^{2+} (5 μ_B) = Fe^{3+} (5 μ_B) > Co^{2+} (3 μ_B) > Ni^{2+} (2 μ_B).[44] Additionally, the magnetic structure of spinel ferrite is described as antiparallel moments on the tetrahedral and octahedral sites, giving the ferro- or ferrimagnetic ordering via an antiferromagnetic super-exchange coupling between the spins on two sites. Therefore, the intrinsic magnetic properties of spinel-structured magnetic NPs are directly affected by the type of cation (M^{2+}) as well as the cation distribution.[45] To investigate the composition effect of the magnetic NPs on M_s, the as-synthesized spinel ferrite NPs with the largest size (*D* = 11 nm) of three compositions was first chosen as an example (**Figure 7.16 (c)**). Based on the hysteresis loop we obtained under measurement at room temperature, M_s exhibited the following order: $CoFe_2O_4$ (80.2 emu/g) > $MnFe_2O_4$ (78.4 emu/g) > $NiFe_2O_4$ (56.3 emu/g). The smallest M_s of $NiFe_2O_4$ was due to the smallest average spin moments of the constituent Ni^{2+} ions, while the order of M_s between $CoFe_2O_4$ and $MnFe_2O_4$ was inconsistent with the average spin moments we have listed above. The reverse order may result from different intrinsic crystal structures, i.e., cation distributions. As supported by previous literature, $MnFe_2O_4$ was believed to be predominantly normal spinel character,[46] i.e., with Mn^{2+} cations located on the tetrahedral sites and Fe^{3+} cations located on the octahedral sites, whereas $CoFe_2O_4$ preferred the inverse spinel arrangement,[36] i.e., with Co^{2+} cations located on the octahedral sites and Fe^{3+} cations located on both sites. In addition, the interactions between the tetrahedral (A) and octahedral (B) sublattices in the spinel structure consisted of intersublattice (A-B) super-exchange interactions and

intrasublattice (A-A and B-B) exchange interactions, and the intersublattice interactions of the cations were much stronger than that of intrasublattice interactions.[47] Therefore, comparing between the two spinel structures, inverse spinel structure possessed more accumulated Fe^{3+} ions on A-sites, introducing larger intersublattice Fe_A^{3+}-Fe_B^{3+} super-exchange interactions that were stronger than intersublattice Mn_A^{2+}-Fe_B^{3+} interactions and other intrasublattice interactions and may lead to an increase in M_s in the as-synthesized $CoFe_2O_4$ spinel NPs.[48] Finally, based on the comparison of the M_s value of the as-synthesized NPs with the largest size with those reported from previous research (and even with bulk spinel materials), all three kinds of spinel ferrite NPs demonstrated superparamagnetic behavior with remarkably-high saturation magnetization. For instance, the room temperature M_s of the bulk ferrite materials are generally well-established, i.e., 83 emu/g for $MnFe_2O_4$, 75 emu/g for $CoFe_2O_4$ and 50 emu/g for $NiFe_2O_4$.[49-50] We noted that the M_s value varies hugely among literature because it can be heavily influenced by different synthetic approaches and annealing history. In brief, all the measured M_s values with the as-synthesized spinel ferrite NPs lied well within their respective expected regime.

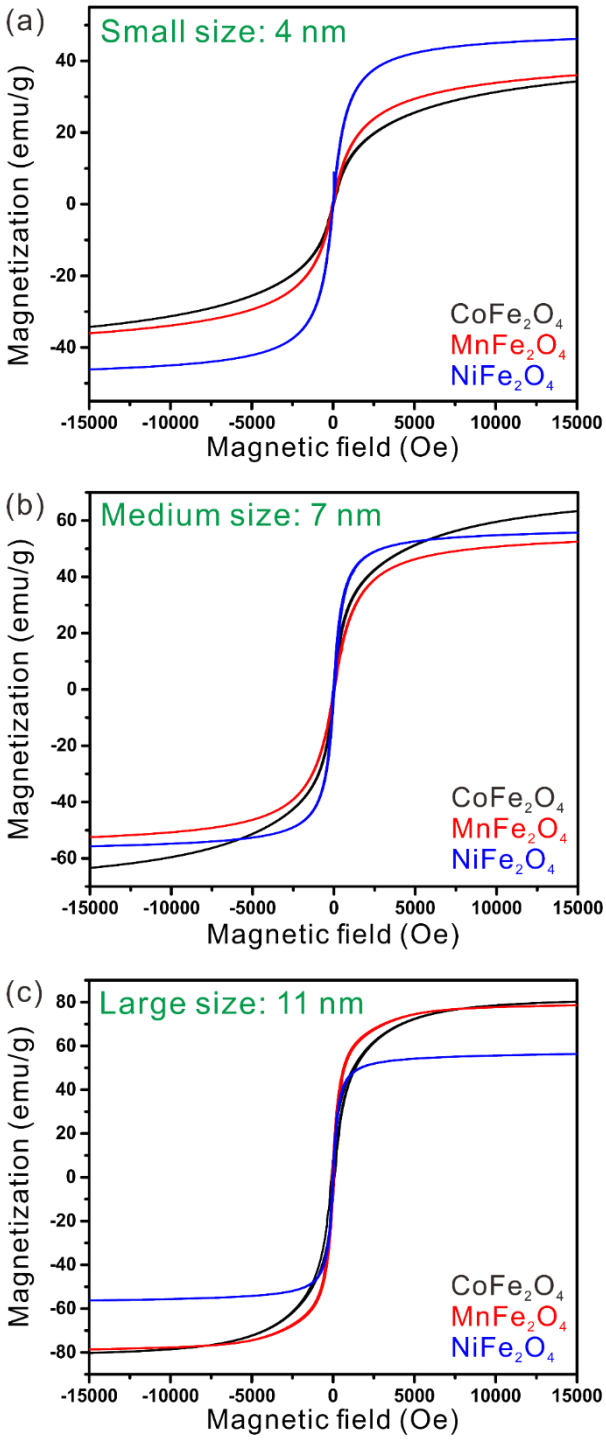

Figure 7.16 M-H curves of $CoFe_2O_4$, $MnFe_2O_4$, and $NiFe_2O_4$ nanoparticles with varied average nanoparticle sizes: **(a)** 4 nm **(b)** 7 nm and **(c)** 11 nm.

Comparing the same materials with different sizes, i.e., size effect on magnetic properties, we observed a clear relationship between the decrease of the saturation magnetization with the decrease of the particle dimensions (d) for all three kinds of spinel ferrite NPs. The correlation can be attributed to the surface spin disorder that occurred in the NPs. Assuming the thicknesses (*t*) of this magnetically dead layer were constant (or similar within the size range we had), the magnetization of the NPs follows the equation below:[51]

$$\sigma_S = \sigma_S(bulk) \times (1 - \frac{6t}{d})$$

Hence, the smaller the size of the NPs, i.e., the larger surface to volume ratio, the more intense this surface-spin-disorder effect can be. **Figure 7.17** represented the M_s of all three kinds of spinel ferrite NPs at 300 K plotted against particle diameter. Data points of $CoFe_2O_4$ and $MnFe_2O_4$ can be fitted by a straight line, whereas in $NiFe_2O_4$ cases, M_s increased between the first two points (from 4 nm to 7 nm), then reached a plateau (with values comparable to that of bulk $NiFe_2O_4$) despite continuously-increased NPs size. Consequently, we believe the critical size, i.e., at which the transition between single-domain regime to multidomain regime occurred, of $CoFe_2O_4$ and $MnFe_2O_4$, had not yet been reached within the size range of the NPs synthesized, while the critical size for $NiFe_2O_4$ NPs should fall within the range from 7 nm to 11 nm. This value is generally lower than most of the reported value in literature,[52] indicating synthetic method as well as surface chemistry can have significant influences on the magnetic properties of spinel ferrite nanomaterials.

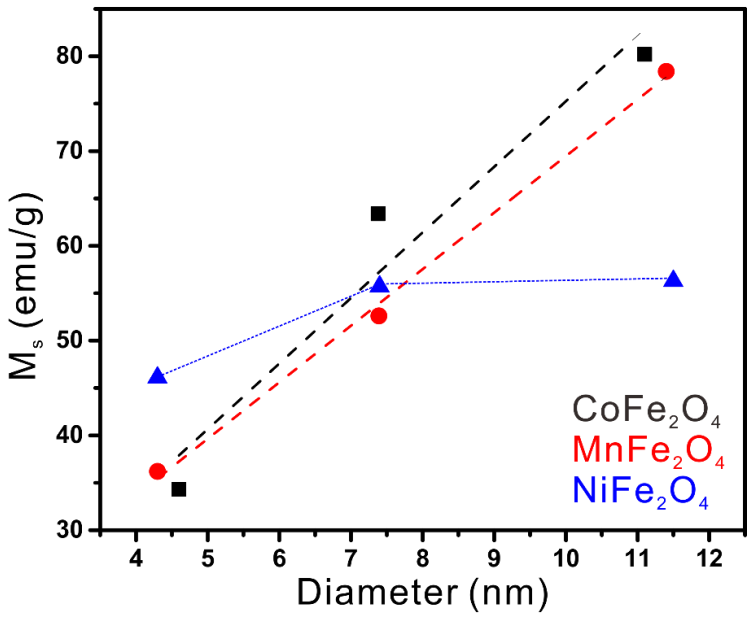

Figure 7.17 Saturation magnetization at 300 K versus particle size of three compositions: $CoFe_2O_4$ (black), $MnFe_2O_4$ (red), and $NiFe_2O_4$ (blue).

7.4 Conclusion

In this study, three kinds of spinel ferrite NPs, i.e., $MnFe_2O_4$, $CoFe_2O_4$, and $NiFe_2O_4$ NPs, were successfully synthesized via using star-like PAA-*b*-PSAN diblock copolymer as nanoreactors. By the coordination interaction between functional group of PAA and precursors, the precursors were loaded within the PAA compartment, followed by thermolysis of the precursor and formation of the spinel ferrite NPs. Therefore, the size of the as-synthesized nanoparticle can be facilely tailored by changing the molecular weight of the inner PAA block. Furthermore, those as-synthesized NPs can be well-dispersed in various organic solvents even after multiple purification steps because of the covalently-ligated outer PSAN block on the surface of the NPs. In addition, by capitalizing different star-like diblock copolymer, i.e., star-like PAA-b-PEO diblock copolymer, hydrophilic PEO-ligated spinel ferrite NPs can be attained. The morphology, structure, and composition of all three kinds of PSAN-ligated spinel ferrite NPs had been meticulously scrutinized. In particular,

the XPS results revealed all the as-synthesized ferrites NPs possessed mixed spinel structure with both divalent M^{2+} and trivalent Fe^{3+} ions located on both sites.

With the proposed nanoreactor-assisted approach, size, and composition effect on the magnetic properties can be elucidated. Notably, by using the same star-like diblock copolymer as nanoreactor, the sizes among three spinel ferrites were highly consistent, opening an avenue to investigate the two effects independently. Here, all nine samples rendered superparamagnetic behavior with the increasing M_s from $NiFe_2O_4$, $MnFe_2O_4$ to $CoFe_2O_4$ NPs of the largest size. The smallest M_s that $NiFe_2O_4$ showed can be explained by smaller spin moments that divalent Ni^{2+} ions provided, whereas the inversed order of $MnFe_2O_4$ and $CoFe_2O_4$ based on the spin moments of the divalent ions may be originated from different intrinsic cation distributions. In terms of size effect, increased M_s were observed with increased nanoparticle size disregarding the type of the spinel ferrites, which can be explained by the existence of the surface magnetically-disordered layer. Moreover, the critical size had been identified to fall within the 7-11 nm range for $NiFe_2O_4$ since the M_s reached a plateau even with further increased size in this range. To sum up, by capitalizing star-like diblock copolymers with controlled molecular weight, various kinds of inorganic NPs with tailorable dimension and composition can be acquired and the dependence of desired properties on size and composition can be clarified. In addition, the spinel ferrite NPs synthesized in this study with excellent features, including superparamagnetic behavior, high M_s, and good solubility in different kinds of solvents, exhibit great potential in both catalytic and biomagnetic applications.

7.5 References

1. Deng, H.; Li, X.; Peng, Q.; Wang, X.; Chen, J.; Li, Y., Monodisperse magnetic single-crystal ferrite microspheres. *Angewandte Chemie* **2005,** *117* (18), 2842-2845.
2. Ho, D.; Sun, X.; Sun, S., Monodisperse magnetic nanoparticles for theranostic applications. *Accounts of chemical research* **2011,** *44* (10), 875-882.
3. Park, J.; Lee, E.; Hwang, N. M.; Kang, M.; Kim, S. C.; Hwang, Y.; Park, J. G.; Noh, H. J.; Kim, J. Y.; Park, J. H., One-nanometer-scale size-controlled synthesis of monodisperse magnetic Iron oxide nanoparticles. *Angewandte Chemie International Edition* **2005,** *44* (19), 2872-2877.
4. Vestal, C. R.; Zhang, Z. J., Effects of surface coordination chemistry on the magnetic properties of MnFe2O4 spinel ferrite nanoparticles. *Journal of the American Chemical Society* **2003,** *125* (32), 9828-9833.
5. Song, Q.; Zhang, Z. J., Shape control and associated magnetic properties of spinel cobalt ferrite nanocrystals. *Journal of the American Chemical Society* **2004,** *126* (19), 6164-6168.
6. Ramirez, A.; Cava, R. J.; Krajewski, J., Colossal magnetoresistance in Cr-based chalcogenide spinels. *Nature* **1997,** *386* (6621), 156-159.
7. Cheng, F.; Liao, C.; Kuang, J.; Xu, Z.; Yan, C.; Chen, L.; Zhao, H.; Liu, Z., Nanostructure magneto-optical thin films of rare earth (RE= Gd, Tb, Dy) doped cobalt spinel by sol–gel synthesis. *Journal of applied physics* **1999,** *85* (5), 2782-2786.
8. Bárcena, C.; Sra, A. K.; Chaubey, G. S.; Khemtong, C.; Liu, J. P.; Gao, J., Zinc ferrite nanoparticles as MRI contrast agents. *Chemical communications* **2008,** (19), 2224-2226.
9. Sanpo, N.; Berndt, C. C.; Wen, C.; Wang, J., Transition metal-substituted cobalt ferrite nanoparticles for biomedical applications. *Acta Biomaterialia* **2013,** *9* (3), 5830-5837.
10. Gao, X.; Zhang, H.; Li, Q.; Yu, X.; Hong, Z.; Zhang, X.; Liang, C.; Lin, Z., Hierarchical NiCo2O4 hollow microcuboids as bifunctional electrocatalysts for overall water-splitting. *Angewandte Chemie International Edition* **2016,** *55* (21), 6290-6294.
11. Lottini, E.; López-Ortega, A.; Bertoni, G.; Turner, S.; Meledina, M.; Van Tendeloo, G.; de Julián Fernández, C.; Sangregorio, C., Strongly exchange coupled core| shell nanoparticles with high magnetic anisotropy: a strategy toward rare-earth-free permanent magnets. *Chemistry of Materials* **2016,** *28* (12), 4214-4222.
12. Kharat, P. B.; Somvanshi, S. B.; Kounsalye, J. S.; Deshmukh, S. S.; Khirade, P. P.; Jadhav, K. In *Temperature dependent viscosity of cobalt ferrite/ethylene glycol ferrofluids*, AIP Conference Proceedings, AIP Publishing LLC: 2018; p 050044.
13. Parker, F.; Spada, F.; Cox, T.; Berkowitz, A., Spin-glass behavior of spinel iron oxide particles on iron metal particle recording media. *Journal of applied physics* **1995,** *77* (11), 5853-5864.
14. Sun, S.; Zeng, H.; Robinson, D. B.; Raoux, S.; Rice, P. M.; Wang, S. X.; Li, G., Monodisperse mfe2o4 (m= fe, co, mn) nanoparticles. *Journal of the American Chemical Society* **2004,** *126* (1), 273-279.
15. Frey, N. A.; Peng, S.; Cheng, K.; Sun, S., Magnetic nanoparticles: synthesis, functionalization, and applications in bioimaging and magnetic energy storage. *Chemical Society Reviews* **2009,** *38* (9), 2532-2542.
16. Sharifi Dehsari, H.; Asadi, K., Impact of Stoichiometry and Size on the Magnetic Properties of Cobalt Ferrite Nanoparticles. *The Journal of Physical Chemistry C* **2018,** *122* (51), 29106-29121.
17. Lee, J.-H.; Huh, Y.-M.; Jun, Y.-w.; Seo, J.-w.; Jang, J.-t.; Song, H.-T.; Kim, S.; Cho, E.-J.; Yoon, H.-G.; Suh, J.-S., Artificially engineered magnetic nanoparticles for ultra-sensitive molecular imaging. *Nature medicine* **2007,** *13* (1), 95-99.
18. Chinnasamy, C.; Jeyadevan, B.; Shinoda, K.; Tohji, K.; Djayaprawira, D.; Takahashi, M.; Joseyphus, R. J.; Narayanasamy, A., Unusually high coercivity and critical single-domain size of nearly monodispersed CoFe 2 O 4 nanoparticles. *Applied Physics Letters* **2003,** *83* (14), 2862-2864.

19. Zavyalova, U.; Nigrovski, B.; Pollok, K.; Langenhorst, F.; Müller, B.; Scholz, P.; Ondruschka, B., Gel-combustion synthesis of nanocrystalline spinel catalysts for VOCs elimination. *Applied Catalysis B: Environmental* **2008,** *83* (3-4), 221-228.
20. Liu, C.; Zhang, Z. J., Size-dependent superparamagnetic properties of Mn spinel ferrite nanoparticles synthesized from reverse micelles. *Chemistry of Materials* **2001,** *13* (6), 2092-2096.
21. Liu, J.; Sun, B.; Hu, J.; Pei, Y.; Li, H.; Qiao, M., Aqueous-phase reforming of ethylene glycol to hydrogen on Pd/Fe3O4 catalyst prepared by co-precipitation: Metal–support interaction and excellent intrinsic activity. *Journal of Catalysis* **2010,** *274* (2), 287-295.
22. Bao, N.; Shen, L.; Wang, Y.; Padhan, P.; Gupta, A., A facile thermolysis route to monodisperse ferrite nanocrystals. *Journal of the American Chemical Society* **2007,** *129* (41), 12374-12375.
23. Pang, X.; Feng, C.; Xu, H.; Han, W.; Xin, X.; Xia, H.; Qiu, F.; Lin, Z., Unimolecular micelles composed of inner coil-like blocks and outer rod-like blocks crafted by combination of living polymerization with click chemistry. *Polymer Chemistry* **2014,** *5* (8), 2747-2755.
24. Kim, D. H.; Kim, T. C.; Lee, S. H.; Han, S. H.; Han, K.-S.; Ross, C., Self-assembled growth of Sr (Ti, Fe) O3–CoFe2O4 magnetic nanocomposite thin films. *Journal of Applied Physics* **2017,** *121* (16), 163902.
25. Kumar, Y.; Sharma, A.; Shirage, P. M., Shape-controlled CoFe 2 O 4 nanoparticles as an excellent material for humidity sensing. *RSC advances* **2017,** *7* (88), 55778-55785.
26. Cao, D.; Pan, L.; Li, J.; Cheng, X.; Zhao, Z.; Xu, J.; Li, Q.; Wang, X.; Li, S.; Wang, J., Investigation on the structures and magnetic properties of carbon or nitrogen doped cobalt ferrite nanoparticles. *Scientific reports* **2018,** *8* (1), 1-9.
27. Pal, M.; Rakshit, R.; Mandal, K., Surface modification of MnFe2O4 nanoparticles to impart intrinsic multiple fluorescence and novel photocatalytic properties. *ACS applied materials & interfaces* **2014,** *6* (7), 4903-4910.
28. Yu, J.; Kudo, A., Effects of structural variation on the photocatalytic performance of hydrothermally synthesized BiVO4. *Advanced Functional Materials* **2006,** *16* (16), 2163-2169.
29. Zenoozi, S.; Agbolaghi, S.; Poormahdi, E.; Hashemzadeh-Gargari, M.; Mahmoudi, M., Verification of Scherrer formula for well-shaped poly (3-hexylthiophene)-based conductive single crystals and nanofibers and fabrication of photovoltaic devices from thin film coating. *Macromolecular Research* **2017,** *25* (8), 826-840.
30. Liu, S.; Xie, J.; Su, Q.; Du, G.; Zhang, S.; Cao, G.; Zhu, T.; Zhao, X., Understanding Li-storage mechanism and performance of MnFe2O4 by in situ TEM observation on its electrochemical process in nano lithium battery. *Nano Energy* **2014,** *8*, 84-94.
31. Aghavnian, T.; Moussy, J.-B.; Stanescu, D.; Belkhou, R.; Jedrecy, N.; Magnan, H.; Ohresser, P.; Arrio, M.-A.; Sainctavit, P.; Barbier, A., Determination of the cation site distribution of the spinel in multiferroic CoFe2O4/BaTiO3 layers by X-ray photoelectron spectroscopy. *Journal of Electron Spectroscopy and Related Phenomena* **2015,** *202*, 16-21.
32. Li, P.; Ma, R.; Zhou, Y.; Chen, Y.; Zhou, Z.; Liu, G.; Liu, Q.; Peng, G.; Liang, Z.; Wang, J., In situ growth of spinel CoFe 2 O 4 nanoparticles on rod-like ordered mesoporous carbon for bifunctional electrocatalysis of both oxygen reduction and oxygen evolution. *Journal of Materials Chemistry A* **2015,** *3* (30), 15598-15606.
33. Liu, J.; Zhu, D.; Ling, T.; Vasileff, A.; Qiao, S.-Z., S-NiFe2O4 ultra-small nanoparticle built nanosheets for efficient water splitting in alkaline and neutral pH. *Nano Energy* **2017,** *40*, 264-273.
34. Yadav, R. S.; Kuřitka, I.; Vilcakova, J.; Havlica, J.; Masilko, J.; Kalina, L.; Tkacz, J.; Švec, J.; Enev, V.; Hajdúchová, M., Impact of grain size and structural changes on magnetic, dielectric, electrical, impedance and modulus spectroscopic characteristics of CoFe2O4 nanoparticles synthesized by honey mediated sol-gel combustion method. *Advances in Natural Sciences: Nanoscience and Nanotechnology* **2017,** *8* (4), 045002.
35. Grosvenor, A.; Kobe, B.; Biesinger, M.; McIntyre, N., Investigation of multiplet splitting of Fe 2p XPS spectra and bonding in iron compounds. *Surface and Interface Analysis: An International Journal*

devoted to the development and application of techniques for the analysis of surfaces, interfaces and thin films **2004,** *36* (12), 1564-1574.
36. Szotek, Z.; Temmerman, W.; Ködderitzsch, D.; Svane, A.; Petit, L.; Winter, H., Electronic structures of normal and inverse spinel ferrites from first principles. *Physical Review B* **2006,** *74* (17), 174431.
37. Chinnasamy, C.; Narayanasamy, A.; Ponpandian, N.; Chattopadhyay, K.; Shinoda, K.; Jeyadevan, B.; Tohji, K.; Nakatsuka, K.; Furubayashi, T.; Nakatani, I., Mixed spinel structure in nanocrystalline NiFe 2 O 4. *Physical Review B* **2001,** *63* (18), 184108.
38. Patange, S.; Shirsath, S. E.; Jangam, G.; Lohar, K.; Jadhav, S. S.; Jadhav, K., Rietveld structure refinement, cation distribution and magnetic properties of Al3+ substituted NiFe2O4 nanoparticles. *Journal of Applied Physics* **2011,** *109* (5), 053909.
39. Wang, W.; Ding, Z.; Zhao, X.; Wu, S.; Li, F.; Yue, M.; Liu, J. P., Microstructure and magnetic properties of MFe2O4 (M= Co, Ni, and Mn) ferrite nanocrystals prepared using colloid mill and hydrothermal method. *Journal of Applied Physics* **2015,** *117* (17), 17A328.
40. Graves, P.; Johnston, C.; Campaniello, J., Raman scattering in spinel structure ferrites. *Materials Research Bulletin* **1988,** *23* (11), 1651-1660.
41. Julien, C.; Massot, M., Raman spectroscopic studies of lithium manganates with spinel structure. *Journal of Physics: Condensed Matter* **2003,** *15* (19), 3151.
42. Kamble, R. B.; Varade, V.; Ramesh, K.; Prasad, V., Domain size correlated magnetic properties and electrical impedance of size dependent nickel ferrite nanoparticles. *AIP Advances* **2015,** *5* (1), 017119.
43. Ahlawat, A.; Sathe, V.; Reddy, V.; Gupta, A., Mossbauer, Raman and X-ray diffraction studies of superparamagnetic NiFe2O4 nanoparticles prepared by sol–gel auto-combustion method. *Journal of Magnetism and Magnetic Materials* **2011,** *323* (15), 2049-2054.
44. Xu, Y.; Sherwood, J.; Qin, Y.; Holler, R. A.; Bao, Y., A general approach to the synthesis and detailed characterization of magnetic ferrite nanocubes. *Nanoscale* **2015,** *7* (29), 12641-12649.
45. Rath, C.; Anand, S.; Das, R.; Sahu, K.; Kulkarni, S.; Date, S.; Mishra, N., Dependence on cation distribution of particle size, lattice parameter, and magnetic properties in nanosize Mn–Zn ferrite. *Journal of Applied Physics* **2002,** *91* (4), 2211-2215.
46. Matzen, S.; Moussy, J.-B.; Mattana, R.; Bouzehouane, K.; Deranlot, C.; Petroff, F.; Cezar, J.; Arrio, M.-A.; Sainctavit, P.; Gatel, C., Epitaxial growth and ferrimagnetic behavior of MnFe 2 O 4 (111) ultrathin layers for room-temperature spin filtering. *Physical Review B* **2011,** *83* (18), 184402.
47. Atif, M.; Hasanain, S.; Nadeem, M., Magnetization of sol–gel prepared zinc ferrite nanoparticles: effects of inversion and particle size. *Solid State Communications* **2006,** *138* (8), 416-421.
48. Li, J.; Yuan, H.; Li, G.; Liu, Y.; Leng, J., Cation distribution dependence of magnetic properties of sol–gel prepared MnFe2O4 spinel ferrite nanoparticles. *Journal of Magnetism and Magnetic Materials* **2010,** *322* (21), 3396-3400.
49. Yáñez-Vilar, S.; Sánchez-Andújar, M.; Gómez-Aguirre, C.; Mira, J.; Señarís-Rodríguez, M. A.; Castro-García, S., A simple solvothermal synthesis of MFe2O4 (M= Mn, Co and Ni) nanoparticles. *Journal of Solid State Chemistry* **2009,** *182* (10), 2685-2690.
50. Andersen, H. L.; Saura-Múzquiz, M.; Granados-Miralles, C.; Canévet, E.; Lock, N.; Christensen, M., Crystalline and magnetic structure–property relationship in spinel ferrite nanoparticles. *Nanoscale* **2018,** *10* (31), 14902-14914.
51. Shaterabadi, Z.; Nabiyouni, G.; Soleymani, M., High impact of in situ dextran coating on biocompatibility, stability and magnetic properties of iron oxide nanoparticles. *Materials Science and Engineering: C* **2017,** *75*, 947-956.
52. George, M.; John, A. M.; Nair, S. S.; Joy, P.; Anantharaman, M., Finite size effects on the structural and magnetic properties of sol–gel synthesized NiFe2O4 powders. *Journal of Magnetism and Magnetic Materials* **2006,** *302* (1), 190-195.

CHAPTER 8. GENERAL CONCLUSION AND BROADER IMPACTS

8.1 General conclusion

In this dissertation, we have first synthesized star-like triblock copolymer consisting of poly(4-vinyl pyridine) (P4VP) and poly(acrylic acid) (PAA) as the first and second block with tailorable molecular weight of each block and narrow molecular weight distribution. In addition, functional nanomaterials with tailorable size, composition, crystal structure, and dopant/doping concentration can be achieved via this robust synthetic strategy based on capitalizing well-defined amphiphilic and hydrophilic star-like diblock copolymers as nanoreactors, enabling systematic studies on the dependence of the desired properties (i.e., electrocatalytic activities and magnetic properties) on these tunable factors.

In the first part of this dissertation, star-like diblock and triblock copolymers with pyridine-group containing polymer (P4VP) as the first block with controlled molecular weight distribution, which is difficult to achieve by atom transfer radical polymerization (ATRP) due to easy occurrence of the coupling reaction, were successfully obtained by addition of linear initiator when polymerizing the second poly(*tert*-butyl acrylate) (P*t*BA) block. By adding the optimal amount of linear initiator, the molar ratio between initiate sites to metal catalysts can be increased to 1 to 1, resulting in suppressed tendency of arm-arm and star-star coupling and reduced polydispersity of the star-like polymers. The kinetic studies of polymerization the second P*t*BA block with and without the addition of linear initiators have been conducted and the linear relationship of $\ln([M]_0/[M]_t)$ vs. time can only be found when additional linear initiator was introduced, indicating constant propagating species during the polymerization only happened under this synthetic condition. In addition, three kinds of monomers, including styrene, methyl methacrylate, and ethylene oxide, were chosen as the monomer for the third block of star-like polymer and successful

polymerizations by ATRP for polystyrene (PS) and poly(methyl methacrylate) as well as click reaction for poly(ethylene oxide) were performed, signifying the high flexibility of modulating the surface chemistry of the star-like triblock copolymers. Finally, the dual pH-responsive behavior of hydrophilic star-like P4VP-*b*-PAA diblock copolymer was explored. By extension, the developed synthetic strategy based on sequential ATRP via cyclodextrin as initiator may enable the synthesis of a large diversity of other stimuli-responsive star-like block copolymer consisting of dissimilar blocks that are either pH-responsive, thermo-responsive or photo-responsive, opening the avenue for fundamental research and potential applications in smart delivery vehicles, sensors, and tunable templates for nanomaterials.

In the second part of this dissertation, by employing star-like PAA-*b*-PS diblock copolymer as nanoreactor, perovskite oxide nanoparticles, including $BaTiO_3$, $PbTiO_3$, $LaFeO_3$, and $LaMnO_3$, as well as layered perovskite oxide nanoparticles (La_2CoO_4) with tailorable dimension, crystal structure, dopant type, and doping concentration can be crafted. Simply by the coordination of metal moieties within precursors and carboxylic acid group of inner PAA block, the precursors can be loaded within the PAA compartment, and nanoparticle can be obtained after thermolysis of the precursors. Therefore, the size of the as-synthesized nanoparticle can be facilely modulated by changing the molecular weight of the inner PAA block. Furthermore, the outer PS block was covalently-ligated on the surface of the nanoparticles, preventing aggregation of nanoparticle during the purification process and enhancing solubility of the as-synthesized nanoparticle in common organic solvents. Furthermore, doping the as-synthesized nanoparticle can be easily achieved by adding the dopant precursors with the pre-determined amount during nanoparticle synthesis. The electrocatalytic performance of pristine and doped perovskite oxide as well as layered perovskite oxide materials, dispersed on graphene oxide, was measured. The improved

oxygen reduction reaction activity when particle size was reduced and doped with other elements (lanthanum (La) and cobalt (Co)-doped $BaTiO_3$) was discovered and discussed, which can be attributed to increased active sites (for reduced particle size) and reduced free energy barrier during oxygen reduction reaction (ORR) as well as increased conductivity (for introducing dopants) based on DFT calculation. On the other hand, the remarkable bifunctional electrocatalytic activities of layered La_2CoO_4 perovskite nanoparticles for both ORR and oxygen evolution reaction (OER) were exhibited, possibly resulting from highly active lattice oxygen and an increased amount of hydroxyl groups on the surface of the catalysts. Overall, this synthetic strategy rendered a new platform for acquiring a rich diversity of electrocatalysts with excellent activities by changing the size, composition, crystal structure, dopant as well as surface chemistry for advanced energy storage and conversion devices.

In the third part of this dissertation, star-like PAA-*b*-poly(styrene-co-acrylonitrile) (PSAN) diblock copolymers were similarly employed as nanoreactors for magnetic spinel nanoparticle synthesis. By capitalizing coordination between precursors and the functional group within PAA, precursors and the as-synthesized nanoparticles can again be formed within the compartment of PAA, rendering the capability of tuning the size of the as-synthesized spinel nanoparticles. In particular, we used diphenyl ether (DPE) as the major solvent for nanoparticle synthesis due to the following reasons. First, due to the different polarity between DPE and star-like diblock copolymer, precursors had a higher tendency to coordinate with the nanoreactor, thus leading to better control over morphology and size uniformity of the as-synthesized nanoparticles as well as higher yield for further characterization. Second, because DPE possessed higher boiling temperature, the reaction temperature (i.e., the refluxing temperature of the solvent) was high enough for obtaining the nanoparticles with great crystallinity, facilitating further properties investigation. Herein,

spinel magnetic nanoparticles with varied compositions, i.e., $CoFe_2O_4$, $MnFe_2O_4$, and $NiFe_2O_4$, as well as varied sizes, i.e., 4, 7, 11 nm, were successfully acquired. Furthermore, simply via changing the outer hydrophobic PS block in hydrophilic PEO block, the surface chemistry of the spinel magnetic nanoparticles can be tailored, providing additional applications, especially in the biomedical field. Finally, we interrogated the size effect and composition effect on magnetic properties with the as-synthesized spinel magnetic nanoparticles. The saturation magnetization (M_s), using the as-synthesized nanoparticles with the largest size as an example, followed the order of $NiFe_2O_4$ < $MnFe_2O_4$ < $CoFe_2O_4$. The smallest M_s for $NiFe_2O_4$ was expected because the magnetic moment that Ni^{2+} ions provided was the smallest. However, the order between $MnFe_2O_4$ and $CoFe_2O_4$ was inconsistent with the expected magnetic moment of respective transition ions, which may be originated from different cation distribution for these two materials. On the other hand, the M_s decreased as the size of the nanoparticle decreased, possibly resulted from the increased ratio of the magnetically-dead surface layer when the size of the nanoparticle decreased. In summary, the spinel nanoparticles that were synthesized with this polymer-assisted strategy demonstrated excellent magnetic properties, including superparamagnetic behavior, high saturation magnetization, and good solubility in various kinds of organic solvents, suggesting their promising potentials in both catalytic and biomedical applications.

8.2 Significance and broader impact

The discoveries presented in this dissertation not only provide a robust synthetic approach for both star-like diblock and triblock copolymer as well as a rich diversity of functional nanoparticles, but also investigate the correlation of morphology, composition, crystal structure and resulting desired properties. Both the electrocatalytic properties, i.e., ORR and OER, and the magnetic

properties measurement and discussion rendered mechanisms behind varied performances, opening avenues for determining/optimizing the materials afterward, which can potentially be used in energy-related and/or biomedical applications.

The first significance of this dissertation was the capability of controlling the size, composition, crystal structure, and uniformity of the desired nanoparticles via employing this polymer-assisted synthetic strategy. A wide range of materials with different crystal structures, i.e., perovskite oxides, layered perovskite oxide, and spinel ferrites, were successfully synthesized with controlled morphology and excellent solubility in common organic solvents. In particular, this precise control over the size and uniformity of perovskite oxides is rarely achieved due to the high formation energy required for synthesizing perovskite oxides, leading to easy aggregation and irregular shape. In the second part of this dissertation, we demonstrated the size of monodispersed perovskite oxides, including $BaTiO_3$ and $PbTiO_3$ nanoparticles can be precisely tailored from 8 nm, 16 nm to 20 nm with narrow size distribution simply by modulating the molecular weight of the inner PAA block of the star-like diblock copolymer. In particular, kinetic studies on the formation of the as-synthesized nanoparticle was conducted by observing the morphological evolution under varied reaction times. Based on this study, we found that nanoparticle size increased abruptly in the beginning and reached a plateau at a specific size. After that, nanoparticle size remained similar and well-dispersed even with prolonged reaction time and relatively high reaction temperature. The capability of synthesizing uniform $BaTiO_3$ nanoparticles with tailorable sizes enables the systematic study of the size effect on the electrocatalytic performance of $BaTiO_3$ nanoparticles, which can be applied for preparing other types of promising electrocatalysts in the future. Additionally, in the third part of this dissertation, spinel ferrites nanoparticles with changeable size, i.e., 4, 7, 11 nm were synthesized by using star-like diblock copolymer as nanoreactor. Similarly,

the size can be facilely tuned by changing the molecular weight of the PAA block. Size-dependent magnetic properties were measured with all the spinel ferrite nanoparticle synthesized. Specifically, the critical size of $NiFe_2O_4$ for the transition from single-domain to multi-domains structure had been identified to located between 7-11 nm, whereas the critical size of the other two spinel ferrites nanoparticles should be larger than 11 nm, suggesting this critical size can be heavily influenced by different synthetic approaches as well as varied surface chemistries.

The second significance of this dissertation lied in identifying the promising electrocatalysts for both ORR and OER. For instance, perovskite oxides have been widely studied as electrocatalysts due to their low-cost, highly-abundant and excellent flexibility for accommodating a rich diversity of cations in both A site and B site, while very limited research looked into the electrocatalytic performance of $BaTiO_3$, possibly because it's intrinsic electrocatalytic activity is not as good as others. Here, we not only investigated the size-effect of $BaTiO_3$ nanoparticle on the ORR performance, but also prove that $BaTiO_3$ nanoparticle, with only small doping concentration, can also be excellent electrocatalysts. Further improvement can be anticipated if the dopant types and doping concentration are judiciously chosen. Besides synthesizing $BaTiO_3$ and $PbTiO_3$, we also successfully obtained La-based nanoparticles, including $LaFeO_3$, $LaMnO_3$, and La_2CoO_4, and employed them as bifunctional electrocatalysts for both ORR and OER. Layered perovskite La_2CoO_4 exhibited the best performance for both reactions among three La-based nanoparticles, which surprised us because the electrocatalytic activity, especially at low temperature, of layered perovskite had seldomly been discussed. The result indicated the possibility to capitalize layered perovskite as potential candidates for bifunctional electrocatalysts, further discussion on the origin for this outperform activity of layered perovskite has also been provided.

The third significance of this dissertation was to elucidate the enhancement after doping $BaTiO_3$ nanoparticle with La and Co by simulation results. Based on the results, the enhancement after doping can be attributed to two main reasons. First, the free energy barrier of ORR was reduced after doping with both dopants, resulting from the enhancement of the adsorption of the intermediates during ORR. However, the origin of the increased adsorption for two dopants was different. In the La-doping case, the increase was due to pronounced charge transfer between catalysts and intermediates, whereas in the Co-doping case, the increase was because of stronger hybridization of t_{2g} orbital of Co with the intermediates. Second, the conductivity was enhanced after doping with both dopants, which is originated from the modification of electronic states. By clearly correlating the fundamental changes with enhanced electrocatalytic activity, these results may provide the guidelines for rationally design the electrocatalysts with optimized performance.

DISIMINATION OF WORK

The work presented in this dissertation has been conveyed to the scientific community by the following publications and presentations.

Publication

1. **Y. W. Harn**, Y. He, Z. Wang, Y. Chen, S. Liang, Z. Li, Q. Li, L. Zhu, and Z. Lin, "Synthesis of Amphiphilic and Double Hydrophilic Star-Like Block Copolymers and the Dual pH-Responsiveness of Unimolecular Micelle", *submitted to Macromolecule (under review)*

2. **Y. W. Harn**, Z. Wang, S. Liu, Y. Yan, J. Jun, Q. Li, Y. He, L. Zhu, H. Cheng, and Z. Lin, "Tailoring Electrocatalytic Activity of in-situ Crafted Perovskite Oxide Nanocrystals via Precise Size and Dopant Control", *submitted to Proceedings of the National Academy of Sciences of the United States of America*

3. **Y. W. Harn**, Y. Yan, Z. Li, and Z. Lin, "Monodisperse, Ruddlesden-Popper Layered perovskite Nanocatalysts with Controllable Size for Enhanced Oxygen Reduction and Evolution Reactions", *in preparation*.

4. **Y. W. Harn**, Z. Wang, J. Yu, M. Mourigal, and Z. Lin, "Facile manipulation of magnetic properties of spinel MFe_2O_4 (M = Co, Ni, Mn) nanoparticles via robust size and composition engineering", *in preparation*.

5. X. Cui, Y. Chen, M. Zhang, **Y. W. Harn**, J. Qi, L. Gao, Z. Wang, J. Huang, Y. Yang and Z. Lin, "Tailoring carrier dynamics in perovskite solar cells via precise dimension and architecture control and interfacial positioning of plasmonic nanoparticles" ***Energy Environ. Sci***., 2020, 13, 1743.

6. Y. He, Y. Yoon, **Y. W. Harn**, G. Biesold-McGee, C. Lin, V. Tsukruk, N. Thadhani, Z. Kang, and Z. Lin, "Unconventional Route to Dual-Shelled Organolead Halide Perovskite Nanocrystals with Controlled Dimensions, Surface Chemistry and Stabilities", ***Sci. Adv.***, 2019, 5, eaax4424.

7. Y. Chen, Z. Wang, **Y. W. Harn**, S. Pan, Z. Li, S. Lin, J. Peng, G. Zhang, and Z. Lin*, "Resolving Optical and Catalytic Activities in Thermoresponsive Nanoparticles by Permanent Ligation with Temperature-Sensitive Polymers" ***Angew. Chem. Int. Ed***, 2019, 58, 2.

8. S. Zhao, Z. Wang, Y. He, H. Jiang, **Y. W. Harn**, X. Liu, C. Su, H. Jin, Y. Li, S. Wang, Q. Shen, and Z. Lin, "A Robust Route to $Co_2(OH)_2CO_3$ Ultrathin Nanosheets with Superior Lithium Storage Capability Templated by Aspartic Acid-Functionalized Graphene Oxide", ***Adv. Energy Mater.***, 2019, 9, 1901093.

9. B. Jiang, J. Iocozzia, L. Zhao, H. Zhang, **Y. W. Harn**, Y. Chen, and Z. Lin*, "Barium Titanate at the Nanoscale: Controlled Synthesis and Dielectric and Ferroelectric Properties", ***Chemical Society Reviews***, 2019, 48, 1194.

10. X. Meng, X. Cui, M. Rager, S. Zhang, Z. Wang, J. Yu, **Y. W. Harn**, Z. Kang, B. K. Wanger, Y. Liu, C. Yu, J . Qiu and Z. Lin*. Cascade charge transfer enabled by incorporating edge enriched graphene nanoribbons for mesostructured perovskite solar cells with enhanced performance. ***Nano Energy***, 2018, 52, 123.

11. Y. He, X. Pang, B. Jiang, C. Feng, **Y. W. Harn**, Y. Chen, Y. Yoon, S. Pan, C. Lu, Y. Chang, M. Zebarjadi, Z. Kang, N. Thadhani, J. Peng and Zhiqun Lin*. Unconventional Route to Uniform Hollow Semiconducting Nanoparticles with Tailorable Dimensions, Compositions, Surface Chemistry, and Near-Infrared Absorption. ***Angew. Chem. Int. Ed***, 2017, 56, 12946.

12. Y. Chen, D. Yang, Y. Yoon, X. Pang, Z. Wang, J. Jung, Y. He, **Y. W. Harn**, M. He, S. Zhang, G. Zhang, and Z. Lin*. Hairy Uniform Permanently-Ligated Hollow Nanoparticles with Precise Dimension Control and Tunable Optical Properties. ***J. Am. Chem. Soc.***, 2017, 139, 12956.

13. S. Zhao, Z. Wang, Y. He, B. Jiang, **Y. W. Harn**, X. Liu, F. Yu, F. Feng, Q. Shen, and Z. Lin*. Interconnected $Ni(HCO_3)_2$ Hollow Spheres Enabled by Self Sacrificial Templating with Enhanced Lithium Storage Properties, ***ACS Energy Letters***, 2017, 2, 111.

Presentation

1. **Y. W. Harn**, and Z. Lin. Monodisperse Perovskite Oxide Nanocrystals with Tunable Size and Composition for Enhanced Oxygen Reduction Reaction. (Oral) 2019/10 Presented at Southeastern Regional ACS Meeting (SERMACS)

2. **Y. W. Harn**, Y. Chen, and Z. Lin*. A Versatile Approach for Functional Nanoparticle Synthesis. (Poster) 2018 Presented at the 2nd National Graduate Research Polymer Conference (NGRPC)

Awards

Jewell Family Fellowship, *Georgia Tech*, 2018